Transition de spin thermo- et photo-induite dans de nouveaux systèmes discrets, polynucléaires et polymériques

Eric Milin

université de bretagne occidentale

THÈSE / UNIVERSITÉ DE BRETAGNE OCCIDENTALE
sous le sceau de l'Université européenne de Bretagne

pour obtenir le titre de
DOCTEUR DE L'UNIVERSITÉ DE BRETAGNE OCCIDENTALE
Mention : Chimie Moléculaire
École Doctorale SICMA

présentée par
Eric Milin
Préparée à l'UFR Sciences et Techniques

Transition de spin thermo- et photo-induite dans de nouveaux systèmes discrets, polynucléaires et polymériques.

Thèse soutenue le 14 décembre 2015
devant le jury composé de :

Rabah Boukherroub
Directeur de Recherche, Université de Lille I / *Rapporteur*

Jean-Luc Fillaut
Directeur de Recherche, Université de Rennes I / *Rapporteur*

Kamel Boukheddaden
Professeur, Université de Versailles / *Examinateur*

Frédéric Gloaguen
Directeur de Recherche, Université de Brest / *Examinateur*

Véronique Patinec
Maître de Conférences, Université de Brest / *Examinateur*

Smail Triki
Professeur, Université de Brest / *Examinateur*

Sommaire

Chapitre III Réseau monodimensionnel

Chapitre IV Réseaux bi- et tri-dimensionnels

Introduction générale

Durant ces dernières années, l'électronique moléculaire et plus particulièrement les matériaux à transition de spin ont suscité beaucoup d'intérêts, en raison de leurs nombreuses applications potentielles telles que le stockage d'information et l'affichage.[1,3] Le phénomène de transition de spin ou SCO en anglais (Spin Cross-Over) se rencontre dans les complexes des métaux de transition de configuration électronique comprise entre d^4 et d^7. Selon la force du champ du ligand, ces complexes présentent une transition réversible "Haut Spin (HS)-Bas Spin (BS)" sous l'effet d'une perturbation extérieure (température, irradiation, champ magnétique, pression...).[3-5] Parmi les complexes à transition de spin, les plus étudiés sont les complexes des ions Fer (II) de configuration d^6. Dans un environnement pseudo-octaédrique de type $[FeN_6]$, ces complexes présentent une transition entre un état haut-spin (HS, S=2, $^5T_{2g}$) paramagnétique et un état bas-spin (BS, S=0, $^1A_{1g}$) diamagnétique si l'énergie du champ de ligand est proche de l'énergie d'appariement des électrons (notée P).

Selon la coopérativité du système, dépendant essentiellement des interactions faibles intermoléculaires et donc de l'élasticité (propagation d'une distorsion moléculaire dans le réseau) ou de l'efficacité du système à propager l'information du changement d'état de spin des centres métalliques, on peut rencontrer des transitions thermiques graduelles, abruptes ou abruptes avec une hystérésis (cf. chapitre 1). Pour ce dernier type de transition, on parle alors de bistabilité moléculaire qui est la caractéristique la plus recherchée dans le domaine des matériaux commutables.

En plus de la transition thermique, un système à transition de spin peut se distinguer également par la présence de transitions photo-induites. Ce phénomène, correspondant à la possibilité d'induire une transition BS→HS ou HS→BS par une irradiation lumineuse, présente également un intérêt en raison des applications potentielles dans le domaine du stockage de l'information notamment. Lorsque la longueur d'onde d'excitation est située dans le vert (autour de 520 nm), on parle de l'effet LIESST (Light-Induced Excited Spin-State Trapping), correspondant à l'obtention de l'état HS métastable photo-induit. Le phénomène inverse connu sous le nom de Reverse-LIESST (Reverse-Light-Induced Excited Spin-State Trapping) peut se produire lorsque la longueur d'onde de l'excitation lumineuse est située dans le rouge (autour de 800 nm). Deux situations sont possibles selon l'état de spin du système à basse

température (10 K). Dans le cas le plus courant, l'état HS photo-induit métastable obtenu par effet LIESST relaxe à l'état BS par augmentation de la température. Dans l'autre cas, si la transition thermique n'est pas complète (présence d'une fraction HS résiduelle après la transition thermique), l'effet reverse-LIESST permet de transformer la totalité ou une partie de la fraction HS résiduelle à l'état BS.[6]

Dans ce contexte, les deux objectifs principaux de ce travail concernent : (i) l'optimisation des caractéristiques de la transition de spin comme la coopérativité et la largeur des hystérésis ; (ii) l'allongement de la durée de vie des états HS métastables photo-induits.

A ce jour, de nombreux matériaux moléculaires à transition de spin ont été synthétisés et décrits dans la littérature, mais l'impact des ligands anioniques sur les propriétés de commutation n'a jamais été étudié. Ainsi, pour atteindre ces deux objectifs, nous avons envisagé, au début de ce travail, l'association d'anions polycyanides, dotés d'un système d'électrons π hautement conjugués et de géométrie et charges très variées aux co-ligands contraignants se caractérisant par des modes de coordination variés et originaux (Schéma 1).

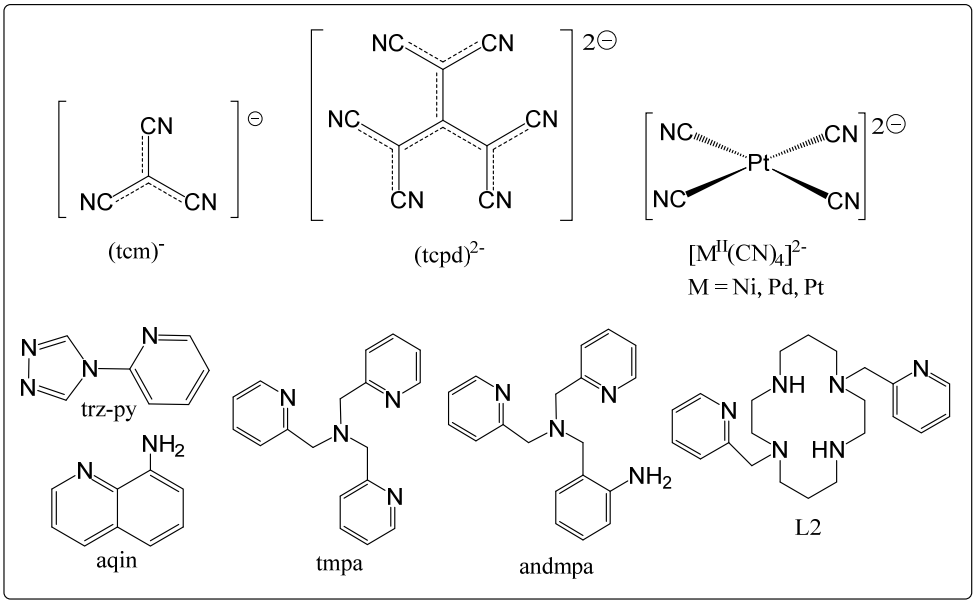

Schéma 1 : Exemples de ligands utilisés pour ce travail

Après avoir rappelé quelques généralités sur la transition de spin dans un premier chapitre, nous verrons dans le deuxième chapitre la synthèse, la caractérisation et les propriétés de deux systèmes discrets : le premier, de formule $[Fe(L2)](tcm)_2.2H_2O$ est un complexe mononucléaire bistable à base de tétraazamacrocycle (L2, Schéma 1) et

le second, de formule $[Fe_2(andmpa)_2(\mu_2\text{-}tcpd)_2].2CH_3OH$, est un complexe dinucléaire. Le troisième chapitre sera dédié à l'étude un système bimétallique monodimensionnel de formule $[Fe(aqin)_2(\mu_2\text{-}M(CN)_4)]$ (M=Ni, Pd, Pt). Enfin, dans la dernière partie, nous présenterons deux systèmes à structures étendues, $[Fe(trz\text{-}py)(tcpd)(H_2O)]$ et $[Fe(trz\text{-}py)_2(Pt(CN)_4)].3H_2O$, faisant intervenir le ligand trz-py et des co-ligands dianioniques organiques ou inorganiques.

Références

[1] O. Kahn, C. J. Martinez, *Science* **1998**, *279*, 44–48; A. Bousseksou, G. Molnár, P. Demont, J. Menegotto, ***J. Mater. Chem.*** **2003**, ***13***, 2069-2071; J. Dugay, M. Giménez-Marqués, T. Kozlova, H. W. Zandbergen, E. Coronado, H. S. J. van der Zant, *Adv. Mat.* **2015**, 27, 1288-1293.

[2] C. Bartual-Murgui, A.Akou, C. Thibault, G. Molnár, C. Vieu, L. Salmon, A. Bousseksou, ***J. Mater. Chem. C***, **2015**, ***3***, 1277-1285; J. Linares, E. Codjovi, Y. Garcia, Sensors **2012**, *12*, 4479–4492; C. M. Jureschi, I. Rusu, E. Codjovi, J. Linares, Y. Garcia, A. Rotaru, *Physica B* **2014**, *449*, 47–51.

[3] a) M. A. Halcrow, Spin-Crossover Materials: Properties and Applications, John Wiley & Sons (Eds.), **2013**; b) P. Gütlich, H. A. Goodwin (Eds.), *Top. Curr. Chem.* **2004**, *233-235.*

[4] a) P. Gütlich, A.-B. Gaspar, Y. Garcia, *Beilstein J. Org. Chem.* **2013**, *9*, 342–391; b) F. J. Muñoz-Lara, Z. Arcís-Castillo, M.-C. Muñoz, J.-A. Rodríguez-Velamazán, A.-B. Gaspar, J.-A. Real, *Inorg. Chem.* **2012**, *51*, 11126-11132; c) J. Olguin, S. Brooker, *Coord. Chem. Rev.* **2011**, *255*, 203-240; e) M. A. Halcrow, *Chem. Soc. Rev.* **2011**, *40*, 4119-4142; d) M. A. Halcrow, *Coord. Chem. Rev.* **2009**, *253*, 2493-2514; e) J.-A. Real, A.-B. Gaspar, V. Niel, M.-C. Muñoz, *Coord. Chem. Rev.* **2003**, *236*, 121-141.

[5] G. Dupouy, M. Marchivie, S. Triki, J. Sala-Pala, J.-Y. Salaün, C. J. Gómez-García, P. Guionneau, *Inorg. Chem.* **2008**, *47*, 8921-8931.

[6] a) G. Dupouy, S. Triki, M. Marchivie, N. Cosquer, C. J. Gómez-García, S. Pillet, E.-E. Bendeif, C. Lecomte, S. Asthana, J.-F. Létard, *Inorg. Chem*. **2010**, *49*, 9358-9368; b) G. Dupouy, M. Marchivie, S. Triki, J. Sala-Pala, C. J. Gomez-Garcia, S. Pillet, C. Lecomte, J.-F. Létard, *Chem. Commun.* **2009**, 3404-3406.

Nom des ligands utilisés (cf. Schéma 1) :

$(tcm)^-$: anion tricyanométhanure

L2: 1,8-bis(2'-pyridylmethyl)-1,4,8,11-tetraazacyclotetradecane

tmpa : tris(2-pyridylmethyl) amine

andmpa : bis-(2-pyridylmethyl)aminomethyl)aniline

$(tcpd)^{2-}$: anion 2-dicyanométhylène-1,1,3,3-tétracyanopropènediure

aqin : 8-amino quinoline

$[M(CN)_4]^{2-}$ (M = Ni, Pd, Pt) : tétracyanométallates

trz-py : 4-(2-pyridyl)-1,2,4,4*H*-triazole

Chapitre I

Commutation moléculaire

1. Généralités sur la transition de spin

1.1. Introduction et rappel historique.

Les ions des métaux de transition de configuration électronique $3d^4$ à $3d^7$, dans un environnement octaédrique ou pseudo-octaédrique, peuvent présenter une transition réversible haut spin (HS)–bas spin (BS) sous l'effet d'une perturbation extérieure (température, irradiation, champ magnétique, pression…)[1], appelée transition de spin ou SCO en anglais (Spin CrossOver).

Ce phénomène a été mis en évidence au début du XX^{ème} siècle. En effet, des anomalies dans la mesure de la susceptibilité magnétique ont été détectées dans des complexes du fer (III) à base de dithiocarbamate N,N-disubstitués. Ces anomalies ont été publiées en 1931 dans la revue allemande Berichte der Deutschen Chemischen Gesellschaft par Cambi et Szegö. Entre 1931 et 1960, sauf rares exceptions, la Seconde Guerre Mondiale met un frein aux recherches sur la transition de spin. Parmi ces rares exceptions, on citera notamment en 1936, les travaux de Pauling[2] qui identifie le phénomène de transition de spin en étudiant l'oxygénation d'un hème.

Entre les années 1960 et 1980, l'étude des complexes à transition suscite à nouveau l'intérêt de différents laboratoires à travers le monde. En Australie, le laboratoire de Martin et Ewald[3] puis celui de Figgis[4] reprennent l'étude des complexes de type $[Fe(R_2NCS_2)_3]$ et montrent l'influence de la pression sur la transition de spin. D'un autre côté, les laboratoires russes de Zelentsov et Gerbeleu[5] synthétisent des complexes du fer (III) à base de thiosemicarbazone du type $\left[Fe(5\text{-X-tsha})_2\right]^-$ et [Fe(5-X-tsha)(5-X-tshaH)]. Par la suite, la conception de nouveaux ligands dérivés des bases de Schiff, va permettre la synthèse de nombreux complexes du fer (III). On peut citer aux USA un complexe du fer (III) à base de bis(N-méthylènediaminesalicylaldimine)[6], au Japon une série de complexes à partir du N,N'-bis(1-méthyl-3-oxobutylidène)éthylènediamine[7] (acen) et en Australie, un complexe $\left[Fe(salen)(imd)_2\right]$[8] (imd :imidazole). A la fin de cette période, en 1981, Hendrickson[9] montre le lien entre la cristallogénèse et les caractéristiques de la transition de spin.

Dans le cas des complexes à transition de spin à base d'ion fer (II), qui fera l'objet du paragraphe suivant, les premiers exemples ont été découverts au milieu

des années 60. Ces découvertes ont entrainé de nombreuses études pour la conception de nouveaux ligands azotés (N-donneur) qui se poursuivent aujourd'hui. Parmi ces premiers complexes, nous pouvons citer le tout premier: le cis-$\left[Fe(NCS)_2(1,10\text{-phen})_2\right]$ et son équivalent avec la 2,2'-bipy découverts par König et Madeja[10]. Par la suite, de nombreux complexes ont été synthétisés utilisant des ligands à base de pyridine: $[Fe(NCS)_2(TPA)]$[11] (TPA : tripicolylamine) et $\left[Fe(NCS)_2(DPA)\right]$[12](DPA : dipyridylamine). En 1981, Gütlich publie un ouvrage[13] détaillant toutes les méthodes d'étude du phénomène de transition de spin : magnétisme, spectroscopie Mössbauer, structure par diffraction de rayons X… En 1982, les premiers complexes présentant une transition abrupte ont été synthétisés par Hassnoot[14] : il s'agit de complexes à base de tétrazole comme par exemple le complexe $\left[Fe(1\text{-propyl-tétrazole})_6\right]^{2+}$. En 1999, Goodwin et al. ont étudié une série de complexes à base de pyrazolyl-pyridine[15] qui a mené à de récentes publications par Halcrow[16], Létard[17], Ruben et al.[18]

Depuis les années 80 jusqu'à aujourd'hui, les complexes à transition de spin ont suscité un nouvel intérêt, notamment grâce aux complexes polynucléaires (Fer (II), Fer(III), Co(II)). En effet, ces études[19,20] avaient pour but de comprendre comment la présence de liaisons covalentes entre ces centres métalliques peut influencer les caractéristiques de la transition de spin: coopérativité, largeur d'hystérésis…

Aujourd'hui, plusieurs centaines de complexes à transition de spin ont été synthétisés sous différentes formes: poudre, monocristaux ou liquides. Leurs principales utilisations[21] portent sur les cristaux liquides[22], les films fins [23], les nanoparticules[23f, 24] et la fonctionnalisation de surface[1,12(e),25]. Les propriétés macroscopiques de ces matériaux ont été décrites et expliquées sur la base d'un couplage électron-phonon et des propriétés élastiques du réseau cristallin[26]. D'un point de vue moléculaire, la théorie du champ de ligand permet d'en expliquer le phénomène.[27]

1.2. Cas de l'ion fer(II)

Parmi tous les complexes à transition de spin, les complexes des ions fer(II), qui passent d'un état paramagnétique à diamagnétique, ont été les plus étudiés. Ces complexes sont d'excellents candidats pour une éventuelle utilisation en électronique moléculaire.

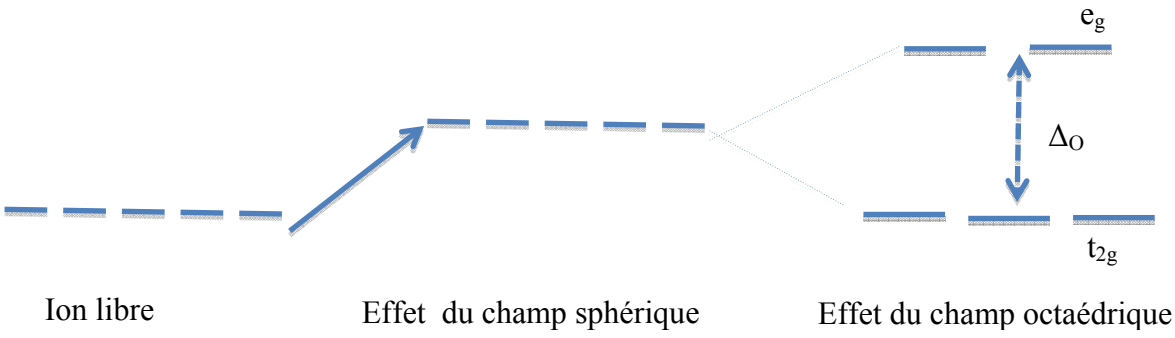

Figure I.1. *Levée de dégénérescence des orbitales d en symétrie octaédrique*

Dans le cas des ions fer(II), le complexe de géométrie octaédrique peut se trouver sous deux états de spins différents selon la valeur de l'intensité du champ ligand Δ_O : un état Bas Spin (BS) diamagnétique (S=0) de configuration$(t_{2g})^6$ ($^1A_{1g}$) et un état Haut Spin (HS) paramagnétique (S=2) ($(t_{2g})^4(e_g)^2$) ($^5T_{2g}$).

Figure I.2. Configuration de l'ion fer(II)(d^6) selon la valeur de Δ_O

Si Δ_O est proche de l'énergie d'appariement des électrons (P), on peut, sous l'effet d'un apport énergétique extérieur (température, pression, irradiation, champ magnétique), passer de façon réversible de l'état BS (stable à basse température) à HS (stable à haute température) et réciproquement. Ce passage d'un état à un autre s'accompagne de modifications des propriétés physiques[28] du complexe étudié :

- les propriétés magnétiques : comme nous l'avons déjà souligné, le complexe passe d'un état diamagnétique à paramagnétique.
- les propriétés structurales[29]: la transition consiste au remplissage des orbitales e_g, orbitales antiliantes. A l'état HS, les longueurs de liaison sont donc plus grandes. Les mesures des longueurs de liaison moyennes Fe-N montrent une variation de 0,16 à

0,24 Å. Cette variation des longueurs de liaison crée une modification des propriétés vibrationnelles du complexe. A l'état solide, une variation des paramètres de maille est alors observée. Le volume de la maille est modifié et une modification des propriétés mécaniques du cristal apparaît.

- les propriétés optiques : nous observons un thermochromisme du complexe qui change de couleur en passant d'un état BS à HS. La couleur d'un complexe est due à des transferts d'électrons entre les orbitales d ou à des transferts de charges qui dépendent de la configuration du complexe. Ce changement de configuration HS/BS entraîne souvent des changements de couleurs selon le complexe : jaune(HS)/rouge(BS) ; vert(HS)/jaune(BS) ; transparent(HS)/rose(BS). Ce thermochromisme permet de détecter rapidement une transition de spin.
- les propriétés conductrices : il a été montré que la constante diélectrique[30] d'un solide à transition de spin pouvait varier de 10% lors de la transition. De la même manière, la résistance électrique[31] peut varier. Ces modifications des propriétés électriques pourraient entraîner des applications en électronique moléculaire.

Certaines modifications de propriétés font de ces matériaux d'excellents candidats pour de nombreuses applications : dispositifs d'affichage, électronique moléculaire, capteurs[32], stockage de l'information[24e], agents de contrastes pour l'IRM[33]…

Comme nous allons le voir, il existe différents types de transition. Certaines transitions thermiques s'effectuent en faisant apparaître une hystérésis. On a donc possibilité d'avoir à une même température coexistence de l'état HS et BS. On parle dans ce cas de bistabilité thermique. Cette dernière caractéristique est recherchée dans le but d'applications. Nous allons voir les différentes caractéristiques de transition de spin puis nous nous intéresserons plus particulièrement aux systèmes bistables et nous expliquerons l'origine de cette bistabilité.

1.3. Transition thermique : notion de coopérativité et bistabilité thermique.

La caractéristique principale d'une transition de spin est la «$T_{1/2}$» qui, par définition, est la température pour laquelle la fraction HS est égale à la fraction BS. Les différents complexes à transition de spin synthétisés ont permis de décrire différents types de transition thermique[34] offrant une large gamme de $T_{1/2}$ (figure I.3).

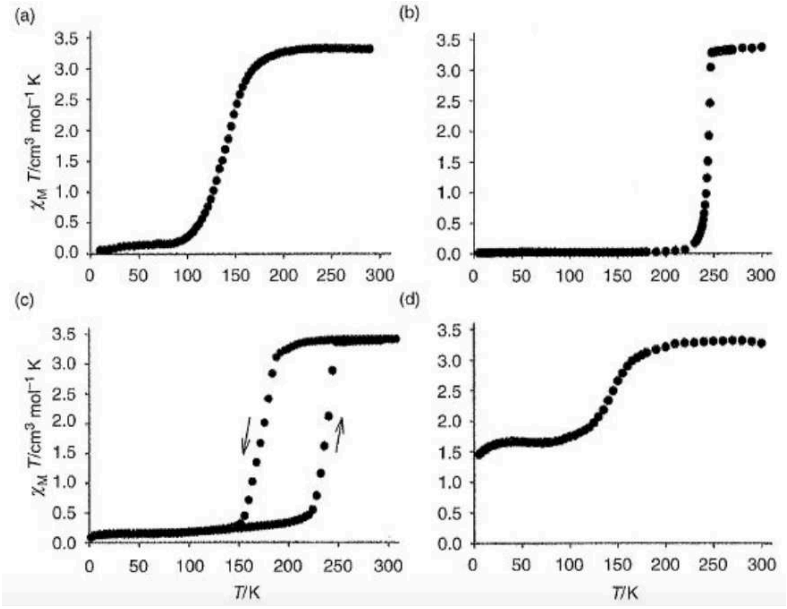

Figure I.3. (a) transition graduelle $T_{1/2}$= 145 K (b) transition abrupte $T_{1/2}$=245 K (c) transition abrupte avec hystérésis ($T_{1/2}$=165 K $T_{1/2}$=235 K) (d) transition incomplète.[21]

La caractéristique de la transition dépend de la coopérativité du système[35]. Plus un système est coopératif, plus la transition est abrupte, plus la probabilité d'obtenir une hystérésis est grande. La coopérativité est l'aptitude d'un système à propager une distorsion moléculaire. Les liaisons covalentes[36], les interactions moléculaires[37] comme les interactions entre les orbitales π (π stacking), les interactions de type Van der Waals et les liaisons hydrogène sont à l'origine de la coopérativité.

Pour obtenir de la bistabilité, il faut synthétiser des matériaux où la coopérativité est renforcée. Pour moduler la coopérativité d'un système, il est possible de modifier différents paramètres: utilisation de ligands rigides et contraignants, favoriser la formation de liaisons hydrogène en ciblant les ligands et/ou solvants, augmenter la présence de noyaux aromatiques, modifier le contre-ion, … etc.

Il est souvent difficile de contrôler l'ensemble des paramètres liés à la coopérativité tant les interactions sur l'ensemble du réseau sont difficilement prévisibles. C'est pourquoi une autre voie s'est développée basée sur l'augmentation de la dimension du réseau. Afin de favoriser la bistabilité thermique, le principe est de construire des édifices polymériques : chaines (réseau 1D), plans bidimensionnels (réseau 2D) et réseaux tridimensionnels (3D). Cette méthode va permettre de

rationnaliser la synthèse de complexes à transition de spin. Nous utiliserons à cet effet des ligands pontants et rigides.

1.4. Edifices polymériques

1.4.1. Réseau 1D

Parmi tous les complexes à transition de spin, les complexes à base du ligand 4-H-1,2,4 -triazole (noté trz) sont les plus nombreux et les plus étudiés[38,39,40].

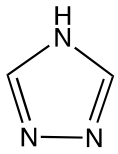

ligand trz

Ce ligand a permis l'obtention de chaîne de formule générale $[Fe(H\text{-}trz)_2(trz)](A)$ ou $[Fe(R\text{-}trz)_3](A)_2$,nsolvant avec R-trz= 4-R-1,2,4-triazole, A^- un contre-ion et des molécules de solvant. La structure de ce type de complexe n'a été résolue que récemment[41]. Il a été clairement montré qu'il s'agit d'une chaîne où la coopérativité est liée aux liaisons hydrogène entre les molécules d'eau et les anions. La plupart des complexes du fer(II) à base de triazole montrent un thermochromisme très marqué, passant du blanc (poudre) ou incolore (monocristal) à l'état HS au rose à l'état BS. De plus, , ils montrent une bistabilité thermique qui s'explique par différentes causes :

- la possibilité de former des liaisons hydrogène : le rôle du solvant est important. La présence de molécules d'eau dans ce type de système et d'une manière générale tout solvant protique, par liaisons hydrogène, va augmenter la coopérativité du système[42].
- les interactions entre chaînes : les exemples montrent que la chaîne polymérique n'est pas uniquement responsable de la coopérativité observée, les interactions entre les chaînes jouent également un rôle
- la nature et la taille du conte-ion : plus le contre-ion est petit, plus l'état BS est stabilisé, plus la $T_{1/2}$ est décalée vers les températures les plus hautes. La $T_{1/2}$ dépend aussi de la nature du contre-ion[38,43].

Citons 2 exemples: $[Fe(Htrz)_2(trz)](BF_4)$[44,28,45] a été le premier de la famille synthétisé par Haasnot et al. en 1977. La transition de spin est très abrupte avec une hystérésis large de 40 K. De plus la température de transition se trouve au-dessus de la

température ambiante ($T_{1/2}$= 345 K et $T_{1/2}$= 385 K). La forte coopérativité du système s'explique par de fortes interactions électrostatiques entre les chaines liées aux ligands anioniques triazolates.

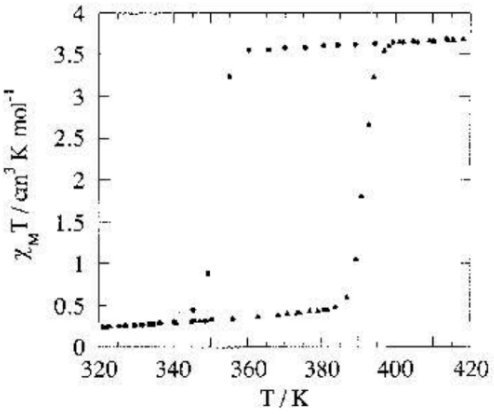

Figure I.4. Produit $\chi_m T$ en fonction de la température pour le complexe $[Fe(Htrz)_2(trz)](BF_4)$.[28]

L'autre complexe est $[Fe(NH_2trz)_3](Br)_2,H_2O$ synthétisé par Olivier Kahn et al. en 1992. Il montre une hystérésis large de 28 K centrée sur la température ambiante ($T_{1/2}$ = 279 K et $T_{1/2}$ = 307 K).

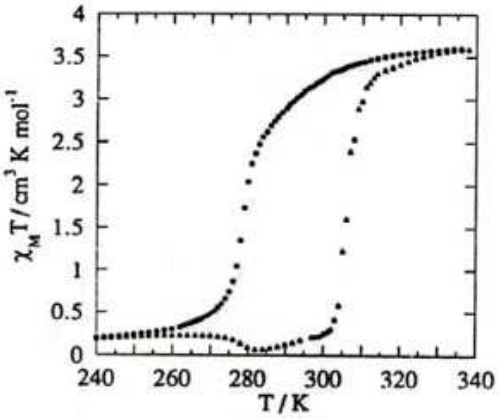

Figure I.5. Produit $\chi_m T$ en fonction de la température pour le complexe $[Fe(NH_2trz)_3](Br)_2,H_2O$[28]

L'obtention de ces chaînes monodimensionnelles a mis en évidence le lien de la dimension du réseau sur la coopérativité. Dans le but d'accéder à de tels réseaux, nous avons utilisé des ligands pontants et rigides. Les tétracyanométallates se sont montrés d'excellents candidats pour synthétiser ce type d'édifice polymérique. De nombreux réseaux 2D ou 3D ont été décrits à partir de ces ligands pour former des réseaux dits de Hofmann ou clathrates d'Hofmann.

1.4.2. Réseaux 2D ou 3D d'Hofmann

Tout réseau bi- ou tri-dimensionnel formé à partir de tétracyanométallates de formule générale $[M(CN)_4]^{2-}$ est appelé réseau ou clathrate d'Hofmann[38]. Les tétracyanométallates et les cations métalliques s'arrangent pour former des réseaux bi ou tri dimensionnels selon le co-ligand. Quatre groupements cyano viennent coordiner le cation métallique formant un carré plan. Le co-ligand occupe les sites de coordination situé au-dessus et en-dessous du plan et conduit à un réseau 2D s'il est monodentate ou à un réseau 3D s'il est pontant.

Des réseaux 2D à transition de spin ont été obtenus avec des ligands à base de pyridine[46,47] et de pyrazine[46,47]

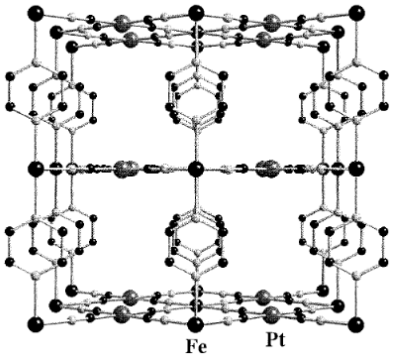

Figure I.6. Structure du composé $[Fe(pyrazine)][Pt(CN)_4]$ [47].

Dans ces deux systèmes, la transition est abrupte avec une hystérésis large de 10 K centrée sur 200 K (cf. figure I.7). Pour obtenir des réseaux 3D, il a fallu remplacer les pyridines par des ligands pontants comme la pyrazine[47]. La température de transition s'est déplacée vers les plus hautes températures, la transition est plus abrupte et l'hystérésis plus large. (cf. figure I.7.) En effet, la rigidité du réseau 3D favorise les interactions entre les plans (coopérativité accrue) et stabilise l'état BS ce qui déplace la température de transition[48].

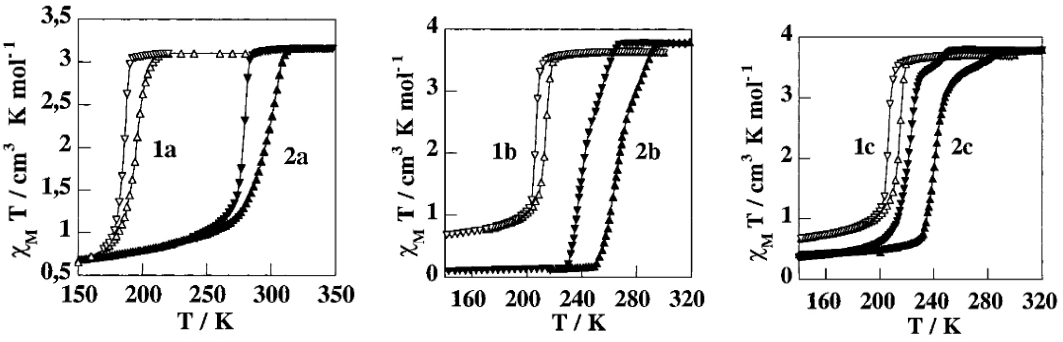

Figure I.7 Produit χ_mT en fonction de la température[47]

Complexe 1 : [Fe(pyridine)][M(CN)$_4$] 1a : M=Ni 1b : M=Pd 1c : M=Pt

Complexe 2 : [Fe(pyrazine)][M(CN)$_4$] 2a : M=Ni 2b : M=Pd 2c : M=Pt

Les caractéristiques de la transition ont été améliorées par déshydratation (cf. figure I.8). La température de transition est alors centrée sur la température ambiante et l'hystérésis est large de 20 K[49].

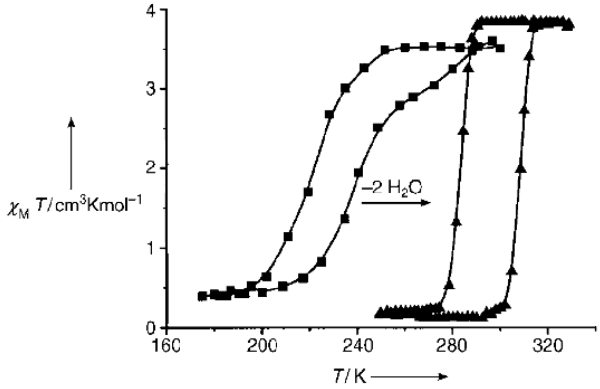

Figure I.8. Produit χ_mT en fonction de la température:[Fe(pyrazine)][Pt(CN)$_4$][49]

Quelle que soit la stratégie appliquée pour obtenir une coopérativité dans les systèmes (augmentation des interactions π et des liaisons hydrogène ou conception d'édifices polymériques), il est très difficile de prévoir avec certitude l'obtention d'un système bistable. De nombreux modèles physiques de la coopérativité ont été construits. S'ils permettent d'expliquer la coopérativité de certains matériaux, ils sont néanmoins difficilement prédictifs, en raison des nombreux facteurs susceptibles d'intervenir : solvant, contre-ion, interaction entre chaines, plans etc.

Parmi ces modèles, certains se basent sur une répartition aléatoire des sites BS et HS dans le solide, citons dans ce cas, les modèles de Slichter et Drickamer[50], de Spiering[51], corrigé par Jung[52] et de Robert et al.[53]. Le modèle d'Ising (correction du modèle de

Wajnflasz)[54,55] se base également sur cette approche. Il introduit un Hamiltonien qui amène à un système d'équations dont la résolution permet de déterminer le taux d'occupation des niveaux d'énergie du système en fonction de la température. On peut ainsi suivre l'aimantation du système en fonction de la température. Il existe une autre approche pour la modélisation des interactions. Il s'agit du modèle de Sorai et Seki[56]. Ils considèrent la répartition des sites HS et BS non aléatoire, et utilisent une approche par domaines de même spin dans le solide.

La transition de spin peut être induite par la variation d'autres paramètres que la température, comme la pression, l'application d'un champ magnétique et une irradiation lumineuse. Cette dernière est à l'origine de l'effet LIESST.

1.5. Transition photo-induite : effet LIESST et Reverse LIESST

La transition de spin photo-induite dans les complexes du Fer(II) a été observée pour la première fois en solution par McGarvey et al.[57] en 1982. Puis, en 1984, ce phénomène a été décrit à l'état solide par Decurtins et al.[58] Ils ont montré qu'il était possible de convertir un état BS en un état HS métastable en utilisant une irradiation de longueur d'onde 514nm (vert). Ce phénomène est appelé Light-Induced Excited Spin-State Trapping d'où l'acronyme LIESST. Ce phénomène a été initialement observé pour des complexes de l'ion fer (II) pour des températures très basses inférieures à 50 K. Hauser[59] a montré plus tard qu'on pouvait de la même manière passer d'un état HS à un état BS par irradiation à une longueur d'onde de 820 nm (proche I.R). Ce phénomène est appelé Reverse-LIESST. Il permet de faire commuter des fractions résiduelles HS à BS à basse température.

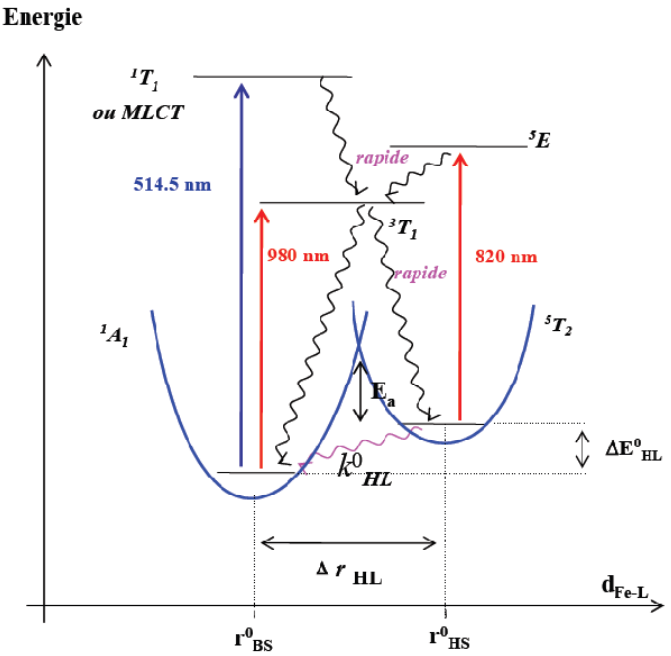

Figure I.9 Diagramme de Jablonski ($E=f(d_{Fe-L})$) montrant les différents processus de relaxation non radiative (flèches ondulées) après irradiations.

D'après la figure I.9, l'irradiation à 514 nm d'un échantillon BS induit une transition permise $^1A_1$-$^1T_1$. Cet état photo-induit n'est pas stable (durée de vie de quelques nanosecondes) et va relaxer rapidement vers l'état initial $^1A_1$. Il existe une autre voie de relaxation. Comme la conversion directe d'un état photo excité singulet ($^1T_1$) en état quintuplet (HS) ($^5T_2$) est interdite, il faut donc un état intermédiaire pour observer cette nouvelle relaxation: il s'agit d'un état triplet $^3T_1$. L'état excité $^1T_1$ se désexcite de façon non radiative par conversion intersystème grâce au couplage spin-orbite vers cet état triplet $^3T_1$. Cet état intermédiaire est instable et va se désexciter soit vers l'état stable $^1A_1$ soit vers l'état métastable $^5T_2$. Cet état, $^5T_2$, est stable à basse température tant que l'énergie thermique, proportionnelle à k_BT, reste inférieure à la barrière énergétique ΔE°_{HL}. Cet état HS peut donc avoir une durée de vie assez longue. On créé ainsi une transition BS-HS photo induite. L'état HS créé est métastable et crée ainsi de la bistabilité photomagnétique.

L'effet LIESST a été observé dans de nombreux complexes du fer(II). On voit sur la figure ci-dessous quelques exemples[60,61,62]:

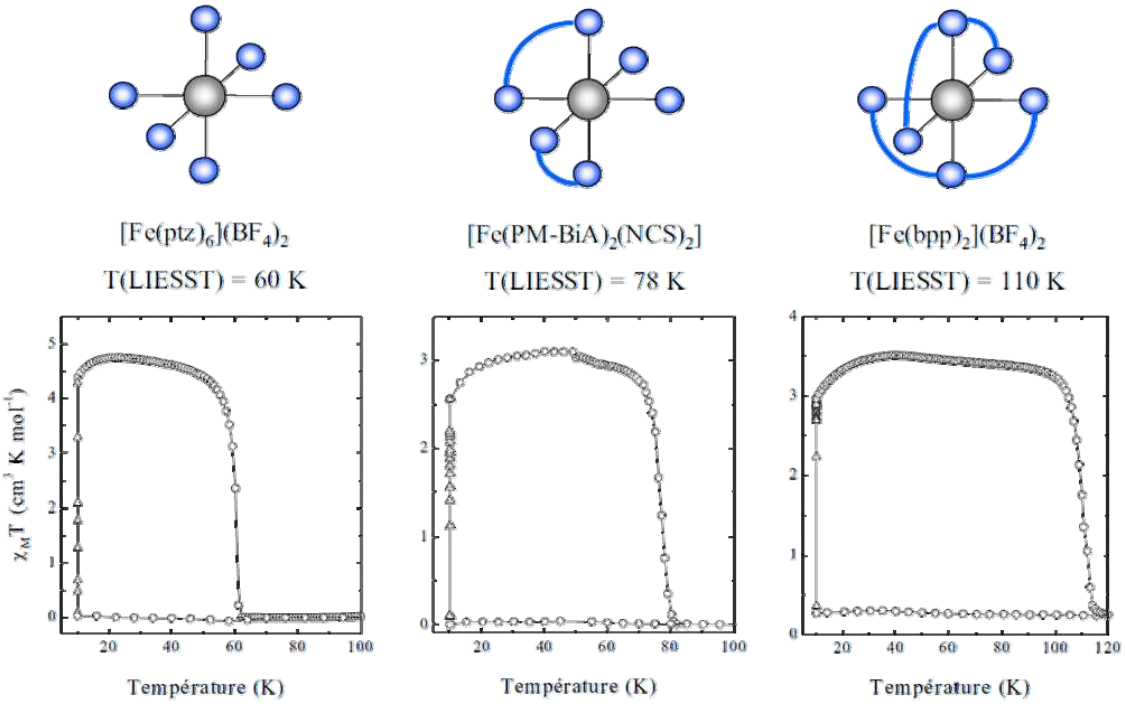

Représentation des points de la courbe : Δ irradiation, o irradiation stoppée.

Figure I.10 Produit $\chi_m T$ en fonction de la température avec effet LIESST pour différents complexes des ions fer(II)[60,61,62].

Le principe de la mesure est le suivant : à très basse température (10 K), on irradie le système BS avec la longueur d'onde appropriée (514 nm). Le produit $\chi_m T$ augmente fortement. Une fois qu'il y a équilibre entre le peuplement et la relaxation de l'état photo-induit métastable, l'irradiation est stoppée. On augmente ensuite lentement la température et on mesure le produit $\chi_m T$ en fonction de la température. Dès que l'énergie thermique est suffisante, le système relaxe rapidement vers l'état BS. La dérivée du produit $\chi_m T$ par rapport à la température va alors admettre un minimum pour une température donnée. Cette température est appelée T_{LIESST}.

Plus la T_{LIESST} est grande, plus l'état photo-induit est stable, plus la bistabilité photo-induite est importante Pour d'éventuelles applications, nous allons chercher à synthétiser des systèmes avec un écart entre T_{LIESST} et $T_{1/2}$ le plus petit possible pour avoir coexistence de l'état HS et BS sur un intervalle le plus grand possible.

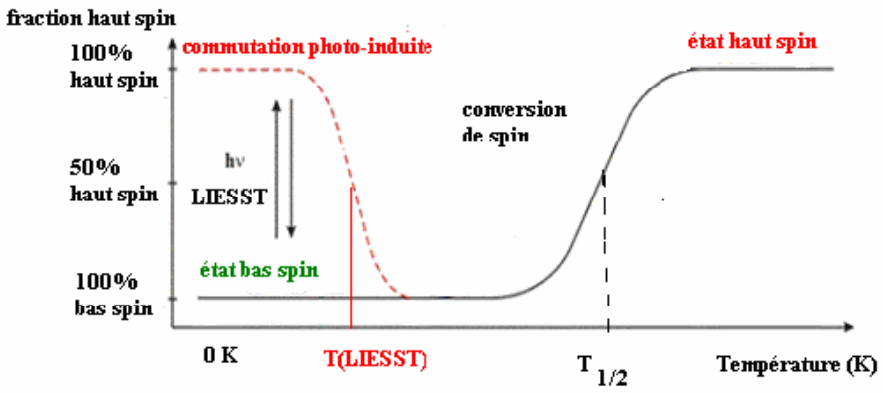

Figure I.11 : Allure schématique de la fraction HS en fonction de la température

Il est admis que la T_{LIESST} augmente avec la denticité du ligand, comme observé sur la figure I.10. Dans le but d'étudier le lien entre T_{LIESST} et $T_{1/2}$, une étude a été réalisée sur de nombreux complexes à transition de spin. Les courbes $T_{LIESST}=f(T_{1/2})$ pour différentes denticités mettent en évidence que les deux grandeurs sont liées. Une équation générale de type affine reliant la T_{LIESST} à $T_{1/2}$ a été proposée, $T_{LIESST}=T_0-0,3T_{1/2}$[63]. Expérimentalement, T_0 est fonction de la rigidité du ligand donneur coordiné à l'ion fer II. Sur la figure I.12, on peut lire que T_0=100 K pour les ligands monodentates, T_0=120 K pour les ligands bidentates etc. Quatre-vingts systèmes ont été étudiés ce qui a permis d'obtenir les 5 droites de la figure I.12 pour cinq températures T_0 différentes. On remarque que plus la T_{LIESST} diminue, plus la $T_{1/2}$ augmente et réciproquement. Il a donc été montré que plus la transition thermique a lieu à haute température, moins l'état photo-induit est stable donc moins l'information photomagnétique perdure.

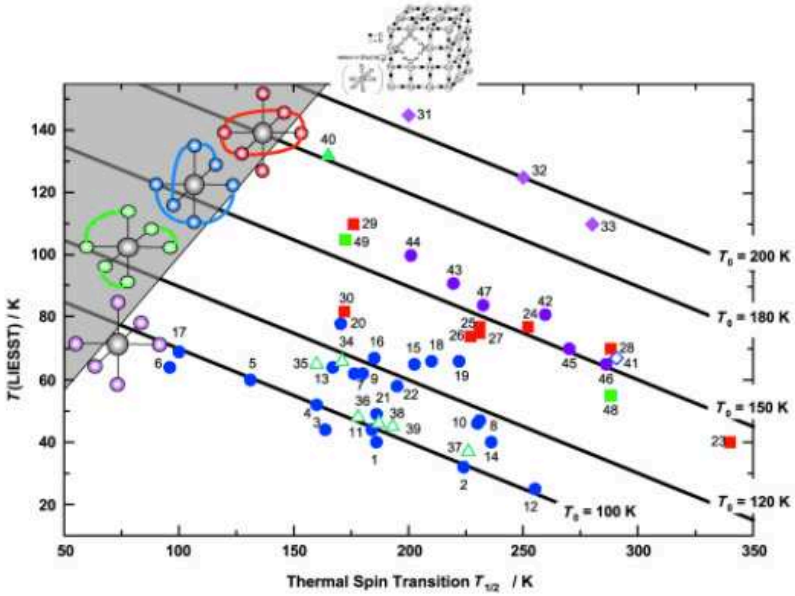

Figure I.12 T_{LIESST} en fonction de la $T_{1/2}$ pour différents complexes à transition de spin[63].

L'objectif est donc d'utiliser des ligands contraignants de grande denticité afin d'obtenir des complexes affichant les T_{LIESTT} les plus hautes possibles. A notre connaissance, la T_{LIESST} la plus haute observée à ce jour est de 150 K dans des complexes de la famille des bleus de Prusse[64].

1.6. Hystérésis thermique induite par irradiation lumineuse (effet LITH).

L'effet LIESST est obtenu par irradiation du complexe à basse température et le système relaxe après arrêt de la photoexcitation par augmentation de la température. Si la photoexcitation est maintenue, une hystérésis thermique induite par l'excitation lumineuse peut être observée: c'est l'effet LITH. Cet bistabilité thermique induite par irradiation a été observée simultanément par les équipes de Versailles[65] et de Bordeaux.[66] Le phénomène s'explique par la compétition présente entre le phénomène de photoexcitation et celui de relaxation quand la température augmente. Il s'agit tout d'abord d'un effet LIESST qui conduit à basse température à un état stationnaire tant que l'irradiation est maintenue. Dès que la température augmente, le phénomène de relaxation HS-BS commence, en même temps que continue la transition BS-HS car la photoexcitation est maintenue. En fonction de la température, le phénomène de photoexcitation ou de relaxation prédomine. Il est ainsi possible d'obtenir de la bistabilité thermique. On obtient une courbe d'hystérésis thermique tant que l'excitation est maintenue.

2. Stratégie

2.1. Choix des ligands

D'une manière générale, nous allons associer aux ions fer(II) un ligand de plus grande denticité possible. Deux possibilités se présentent :

- dans le cas où une géométrie octaédrique ou pseudo-octaédrique est recherchée, un ligand neutre hexadentate est le plus adapté, auquel sera associé un contre-ion susceptible d'induire des chaînes et des interactions.

- dans le second cas, un ligand neutre polydentate laissant des sites de coordination libres sur le cation fer(II) sur lesquels un co-ligand anionique pourra se coordiner pour compléter la sphère de coordination. Ce co-ligand anionique devra être pontant et le plus rigide possible afin d'augmenter la coopérativité et la dimension du système.

Ces deux voies de synthèses peuvent être résumées de la manière suivante :

L : ligand neutre avec i et j denticité .

X : contre ion

A : ligand anionique

$$Fe(II) + L_i + kX^{n-} = [FeL_i](X)_k$$

$$Fe(II) + L_i + A_j^{m-} = [FeL_iA_j]$$

L'objectif de ce travail de thèse est d'obtenir des complexes à transition de spin présentant de la bistabilité en choisissant de façon pertinente L, A ou X et d'être en mesure de proposer une rationnalisation de la synthèse de complexes à transition de spin.

Afin d'augmenter la coopérativité et favoriser l'obtention de propriétés photomagnétiques, notre choix s'est orienté vers des ligands N-donneurs, polydentates, aromatiques et contraignants dérivés du triazole et de la pyridine qui ont déjà démontré leur capacité à donner des complexes à transition de spin. Pour les co-ligands anioniques, nous avons choisi des ligands N-donneurs organiques et inorganiques. si possible pontants pour augmenter la dimension du réseau.

2.2. Caractérisation

Plusieurs méthodes de caractérisation des ligands et des complexes ont été utilisées : Résonance Magnétique Nucléaire, Spectroscopie par Infra-Rouge, Diffraction par rayons X, magnétomètre (SQUID) et Calorimétrie Différentielle à balayage (DSC).

2.3. Cristallogénèse

Dans le but de caractérisation par diffraction de rayons X, l'obtention de monocristaux est impérative. Plusieurs méthodes de cristallogénèse ont été utilisées : évaporation lente, gel, tube H et tubes fins (figure I.12). C'est cette dernière méthode qui a donné les cristaux de meilleure qualité. Elle consiste à placer dans un tube en verre long de 20 cm et de 3mm de diamètre deux solutions miscibles entre elles mais de densités différentes. En effet, la différence de densité entre les deux solvants va ralentir la diffusion déjà ralentie par capillarité grâce à la finesse des tubes. On mélange les ions fer(II) et le ligand neutre dans un solvant 1 et on place le ligand anionique ou le contre-ion dans un solvant 2. On remplit la moitié du tube par la phase la plus dense et on complète par l'autre phase. Les cristaux se forment lentement à l'interface des deux phases.

Figure I.12: Tubes fins

Afin de rationnaliser la synthèse de complexes à transition de spin, le but était de comprendre quelle serait la meilleure association FeL et A ou X. Nous avons réalisé pour un ligand donné toute une série de synthèses combinant différents ligands anioniques ou contre-ions dans différents solvants. Nous réalisions un tableau à double entrée, chaque case représentant une expérience.

	A dans solvant 1	A dans solvant 2	…	A dans solvant n
FeL solvant a				
FeL solvant b				
…				
FeL solvant k				

Le nombre de solvants utilisés dépend de la solubilité des ligands (neutres et anioniques) et de leur miscibilité entre eux. Parmi tous les ligands anioniques testés,

deux dianions ont donné des résultats : $(tcpd)^{2-}$ et $[M(CN)_4]^{2-}$ (avec M=Pt,Pd,Ni). Ces résultats seront présentés dans chacun des chapitres suivants dans trois parties distinctes.

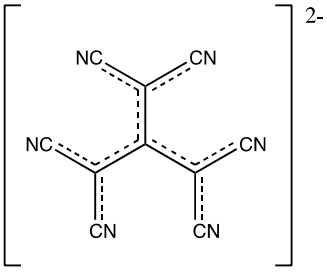

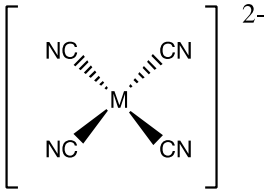

Figure I.13 Ligands $(tcpd)^{2-}$ $[M(CN)_4]^{2-}$ avec M=Ni,Pd,Pt

Le premier chapitre porte sur l'obtention de deux systèmes discrets à transition de spin, l'un mononucléaire et le second dinucléaire du fer. Le deuxième chapitre décrit la synthèse et les propriétés d'un réseau polymérique à une seule dimension. Enfin, dans un dernier chapitre, nous étudierons deux systèmes polymériques, un réseau bi-dimensionnel $[Fe(trz\text{-}py)_2(Pt(CN)_4)]$ et un réseau tri-dimensionnel $[Fe(trz\text{-}py)(tcpd)(H_2O)]$.

Bibliographie

1. a) Gütlich, P., Hauser, A., Spiering, H. *Angew. Chem. Int. Ed.* **1994**, 33, 2024-2054. b) Gütlich, P., Goodwin, H.A. *Top Curr. Chem.* **2004**, 233-235. c) Létard, J-F. J. *Mater. Chem.* **2006**, 16, 2550-2559. d) Sato, O., Tao, J., Zhang, Y.-Z. *Angew. Chem. Int. Ed.* **2007**, 46, 2152-2187. e) Kitchen, J.A., Brooker, S. *Coord. Chem. Rev.* **2008**, 252,2072-2092. f) Weber, B. *Coord. Chem. Rev.* **2009**, 253, 2432-2449. g) Halcrow, M.A. *Coord. Chem. Rev*. **2009**, 253, 2493-2514 h) Murray, K. S. *Aust. J. Chem* . **2009**, 62, 1081-1101. i) Gaspar, A., Seredyuk, M., Gütlich, P. *J. Mol. Struct.* **2009**, 924-926, 9-19. j) Brooker, S., Kitchen, J. A. *Dalton Trans*. **2009**, 7331-7340. k) Koudriavstev, A. B., Linert, W. *J. Struct. Chem.* **2010**, 51, 335-365.
2. Pauling, L., Coryell, C. D., *Proc. Natl. Acad. Sci. USA,* **1936**, *22 : 210-216.*
3. Ewald, A.H., Martin , R. L., Ross, I. G., White, A. H., *Proc. R. Soc. London Ser. A,* **1964**, *280 : 235-257.*
4. Figgis, B. N., Toogood, G.E., *J. Chem. Soc., Dalton Trans.*, **1972**, 2177-2182.
5. Ivanov, E. V., Zelentsov, V., Gerbeleu, N. V., Ablov, A.V., *Dokl. Akad. Nauk. SSSR*, **1970**, 191 :827-830.
6. Petty, R. H., Dose, E. V., Tweedle, M. F., Wilson, L.J., *Inorg. Chem*, **1978**, 17, 1064-1071.
7. Oshio, H., Maeda, Y. Takashima, Y., *Inorg. Chem*, **1983**, 22, 2684-2689.
8. Kennedy, B. J., McGrath, A.C., Murray, K.S., Skelton, B.W., A.H., *Inorg. Chem*, **1987**, 22, 2684-2689.
9. Haddad, M.S., Federer, W.D., Lynch, M.W., Hendrickson, D.N., *Inorg. Chem*., **1981**, 20,131-139.
10. König, E., Madeja, K., *Inorg. Chem*., **1967**, 6, 48-55.
11. Matouzenko, G.S., Bousseksou, A., Lecocq, S., van Koningsbruggen, P.J., Perrin, M., Kahn, O., Collet, A., *Inorg. Chem.*, **1997**, 36, 2975-2981.
12. Gaspar, A.B., Agusti, G., Martinez, V. Munoz, M.C., Levchenko, G., Real, J. A., *Inorg. Chim. Acta*, **2005**,358, 4089-4094.
13. Gütlich, P., Spin Crossover in iron (II) complexes. *Struct. Bonding (Berlin)*, **1981**, 44, 83-195
14. Franke, P.L., Haasnoot, J.G., Zuur, A.P., *Inorg.Chim.Acta*, **1982**, 59, 5-9

15. Harimanow, L.S., Sugiyarto, K.H., Craig, D.C., Scudder, M.L., Goodwin, H.A., *Aust. J.Chem*, **1999**, 52, 109-122
16. Halcrow, M.A, *Polyhedron*, **2007**, 26, 3523-3576
17. Money, V. A., Carbonera, C., Elhaïk, J., Halcrow, M.A., Howard, J. A. K., Létard, J-F., *Chem. Eur. J*., **2007**,13,5503-5514.
18. Rajadurai, C., Schramm, F., Brink, S., Fuhr, O. Ghafari, M., Kruk, R., Ruben, M., *Inorg. Chem*, **2006**, 45, 10019-10021.
19. Real, J. A., Zarembowitch, J., Kahn, O., Solans, X., *Inorg. Chem.*, **1987**, 26, 2939-2943.
20. Murray, K.S., Keppert, C.J., Gütlich, P., Goodwin, H.A. (Eds) Spin Crossover in Transition Metal Compounds I. *Top. Curr. Chem*., 233, 195-228
21. Halcrow, M.A. (Ed) *Spin-Crossover Materials, Properties and Applications*. Wiley, Chichester, UK, **2013**.
22. (a) Galyametdinov, Y., Ksnevofontov, V., Prosvirin, A., Ovchinnikov, I., Ivanova, G., Gütlich, P., Haase, W. *Angew. Chem. Int. Ed*. **2001**, 40, 4269-4271. (b) Seredyuk, M., Gaspar, A.B., Ksenofontov, V. Reiman, S., Galyametdinov, Y. Haase, W., Rentschler, E., Gütlich, P. *Chem. Mater.* **2006**, 18, 2513-2519. (c) Seredyuk, M., Gaspar, A. B., Ksenofontov, V. Galyametdinov, Y. Kusz, J., Gütlich, P. *Adv. Funct. Mater.* **2008**, 18, 2089-2101. (d) Bodenthin, Y., Pietsch, U., Mhwald, H., Kurth, D.G. *J. Am. Chem. Soc.* **2005**, 127, 3110-3114. (e) Bodenthin, Y. , Schwarz, G., Tomkowicz, Z., Geue, T., Haase, W., Pietsch, U. Kurth, D.G. *J. Am. Chem. Soc.* **2009**, 131 2934-2941. (f) Gaspar, A., Seredyuk, M., Gütlich, P. *Coord. Chem. Rev.* **2009**, 253, 2399-2413. (g) Grondin, P., Siretanu, D., Roubeau, O., Achard, M-F., Clérac, R. *Inorg. Chem.* **2012**, 51, 5417-5426. (h) Hayami, S., Razaul Karim, M., Hoon Lee, Y. *Eur. J. Inorg. Chem.* **2013**, 683-696. (i) Gaspar, A.B., Seredyuk, M. *Coord. Chem. Rev.* **2014**, 268, 41-58
23. (a) Létard, J-F., Nguyen, O., Soyer, H., Mingotaud, C., Delhaes, P., Kahn, O. *Inorg. Chem.* **1999**, 38, 3020-3021. (b) Roubeau, O., Agricole, B., Clérac, R., Ravaine, S. *J. Phys. Chem. B* **2004**, 108, 5184-5195. (c) Roubeau, O., Natividad, E., Agricole, B., Ravaine, S. *Langmuir* **2007**, 23, 3110-3117 (d) Thibault, C., Molnar, G., Salmon, L. Bousseksou, A., Vieu, C. *Langmuir* **2010**, 26, 1557-1560. (e) Cavallini, M. *Phys. Chem. Chem.Phys*. **2012** , 14, 11867-11876. (f) Sheperd, H.J., Molnar, G., Nicolazzi, W., Salmon, L., Bousseksou, A. *Eur. J. Inorg. Chem.* **2013**,

653-661. (g) Tanaka, D., Aketa, N., Tanaka, H., Tamaki, T., Inose, T., Akai, T. Toyama, H., Sakata, O., Tajiri, H., Sakata, O., Tajiri, H., Ogawa, T. *Chem. Commun.* **2014**, 50, 10074-10077.

24. (a) Coronado, E., Galan-Mascaros, J.R., Monrabal-Capilla, M., Garcia-Martinez, J., Pardo-Ibanez, P. *Adv. Mater*. **2007**, 19,1359-1361. (b) Forestier, T., Mornet, S., Daro, N., Nishihara, T., Mouri, S., Tanaka, K., Fouché, O., Freysz, E., Létard, J.-F. *Chem. Comm.* **2008**, 4327-4329. (c) Volatron, F., Catala, L., Rivière, E., Gloter, A., Stéphan, O., Mallah, T. *Inorg. Chem.* **2008**, 47, 6433-6437. (d) Boldig, I., Gaspar, A.B.,Martinez, V., Pardo-Ibanez, P., Ksenofontov, V., Bhattacharjee, A., Gütlich, P., Real, J.A. *Angew. Chem. Int. Ed.* **2008**, 47, 6433-6437. (e) Larionova, J., Salmon, L., Guari, Y., Tokarev, A., Molvinger, K., Molnar, G., Bousseksou, A. *Angew. Chem. Int. Ed.* **2008**, 47, 8236-8240. f) Forestier, T., Kaiba, A., Pechev, S., Denux, D., Guionneau, P., Etrillard, C. Daro, N., Freysz, E., Létard, J-F. *Chem. Eur. J.* **2009**, 15, 6122-6130. g) Bousseksou, A., Molnar, G., Salmon, L., Nicolazzi, N. *Chem. Soc. Rev.* **2011**,40, 3313-3335. h) Chakraborty, P., Boillot, M-L., Tissot, A., Hauser, A. *Angew. Chem. Int. Ed.* **2013**, 52-7139-7142. (h) Tissot, A., *New J. Chem.* **2014**, 38, 1840-1845. (i) Dugay, J., Gimenez-Marques, M., Kozlova, T., Zandbergen, H. W., Coronado, E., van der Zant, H.S. *J. Adv. Mater.* **2015**, DOI :10.1002/adma.201404441.

25. (a) Cobo, S., Molnar, G., Real, J. A., Bousseksou, A. *Angew. Chem. Int. Ed.* **2006**, 45, 5786-5789. (b) Molnar, G., Cobo, S., Real. J. A., Carcenac, F., Daran, E., Vieu, C., Bousseksou, A. *Adv. Mater*. **2007**, 19, 2163-2167. (c) Agusti, G., Cobo, G., Gaspar, A. B., Molnar, G., Ould Moussa, N., Szilagyi, P.A., Palfi, V., Vieu, C., Munoz, M. C., Real, J. A., Bousseksou, A. *Chem. Mater.* **2008**, 20, 6721-6732. (d) Cavallini, M., Bergenti, I., Milita, S., Ruani, G., Salitros, I., Qu, Z.-R., Chandrasekar, R., Ruben, M. *Angew. Chem. Int. Ed.*, **2008**, 47, 8596-8600.

26. Spiering, H., Boukheddaden, K., Linares, J., Varret, F. *Phys. Rev.,* **2004**, 70,184106

27. Hauser, A. *Top. Curr. Chem*. 2004, 233, 49-58.

28. Kahn, O., Krober, J., Jay, C. *Adv. Mater.* **1992**, 4, 718-728

29. König, E., *Prog. Inorg. Chem*. **1987**, 35, 527-622

30. (a) A. Bousseksou, G. Molnar, P. Demont and J. Menegotto, *J. Mater. Chem.*, **2003**, 13, 2069-2071; (b) S. Bonhommeau, T. Guillon, L. M. L. Daku, P.

Demont, J. S. Costa, J. F. Letard, G. Molnar and A. Bousseksou, *Angew. Chem.-Int. Edit.*, **2006**, 45, 1625-1629.

31. Matsuda, M., Tajima, H. *Chem.Lett*. **2007**, 36, 700-701.
32. (a) Létard, J.-F., Guionneau, P., Goux-Capes, L. *Top. Curr. Chem.* **2004**, 235, 221-249. (b) Garcia, Y., Ksenofontov, V., Mentior, S., Dîrtu, M., Gieck, C., Bhatthacharjee, A., Gütlich, P. *Chem. Eur. J.* **2008**, 14, 3745-3758.
33. Venkataramani, S., Jana, U., Dommaschk, M., Sonnischen, F.-D., Tuczek, F. Herges, R. *Science* **2011**, 331, 445-448.
34. Halcrow, M. A. (Ed) *Spin-Crossover Materials, Properties and Applications*, Wiley, Chicester, UK, **2013**.
35. (a) Hauser, A., Jeftic, J., Romstedt, H., Hinek, R., Spiering, H. *Coord. Chem. Rev.* **1999**, 190-192, 471-491. (b) Halcrow, M.A. *Chem. Commun.* **2013**, 49, 10890-10892.
36. Munoz, M.C., Real, J.A. *Coord. Chem. Rev*. **2011**, 255, 2068-2093
37. (a) Real, J. A., Gaspar, A. B., Niel, V., Munoz, M. C. *Coord. Chem. Rev.* **2003,** 236, 121-141. (b) Halcrow, M. A. *Chem. Soc. Rev*. **2011**, 40, 4119-4142.
38. Garcia, Y., Niel, V., Munoz, M. C., Real, J. A. *Top. Curr. Chem.*, Spin Crossover in Transition Metal Compounds I, Spinger-Verlag, Berlin, **2004**, 233, 229-257.
39. Haasnoot, J. G., *Coord. Chem. Rev.*, **2000**, 200, 131-185.
40. Kahn, O., Martinez, C. J., *Science*, **1998,** 279, 44-48.
41. Grosjean, A., Daro, N., Kauffmann, B., Kaiba, A., Létard, J.-F., Guionneau, P., *Chem. Comm*, **2011**, 47, 12382-12384.
42. Garcia, Y., van Koningsbruggen, P. J., Lapouyade, R., Fournes, L., Rabardel, L., Kahn, O., Ksenofontov, V., Levchenko, G., Gütlich, P., *Chem. Mat*, **1998**, 10, 2426-2433.
43. Varnek, V. A., Lavrenova, L. G., *J. Struct. Chem*., **1995**, 36, 104-111
44. Haasnoot, J. G., and al. *Z. Naturforsch. B,* **1977**, *32*, 1421**.**
45. Krober, J., Audière, J. P., Claude, Codjovi, E., Kahn, O., Haasnoot, J. G., Grolière, F., Jay, C., Bousseksou, A., Linarès, J., Varret, F., Gonthiervassal, A., *Chem. Mat*., **1994**, 6, 1404-1412.
46. Kitazawa, T., Gomi, Y., Takahashi, M., Takeda, M., Enomoto, M., Miyazaki, A., Enoki, T., *J. Mater. Chem*., **1996**, 6, 119-121.

47. Niel, V., Martinez-Agudo, J. M., Munoz, M. C., Gaspar, A. B., Real, J. A., *Inorg. Chem.,* **2001**, 40, 3838-3839.

48. Molnar, G., Niel, V., Gaspar, A. B., Real, J. A., Zwick, A., Bousseksou, A., Mc Garvey, J. J., *J. Phys. Chem. B*, **2002**, 106, 9701-9707

49. Bonhommeau, S., Molnar, G., Galet, A., Zwick, A., Real, J. A., Mc Garvey, J. J., Bousseksou, A. *Angew. Chem.-Int. Edit.*, **2005**, 44, 4069-4073.

50. Slichter, C. P., Drickhamer, H. G., *J. Chem. Phys.*, **1972**, 56, 2142-2160.

51. (a) Spiering, H., Meissner, E., Koppen, E., Müller, E. W., Gütlich, P., Chem. Phys., 1982, 68, 65-71 (b) Spiering, H., *Top. Curr. Chem*., Spin Crossover in Transition Metal Compounds III, Springer-Verlag, Berlin, **2004**, 235, 171-195

52. (a) Jung, J., Bruchlauser, F., Feile, R., Spiering, H., Gütlich, P., *Z. Phys. B-Condens. Mat.*, **1996**, 100, 517-522. (b) Jung, J., Schmitt, G., Wiehl, L., Hauser, A., Knorr, K., Spiering, H., Gütlich, P., *Z. Phys. B-Condens. Mat.*, **1996**, 100, 523-534.

53. (a) Kepenekian, M., Le Guennic, B., Robert, V., *Phys. Rev. B*, **2009**, 79, 5. (b) Kepenekian, M., Le Guennic, B., Robert, V., *J. Am. Chem. Soc*., **2009**, 131, 11498-11502. (c) Kepenekian, M., Robert, V., Le Guennic, B., De Graaf, C., J. *Comput. Chem.*, **2009**, 30, 2327-2333.

54. (a) Wajnflasz, J., Pick, R., *J. Phys. Colloques*, **1971**, 32, C1-91. (b) Bousseksou, A., Nasser, J., Linares, J., Boukheddaden, K., Varret, F., *J. Phys. I*, **1992**, 2, 1381-1403. (c) Bousseksou, A., Varret, F., Nasser, J., *J. Phys. I*, **1993**, 3, 1463-1473.

55. (a) Bousseksou, A., Constant-Machado, H., Varret, F., *J. Phys. I*, **1995**, 5, 747-760. (b) Tuchagues, J. P., Bousseksou, A., Molnar, G., McGarvey, J. J., Varret, F., *Top. Curr. Chem.* Spin Crossover in Transition Metal Compounds III, Springer-Verlag, Berlin, **2004**, 235, 85-103.

56. Sorai, M., Seki, S., *J. Phys. Chem. Solids*, **1974**, 35, 555-570.

57. McGarvey, J. J., Lawthers, I., *J. Chem. Soc. Comm.*, **1982**, 16, 906-907.

58. Decurtins, S., Gütlich, P., Köhler, C. P., Spiering, H., Hauser, *A. Chem. Phys. Lett.* **1984**, 105, 1-4.

59. Hauser, A., *Chem. Phys. Lett*., **1986**, 124, 543-548.

60. Hauser, A., *J. Chem. Phys.*, **1991**, 94, 2741.

61. Létard, J. F., *J. Mater. Chem*., **2006**, 16, 2550-2559.

62. Money, V. A., Costa, J. S., Marcen, S., Chastanet, G., Elhaik, J., Halcrow, M., A., Howard, J. A. K., Létard, J.-F., *Chem. Phys. Lett*., **2004**, 391, 273-277.

63. Létard, J.–F., Capes, L., Chastanet, G., Moliner, N., Létard, S., Real, J.-A., Kahn, O. *Chem. Phys. Lett*. **1999**, 313, 115-120.

64. (a) Shimamoto, N., Ohkoshi, S. S., Sato, O., Hashimoto, K. *Inorg. Chem.* **2002**, 41, 678-684. (b) Lebris, R., Mathonière, C., Létard, J.-F., *Chem. Phys. Lett.* **2006**, 426, 380-386.

65. Desaix, A., Roubeau, O., Jeftic, J., Haasnoot, J.G., Boukheddaden, K., Codjovi, E., Linares, J., Nogues, M., Varret, F., *Eur. Phys. J. B*, **1998**, 6, 183

66. Létard, J.-F. et al., *Inorg. Chem*., **1998**, 37, 4432.

Chapitre II

Systèmes discrets

Introduction

Avec l'objectif de concevoir de nouvelles séries de complexes à transition de spin, nous avons envisagé depuis quelques années l'utilisation des tétraazamacrocycles connus pour leurs propriétés complexantes exceptionnelles. Ces ligands (figure II.1) peuvent être fonctionnalisés sélectivement par un ou plusieurs groupements chimiques permettant la modification et le contrôle de leurs propriétés de coordination. Ces caractéristiques essentielles font de ces molécules cycliques de très bons ligands pour la conception de matériaux moléculaires à transition de spin.

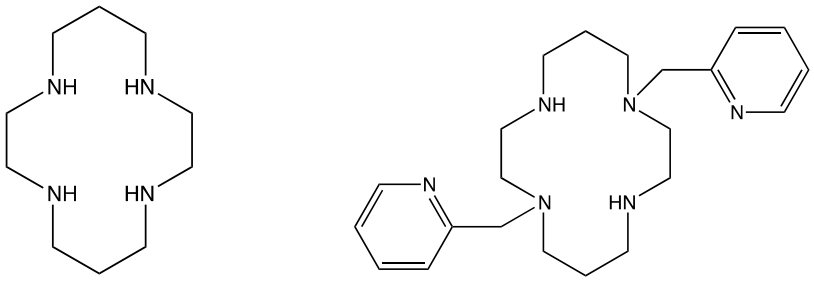

Cyclam L2

Figure II.1 Ligands tétrazamacrocycliques

L'étude de ces ligands a fait l'objet de la thèse de Fatima El Hajj soutenue en 2010 à Brest. Un premier complexe à transition de spin $[Fe(L2)](BF_4)_2$ a été décrit[1], où L2 est un cyclam fonctionnalisé par 2 groupements méthylpyridine. L'influence du contre-ion sur ce système a été clairement mis en évidence et a permis de synthétiser le premier complexe à transition de spin présentant de la bistabilité en associant ce système discret à l'anion $(tcm)^-$. Nous avons poursuivi le travail de Fatima El Hajj en optimisant les synthèses et en complétant les premiers résultats présentés dans sa thèse par d'autres études cristallographiques, magnétiques et par calorimétrie différentielle. Le premier paragraphe de ce chapitre sera consacré aux résultats publiés obtenus pour ce système. Puis, dans une seconde partie, après avoir étudié l'influence du contre-ion, nous

[1] F. El Hajj, G. Sebki,V. Patinec, M. Marchivie, S. Triki, H. Handel, S. Yefsah, R. Tripier, C.J. Gómez-García, E. Coronado , *Inorg. Chem.* **2009** , 48, 10416

étudierons la modification du ligand par substitution des groupements pyridine du ligand L2 par des groupements aniline (figure II.2)

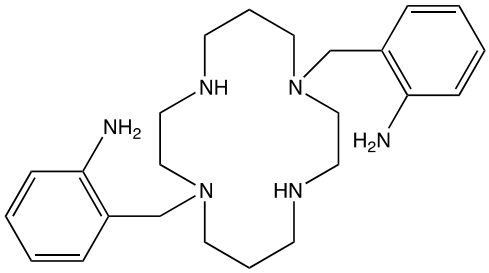

Figure II.2 Ligand L'2

Ce concept a été transposé au système tripodal tmpa (tris(2-pyridylmethyl) amine) déjà très étudié, pour obtenir le ligand andmpa (bis(2-pyridylmethyl)aminomethyl)aniline). Associé aux ions fer(II) et au co-ligand $(tcpd)^{2-}$ (anion dicyanomethylene-1,1,3,3-tetracyanopropanediure) , un nouveau complexe à transition de spin a été obtenu. Dans cette dernière partie, nous étudierons la synthèse, la caractérisation et les propriétés de ce nouveau système. Ces résultats ont également fait l'objet d'une publication présentée dans ce paragraphe.

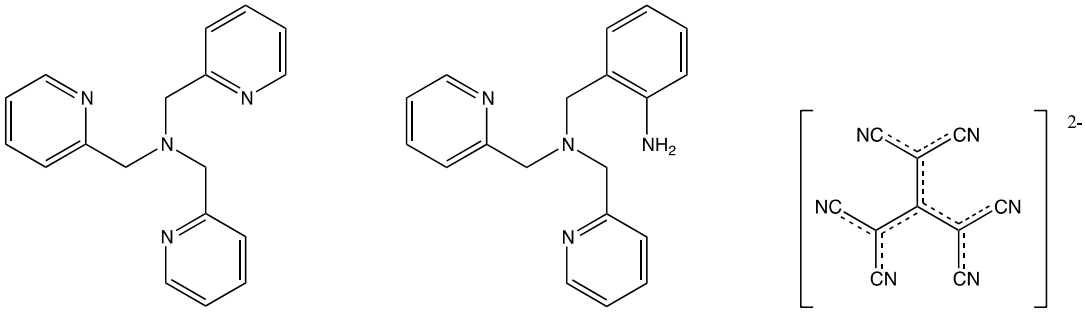

Figure II.3 Ligands tmpa andmpa $(tcpd)^{2-}$

1. Bistabilité magnétique dans un complexe macrocyclique

Magnetic Bistability in a Macrocycle-Based Iron (II) complex

Eric Milin,[†] Fatima El Hajj,[†] Véronique Patinec,[†] Smail Triki,*[,†] Mathieu Marchivie,[†,‡] Carlos J. Gómez-García,[§] Sébastien Pillet.[II]

[†]UMR CNRS 6521, Chimie, Electrochimie Moléculaires, Chimie Analytique, Université de Bretagne Occidentale, BP 809, 29285 Brest Cedex, France.
E-mail: smail.triki@univ-brest.fr
[§]Instituto de Ciencia Molecular (ICMol), Universidad de Valencia, C/ Catedrático José Beltrán, 2, 46980 Paterna, Valencia, Spain.
[‡]Université Bordeaux, ICMCB, 87 Av. Doc. A. Schweitzer, F-33608 Pessac, France.
[II]CRM2, UMR CNRS 7036, Institut Jean Barriol, Université de Lorraine, B.P. 70239, F-54506 Vandoeuvre-lès-Nancy, France.

ABSTRACT: A new iron(II) complex of formula [Fe(L2)](tcm)$_2$.2H$_2$O (1) has been synthesized and characterized by variable temperature X-ray diffraction and magnetic measurements. The crystal structure of 1 reveals discrete iron(II) monomers in which the Fe(II) ion adopts a

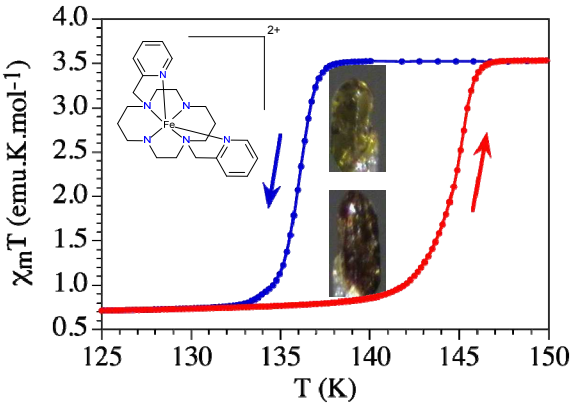

distorted FeN$_6$ octahedral geometry. A hydrogen bond network involving the water molecules and the (tcm)$^-$ counter-ions leads to a supramolecular 1D architecture. The magnetic measurements show an incomplete *HS-LS* SCO transition with a 9 K wide hysteresis loop ($T_{½}^{down}$ = 136 K; $T_{½}^{up}$ = 145 K) which is also observed optically. Detailed X-ray diffraction studies as a function of temperature (293-120 K) showed a strong modification of the iron coordination sphere, whose characteristics are in agreement with the presence of a spin crossover (*SCO*) transition from high spin (*HS*) to low spin (*LS*) in **1**. The average Fe-N distance at room temperature (2.196(2) Å) and at 120K (2.053(4) Å) are in the range expected for 100 % and *ca.* 22 % fractions of *HS* iron (II), respectively. These observations are consistent with the presence of *ca.* 20 % residual *HS* species at low temperatures, as derived from the magnetic data.

■ INTRODUCTION

The design of new coordination complexes exhibiting the spin crossover phenomenon (SCO) is one of the most relevant and challenging questions in the field of magnetic molecular materials.[1] In such systems, the magnetic state can be switched from the high-spin (*HS*) to the low-spin (*LS*) configuration through external stimuli such as temperature, pressure, magnetic field or light irradiation.[1-2] The SCO phenomenon occurs in the d^4-d^7 transition metal complexes, but the most studied examples to date are those based on Fe(II) (d^6 configuration), for which a paramagnetic-diamagnetic transition from the *HS* ($S = 2$, $^5T_{2g}$) to the *LS* ($S = 0$, $^1A_{1g}$) state is observed.[2,3] We and others have recently reported a very scarcely investigated approach consisting on the use of functionalized polyazamacrocycle ligands to design new SCO systems.[4,5] The chemical flexibility of such ligands can be viewed as an excellent starting point for the design of new parent macrocycle ligands able to create moderate or strong intermolecular interactions in their corresponding metal complexes.[6,7] In this recent report based on the bis-N-functionalized tetraazamacrocycles (Scheme 1),[4] we have shown that the coordination sphere, and subsequently the ligand field energy, can be efficiently fine-tuned by varying the size of the fully saturated heterocycle. As expected, this approach previously led us to a series of two Fe(II) complexes, $[Fe(L1)](BF_4)_2$ and $[Fe(L2)](BF_4)_2.H_2O$,[4] which are based respectively on functionalized cyclen (L1 = 1,7-bis(2'-pyridylmethyl)-1,4,7,10-tetraazacyclododecane) and cyclam (L2 = 1,8-bis(2'-pyridylmethyl)-1,4,8,11-tetraazacyclotetradecane) ligands (Scheme 1). In both cases, the structure consists of a discrete monomeric $[FeL]^{2+}$ cation and two uncoordinated $(BF_4)^-$ anions. Despite their structural similarities, the two complexes display different magnetic behaviours. Thus, the complex based on functionalized cyclen ligand remains in the high spin ground state ($S = 2$) in the whole temperature range, while the complex based on a slightly larger macrocycle (cyclam) presents a *HS*↔*LS* SCO conversion with a transition temperature ($T_{1/2}$) around 150 K.[4]

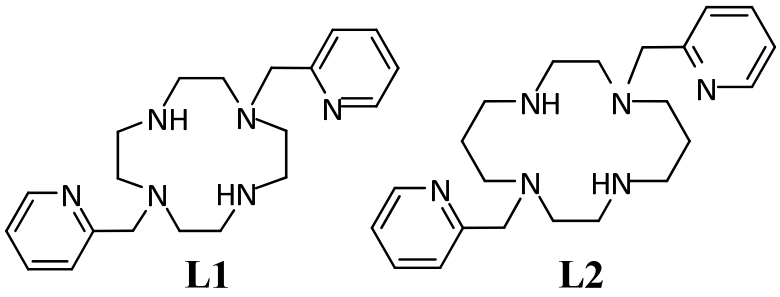

Scheme 1. Two examples of N-functionalized macrocycle ligands.

The cationic character of the L2 metal complex and its relatively high stability in solution allowed us to investigate the effect of the nature of the counter-ion on the magnetic properties. Herein, we report the synthesis, structural characterisation and magnetic properties of $[Fe(L2)](tcm)_2.2H_2O$ (**1**) (tcm^- = $[C(CN)_3]^-$ = *tricyanomethanide anion*), the first tetraazamacrocycle-based iron(II) compound exhibiting magnetic bistability.

■ EXPERIMENTAL SECTION

General remarks. All reactions were carried out under aerobic conditions. The $Fe(BF_4)_2.6H_2O$ starting material and solvents used for the synthesis were purchased from commercial sources and used without further purification. Cyclam was prepared according to the method previously reported.[7] The K(tcm) salt was prepared according to the reference 8.

Syntheses.

The tetraazamacrocycle 1,8-bis(2'-pyridylmethyl)-1,4,8,11-tetraazacyclotetradecane (L2) was prepared as previously described and characterized by NMR spectroscopy (see figures S1 and S2).[9] NMR ^1H ($CDCl_3$, 300 MHz) 8.20 (d, 1H, C_5H_4N) 7.28 (td, 1H, C_5H_4N) 7.10 (d, 1H, C_5H_4N) 6.78 (dd, 1H, C_5H_4N) 3.53 (s, 2H, CH_2-C_5H_4N) 2.45-2.35 (m, 6H, $CH_2\alpha$-N) 2.32-2.25 (m, 2H, $CH_2\alpha$-N) 1.47-1.58 (m, 2H, $CH_2\beta$-N). NMR ^{13}C ($CDCl_3$, 75.4 MHz) 158.0, 148.3, 135.4, 122.5, 121.1 (C_5H_4N) 58.7 (CH_2- C_5H_4N) 53.8, 51.1, 48.9, 46.9 ($CH_2\alpha$-N) 25.4 ($CH_2\beta$-N).

Compound **1** was prepared by adding progressively 5 mL of an aqueous solution of $Fe(BF_4)_2.6H_2O$ (33.7 mg, 0.1 mmol) to an aqueous solution (5 mL) of the L2 ligand (38.2 mg, 0.1 mmol), in a 1:1 molar ratio. The resulting yellow solution was treated by an aqueous solution (5 mL) containing 25.8 mg (0.2 mmol) of the K(tcm) salt, giving a slight white precipitate which was dissolved by a small amount of water (2 mL). Slow evaporation of the dark yellow resulting solution, at room temperature, gave green-yellow prismatic single crystals of **1** (yield: 32.4 mg, 49 %). Complex **1**. Anal. Calcd. for $C_{30}H_{38}FeN_{12}O_2$: C, 55.0; N, 25.7; H, 5.9 %. Found: C, 54.8; N, 25.6; H, 6.0 %. IR data (υ/cm^{-1}) on KBr pellets: 3421(br), 3233(m), 3195(m), 2939(m), 2910(m), 2852(m), 2168(vs), 1605(m), 1484(s), 1462(s), 1442(m), 1297(m), 1157(s), 1092(m), 1074(s), 965(m), 773(s), 761(m), 645(s), 563(m).

X-ray Crystallography. Crystallographic studies of compound **1** were performed at 293 K using an Oxford Diffraction Xcalibur CCD diffractometer with Mo Kα radiation. A small single-crystal of $0.09 \times 0.10 \times 0.32$ mm^3 was used to collect the data. The data collection was performed using 1° ω-scans with an exposure time of 150 s per frame. The unit cell determination and data reduction were performed using the CrysAlis program suite[10] on the

full set of data. The crystal structure was solved by direct methods and successive Fourier difference syntheses with the Sir97 program[11] and refined on F^2 by weighted anisotropic full-matrix least-square methods using the SHELXL97 program.[12] Both softwares were used within the WINGX package.[13] No absorption correction was needed owing to the low absorption coefficient of these compounds. Details are listed in table 1. Several attempts to solve the crystal structure in the *LS* state below 130 K failed. As shown by photographs depicted in Figure 1, the single crystal was subjected to strong constraints induced by the sharp magnetic transition, leading to multiple deep cracks that make difficult the crystal data collections at low temperatures. However, when a relatively small single crystal (0.09 × 0.10 × 0.32 mm^3) was covered by oil and very slowly cooled, the deep cracks observed on bigger single crystals have been avoided. This led us to relatively correct crystal data collections at high temperatures (293K, 140K↓ and 135K↓) and low temperatures (120↓ and 140K↑) to reach the HS and LS states respectively (See Table 1).

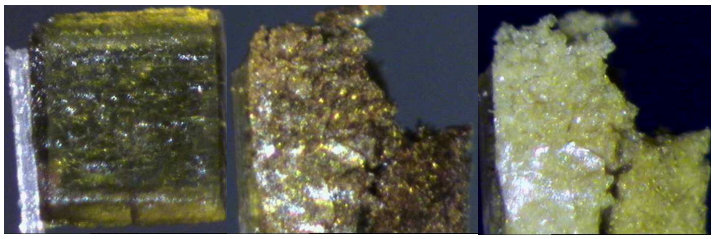

Figure 1. Deep cracks observed from T = 170↓ to T = 170 K↑.

Physical measurements. Infrared spectra were recorded in the range 4000-200 cm^{-1} on a FT-IR BRUKER ATR VERTEX70 Spectrometer. Diffraction analyses were performed using an Oxford Diffraction Xcalibur κ-CCD diffractometer. Variable temperature magnetic susceptibility measurements were carried out in the temperature range 2-300 K in cooling and warming scans with an applied magnetic field of 0.5 T on crushed single crystals of compound **1** (mass = 6.30 mg) with a Quantum Design MPMS-XL-5 SQUID magnetometer. The susceptibility data were corrected for the sample holders previously measured under the same conditions, and for the diamagnetic contributions as deduced by using Pascal´s constant tables (χ_{dia} = -383.8x10^{-6} emu.mol^{-1}).[14] The magnetic measurements were done with different cooling and warming rates in the range 0.5-5 K/min. The DSC measurements were performed on a DSC-1/LN2 Mettler Toledo calorimeter. Elemental analyses were performed at the "Service de microanalyse", CNRS, 91198 Gif-sur-Yvette.

Table 1. Crystal data and structural refinement parameters for $[FeL2](tcm)_2(H_2O)_2$ (**1**)

***T* (K)**	**293**	**140↓**	**135↓**	**120↓**	**140↑**
Color	yellow	yellow	yellow	red	red
Empirical formula			$C_{30}H_{38}FeN_{12}O_2$		
Molecular weight	654.57	654.57	654.57	654.57	654.57
Space group	$P2_1/c$	$P2_1/c$	$P2_1/c$	$P2_1/c$	$P2_1/c$
a (Å)	11.9999(7)	11.973(5)	11.9692(3)	11.3188(6)	11.3229(10)
b (Å)	13.8611(7)	13.617(5)	13.6182(3)	13.8978(8)	13.8694(12)
c (Å)	20.2894(10)	20.186(5)	20.1825(5)	20.5887(10)	20.5558(17)
β (°)	105.831(5)	106.227(5)	106.265(2)	106.757(5)	106.737(7)
V (Å^3)	3246.8(3)	3159.9(19)	3158.06(13)	3101.2(3)	3091.4(5)
Z	4	4	4	4	4
ρ_{calc} (g.cm^{-3})	1.339	1.376	1.377	1.402	1.406
μ (cm^{-1})	5.12	5.26	5.27	5.36	5.38
F(000)	1376	1376	1376	1376	1376
Refl. measured	25904	25184	23842	22812	23830
2θ range (°)	5.88-54.00	5.48-54.00	5.98-54.00	5.86-54.00	5.88-54.00
Refl. unique / R_{int}	7087/0.0609	6892/0.0448	6886/0.02660	96760/0.1237	6744/0.3085
Refl. with I>2σ(I)	3771	4755	5198	3587	3356
N_v	422	422	422	422	396
[a]*R1* / [b]*wR2*	0.0434/0.0867	0.0358/0.0777	0.0311/0.0786	0.0801/0.1983	0.1394/0.3936
[c]GooF	0.846	0.911	0.944	1.010	1.096
$\Delta\rho_{max/\,min}$ (eÅ^{-3})	0.362/-0.163	0.302/-0.203	0.318/-0.224	1.021/-0.456	1.456/-0.707

[a]$R1 = \sum|Fo-Fc|/Fo$. [b]$wR2 = \{\sum[w(F_o^2-F_c^2)^2]/\sum[w(F_o^2)^2]\}^{1/2}$. [c]$GooF = \{\sum[w(F_o^2-F_c^2)^2]/(N_{obs}-N_{var})\}^{1/2}$

■ RESULTS AND DISCUSSION

The compound $[Fe(L2)](tcm)_2.2H_2O$ (**1**) was synthesized by reaction of an aqueous solution containing both $Fe(BF_4)_2.6H_2O$ and L2 ligand with an aqueous solution of the K(tcm) salt, in a 1:1:2 molar ratio, respectively. Single yellow crystals of compound **1** were obtained by slow evaporation of the yellow solution. The IR spectrum of **1** shows sharp peaks around 3300 cm^{-1} and in the 3000-2800 cm^{-1} regions, which are respectively attributed to the symmetric and antisymmetric N-H and C-H stretching modes from the L2 ligand; also, two strong absorption bands around 1450 cm^{-1} are assigned to CH_2 bending modes while the vibration band at 1605 cm^{-1} is attributable to the υ(pyridine ring) stretching vibrations.[15] In addition, the spectrum exhibits a strong absorption band at 2168 cm^{-1}, ascribed to the υ_{CN} of

the tcm^- anions. The value of this absorption band is close to that observed in the spectrum of K(tcm) corresponding to the uncoordinated tcm^- moiety (2178 cm^{-1}).

Based on the conclusions derived from the thermal variation of the magnetic data and from the calorimetric measurements (see below), the crystal structure of **1** has been determined at different temperatures. The following general structural description is relative to the room temperature data (293 K); the relevant structural modifications induced by a variation of temperature will be discussed further in the following sections. The unit cell parameters, crystal and refinement and the pertinent bond lengths and bond angles are given in tables 1-2 respectively. The molecular structure of the cationic Fe(II) complex ($[FeL2]^{2+}$), at room temperature, is depicted in figure 2.

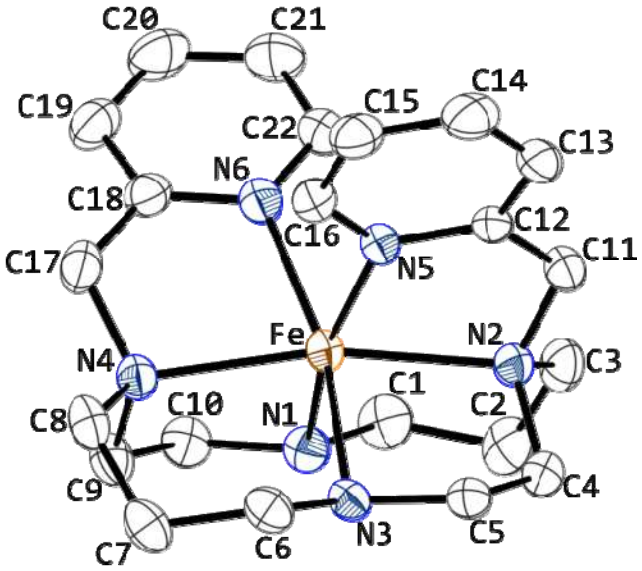

Figure 2. ORTEP[16] drawing (50% probability ellipsoids) of the cationic complex of **1** showing the asymmetric unit of the metal complex, the atom labelling scheme and the coordination environment of the iron ion.

Table 2. Thermal variation of bond lengths (Å), bond angles (°) and distortion parameters (°) of the Fe(II) coordination sphere for **1**.

***T* (K)**	**293**	**140↓**	**135↓**	**120↓**	**140↑**
Fe-N1	2.1933(17)	2.1940(16)	2.1929(12)	2.063(4)	2.069(7)
Fe-N2	2.2352(17)	2.2326(15)	2.2312(12)	2.093(4)	2.089(6)
Fe-N3	2.1703(18)	2.1628(17)	2.1653(13)	2.059(4)	2.051(7)
Fe-N4	2.2271(17)	2.2315(15)	2.2303(12)	2.095(4)	2.098(6)
Fe-N5	2.1952(19)	2.1980(17)	2.1930(13)	2.007(4)	2.005(7)
Fe-N6	2.1572(18)	2.1474(17)	2.1501(12)	2.003(4)	1.999(6)
<Fe-N>	**2.196(2)**	**2.194(2)**	**2.194(2)**	**2.053(4)**	**2.052(7)**
N6 Fe N3	166.82(7)	166.93(5)	167.02(5)	172.23(16)	171.8(3)
N6 Fe N1	89.26(7)	88.93(6)	88.89(5)	90.16(17)	90.0(3)
N3 Fe N1	94.57(7)	94.70(6)	94.64(5)	93.84(17)	94.4(3)
N6 Fe N5	89.82(7)	90.31(6)	90.34(5)	87.99(17)	87.5(3)
N3 Fe N5	89.32(7)	88.99(6)	89.03(5)	88.86(17)	89.0(3)
N1 Fe N5	166.62(7)	166.77(5)	166.79(5)	172.66(16)	172.4(3)
N6 Fe N4	78.58(7)	78.82(5)	78.99(5)	82.99(16)	83.0(3)
N3 Fe N4	89.46(7)	89.25(5)	89.15(5)	90.76(15)	90.6(3)
N1 Fe N4	81.90(6)	81.86(5)	81.76(4)	84.46(16)	83.8(3)
N5 Fe N4	110.98(7)	110.93(5)	111.02(5)	102.35(16)	102.8(3)
N6 Fe N2	110.46(7)	110.15(5)	109.98(5)	102.31(16)	103.0(3)
N3 Fe N2	82.22(6)	82.47(5)	82.57(5)	84.34(15)	84.6(3)
N1 Fe N2	89.62(7)	89.71(5)	89.70(4)	90.48(16)	90.7(3)
N5 Fe N2	78.21(7)	78.17(5)	78.18(5)	82.98(16)	82.9(3)
N4 Fe N2	167.62(7)	167.68(5)	167.60(5)	172.72(16)	172.4(3)
$^{a}\Sigma$	87.62	87.89	87.71	58.28	60.3
$^{b}\Theta$	227.27	225.45	224.58	139.2	145.65

$^{a}\Sigma$[17] is the sum of the deviation from 90° of the 12 *cis*-angles of the FeN_6 octahedron; $^{b}\Theta$[17] is the sum of the deviation from 60° of the 24 trigonal angles of the projection of the FeN_6 octahedron onto its trigonal faces.

At room temperature, the structure consists of a discrete monomeric $[FeL2]^{2+}$ cation, two $(tcm)^{-}$ anions and two water molecules, all located on general positions. The complexation of the Fe(II) ion with the L2 ligand results in a distorted octahedral geometry with four nitrogen atoms from the macrocycle (N1, N2, N3 and N4) and two from the pyridine rings (N5 and N6). The four amine nitrogen span two contiguous faces of the coordination polyhedron, and the pyridine nitrogen atoms occupy the remaining pair of *cis* positions, as observed in $[Fe(L2)](BF_4)_2.H_2O$,[4] involving similar complex ($[Fe(L2)]^{2+}$) and in parent Ni(II) complexes based on similar macrocycle ligands (figure 2).[15d]

The average value of the six Fe-N distances (2.196(2) Å, table 2) is in good agreement with the values expected for *HS* Fe(II) complexes in octahedral geometry.[17] As for the previously reported parent compound [FeL2]$(BF_4)_2.H_2O$ (**2**),[4] the bond distances involving the secondary amines of the cyclam ring (Fe-N1 2.195(2) and Fe-N3 2.172(2) Å) and the Fe-N(py) distances (Fe-N5 2.196(2) and Fe-N6 2.159(2) Å) are shorter than the two distances involving the nitrogen atoms (N2 and N4) connected to the pyridinemethyl groups (2.237(2) and 2.229(2) Å, respectively). Consequently, the octahedral geometry around the iron atom is highly distorted, as demonstrated by the high values of Σ and Θ parameters (table 2).[17]

The magnetic susceptibility (χ_m) for **1** was determined over the 2-300 K range in a field of 0.1 T, with different cooling and warming rates in the range 0.2-5 K/min. The $\chi_m T$ versus T plot (where T is the temperature) observed in cooling and warming mode is depicted in figure 3. In the high-temperature region, the $\chi_m T$ value (3.51 $cm^3.K.mol^{-1}$) is consistent with a $S = 2$ *HS* state of the hexacoordinated iron (II) ions. Upon cooling, $\chi_m T$ remains almost constant down to a temperature value of *ca.* 137 K. Below this temperature, it shows a sharp decrease indicating the presence of an abrupt *HS-LS SCO* transition. The remaining $\chi_m T$ value of *ca.* 0.7 $cm^3.K.mol^{-1}$ indicates that, at low temperature, there exists a fraction of *ca.* 20 % of residual Fe(II) ions in the *HS* configuration. In the temperature range 137-10 K, the $\chi_m T$ product remains constant, indicative of a paramagnetic behavior of the residual Fe(II) *HS* species. Below 10 K the $\chi_m T$ product shows an abrupt decrease reaching a value of 0.1 $cm^3.K.mol^{-1}$ at 2 K, which can be attributed to the zero field splitting (ZFS) of the *HS* Fe(II) residual fraction.

The warming mode reveals the presence of thermal hysteresis. The spin transition temperatures ($T_{½}$) for the cooling ($T_{½}^{down}$) and warming ($T_{½}^{up}$) scans are 136 and 145 K, respectively, indicating the occurrence of approximately a 9 K wide hysteresis loop.

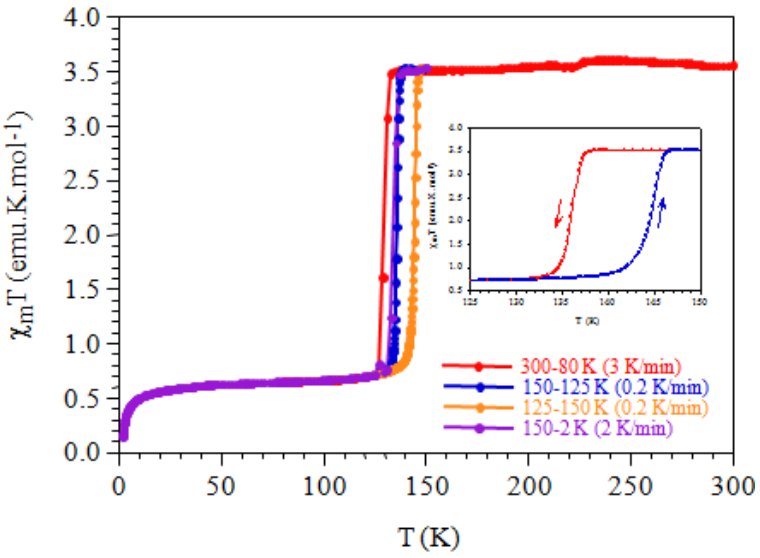

Figure 3. Magnetic properties displaying the first order spin transition for **1**: thermal variation of the $\chi_m T$ product and hysteresis loop (inset) observed with a scan rate of 0.2K/min.

The photographs depicted in figure 4 show clearly that this molecular bistability can be also illustrated by the thermochromism observed for this compound since the magnetic hysteresis is reproducible optically. The study of such thermochromic effect also reveals multiple deep cracks in the crystal, probably due to the strong constraints induced by the sharp magnetic transition, as also revealed in figure 1. However, even after several thermal cycles, this mechanical fragility does not alter the magnetic nor the thermochromic bistability of the system.

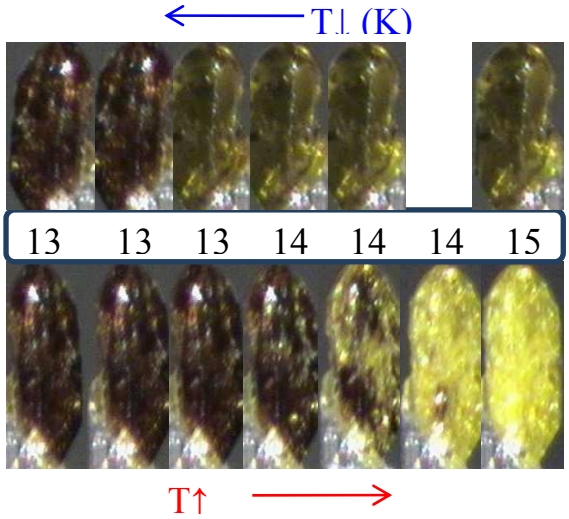

Figure 4. Photographs showing the color change around the critical region (green-yellow and red colors correspond to *HS* and *LS* states, respectively), the thermochromic bistability and the deep cracks observed on a single crystal of **1**.

The effect of scan rate on the hysteresis width has been investigated by measuring the magnetic susceptibility at different scan rates in the cooling and warming modes. This effect is depicted in figure 5 for the scan rate of 0.2, 1, 2, 5 and 10 K.mn^{-1}.

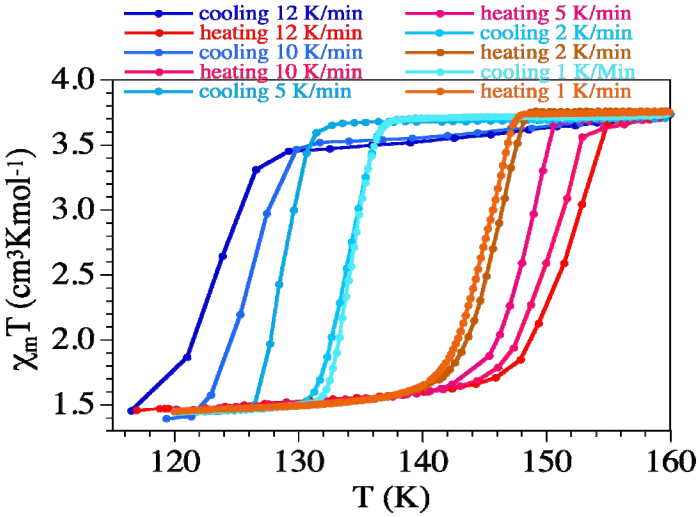

Figure 5. Thermal variation of the χMT product for compound 1 at scan rate of 0.2, 1, 2, 5 and 10 K.mn^{-1}

As clearly shown in figure 5, the hysteresis width increases from ca. 9.2 K to ca. 23.0 K when the scan rate is increased from 0.2 to 10 K.min^{-1}. However, this kinetic effect appears clearly less pronounced at low scan rates since below 0.5 K.min^{-1}, the hysteresis width remains relatively constant. The differential scanning calorimetry (DSC) measurements were performed using similar sample than that used for the magnetic studies. The thermal variation of the heat flow shows exo- and endothermic transitions, in agreement with the magnetic bistablity observed from the magnetic data (figure 6).

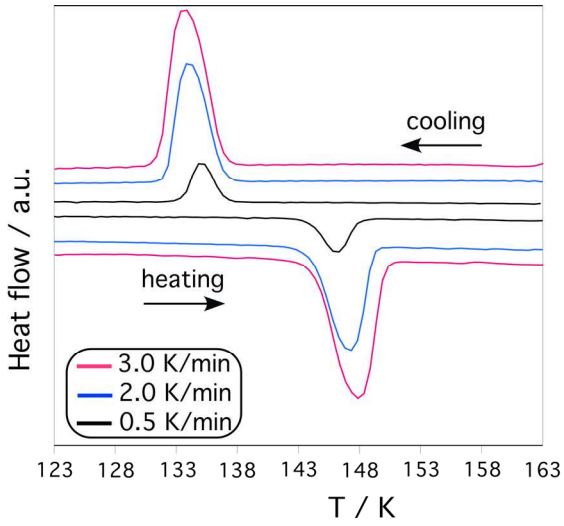

Figure 6. DSC curves of compound **1** in cooling and heating modes with scan rates of 2.0, 2.0 and 0.5 K.min^{-1}.

Based on the conclusions drawn from the magnetic data, the crystal structure of **1** has been determined at different temperatures: at 293 K 140 K, 135 K, 120 K in cooling mode, at and at 140 K in warming mode (140↑ K). The corresponding structural parameters (tables 1) show that compound **1** crystallizes in the monoclinic $P2_1/c$ space group and do not reveal any structural phase transition within the measured temperature range (293-120 K). In the following discussion, the average coordination distances <Fe-N> and the trigonal distortion parameters (Σ and Θ) depicted in table 2, will be used to assign the spin state on the Fe(II) crystallographic centers ($<Fe\text{-}N>_{LS}$ ~ 2.0 Å; $<Fe\text{-}N>_{HS}$ ~ 2.2 Å), since these parameters are known to be highly sensitive on the Fe^{II} spin configuration. In the 293-135 K temperature range, the average values of the six Fe-N distances (2.196(2), 2.194(2), 2.194(2) Å at 293, 140 and 135 K, respectively) remain relatively constant and the corresponding distortion parameters (Σ and Θ) observed are relatively high (table 2). These values are in good agreement with that expected for *HS* Fe(II) complexes in distorted octahedral geometry.[17]

Strong modifications of the iron coordination sphere are observed while varying the temperature with cooling mode below 135 K and with warming mode above 120 K (140↑ K). Upon cooling from 135 to 120 K the <Fe-N> parameters decreases from 2.194(2) Å to 2.053(4) Å. In the same time, the trigonal distortion parameters (Σ and Θ) decrease significantly, owing to the more regular FeN_6 octahedral geometry expected for the *LS* state. When a single crystal of **1** is warmed from 120 to 140 K, the average Fe-N distance and the trigonal distortion parameters remain unchanged, in agreement with the hysteretic behavior shown by the magnetic data. The averaged values <Fe-N> observed at 120 K and at 140↑ K (2.053(4) and 2.052(7) Å respectively) indicate that the corresponding *HS* fraction is about 22 %, synonym of the presence of an incomplete *HS*-*LS* thermal conversion in **1** as revealed by the magnetic data. The fact that the value of *HS* fraction deduced from the structural parameters (*ca.* 22 %) is slightly higher than that derived from the magnetic data (*ca.* 20%), can be attributed to the differences between the thermal treatments of compound **1**.

The magnetic behavior observed for **1** is strongly different from that previously observed for the parent compound $[FeL2](BF_4)_2.H_2O$ (**2**), the latter exhibiting a gradual SCO transition at higher temperatures without magnetic bistability.[4] The most important intramolecular structural difference between complexes **1** and **2** concerns the trigonal distorsion of the iron coordination sphere which is significantly higher for **1** than for **2** (Θ = 350(4)° and Θ = 335(4)°, respectively). Indeed, it has been previously established that higher trigonal distorsion was related to lower spin transition temperature.[17c] Interestingly, this last

observation confirms this assumption, as $T_{½}^{down}$ and $T_{½}^{up}$ are 136 and 145 K respectively for **1** while $T_{½}$ is 150 K for **2**. Besides, the sharpness of the transition may explain the crystal damages as it was also observed, with a smaller amplitude, on complexes with smoother spin transitions.[18] As it has been previously demonstrated, the intermolecular interactions, and particularly hydrogen bonding, play a crucial role on the cooperativity of such transitions.[17b,19] With the aim to better understand this difference, we have examined the intermolecular contacts (π-stacking, hydrogen bonding and van der Waals contacts) in both complexes (figure 7).

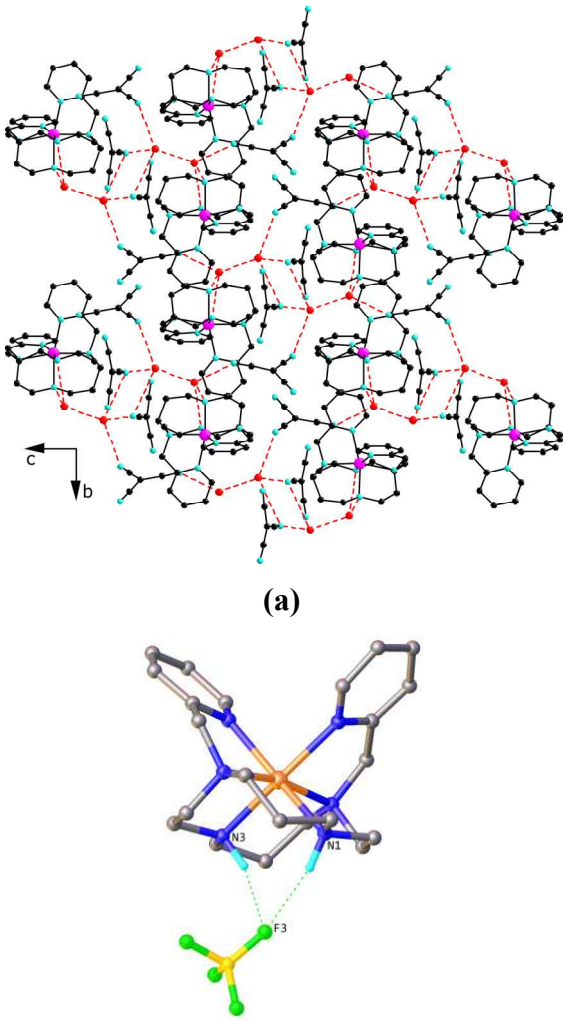

(a)

(b)

Figure 7. (a) Projection view along the [100] direction of the overall molecular structure of $[Fe(L2)](tcm)_2 \cdot 2H_2O$ (**1**) showing the 2-D layers induced by intermolecular hydrogen bonding (see dashed lines: N…O and O….O < 3.5 Å); (b) Intermolecular contact showing the discrete structure in $[Fe(L2)](BF_4)_2.H_2O$ (**2**).[4]

This study revealed, as expected, the existence of significant hydrogen bonding in **1,** mediated by the $(tcm)^-$ anions and the water molecules, leading to the supramolecular bidimensional structure depicted in figure 7a, and the absence of any significant long range intermolecular interactions in compound **2** (figure 7b). This observation perfectly agrees with a recent study on the parent macrocyclic complex $[Fe(L)](ClO_4)_2$ (L=1,4,7-tris(2-aminophenyl)-1,4,7-triazacyclononane) that undergoes a gradual spin crossover.[5a] In this example, the authors explained such magnetic behaviour by the lack of significant long range intermolecular interactions. The presence of the hydrogen bond network in **1** may thus explain the cooperative magnetic properties of this compound.

To understand how the crystal and the lattice parameters were affected by the strong magnetic bistability observed for **1**, the temperature dependence of the lattice parameters of a single crystal of **1** were measured in the range 293-120 K. As expected, all the structural parameters such as the cell parameters (a, b, c, β, V) as well as the averaged values of the Fe-N distances show dramatic changes at transition temperature (figure 8 and S3). The thermal variation of the unit cell volume reveals strong decrease below the transition temperature and this volume remains relatively constant when the crystal is warmed from 120 to 140 K, as expected from the hysteretic behavior of **1**. However, as shown by the thermal variation of the three metric parameters (*a, b, c*), this contraction is strongly anisotropic, since below the transition, only the *a* parameter shows thermal decrease as expected from the presence of the elastic transition in **1**; the two other metric parameters (*b* and *c* parameters) reveal unexpected significant increases below the magnetic transition. The positive thermal expansion occurring in the *bc* plane and the negative thermal expansion along the *a* axis can be related, respectively, to the presence of intermolecular interactions observed in the *bc* plan (see figure 7a) and to the absence of any significant hydrogen bonding along the *a* axis.

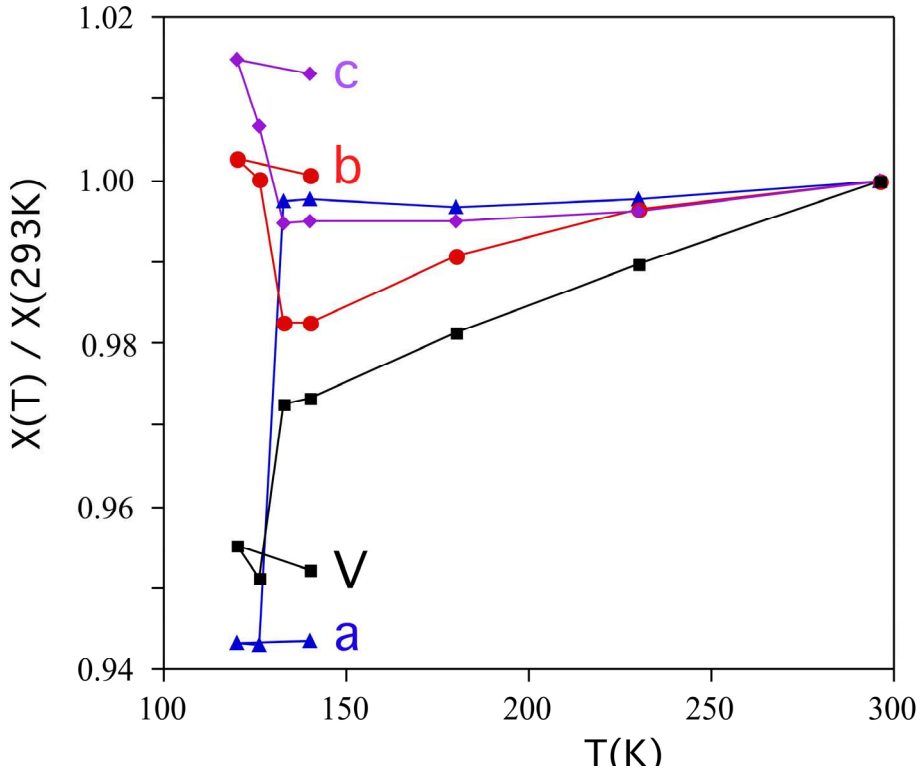

Figure 8. Thermal evolution of the lattice parameters of complex **1**; *a* (▲), *b* (●) and *c* (■) parameters and unit cell volume (♦) showing the anisotropic contraction of the crystal below the SCO transition.

■ CONCLUSIONS

A new SCO macrocycle-based complex $[Fe(L2)](tcm)_2.H_2O$ (**1**) has been prepared and characterized. The molecular structure of the iron (II) complex cation was characterized as mononuclear discrete complex generated by the hexadentate N-functionalized macrocycle ligand (L2). Despite a molecular structure similar to that described previously for the parent complex $[Fe(L2)](BF_4)_2.H_2O$ (**2**) exhibiting a gradual SCO behaviour ($T_{1/2}$ = 150 K) without magnetic bistability, the thermal variation of the $\chi_m T$ product in **1** shows a SCO transition with a hysteresis loop of 9 K (T_c^{down} = 136 K; T_c^{up} = 145 K). This difference results from the presence of significant hydrogen bonding through the tcm^- counter-ions in **1** which is significantly less important in compound **2** involving $(BF_4)^-$ counter-ions. In addition to the magnetic bistability observed in **1**, this study confirms also that slight structural changes in such systems may generate dramatic changes in the physical properties.

■ ASSOCIATED CONTENT

Supporting information

Electronic Supplementary Information (ESI) available: This material is available free of charge via the Internet. CCDC 892671 at 293K and 120 K, and XXXX-XXXX (140K↓, 135K↓, 120↓ and 140K↑) contains the supplementary crystallographic data for this paper. These data can be obtained free of charge from The Cambridge Crystallographic Data Centre via www.ccdc.cam.ac.uk/data_request/cif.

■ AUTHOR INFORMATION

Corresponding author

*E-mail: smail.triki@univ-brest.fr. Phone: +33 298 016 146, Fax: +33 298 017 001

Notes

The authors declare no competing financial interest.

■ ACKNOWLEDGMENTS

The authors acknowledge the CNRS ("Centre National de la Recherche Scientifique"), the Brest University, the french "Ministère de la Recherche" and "Ministère des Affaires Etrangères et Européennes" (PHC Maghreb project **N° 30255ZJ)**, the "Agence Nationale de la Recherche" (ANR project BISTA-MAT: ANR-12-BS07-0030-01), the "Spanish Ministerio de Economía y Competitividad" (Project CTQ2011-26507), and the "Generalitat Valenciana" (projects Prometeo 2009/095 and ISIC). F.E.H. thanks the "Région Bretagne" for a PhD grant.

■ REFERENCES

(1) see for example: a) Gómez, V.; Sáenz de Pipaón, C.; Maldonado-Illescas, P.; Waerenborgh, J.-C.; Martin, E.; Benet-Buchholz, J.; Galán-Mascarós, J.-R., *J. Am. Chem. Soc.* **2015**, *137*, 11924–11927; b) Chen, M.-Y.; Chen, X.-R.; Ninga, W.-H.; Ren, X.-M., *RSC Adv.* **2014**, *4*, 39126–39131; c) Olguin, J.; Brooker, S.,*Coord. Chem. Rev.* **2011**, *255*, 203-240; d) Halcrow, M. A., *Chem. Soc. Rev.* **2011**, *40*, 4119-4142; e) Bousseksou, A.; Molnar, G.; Salmon, L.; Nicolazzi, W., *Chem. Soc. Rev.* **2011**, *40*, 3313-3335; f) Garcia, Y.; Robert, F.; Naik, A.-D.; Zhou, G.; Tinant, B.; Robeyns, K.; Michotte, S.; Piraux, L., *J. Am. Chem. Soc.* **2011**, *133*, 15850–15853; g) Félix, G.; Abdul-Kader, K.; Mahfoud, T.; Gural'skiy, I. A.; Nicolazzi, W.; Salmon, L.; Molnar, G.; Bousseksou, A., *J. Am. Chem. Soc.* **2011**, *133*,15342–15345; h) Gamez, P.; Sanchez Costa, J.; Quesada, M.; Aromi, G., *Dalton trans.* **2009**, 7845-

7853; i) Titos-Padilla, S.; Herrera, J. M.; Chen, X.-W.; Delgado, J. J.; Colacio, E., *Angew. Chem., Int. Ed.* **2011**, *50*, 3290-3293; j) Setifi, F.; Benmansour, S.; Marchivie, M.; Dupouy, G.; Triki, S.; Sala-Pala, J.; Salaün, J.-Y.; Gómez-García, C. J.; Pillet, S.; Lecomte, C.; Ruiz, E., *Inorg. Chem.* **2009**, *48*, 1269-1271.

(2) see for example: a) Zhao, X.-H.; Zhang, S.-L.; Shao, D.; Wang, X.-Y., *Inorg. Chem.* **2015**, *54*, 7857–7867; b) Guionneau, P., *Dalton Trans.* **2014**, 43,382-393; c) Chakraborty, P.; Bronisz, R.; Besnard, C.; Guénée, L.; Pattison, P.; Hauser, A., *J. Am. Chem. Soc.* **2012**, *134*, 4049−4052; d) Atmani, C.; El Hajj, F.; Benmansour, S.; Marchivie, M.; Triki, S.; Conan, F.; Patinec, V.; Handel, H.; Dupouy, G.; Gómez-García, C. J., *Coord. Chem. Rev.* **2010**, *254*, 1559-1569; e) Capes, L.; Létard, J.-F.; Kahn, O., *Chem. Eur. J.* **2000**, *6*, 2246-2255; f) Dupouy, G.; Marchivie, M.; Triki, S.; Sala-Pala, J.; Gómez-García, C. J.; Pillet, S.; Lecomte, C.; Létard, J.-F., *Chem. Commun.* **2009**, 3404-3406; g) Dupouy, G.; Triki, S.; Marchivie, M.; Cosquer, N.; Gómez-García, C. J.; Pillet, S.; Lecomte, C.; Létard, J.-F., *Inorg. Chem.* **2010**, *49*, 9358-9368; h) Marchivie, M.; Guionneau, P.; Howard, J. A. K.; Chastanet, G.; Létard, J.-F.; Goeta, A. E.; Chasseau, D., *J. Am. Chem. Soc.* **2002**, *124*, 194-195; i) Niel, V.; Muñoz, M. C.; Gaspar, A. B.; Galet, A.; Levchenko, G.; Real, J.-A., *Chem. Eur. J.* **2002**, *8*, 2446-2453.

(3) a) Costes, J. P.; Dahan, F.; Laurent, J. P., *Inorg. Chem.* **1990**, *29*, 2448-2452; b) Garcia, Y.; Niel, V.; Muñoz, M. C.; Real, J.-A., *Top. Curr. Chem.* **2004**, *233*, 229; c) Hayami, S.; Moriyama, R.; Shigeyoshi, Y.; Kawajiri, R.; Mitani, T.; Akita, M.; Inoue, K.; Maeda, Y., *Inorg. Chem.* **2005**, *44*, 7295-7297; d) Ishikawa, R.; Matsumoto, K.; Onishi, K.; Kubo, T.; Fuyuhiro, A.; Hayami, S.; Inoue, K.; Kaizaki, S.; Kawata, S., *Chem. Lett.* **2009**, *38*, 620-621; e) Morgan, G. G.; Murnaghan, K. D.; Muller-Bunz, H.; McKee, V.; Harding, C. J., *Angew. Chem. Int. Ed.* **2006**, *45*, 7192-7195.

(4) El Hajj, F.; Sebki, G.; Patinec, V.; Marchivie, M.; Triki, S.; Handel, H.; Tripier, R.; Gómez-García, C. J.; Coronado, E., *Inorg. Chem.* **2009**, *48*, 10416-10423.

(5) a) Shepherd, H. J.; Rosa, P.; Fallis, I. A.; Guionneau, P.; Howard, J. A. K.; Goeta, A. E., *J. Phys. Chem. Solids* **2012**, *73*, 193-197; b) Kruger, H. J., *Coord. Chem. Rev.* **2009**, *253*, 2450-2459.

(6) a) Bellouard, F.; Chuburu, F.; Kervarec, N.; Toupet, L.; Triki, S.; Le Mest, Y.; Handel, H., *J. Chem. Soc., Perkin Trans.* **1999**, 3499-3505; b) Li, C.; Wong, W.-T., *J. Org. Chem.* **2003**, *68*, 2956-2959; El Hajj, F.; Patinec, V.; Triki, S.; Handel, H.; Marchivie, M., *Inorg. Chem. Commun.* **2010**, *13*, 1314-1316

(7) Herve, G.; Bernard, H.; Le Bris, N.; Yaouanc, J. J.; Handel, H.; Toupet, L., *Tetrahedron Lett.* **1998**, *39*, 6861-6864.

(8) Carboni, R. A., *Org. Synth.* **1959**, *39*, 64-68.

(9) Royal, G.; Dahaoui-Gindrey, V.; Dahaoui, S.; Tabard, A.; Guilard, R.; Pullumbi, P.; Lecomte, C., *Eur. J. Org. Chem.* **1998**, 1971-1975.

(10) Oxford Diffraction (2006). Xcalibur CCD/RED CrysAlis Software system. Oxford Diffraction Ltd, Abingdon, England.

(11) Altomare, A.; Burla, M. C.; Camalli, M.; Cascarano, C.; Giacovazzo, C.; Guagliardi, A.; Moliterni, A. G. G.; Polidori, G.; Spagna, R., *J. Appl. Cryst.* **1999**, *32*, 115-119.

(12) a) Sheldrick G. M., SHELX97. Programs for Crystal Structure Analysis; b) Sheldrick, G. M., *Acta Crystallogr. Sect. A* **2008**, *64*, 112-122.

(13) Farrugia, L. J., *J. Appl. Cryst.* **1999**, *32*, 837-838

(14) Bain, G. A.; Berry J. F., *J. Chem. Educ.* **2008**, *85*, 532-536.

(15) a) Bu, X.-H.; Cao, X.-C.; Chen, W.; Zhang, R.-H.; Clifford, T., *Polyhedron* **1998**, *17*, 289; b) Bu, X.-H.; Chen, W.; Mu, L.-J.; Zhang, Z.-H.; Zhang, R.-H.; Clifford, T., *Polyhedron* **2000**, *19*, 2095-2100; c) Bu, X.-H.; Chen, W.; Zhang, Z.-H.; Zhang, R.-H.; Kuang, S.-M.; Clifford, T., *Inorg. Chim. Acta* **2000**, *310*, 110; d) Batsanov, A. S.; Goeta, A. E.; Howard, J. A. K.; Maffeo, D.; Puschmann, H.; Williams, J. A. G., *Polyhedron* **2001**, *20*, 981.

(16) a) Farrugia, L. J., *J. Appl. Cryst.* **1997**, *30*, 565; b) Farrugia, L. J., *J. Appl. Cryst.* **2012**, *45*, 849-854.

(17) a) Dupouy, G.; Marchivie, M.; Triki, S.; Sala-Pala, J.; Salaün, J.-Y.; Gómez-García, C. J.; Guionneau, P., *Inorg. Chem.* **2008**, *47*, 8921-8931; b) Guionneau, P.; Marchivie, M.; Bravic, G.; Létard, J.-F.; Chasseau, D., *Top. Curr. Chem.* **2004**, *234*, 97-128; c) Marchivie, M.; Guionneau, P.; Létard, J.-F.; Chasseau, D., *Acta Cryst. B* **2005**, *B61*, 25-28.

(18) Guionneau, P.; Lakhloufi, S.; Lemee-Cailleau, M. H.; Chastanet, G.; Rosa, P.; Mauriac, C.; Letard, J. F., *Chem. Phys. Lett.* **2012**, *542*, 52-55.

(19) Marchivie, M.; Guionneau, P.; Létard, J.-F.; Chasseau, D, *.Acta Cryst. B* **2003**, *59*, 479-486.

Synopsis and structural diagram

Magnetic Bistability in a Macrocycle-Based Iron (II) complex

Eric Milin, Fatima El Hajj, Véronique Patinec, Smail Triki,* Mathieu Marchivie, Carlos J. Gómez-García, Sébastien Pillet.

A new Fe(II) spin crossover (SCO) complex based on a N-functionalized macrocycle ligand has been prepared and fully characterized. It exhibits magnetic bistability with a 9 K wide hysteresis loop ($T_{½}^{down}$ = 136 K; $T_{½}^{up}$ = 145 K).

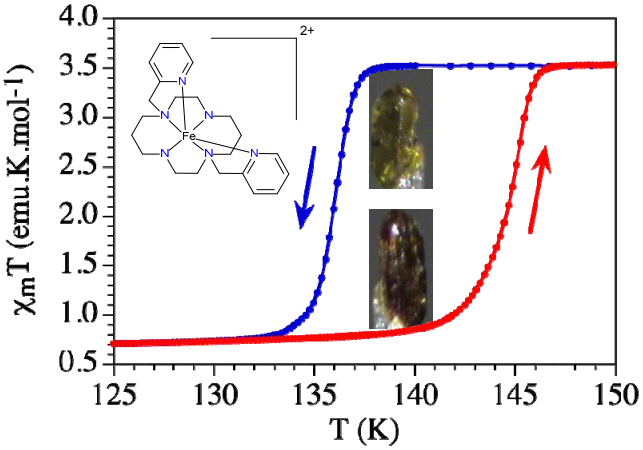

Supplementary information

Magnetic Bistability in a Macrocycle-Based Iron (II) complex

Eric Milin,[†] Fatima El Hajj,[†] Véronique Patinec,[†] Smail Triki,*[,†] Mathieu Marchivie,[†,‡] Carlos J. Gómez-García,[§] Sébastien Pillet.[II]

[†]UMR CNRS 6521, Chimie, Electrochimie Moléculaires, Chimie Analytique, Université de Bretagne Occidentale, BP 809, 29285 Brest Cedex, France.
E-mail: smail.triki@univ-brest.fr
[§]Instituto de Ciencia Molecular (ICMol), Universidad de Valencia, C/ Catedrático José Beltrán, 2, 46980 Paterna, Valencia, Spain.
[‡]Université Bordeaux, ICMCB, 87 Av. Doc. A. Schweitzer, F-33608 Pessac, France.
[II]CRM2, UMR CNRS 7036, Institut Jean Barriol, Université de Lorraine, B.P. 70239, F-54506 Vandoeuvre-lès-Nancy, France.

1 – Synthesis of L2.

The tetraazamacrocycle 1,8-bis(2'-pyridylmethyl)-1,4,8,11-tetraazacyclotetradecane (L2) was prepared as previously described and characterized by NMR spectroscopy (see figures S1 and S2).[1]

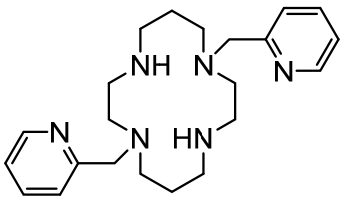

Structure of tetraazamacrocycle 1,8-bis(2'-pyridylmethyl)-1,4,8,11-tetraazacyclotetradecane (L2)

References:

1 - Carboni, R. A., *Org. Synth.* **1959**, *39*, 64-68.

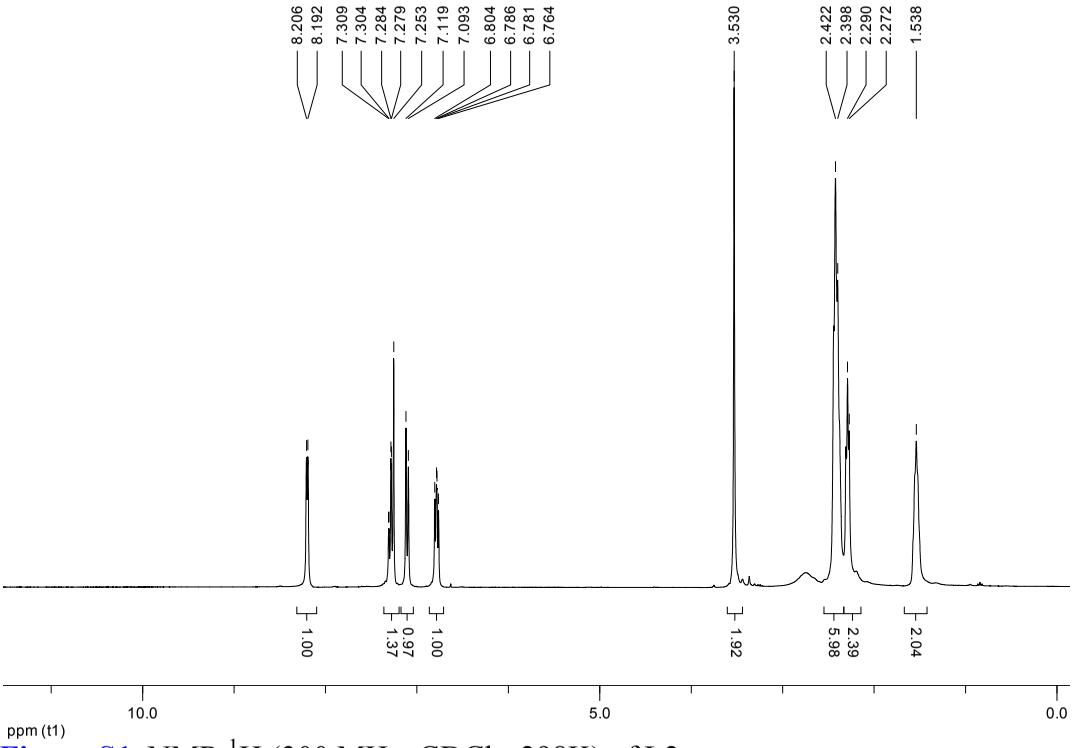

Figure S1. NMR ^{1}H (300 MHz, $CDCl_3$, 298K) of L2

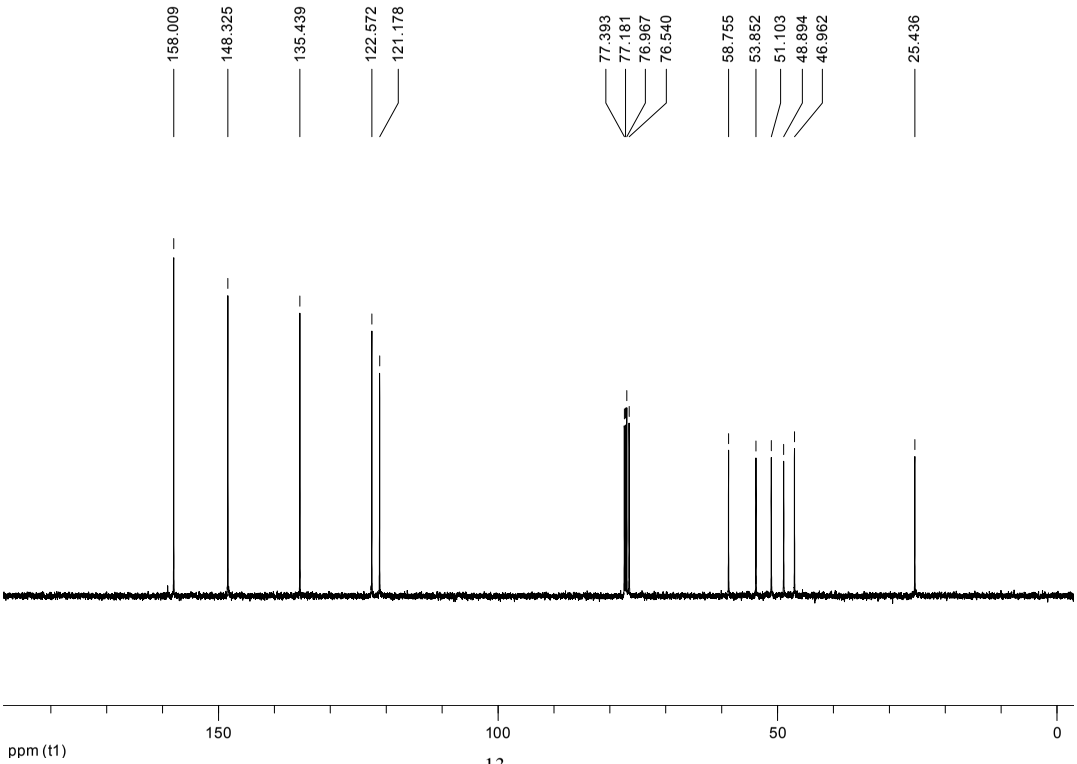

Figure S2. NMR ^{13}C (75,4 MHz, $CDCl_3$, 298K) of L2

2 – Thermal evolution of the Fe-N distances and the β parameter in [Fe(L2)](tcm)$_2$.H$_2$O (1)

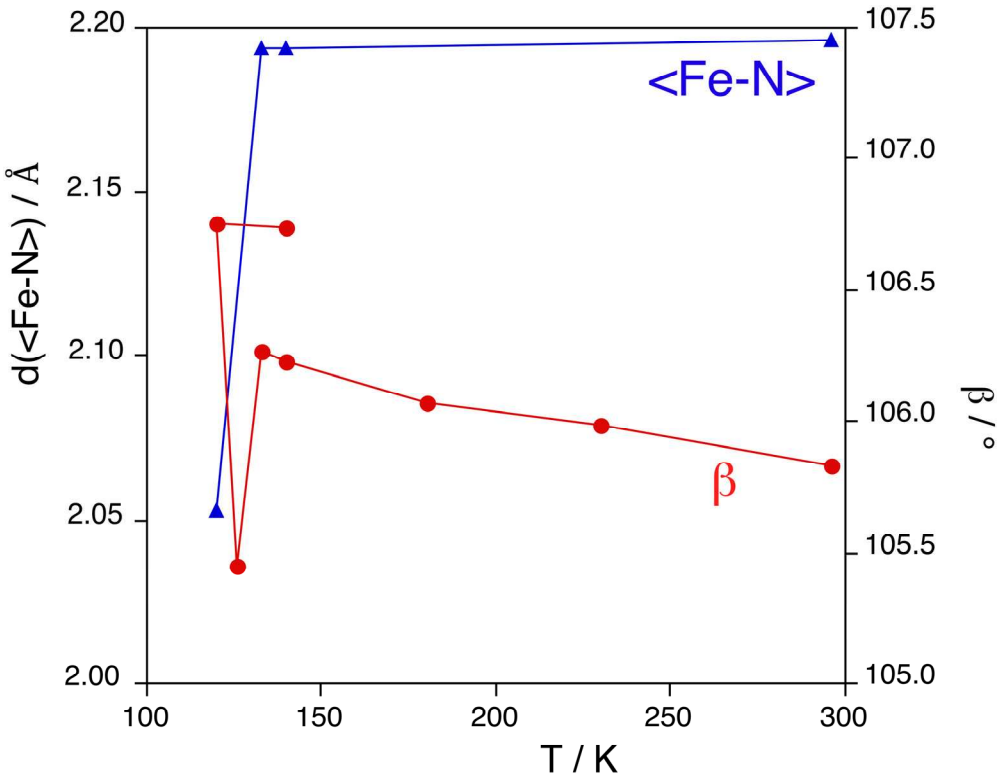

Figure S3. Thermal variation of the averaged Fe-N distances and the β parameter

2. Modification du ligand L2

La première partie de cette thèse avait pour objectif de poursuivre le travail de Fatima El Hajj et s'est divisé en deux étapes :

1°) l'étude de l'effet du contre-ion sur les caractéristiques de la transition de spin.

2°) l'étude de l'effet de la modification du ligand sur les caractéristiques de la transition de spin.

Notre choix s'est porté dans un premier temps sur la modification de la nature des bras coordinants liés à l'unité macrocyclique. Dans la prochaine partie, seront présentées la synthèse, la caractérisation et les propriétés de ce ligand associé aux ions fer(II) et cuivre(II).

2.1. Synthèse du ligand L'2: 2,2'-((1,4,8,11-tetraazacyclotetradecane-1,8-diyl)bis(methylene))dianiline

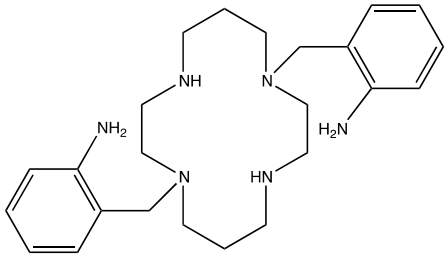

Figure II.2 Ligand L'2

Le but était de modifier le ligand L2 en conservant sa denticité. Nous avons donc substitué les groupements pyridine par des groupements aniline. Nous gardions ainsi le caractère hexadentate du ligand. La voie de synthèse est décrite dans la partie expérimentale de ce chapitre, dont on peut voir un schéma récapitulatif ci-après:

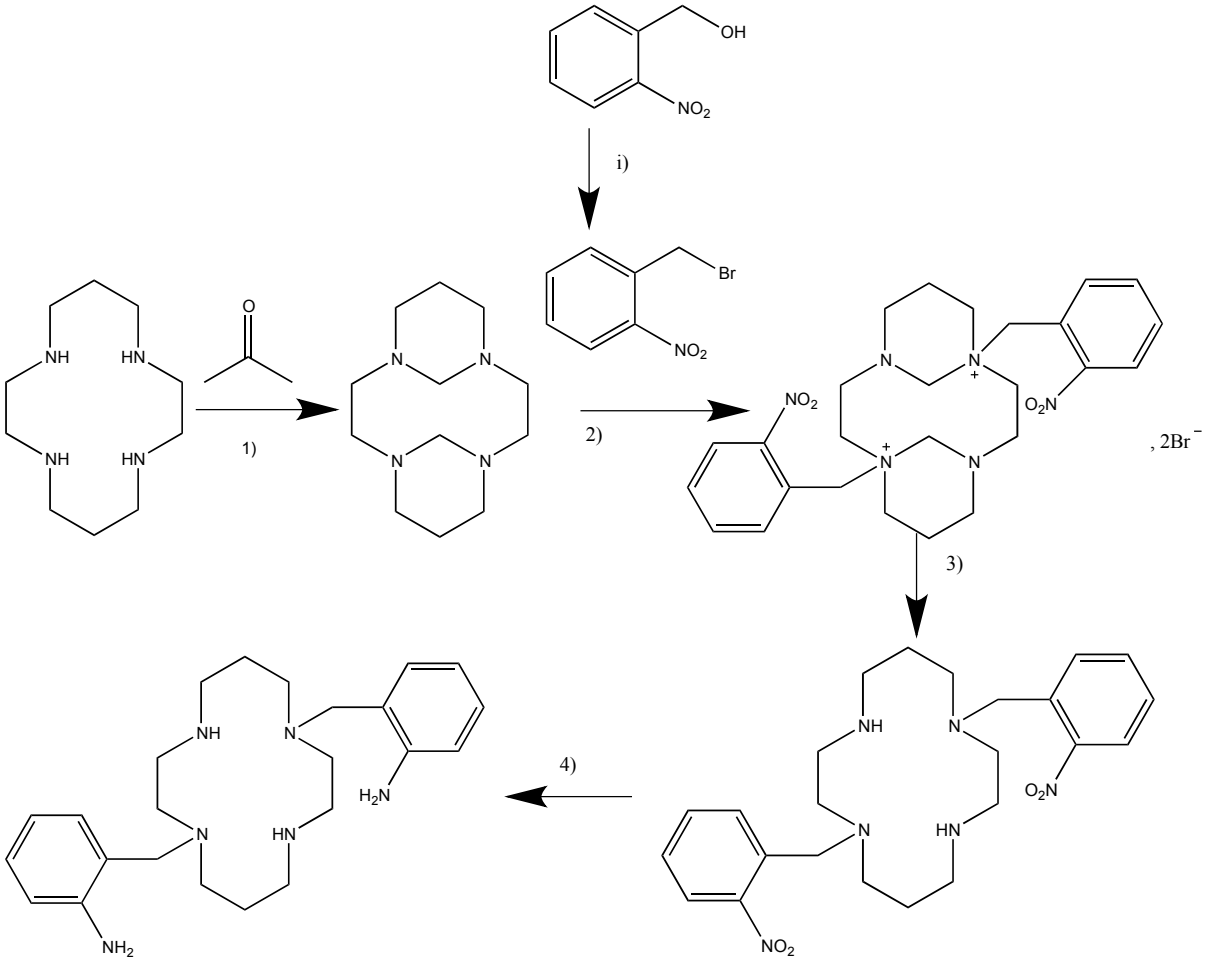

Schéma II.1. Schéma de la synthèse du ligand L'2

i) 1.1 eq PBr_3, Et_2O, 0°C, 2h ; 1) H_20, 0°C, 2h 2) CH_3CN, 7 jours, température ambiante; 3) NaOH 3M, 24h ; 4) NH_2NH_2-H_2O, EtOH, sous N_2, charbon actif, 48h.

2.2. Complexation

Nous avons effectué les complexations dans les mêmes conditions que l'obtention du complexe $[Fe(L2)](tcm)_2$ par évaporation lente. Les ions Fe(II) sont associés au ligand neutre dans un solvant et placés dans un tube fin. On ajoute au dessus une autre solution contenant le contre-ion. En dépit du nombre d'essais réalisés avec tous les contre-ions disponibles, nous n'avons pas obtenu de cristaux avec les ions fer(II). En parallèle, des essais de cristallisation avec le cation Cu(II) ont été effectués. Des monocristaux du complexe $[Cu(L'2)](BF_4)_2$ ont été obtenus et la description de sa structure fait l'objet du paragraphe suivant.

2.3. Description de la structure cristalline du composé $[Cu(L'2)](BF_4)_2$

La structure de ce complexe a été déterminée à température ambiante à 293 K. Ce composé cristallise dans le groupe d'espace $P_{2_1/c}$ du système monoclinique.

Tableau II.1 Paramètres structuraux et résultats des affinements pour $[Cu(L'2)](BF_4)_2$ à 293K

	$[Cu(L'2)](BF_4)_2$
Formule brute	$C_{24}H_{38}B_2CuF_8N_6$
Forme/couleur	Prisme violet
M/g.mol^{-1}	647,76
Système	monoclinique
Groupe d'espace	$P_{2_1/c}$
a/Å	9,3702(15)
b/Å	16,067(3)
c/Å	9,5374(14)
α/°	90
β/°	90,324(13)
γ/°	90
V/Å^3	1435,9(4)
R1	0,0994
R2	0,1695
GooF	0,916

La détermination de la structure a révélé que l'unité asymétrique de $[Cu(L'2)](BF_4)_2$ se compose d'un ion Cu(II), d'un ligand L'2 et de deux anions tétrafluoroborates BF_4^-. Le cation Cu^{2+} se trouve sur une position spéciale.

La structure du complexe cationique $[Cu(L'2)]^{2+}$ est représentée sur la figure II.3 et les longueurs et angles de liaison sont donnés dans les tableaux II.2 et II.3. Le polyèdre de coordination de l'ion métallique, de type (CuN_4N_2), présente une géométrie octaédrique déformée. Ce polyèdre peut être décrit en considérant un plan équatorial CuN_4, comprenant les quatre atomes d'azote du ligand L'2 (N1, N1$^{(a)}$, N2, N2$^{(a)}$), caractérisé par des longueurs de liaison Cu-N longues de 2,021(4) et 2,059(5) Å, et deux atomes d'azote

des bras méthylaniline (N3 et $N3^{(a)}$) en position apicale caractérisés par des longueurs de liaison Cu-N longues de 2,767(4) Å. Ces longueurs de liaison nous autorisent à considérer la sphère de coordination de l'ion cuivre (II) comme un pseudo-octaèdre allongé, proche de de la symétrie D_{4h} dans lequel les liaisons axiales Cu-N_3 sont plus longues que les liaisons équatoriales, Cu-N_1 et Cu-N_2 en raison de l'effet Jahn-Teller. Par rapport au complexe $[Fe(L2)]^{2+}$ décrit dans la publication dans le paragraphe précédent, le cation métallique se trouve cette fois-ci dans le plan défini par les 4 atomes d'azote N1, $N1^{(a)}$, N2, $N2^{(a)}$ du macrocycle. En effet, la modification du ligand a contribué à l'ajout d'une liaison supplémentaire. D'un métallocycle à cinq chaînons (Fe-N-C-C-N-Fe), on obtient un métallocycle (Cu-N-C-C-C-N-Cu) à six chaînons. Cette liaison supplémentaire permet la coordination des groupements $-NH_2$ en mode *trans* de part et d'autre du macrocycle. Ce mode de coordination diminuerait les contraintes stériques au sein de la cavité macrocyclique et permet ainsi à l'ion Cu^{2+} (Z=29) pourtant plus gros que l'ion Fe^{2+}(Z=26) de s'insérer parfaitement dans la cavité. On note en effet une légère augmentation des longueurs de liaisons N-C au sein du macrocycle du complexe $[Fe(L2)]^{2+}$ (<N-C> 1,477 Å) au complexe $[Cu(L'2)]^{2+}$ (<N-C> 1,491 Å).

La figure II.4 montre que le cation $[Cu(L'2)]^{2+}$ est isolé. Les seuls contacts significatifs sont de type intramoléculaire.

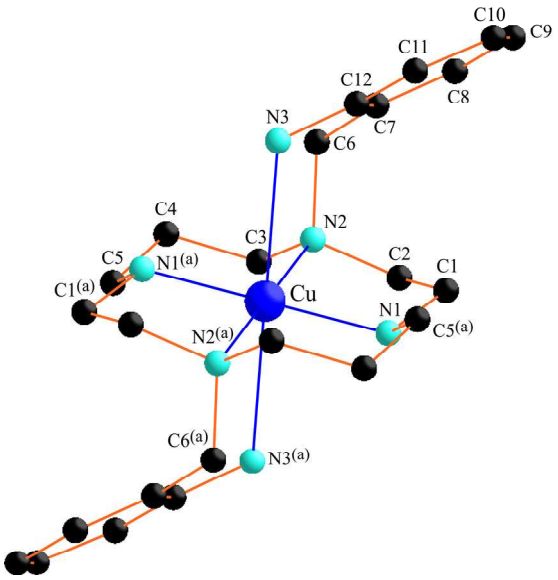

Figure II.3 Structure moléculaire du cation complexe $[Cu(L'2)]^{2+}$ (les atomes d'hydrogène ont été volontairement omis), position équivalente (a) (–x,-y,-z)

Tableau II.2 Longueurs (Å) de liaison autour du cation Cu(II) dans $[Cu(L'2)](BF_4)_2$

	$[Cu(L'2)](BF_4)_2$		$[Cu(L'2)](BF_4)_2$
Cu-N1	2,021(4)	$Cu-N1^{(a)}$	2,021(4)
Cu-N2	2,059(5)	$Cu-N2^{(a)}$	2,059(5)
Cu-N3	2,767(4)	$Cu-N3^{(a)}$	2,767(4)
<Cu-N>	2,282(4)	<Cu-N>	2,282(4)

Tableau II.3 Angles (°) de liaison autour du Cu(II) dans $[Cu(L'2)](BF_4)_2$

	$[Cu(L'2)](BF_4)_2$		$[Cu(L'2)](BF_4)_2$
$N1-Cu-N1^{(a)}$	180,0	$N3-Cu-N1^{(a)}$	93,5(2)
$N1-Cu-N2^{(a)}$	93,4(2)	$N3-Cu-N2^{(a)}$	95,2(8)
$N1^{(a)}-Cu-N2^{(a)}$	86,6(2)	N3-Cu-N2	84,7(2)
N1-Cu-N2	86,6(2)	N3-Cu-N1	86,4(8)
$N1^{(a)}-Cu-N2$	93,4(2)	$N3^{(a)}-Cu-N1$	93,4(2)
$N2^{(a)}-Cu-N2$	180,0	$N3^{(a)}-Cu-N2$	180,0
$N3^{(a)}-Cu-N2^{(a)}$	84,7(2)	$N3^{(a)}-Cu-N1^{(a)}$	86,4(8)

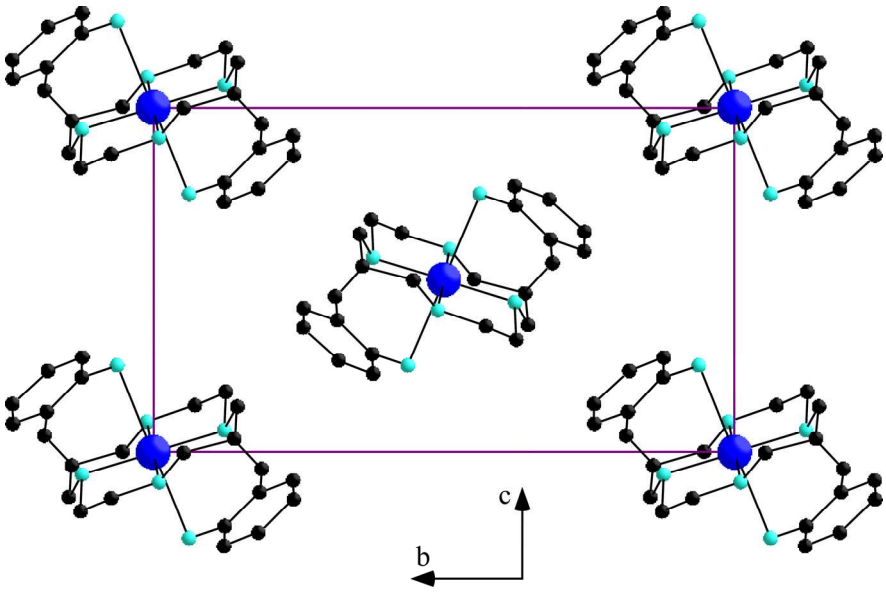

Figure II.4 Projection de la structure cristalline du composé $[Cu(L'2)](BF_4)_2$ dans le plan bc.

Comme nous l'avons vu, la substitution d'un groupement pyridine par un groupement aniline sur un macrocycle n'a pas abouti à la synthèse de complexe à partir des ions fer(II). Néanmoins, nous avons observé que cette substitution a permis d'obtenir un nouveau mode de coordination. Le cation métallique, Cu^{2+}, bien que plus gros, s'insère parfaitement dans la cavité macrocyclique permettant un mode de coordination en *trans* des deux anilines.

Nous avons ensuite transposé cette étude à un autre ligand, le tmpa (tris(2-pyridylmethyl) amine. Ce ligand n'est pas hexadentate et un co-ligand a été associé afin de compléter la sphère de coordination des ions fer(II). Ce co-ligand anionique vérifie également l'électroneutralité du système. Dans le but d'augmenter la coopérativité du système, nous avons choisi les co-ligands pontants, les anions tétracyanométallates et l'anion $(tcpd)^{2-}$, afin de générer des édifices polymériques. Nous avons obtenu des cristaux avec les tétracyanométallates mais leur instabilité nous a empêchés de les caractériser. Seuls les ions $(tcpd)^{2-}$ nous ont permis de caractériser un nouveau système dont la synthèse, les caractérisations et les propriétés sont présentées dans la publication ci-après.

3. Effet de la substitution d'une fonction chimique sur les caractéristiques de la transition de spin d'un complexe dinucléaire.

Ligand substitution effects on the Spin Cross-Over (SCO) Behaviour of Dinuclear Cyanocarbanions-Based Complexes

Eric Milin,[a] Sabrina Belaïd,[a,b] Véronique Patinec,[a] Smail Triki,*[a] Guillaume Chastanet,[c,d] Mathieu Marchivie[c,d]

Keywords: Spin crossover / Cyanocarbanion / Bridging ligand / Iron (II) / Dinuclear

ABSTRACT: New Fe(II) dinuclear complexes of formula $[Fe_2(L)_2(\mu_2\text{-tcpd})_2]\bullet 2CH_3OH$ (L = tmpa = tris(2-pyridylmethyl)amine (**1**); L = andmpa = bis-(2-pyridylmethyl)aminomethyl)aniline (**2**); $(tcpd)^{2-}$ = 2-dicyanomethylene-1,1,3,3-tetracyanopropanediide anion) have been synthesized and characterized by infrared spectroscopy, X-ray diffraction and magnetic measurements. The crystal structure determinations of **1-2** reveal in both cases a centrosymetrical dinuclear structure in which the $(tcpd)^{2-}$ cyanocarbanion acts as a double μ_2-bridging ligand between two $[FeL]^{2+}$ (L = tmpa (**1**), andmpa (**2**)) units *involving two free coordination sites in the cis configuration*. Examination of the shortest intermolecular contacts in **1** reveals no significant hydrogen bonding between the dinuclear units, while the dinuclear units in **2** held together by significant hydrogen bond between one of the uncoordinated nitril groups and the anilate group, giving rise 1D structure. Both complexes exhibit spin-crossover (SCO) behavior as evidenced by the evolution of the $\chi_m T$ product and the average values of the six Fe-N distances observed respectively at room temperature (293 K) and low temperature (100 K) – *i.e.* 2.160(4) and 1.992(3) Å that reveal a gradual conversion with transition temperatures $T_{1/2}$ around 356 K (**1'**) and 190 K (**2**).

---

[a] UMR CNRS 6521, Chimie, Electrochimie Moléculaires,
Chimie Analytique, Université de Bretagne Occidentale,
BP 809, 29285 Brest Cedex, France.
Fax: +33-2-9801-7001
E-mail : Smail.Triki@univ-brest.fr
[b] Laboratoire de Physico-chimie des Matériaux
et Catalyse, Université de Béjaia, Algeria.
[c] CNRS, ICMCB, UPR 9048, F-33600 Pessac, France
[d] Univ. Bordeaux, ICMCB, UPR 9048, F-33600 Pessac, France

Supporting information for this article is available on the WWW under http://dx.doi.org/xxxx/ejic.xxxxxx.

Introduction

Among the molecular switchable materials, the spin crossover (SCO) complexes are by far the most studied during the last decade, because of their several potential applications such as in memory display devices and sensing technology.[1-3] These complexes can be switched reversibly from a high spin (HS) to a low spin (LS) by external stimuli such as temperature, pressure, magnetic field or light irradiation. Although the spin transition can occur in d^4-d^7 transition metal complexes, the most studied examples to date are those based on Fe(II) (d^6 configuration), for which a paramagnetic-diamagnetic transition from the *HS* (S =2) to the *LS* (S = 0) state is observed.[3,4] The [FeN_6] SCO compounds can be roughly divided into two categories: the cationic complexes in which the six donating nitrogen atoms arise from one or several neutral ligands to generate the $[FeL_n]^{2+}$ complexes, and neutral or anionic complexes for which three or four nitrogen atoms arise from neutral ligands and the octahedral environment of the iron centers completed by two or three nitrogen atoms arising from monodentate or bridging anionic ligands.[3-5] This last category which can be formulated as $[FeL_nA_m]^{0/-}$ (L = polydentate neutral ligand, A^- or A^{2-} = terminal or bridging N-donating anion) presents a richer chemical diversity since the structure of the complex can be designed with a planned dimension or with a desired nuclearity, with only appropriate choice of the anionic ligand owing to its chemical structure including its coordination properties.

In this context, we have reported in the last few years the first *SCO* series based on cyanocarbanion ligands together with abpt chelating neutral ligand (Scheme 1).[6] In this series, the single charge on the anion induces a terminal coordination mode for the cyanocarbanion unit, resulting in neutral discrete *SCO* complexes.

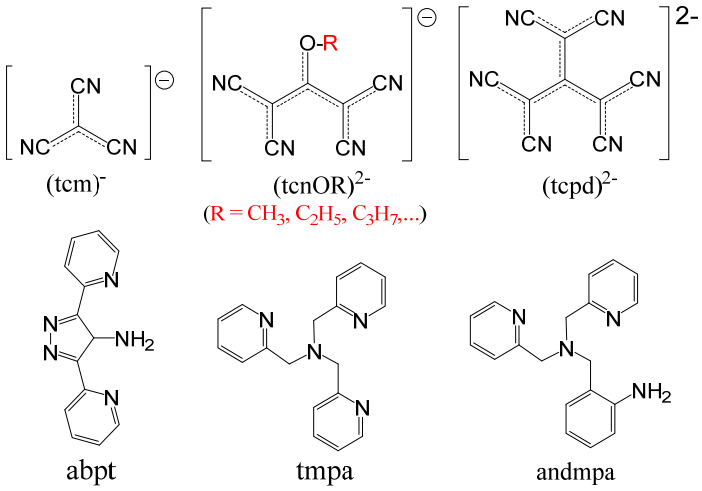

Scheme 1

Afterward, we have showed, in a second report,[7] that the use of the $(tcpd)^{2-}$ cyanocarbanion ($(tcpd)^{2-} = [C_{10}N_6]^{2-} = (C[C(CN)_2]_3)^{2-}$ = 2-dicyanomethylene-1,1,3,3-tetracyanopropanediide anion) ligand bearing two negative charges induces bridging coordination modes to lead to an original thermo- and photoswitchable SCO chain. With the aim to better explore the potential impact of such anionic ligands on the structural features of their complexes, and then on the switching properties (transition temperatures, hysteresis width, abruptness of the transition, photo-induced effects…), we have extended this work to the use of other polydentate neutral ligands such as the polypyridine ligands. For the tmpa ligand (tmpa = tris(2-pyridylmethyl)amine), few SCO molecular systems have been reported recently. The $[Fe(tmpa)]^{2+}$ entity possesses two free coordination sites in the cis configuration which allows the coordination of terminal ligands as observed in the polymorphic $[Fe(tmpa)(NCS)_2]$ system,[8] or the coordination of potentially bridging ligands to design polynuclear SCO derivatives, such as the tetranuclear complex $[Fe(tmpa)(N(CN))_2]_4$ or the diminoquinonoid-bridged dinuclear series $[Fe_2(tmpa)_2(\mu_2\text{-}^{X}L)]^{2+}$ $^{X}L^{2-}$ = double deprotonated form of 3,6-disubstituted-2,5-dianilino-1,4-benzoquinone; X = H, Br, Cl, F) in which the authors showed that the slight chemical modifications of the anionic bridging ligand ($^{X}L^{2-}$) affect strongly the transition temperature ($T_{1/2}$).[9,10]

We report herein the synthesis, the crystallographic and the magnetic studies of the two iron (II) dinuclear complexes $[Fe_2(L)_2(\mu_2\text{-}tcpd)_2]\bullet 2CH_3OH$ (L = tmpa (**1**); L = andmpa = bis-(2-pyridylmethyl)aminomethyl)aniline (**2**)) involving tetradentate chelating neutral ligands and the $(tcpd)^{2-}$ cyanocarbanion as bridging ligand.

Results and discussion.

Synthesis.

The andmpa ligand was synthesized according to a two-step method described by S. Lippard,[11] which was slightly modified. The starting reactant 2-nitrobenzyl bromide was obtained as previously published, by reacting the 2-nitrobenzyl alcohol and PBr_3 in Et_2O as the solvent in place of CCl_4.[12] Reaction of this bromo- derivative with dipicolylamine (dpa) in SN2 conditions gave rise to the formation of the 2-[bis(2-pyridylmethyl)aminomethyl]nitrobenzene intermediate in 67 % yield after purification. Reduction of the nitro- group into a primary amine function was carried out using hydrazine hydrate in ethanol with activated charcoal[13] instead of hydrogenation in Pd/C catalytic conditions[11] and yielded the andmpa ligand with a very good yield (92 %) (Scheme 2).

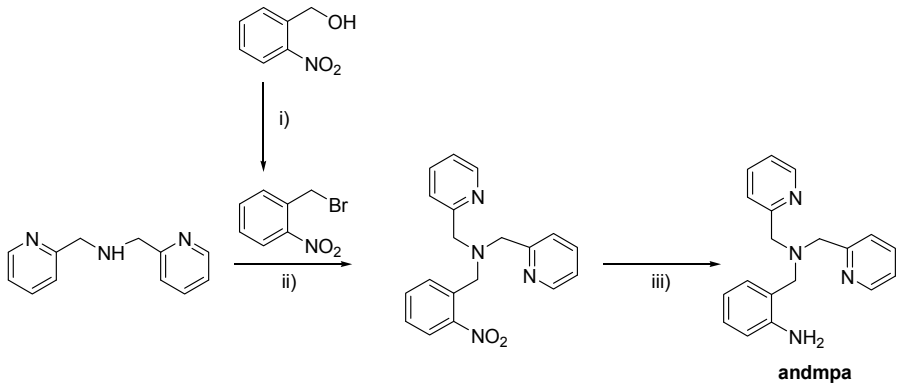

Scheme 2. Synthesis of the ligand andmpa i) 1.1 eq PBr_3, Et_2O, 0°C, 2h ; ii) K_2CO_3, CH_3CN, reflux, 5 days; iii) NH_2NH_2-H_2O, EtOH, activated charcoal, 48h.

Both Fe(II) complexes (**1** and **2**) have been synthesized, as single crystals, using diffusion technique in fine glass tube (3.0 mm diameter) by carefully layering 2 mL of methanolic solution of K_2tcpd onto a methanolic solution containing $Fe(BF_4)_2.6H_2O$ and the tetradentate neutral ligand in 1:1 ratio (tmpa for **1**; andmpa for **2**). In each case, single crystals suitable for X-ray analysis were formed after three days. Compounds **1** and **2** display similar infrared patterns. As expected, both show absorption bands assigned to the ν_{CN} stretching vibrations of the cyanocarbanion (2192 and 2165 cm^{-1} for **1**; 2187 and 2164 cm^{-1} for **2**). These absorption bands, distinct from the stretching vibration modes observed for the tetrabutylammonium salt ($[(C_4H_9)_4N]_2$(tcpd)) containing the uncoordinated cyanocarbanion (2094-2174 cm^{-1}),[7] can be assigned to the presence of both bridging (2192 cm^{-1} (**1**); 2187 cm^{-1} (**2**)) and terminal (2165 cm^{-1} (**1**); 2164 cm^{-1} (**2**)) nitrile groups, in agreement with the single crystal structure determination (see below).

Descriptions of the Crystal structures

Pertinent crystal data and selected bond distances and bond angles for compounds **1** and **2** are summarized in tables 1-4. Both compounds (**1** and **2**) crystallize in the monoclinic $P2_1/n$ space group for all the studied temperatures (see table 4). The asymmetric unit of **1** is built from one Fe(II) ion, one tmpa neutral ligand, one $(tcpd)^{2-}$ anion and a methanol solvent molecule with a partial occupation factor of 42% at room temperature, all located on general positions. The molecular structure consists of centrosymmetric neutral dinuclear entities of the formula $[Fe_2(tmpa)_2(\mu_2\text{-tcpd})_2]$ and 0.83 methanol molecules (Figure 1). Warming above room temperature, **1** loses its solvent molecule to reach a completely unsolvated state. This unsolvated crystal, which can be also obtained with time at room temperature as revealed by elemental analysis (see experimental section), is denoted **1'** and is isostructural of the solvated one with only slightly structural modifications.

In this dinuclear complex, each tmpa molecule acts as a tetradentate ligand leading to the $[Fe(tmpa)]^{2+}$ entities which are connected by two $(tcpd)^{2-}$ anions acting as a μ_2–bridging ligand through two nitrile groups of the same $C(CN)_2$ wing.

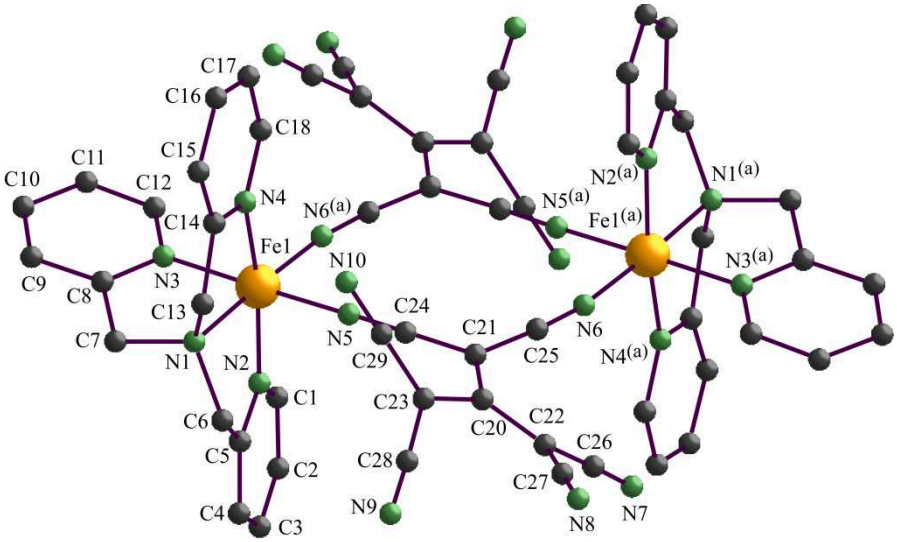

Figure 1. Molecular structure of the dinuclear iron (II) complex of **1,** (a) = 1-x,-y,-z+2

.

Each iron (II) metal ion presents a distorted FeN_6 octahedral environment assumed by four nitrogen atoms (N1, N2, N3, N4) arising from the tmpa neutral ligand and by two nitrogen atoms of two equivalent $(tcpd)^{2-}$ anions (N5 and $N6^{(a)}$). As indicated in table 4, compounds **1** and **2** display different crystallographic parameters, and consequently different crystal packing are expected (see below). However, despite this difference, the structure of **2** is built from similar asymmetrical unit described above for **1**, leading to a dinuclear molecular structure of the formula $[Fe_2(andmpa)_2(\mu_2\text{-}tcpd)_2]\bullet 2CH_3OH$, similar to that described for **1** (Figure 2).

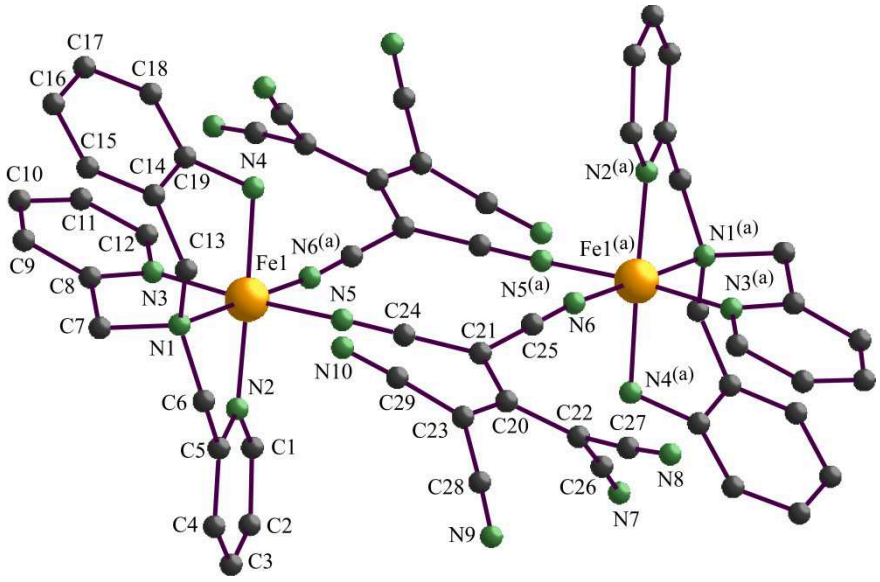

Figure 2. Molecular structure of the dinuclear iron (II) complex of **2,** (a) = -x,-y+1,-z+1

Examination of the shortest intermolecular contacts in **1** and **1'** reveals no significant hydrogen bonding between the dinuclear units, excepting the hydrogen bonding observed between the dinuclear units and the oxygen of the methanol molecule (N10…O1: 2.849(8) Å, figure 3a) in **1**. However, as depicted in figure 3a, the packing cohesion in **1** and **1'** is ensured by the π-π contact between the tcpd anions of the adjacent dinuclear units (shortest contact: N8…C20: 3.327(5)) Å. Despite the loss of the solvent molecule the packing cohesion in **1'** is very similar to that in **1** but with slightly more pronounced π-π contact between the tcpd anions (shortest contact: N8…C21: 3.278(4)) Å. In contrast, a different situation is observed in complex **2** since the dinuclear units held together by significant hydrogen bond between the anilate -NH_2 group (N4) of the andpma ligand and one of the uncoordinated nitrile groups (N4…N8: 3.183(6) Å), giving rise to 1D structure as highlighted in figure 3b.

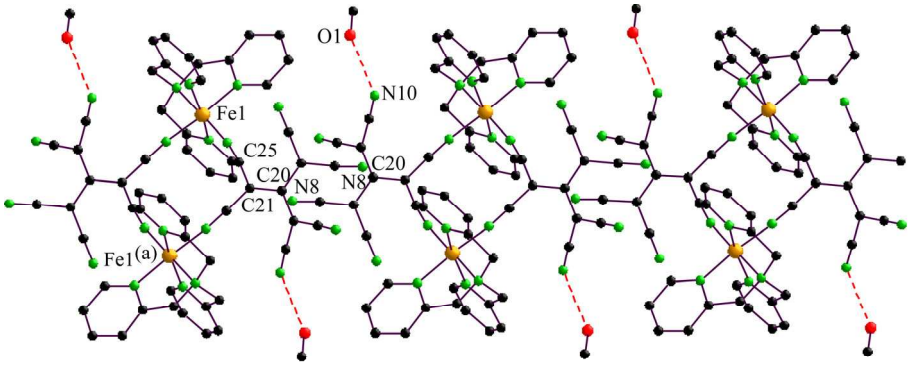

a)

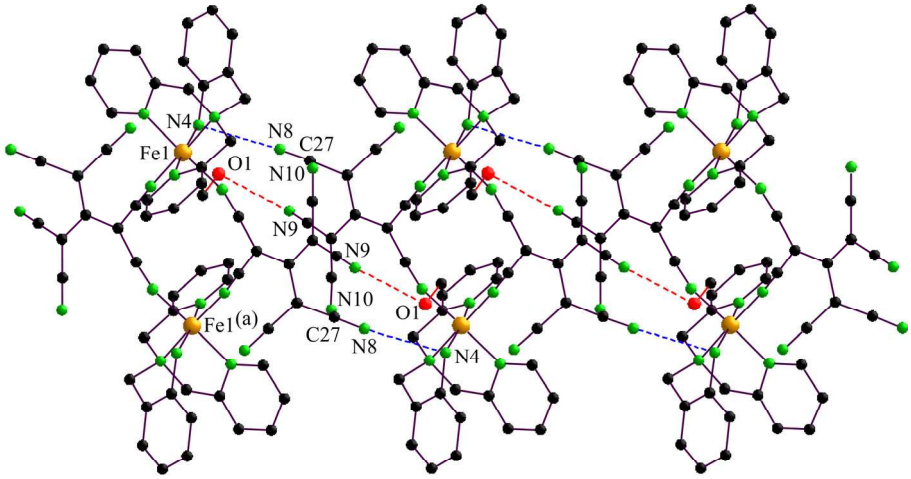

b)

Figure 3. Intermolecular contacts in compounds **1** (**a**) and **2** (**b**).

As in **1**, the adjacent $(tcpd)^{2-}$ anions are involved in the π-π stacking (N10…C27: 3.388(8)) to enhance the intermolecular cohesion; and hydrogen bonding (O1…N9: 2.843(7)) occurs between the methanol molecule (O1) and one of the non coordinated nitrile groups (N9) of the cyanocarbanion (see table 1 and 2). According to table 2, this hydrogen bond is slightly stronger in **2** that in **1**, that could explain that the MeOH molecule remains in the network of **2** at room temperature whereas it slowly goes out the crystal structure of **1**.

Table 1. Shortest intermolecular contacts (Å) in **1**, **1'** and **2** at 296 K

	1	**1'**	**2**
N8···C20[(a)]	3.327(5)	3.359(4)	
N8···C21[(a)]	3.328(4)	3.278(4)	
N8···C25[(a)]	3.362(4)	3.294(4)	
N10···C27[(b)]			3.388(8)
C25···C29[(b)]			3.590(7)
N4···N8[(b)]			3.183(6)

(a) = 2-x, 1-y, 2-z ; (b) = 1-x,1-y,1-z

Table 2. Hydrogen bonds with the MeOH molecule in **1** and **2** at 296 K in (Å).

D-H···A	**d(D-A)/Å**	**d(D-H···A)/Å**	**D-H-A/°**
1 : O1-H···N10[(a)]	2.849(8)	2.079(3)	156.4(8)
2 : O1-H···N9[(b)]	2.843(7)	2.045(5)	164.7(4)

(a) = 3/2-x, y-1/2, 3/2-z ; (b) = 1-x,1-y,1-z

Magnetic Properties

The thermal dependence of the product of the molar magnetic susceptibility times the temperature ($\chi_m T$) for the two complexes have been studied in the temperature range 10-400 K. As evidenced by the X-Ray studies, the solvent molecule is easily removed and the vacuum made in the SQUID magnetometer is likely to remove it. We have then measured the properties of **1'** and of **2** for which its methanol solvate molecules ($2CH_3OH$ molecules per dinuclear units) are maintained in the crystal packing even at 400 K. The $\chi_m T$ product of complex **1'** shows a room temperature value of 0.59 $cm^3 \cdot K \cdot mol^{-1}$, in agreement with the low spin (LS) state of the Fe(II) centres as expected from the structural data. Upon warming, the $\chi_m T$ product gradually increases up to 5.68 $cm^3 \cdot K \cdot mol^{-1}$ at 380 K (figure 5). This high temperature value is coherent with 80 % of HS iron (II) ions (if we assume a $\chi_m T$ value of 3.5 cm^3 K mol^{-1} per iron(II) as usually reported) as suggested by the X-Ray studies. This conversion is reversible and is characterized by a $T_{1/2}$ value of 356 K. Compound **2** shows a room temperature $\chi_m T$ value of 6.29 $cm^3 \cdot K \cdot mol^{-1}$, in agreement with the presence of two isolated high spin Fe(II) metal ions with a g value of 2.05. The $\chi_m T$ product for **2** decreases

upon cooling, first smoothly down to ca. 5.5 cm^3•K•mol^{-1} at ca. 225 K where the $\chi_m T$ drops more rapidly to reach a value close to zero at ca. 100 K (Figure 5). This *HS*↔*LS* SCO conversion is characterized by a $T_{1/2}$ value of 190 K.

The photomagnetic properties were investigated on these two compounds by irradiating the sample at 10 K. Irradiation was tested at different wavelengths. Whereas compound **1'** does not reveal any light-induced changes at 10 K, compound **2** present a small increase of the $\chi_m T$ from 0.18 to 0.88 cm^3•K•mol^{-1} under a 650 nm irradiation at a 5mW/cm^2 power. The photo-conversion efficiency is very low since only 10 % of LS ions are converted to the HS state (Figure 5). The T(LIESST)[17] curve was recorded and the $\chi_M T$ product rapidly decreases and the baseline is recovered around 40 K. The fast decrease indicates a highly efficient HS → LS relaxation process which prevents the observation of a better photo-conversion ratio.

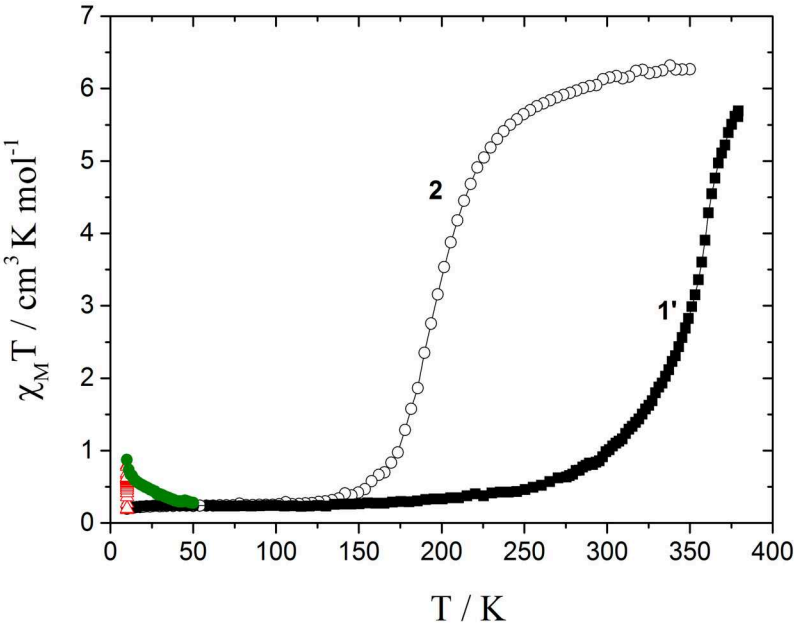

Figure 5. Thermal variation of the $\chi_m T$ product of **1'** and **2** showing the gradual thermal spin conversion and the photomagnetic properties of **2**.

To know more about the two spin states of both compounds and to better understand the incomplete nature of the SCO transition of **1'**, deduced from the magnetic data, we have solved the crystal structures for both compounds at different temperatures.The iron sites present an octahedral FeN_6 geometry for all compounds. As shown in table 3**,** at 296 K, the mean Fe-N distances observed for the solvated (**1**) and for the unsolvated phase (**1'**) (1.965(3) and 1.966(3) Å, respectively) are in the range of those expected for Fe(II) ion in the low spin state, in good agreement with the magnetic data.

Table 3. Selected bond lengths (Å), bond angles (°) and distortion parameters of the coordination sphere in **1**-**2**.

	1	**1'**		**2**	
T / K	**296**	**296**	**380**	**100**	**296**
Fe1-N1	1.985(2)	1.991(2)	2.191(4)	2.025(3)	2.232(4)
Fe1-N2	1.973(2)	1.973(2)	2.131(6)	1.973(3)	2.145(4)
Fe1-N3	1.966(2)	1.971(2)	2.149(5)	1.972(3)	2.136(4)
Fe1-N4	1.975(2)	1.973(2)	2.121(5)	2.068(3)	2.200(4)
Fe1-N5	1.949(3)	1.951(3)	2.118(6)	1.956(3)	2.149(4)
Fe1-N6[(a)]	1.939(3)	1.939(2)	2.055(5)	1.955(3)	2.100(4)
<Fe-N>	**1.965(3)**	**1.966(3)**	**2.128(5)**	**1.992(3)**	**2.160(4)**
N1-Fe1-N2	82.21(10)	82.16(10)	77.0(2)	81.30(12)	76.14(16)
N1-Fe1-N3	85.22(11)	85.13(10)	80.1(2)	84.68(13)	79.57(16)
N1-Fe1-N4	84.36(10)	83.85(10)	78.3(2)	90.95(13)	86.53(15)
N1-Fe1-N5	92.88(10)	93.58(10)	96.0(2)	95.87(12)	97.94(16)
N1-Fe1-N6[(a)]	177.91(10)	178.42(10)	175.8(2)	177.66(13)	173.21(17)
N2-Fe1-N3	93.11(10)	94.22(10)	97.31(18)	95.67(12)	95.62(15)
N2-Fe1-N4	166.42(11)	165.84(11)	155.0(2)	171.69(14)	161.50(15)
N2-Fe1-N5	89.14(10)	88.53(10)	87.4(2)	88.07(12)	86.95(16)
N2-Fe1-N6[(a)]	95.94(10)	96.44(10)	100.6(2)	97.07(12)	99.45(17)
N3-Fe1-N4	87.78(10)	86.76(10)	82.16(17)	86.56(13)	87.41(15)
N3-Fe1-N5	176.82(10)	176.77(10)	172.99(19)	176.26(12)	175.85(16)
N3-Fe1-N6[(a)]	95.87(10)	95.73(10)	97.0(2)	93.83(12)	95.89(16)
N4-Fe1-N5	89.50(10)	90.16(10)	91.37(19)	89.73(13)	89.13(15)
N4-Fe1-N6[(a)]	97.45(10)	97.52(10)	104.3(2)	90.76(13)	98.37(15)
N5-Fe1-N6[(a)]	86.12(9)	85.63(10)	87.24(19)	85.74(12)	86.88(15)
Distorsion					
[b]Σ(Fe1) (°)	51(2)	56(2)	94(3)	48(2)	75(2)
[c]Θ(Fe1) (°)	133(3)	143(3)	248(5)	141(4)	214(4)

(a) = 1-x,-y,-z+2 (**1**) or -x,-y+1,-z+1 (**2**)

[b] Σ is the sum of the deviation from 90° of the 12 *cis*-angles of the FeN_6 octahedron; [14,15] [c] Θ is the sum of the deviation from 60° of the 24 trigonal angles of the projection of the FeN_6 octahedron onto its trigonal faces.[15,16]

The octahedral geometry appears slightly more distorted for compound **1'** than for **1** since the trigonal distortion parameter calculated for **1'** (Θ = 143(3)°) is significantly higher than the corresponding value calculated for **1** (Θ = 133(3)°). At 380 K, **1** irreversibly loses its methanol molecule becoming **1'**. The coordination sphere volume of the metal increases as the mean Fe-N distance rises to 2.128(5) Å and conjointly the octahedral geometry becomes more distorted (see table 3). Both features are a signature of a LS to HS transition. Nevertheless, the mean Fe-N distance appears smaller than those observed for the HS Fe(II) in compound **2**. This can be due to an incomplete spin transition at 380 K, corresponding to about 20 % of remaining LS Fe(II) in the crystal structure. Even if this observation agree perfectly the the magnetic observations, the crystal data at 380K did not reveal clearly if at this temperature, the plateau corresponding to the HS sate is reached. Thus, in order to investigate further this incomplete spin transition, the crystal structure of compound 1' has been solved every 5 K between 296 K and 380 K. These additional structural investigations did not reveal any lost of symmetry on the whole temperature range suggesting that both iron centers of the dinuclear complex are similarly affected by the spin transition.According to figure 4, that shows the evolution of the cell volume and the mean Fe-N bond length between 296 K and 380 K, the incomplete spin transition reaches a plateau at 370 K, that indicates that about 20% of the complexes are trapped in the LS state and that the transition should not reach 100 % of conversion even at higher temperatures.

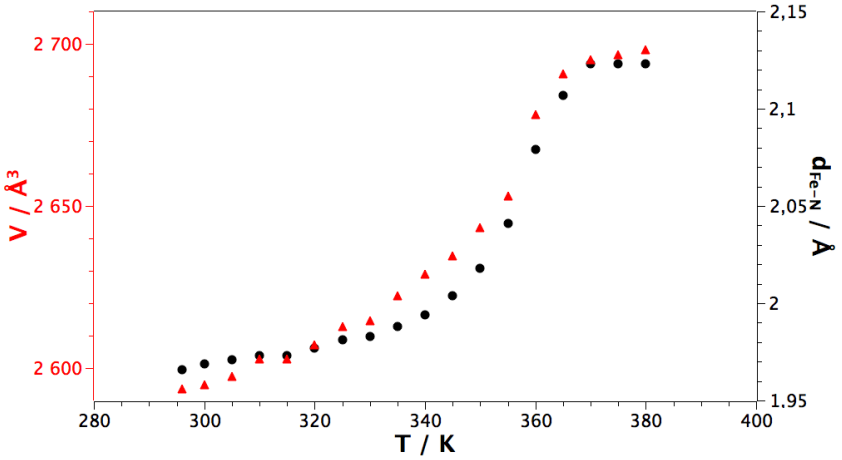

Figure 4. Evolution of the unit cell volume (left axis) and the mean Fe-N distance (right axis) for compound **1'** from room temperature to 380 K.

For compound **2**, the mean Fe-N distance observed at room temperature (d_{Fe-N} = 2.160(4) Å) is characteristic of the presence of the iron (II) ion in the HS state. At 100 K, the octahedral geometry of **2** becomes more regular and the mean Fe-N distance decreases drastically to

reach 1.992(3) Å. In agreement with the magnetic data, this feature is the signature of the change of the spin state from HS to LS at low temperature.

Conclusions

A series of two dinuclear complexes of formula $[Fe_2(L)_2(\mu_2\text{-tcpd})_2]\bullet 2CH_3OH$ are obtained from reaction of two tetradentate neutral ligands (L = tmpa (**1**) and L = andmpa (**2**)) and a potentially bridging $(tcpd)^{2-}$ anionic ligand. Both complexes display similar molecular structures described as neutral dinuclear neutral units involving similar double μ_2-tcpd bridges. However, as shown by the crystallographic data and confirmed by the intermolecular contacts, the two complexes display different crystal packing. One of the principle objectives of this study concerns the investigation of the subtle chemical substitution of the tetradentate ligand on the SCO behavior. Complex **1** based on the tmpa ligand shows *LS* state even at room temperature but undergoes an incomplete and gradual spin crossover around ca. 355 K. The spin crossover is accompanied by a loss of the solvent molecule without drastic structural changes as the resulting compound **1'** is isostructural of **1**. Complex **2** involving a slightly different tetradentate ligand (andmpa) shows a SCO behavior with a transition temperature of *ca.* 190 K. It is worthy to note that this modulation of the ligand field cannot be attributed exclusively to the ligand substitution performed on the tmpa initial ligand but also to the solid-state packing which affects significantly the elastic interactions and the SCO behavior as exemplified by several polymorphic systems.[8,18]

Experimental section

General Remarks. Tetracyanoethylene, urea, potassium tert-butoxide (C_4H_9OK), malononitrile ($CH_2(CN)_2$), 2-nitrobenzyl alcohol, di-picolyl amine, PBr_3, K_2CO_3 and $Fe(BF_4)_2.6H_2O$ were purchased from commercial sources and used without further purification. Solvents were used and purified by standard procedures. The potassium salt K_2(tcpd) and tmpa ligand (tris(2-pyridylmethyl)amine) were prepared according to published procedures.[19,20] Elemental analyses were performed by the "Service Central d'Analyses du CNRS", Gif-sur-Yvette, France. Infrared spectra were recorded in the range 4000-50 cm^{-1} on a FT-IR Brucker ATR Vertex 70 Spectrometer. Diffraction analyses were performed using an Oxford Diffraction Xcalibur κ-CCD diffractometer. NMR spectra were recorded on a Brucker DRX 300 MHz or Brucker Avance 400 and 500 MHz. Magnetic measurements were performed with a Quantum Design MPMS-XL-5 SQUID magnetometer in the 10-400 K

temperature range with an applied magnetic field of 2 T on crushed single crystals of compounds **1** and **2**. The susceptibility data were corrected for the sample holders previously measured under the same conditions, and for the diamagnetic contributions as deduced by using Pascal´s constant tables (χ_{dia} = -547.4x10^{-6} and -571.6x10^{-6} emu.mol^{-1} for **1** and **2**, respectively).[21] Photomagnetic measurements were performed using a set up of photo-diodes (405 nm, 532 nm, 650 nm or 830 nm), coupled by means of an optical fibre to the cavity of a MPMS-5S Quantum Design SQUID magnetometer. The optical power at the sample surface was adjusted to prevent important warming of the sample. The compound consists of a thin layer. After being slowly cooled at 10K, the sample is irradiated and the change in magnetic susceptibility was followed. When the saturation point was reached the laser was switched off and the temperature increased at a rate of ~ 0.4 K•min^{-1}. The magnetization was measured every 1K. T(LIESST)[17] was determined from the minimum of a dχ_MT/dT vs. T plot for the relaxation process.

Crystallographic Data Collection and Refinement

Crystallographic studies of the two derivatives (**1-2**) were performed at 296 K, 100 K and 380K, using an Oxford Diffraction Xcalibur κ-CCD diffractometer equipped with a graphite monochromated Mo$K\alpha$ radiation (λ= 0.71073 Å) or a Brucker APEX-II CCD diffractometer (λ= 0.71073 Å). The full sphere data collections were performed using 1.0° ω-scans with an exposure time of 200 s and 35s per frame for **1** and **1'**, 60 s and 80 s per frame for **2** at 296 K and 100 K, respectively. Data collection and data reduction were done with the CRYSALIS-CCD and CRYSALIS-RED programs or on the Brucker APEX-II program suite on the full set of data.[22] The crystal structures were solved by direct methods and successive Fourier difference syntheses, and were refined on F^2 by weighted anisotropic full-matrix least-square methods.[23] All non-hydrogen atoms were refined anisotropically, while the hydrogen atoms were calculated and therefore included as isotropic fixed contributors to F_c. All other calculations were performed with standard procedures (WINGX, OLEX2).[24,25] Crystal data, structure refinement and collection parameters are listed in table 4.

Table 4. Crystal data and structural refinement parameters for compounds **1, 1'** and **2**

	1	**1'**		**2**	
Temperature / K	296(2)	296(2)	380(2)	100(2)	296(2)
Empirical formula	$(C_{56}H_{36}Fe_2N_{20})$, $0.83(CH_3OH)$	$C_{56}H_{36}Fe_2N_{20}$		$(C_{58}H_{40}Fe_2N_{20})$, $2(CH_3OH)$	
Formula weight /g.mol^{-1}	1127.49	1100.75		1192.88	
Wavelength / Å	0.71073 Å	0.71073 Å		0.71073 Å	
Crystal system	Monoclinic	Monoclinic		Monoclinic	
Space group	$P2_1/n$	$P2_1/n$		$P2_1/n$	
a / Å	11.7269(5)	11.468(4)	10.894(4)	9.6690(10)	9.6831(12)
b / Å	16.6966(6)	17.0057(9)	18.7523(9)	24.658(2)	25.065(3)
c / Å	13.9317(6)	13.7743(6)	13.7750(6)	11.5670(10)	12.0485(16)
β /°	104.672(4)	105.098(9)	106.492(9)	102.631(6)	103.711(14)
Volume / Å^3	2638.87(19)	2593.6(10)	2698.3(11)	2691.0(4)	2840.9(7)
Z	2	2	2	2	2
D_{calc} / g.cm^{-3}	1.419	1.409	1.355	1.472	1.395
Abs. coef. / cm^{-1}	6.12	6.20	5.96	6.06	5.74
F(000)	1158	1128.0	1128.0	1232	1232
Crystal size / mm^3	0.22 x 0.15 x 0.11	0.2 × 0.15 × 0.1		0.28 x 0.07 x 0.06	
2θ range / °	6.664 - 50.496	7.196 - 50.504	7.104 - 50.502	7.03 - 50.504	6.894 - 50.502
Refl. collected	22679	17601	17702	18396	18091
Unique refl. / Rint	4765 / 0.0705	4688 / 0.0698	4844 / 0.1462	4864 / 0.1069	5120 / 0.1581
Data / restr. / N_v	4765/1/373	4688/0/352	4844/0/352	4864/0/389	5120/0/381
[b]R1/[c] wR2	0.0506 / 0.1366	0.0498 / 0.0798	0.0768 / 0.1485	0.0582 / 0.1400	0.0710/ 0.1270
[d]GooF	1.047	1.021	0.998	1.027	0.959
$\Delta\rho_{max/\ min}$ / eÅ^{-3}	+0.40 / -0.33	0.29/-0.25	0.28/-0.19	+1.00 / - 0.63	+0.34 / - 0.29
CCDC No.	1413422	1435809	1435810	1413424	1413423

[a]The asymmetric unit contains 0.5 of the chemical formula. [b]$R1 = \sum|F_o-F_c|/F_o$.

[c]$wR2 = \{\Sigma[w(F_o^2-F_c^2)^2]/\ \Sigma[w(F_o^2)^2]\}^{1/2}$. [d]$GooF = \{\Sigma[w(F_o^2-F_c^2)^2]/\ (N_{obs}-N_{var})\}^{1/2}$

Ligand Syntheses

Synthesis of Bis-(2-pyridylmethyl)aminomethyl)aniline (**andmpa**). 2-nitrobenzylbromide (1.08g, 5.0 mmol) was added to a solution of dipicolyl amine (dpa) (1.00 g, 5.0 mmol) in distilled CH_3CN (20mL) with K_2CO_3 (1.38g, 10.0 mmol). The reaction mixture was heated to reflux with stirring for 5 days. After cooling and filtration of the solution, the solvent was removed by evaporation. Purification of the crude product by column chromatography on neutral alumine (CH_2Cl_2/MeOH from 100/0 to 99/1) produced a brown oil of bis-(2-pyridylmethyl)aminomethyl)nitrobenzene (1.12 g, 67%). IR data (ν/cm^{-1}): 3060 (w) 3008 (w) 1648 (m) 1523 (s) 1432 (m) 1358(m) 764 (m) 731 (m); ^{1}H RMN δ (300MHz, $CDCl_3$) 3.78 (4H, s, CH_2) 4.07 (2H, s, CH_2) 7.12 (2H, dd) 7.33 (1H, t) 7.40 (2H, d) 7.48 (1H, t) 7.63 (2H, t) 7.70 (1H, d) 7.75 (1H, d) 8.49 (d, 2H) ^{13}C RMN δ (75MHz, $CDCl_3$): 55.7 60.3(2C) (*C*H_2); 121.2(2C) 123.1(2C) 124.2 127.8 131.2 132.2(C_{quat}) 134.2(2C) 148.8(2C) 149.8($_{Cquat}$) 158.5(C_{quat}) (*C*$_{aromatic}$). Oxygen-free hydrazine hydrate (15 mL, excess) was added to a solution of bis-(2-pyridylmethyl)aminomethyl)nitrobenzene (1.00 g, 3.0 mmol) in absolute ethanol (50 mL) with activated carbon (1.0 g). The reaction mixture was heated to reflux with stirring under nitrogen atmosphere for 48 hours. After cooling, the solution was filtered through celite and the filtrate was evaporated under reduced pressure. The residue was dissolved in $CHCl_3$ (30mL) and dried with $MgSO_4$. After filtration, the solvent was removed to yield a brown solid of bis-(2-pyridylmethyl)aminomethyl)aniline (andmpa) (840 mg, 92%). IR data (ν/cm^{-1}): 3400 (m) 3312 (m) 3200 (m) 1632 (m) 1589 (s) 1492 (m) 1432 (m) 752 (vs); ^{1}H RMN δ (300MHz, $CDCl_3$) 3.65 (2H, s, CH_2) 3.78 (2H, s, CH_2) 6.58-6.65 (2H, m) 7.01-7.05 (2H, m) 7.11-7.15 (m, 2H) 7.37 (d, 2H) 7.60 (t, 2H) 8.53 (d, 2H); ^{13}C RMN δ (75MHz, $CDCl_3$) 57.8 60.0(2C) (CH_2) 115.4 117.0 121.8(2C) 122.2(C_{quat}) 123.3(2C) 128.3 131.2 136.2(2C) 146.9(C_{quat}) 149.0(2C) 159.1(C_{quat}) (*C*$_{aromatic}$).

Complex Syntheses

$[Fe_2(tmpa)_2(\mu_2\text{-}tcpd)_2]\bullet xCH_3OH$ (1): $Fe(BF_4)_2.6H_2O$ (6.7 mg, 0.02 mmol) was added to a solution of tmpa (0.02mmol, 5.8 mg) in methanol (2mL). The resulting yellow solution was placed in a glass capillary (diameter 0.3mm). Then a solution of K_2tcpd (5.6 mg, 0.02 mmol) in methanol (2mL) was carefully added in the capillary. Red crystals suitable for X-ray diffraction were obtained after 3 days. Anal. Calcd. (%) for [$C_{56}H_{36}Fe_2N_{20}$], 0.3(CH_3OH): 60.9; H, 3.4; N, 25.2. Found (%): C, 61.3; H, 3.4; N, 25.4. IR data (ν/cm^{-1}): 3417(w), 3078(w), 2192(s), 2165(s), 1606(s), 1433(s), 1399(s), 1287(w), 1243(w), 1157(m), 1034(m),

991(m), 957 (m), 902(w), 771(m), 759(s), 735(m), 645(m), 626(w), 503(m), 466(m), 442(m). **$[Fe_2(andmpa)_2(\mu_2\text{-}tcpd)_2]\bullet 2CH_3OH$ (2):** $Fe(BF_4)_2.6H_2O$ (6.7 mg, 0.02 mmol) was added to a solution of andmpa (0.02mmol, 6.1 mg) in methanol (2mL). The resulting yellow solution became green after standing overnight, and then placed in a glass capillary (diameter 0,3mm). A solution of K_2tcpd (5.6 mg, 0.02 mmol) in methanol (2mL) was carefully added in the capillary. Green crystals suitable for X-ray diffraction were obtained after 3 days. Anal. Calcd. (%) for $C_{60}H_{48}Fe_2N_{20}O_2$: C, 60.4; H, 4.1; N, 23.5. Found (%): C, 59.9; H, 4.2; N, 23.2. IR data (ν/cm^{-1}): 3259(w), 3220(w), 3124(w), 2859(w), 2187(s), 2164(s), 1605(m), 1570(w), 1440(s), 1386(s), 1295(w), 1263(w), 1240(w), 1150(w), 1074(s), 1051(m), 1036(s), 1020(s), 1002(m), 974(w), 943(w), 867(m), 759(s), 738(s), 687(w), 642(w), 617 (w), 570(w), 539(m), 522(w), 508 (s), 484(w), 459 (w).

Supporting Information (see footnote on the first page of this article): Crystallographic data have been deposited in the Cambridge Crystallographic Data Centre under the CCDC numbers 1413422 – 1413424 and 1435809 - 1435810 that contains the supplementary crystallographic data for this paper. These data can be obtained free of charge via the web application at www.ccdc.cam.ac.uk/conts/retrieving.html [or from the Cambridge Crystallographic Data Center, 12 Union Road, Cambridge CB2 1EZ, UK: Fax: (internt.) + 44-1223-336-033; E-mail: deposit@ccdc.cam.ac.uk].

Acknowledgments.

We acknowledge the CNRS (Centre National de la Recherche Scientifique), the Brest University, the "Agence Nationale de la Recherche" (ANR project BISTA-MAT: ANR-12-BS07-0030-01), the French ″Ministère de la Recherche and Ministère des Affaires Etrangères et Européennes (PHC MAGHREB Project N° 30255ZJ)″, the Aquitaine Region for the support of the International Center of Photomagnetisme in Aquitaine. Authors especially thank the “Service Commun” of NMR facilities of the University of Brest

References

[1] O. Kahn, C. J. Martinez, *Science* **1998**, *279*, 44–48; A. Bousseksou, G. Molnár, P. Demont, J. Menegotto, ***J. Mater. Chem.*** **2003**, ***13***, 2069-2071; J. Dugay, M. Giménez-Marqués, T. Kozlova, H. W. Zandbergen, E. Coronado, H. S. J. van der Zant, *Adv. Mat.* **2015**, 27, 1288-1293.

[2] C. Bartual-Murgui, A.Akou, C. Thibault, G. Molnár, C. Vieu, L. Salmon, A. Bousseksou, ***J. Mater. Chem. C***, **2015**, ***3***, 1277-1285; J. Linares, E. Codjovi, Y. Garcia, Sensors **2012**, *12*, 4479–4492; C. M. Jureschi, I. Rusu, E. Codjovi, J. Linares, Y. Garcia, A. Rotaru, *Physica B* **2014**, *449*, 47–51.

[3] a) M. A. Halcrow, Spin-Crossover Materials: Properties and Applications, John Wiley & Sons (Eds.), **2013**; b) P. Gütlich, H. A. Goodwin (Eds.), *Top. Curr. Chem.* **2004**, *233-235.*

[4] see for example: a) P. Gütlich, A.-B. Gaspar, Y. Garcia, *Beilstein J. Org. Chem.* **2013**, *9*, 342–391; b) F. J. Muñoz-Lara, Z. Arcís-Castillo, M.-C. Muñoz, J.-A. Rodríguez-Velamazán, A.-B. Gaspar, J.-A. Real, *Inorg. Chem.* **2012**, *51*, 11126-11132; c) J. Olguin, S. Brooker, *Coord. Chem. Rev.* **2011**, *255*, 203-240; e) M. A. Halcrow, *Chem. Soc. Rev.* **2011**, *40*, 4119-4142; d) M. A. Halcrow, *Coord. Chem. Rev.* **2009**, *253*, 2493-2514; e) J.-A. Real, A.-B. Gaspar, V. Niel, M.-C. Muñoz, *Coord. Chem. Rev.* **2003**, *236*, 121-141.

[5] a) M. Yamasaki, T. Ishida, *Polyhedron* **2015**, *85*, 795-799; b) N. Hirosawa, Y. Oso, T. Ishida, *Chem. Lett.* **2012**, *41*, 716-718.

[6] G. Dupouy, M. Marchivie, S. Triki, J. Sala-Pala, J.-Y. Salaün, C. J. Gómez-García, P. Guionneau, *Inorg. Chem.* **2008**, *47*, 8921-8931.

[7] a) G. Dupouy, S. Triki, M. Marchivie, N. Cosquer, C. J. Gómez-García, S. Pillet, E.-E. Bendeif, C. Lecomte, S. Asthana, J.-F. Létard, *Inorg. Chem*. **2010**, *49*, 9358-9368; b) G. Dupouy, M. Marchivie, S. Triki, J. Sala-Pala, C. J. Gomez-Garcia, S. Pillet, C. Lecomte, J.-F. Létard, *Chem. Commun.* **2009**, 3404-3406.

[8] a) R.-J. Wei, B. Li, J. Tao, R.-B. Huang, L.-S. Zheng, Z. Zheng, *Inorg. Chem. **2011**, 509,* 1170-1172; F. Højland, H. Toftlund, S. Yde-Anderson, *Acta Chem. Scand.* **1983**, *A37*, 251-257; c) H. Paulsen, H. Grünsteudel, W. Meyer-Klaucke, M. Gerdan, H. F. Grünsteudel, A. I. Chumakov, R. Rüffer, H. Winkler, H. Toftlund, A. X. Trautwein, *Eur. Phys. J.* **2001**, *B23*, 463-; d) B. Li, R.-J. Wei, J. Tao, R.-B. Huang, L.-S. Zheng, Z. Zheng, *J. Am. Chem. Soc.* **2010**, *132*, 1558-1566.

[9] R.-J. Wei, Q. Huo, J. Tao, R.-B. Huang, L.-S. Zheng, Angew. Chem. Int. Ed. **2011**, 50, 8940-8943.

[10] J. G. Park, I.-R. Jeon, T. D. Harris*, Inorg. Chem. **2015**, 54, 359-369.*

[11] S. C. Burdette, C. J. Frederickson, W. Bu, S. J. Lippard, *J. Am. Chem. Soc.* **2003**, *125*, 1778-1787.

[12] O. Schlager, K. Wieghardt, H. Grondey, A. Rufinska, B. Nuber, *Inorg. Chem.* **1995**, *34*, 6440-6448.

[13] M. Roger, V. Patinec, R. Tripier, S. Triki, N. Le Poul, Y. Le Mest, *Inorg. Chim. Acta*, **2014**, *417*, 201-207.

[14] F. A. Deeney, C. J. Harding, G. G. Morgan, V. McKee, J. Nelson, S. J. Teat, W. Clegg, *Dalton Trans.* **1998**, 1837-1844

[15] P. Guionneau, M. Marchivie, G. Bravic, J.-F. Létard, D. Chasseau, *Top. Curr. Chem.,* **2004,** *234*, 97-128.

[16] M. Marchivie, P. Guionneau, J.-F. Létard, D. Chasseau, *Acta Cryst. B,* **2005,** *B61*, 25-28.

[17] J.-F. Létard, L. Capes, G. Chastanet, N. Moliner, S. Létard, J.A. Real, O. Kahn, *Chem. Phys. Lett.* **1999**, *313*, 115.

[18] J. Tao, R.-J. Wei, R.-B. Huang, L.-S. Zheng, Chem. Soc. Rev. **2012**, *41*, 703–737.

[19] Middleton, W. J.; Little, E. L.; Coffman, D. D.; Engelhardt, V. A., *J. Am. Chem. Soc.* **1958**, *80*, 2795-2809.

[20] G. J. P. Britovsek, J. England, A. J. P. White, *Inorg.Chem*. **2005**, *44*, 8125-8134.

[21] G. A. Bain, J. F. Berry, *J. Chem. Educ.* **2008**, *85*, 532-536.

[22] *CRYSALIS-CCD 170*, Oxford-Diffraction, **2002**; *CRYSALIS-RED 170*, Oxford-Diffraction, **2002**.

[23] M. Sheldrick, SHELX97, *Program for Crystal Structure Analysis*, University of Gottingen, Gottingen, Germany, **1997**.

[24] L.J. Farrugia, *J. Appl. Crystallogr.* **1999**, *32*, 837-838.

[25] O. V. Dolomanov, L. J. Bourhis, R. J. Gildea, J. A. K. Howard and H. Puschmann, J. *Appl. Cryst.*, **2009**, *42*, 339-341.

Conclusion

Nous avons vu dans ce deuxième chapitre la synthèse de deux systèmes discrets à transition de spin. Le premier système mononucléaire à base de macrocycle où l'influence du contre-ion sur les caractéristiques de la transition de spin a été clairement mis en évidence. Nous avons également obtenu de la bistabilité thermique grâce aux interactions générées par le contre-ion $(tcm)^-$. Nous avons également vu que la substitution d'un bras méthylpyridine par une fonction aniline pouvait moduler le champ de ligand et modifier les caractéristiques de la transition de spin. En effet, le deuxième système à base du ligand andmpa a permis l'obtention d'un dimère à transition de spin avec une $T_{1/2}$ proche de 200 K. La transition est restée graduelle sans bistabilité. Dans les deux cas, nous avons obtenu deux systèmes discrets.

Afin d'augmenter la coopérativité pour obtenir un système commutable, nous nous sommes alors intéressés à un autre système à base du ligand aminoquinoline (aqin) auquel nous avons associé un co-ligand anionique et pontant de type $[M(CN)_4]^{2-}$. C'est l'étude de la chaîne obtenue pour ce système qui sera présentée dans le chapitre suivant.

Partie expérimentale

Synthèse du 1-(bromométhyl)- 2-nitrobenzène

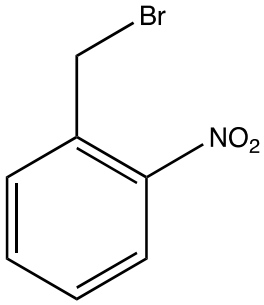

M=216,03 g.mol^{-1} $C_7H_6BrNO_2$

Référence : O. Schlager, K. Wieghardt,H. Grondey, A. Rufinska, B. Nuber, *Inorg. Chem*, **1995,** 34, 6440-6448.

Synthèse :

Une solution de 2-nitrophényl méthanol (1 g, 6,5 mmole) dans 15 mL de diéthyléther est refroidie à 4-5°C. On y ajoute goutte à goutte sous forte agitation une solution de tribromure de phosphore PBr_3 (1,17 g (0,4 mL), 4,3 mmole) dans le diéthyléther (10 mL). Après 1 heure d'agitation, le mélange réactionnel est ramené à température ambiante puis transféré dans une ampoule à décanter. La solution est lavée trois fois par 100 mL d'eau (la réaction avec l'eau est vive et exothermique). La phase organique est ensuite séchée par $MgSO_4$, et le solvant évaporé à l'évaporateur rotatif. On obtient un liquide marron qui cristallise au bout d'une nuit.

Produit : solide marron

Rendement : 60%

RMN ^{1}H δ (300MHz, ppm) ($CDCl_3$, 298K)

4,82 (2H, s, CH_2-Br); 7,45-7,50 (1H, t, $CH_{aromatique}$); 7,55-7,63 (2H, m, $CH_{aromatique}$); 7,99-8,02(1H, d, $CH_{aromatique}$)

RMN ^{13}C δ (300MHz, ppm) ($CDCl_3$, 298K)

28,8 (CH_2-Br); 125,5(C(α) C-NO_2); 130,2($C_{aromatique}$); 133,0 ($C_{aromatique}$); 133,1(C-(CH2-Br)$_{aromatique}$); 134,4 ($C_{aromatique}$); 148,2(C-NO_2)

Synthèse du ligand 1,8-di-(2-méthyl-2-aminobenzène)cyclam (L'2)

1, 4, 8, 11-tetraazatricyclo-[9, 3, 1, 1]-hexadecane (A)

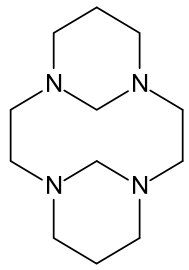

224,345 g/mol $C_{12}H_{24}N_4$

Référence: G. Royal, V. Dahaoui-Gindrey, A. Dahaoui, R. Guilard, P. Pullumbi, C. Lecomte, *Eur. J. Org. Chem.* **1998**, 1971.

Réaction: 0,90 mL (2,4 équivalents, 12 mmoles) de formaldéhyde (37 % dans l'eau) sont ajoutés sous agitation vigoureuse, rapidement, à une solution de 1 g de cyclam (1 équivalent, 5 mmoles) en suspension dans 50 mL d'eau distillée, à 0°C. Le mélange réactionnel est laissé sous agitation à température ambiante pendant deux heures. Le précipité obtenu est filtré et lavé à l'eau, puis séché sous le vide de la rampe.

Produit : poudre blanche.

Rendement : 98%.

RMN ^{1}H δ (ppm) ($CDCl_3$, 298K)

1,14-1,18 (m, 2H, C*H*$_2$ β-N) ; 2,19-2,28 (m, 2H, C*H*$_2$ β-N) ; 2,34-2,37 (m, 4H, C*H*$_2$ α-N) ; 2,56-2,63 (td, 4H, C*H*$_2$ α-N) ; 2,85-2,88 (d, 4H, C*H*$_2$ α-N) ; 3,12-3,14 (d, 4H, C*H*$_2$α-N) ; 5,40-5,42 (dt, 2H, C*H*$_{2\ aminal}$).

RMN ^{13}C δ (ppm) ($CDCl_3$, 298K)

20,3 (2C, *C*H$_2$ β-N) ; 49,4 (4C, *C*H$_2$ α-N) ; 53,7 (4C, *C*H$_2$ α-N) ; 68,96 (2C, *C*H$_{2\ aminal}$).

Dibromure de 1,8-bis (2-nitrobenzyl)-1,4,8,11-tetraazatricyclo-[9, 3, 1, 1]-hexadecane (B)

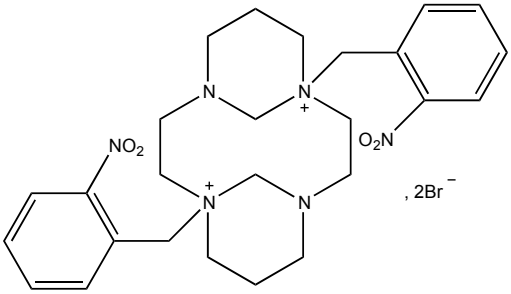

656,41 g/mol $C_{26}H_{36}Br_2N_6O_4$

Référence : G. Royal, V. Dahaoui-Gindrey, A. Dahaoui, R. Guilard, P. Pullumbi, C. Lecomte, *Eur. J. Org. Chem.* **1998**, 1971.

Réaction: 2,5 g de 1-(bromomethyl)-2-nitrobenzène (2,1 équivalents, 11,6 mmoles) sont placés dans un ballon avec 1,3g de **A** (0,998 g, 5,79 mmoles) dissous dans 50 mL d'acétonitrile distillé. Le mélange est laissé sous agitation à température ambiante pendant cinq jours. Le précipité formé est ensuite filtré, lavé trois fois par de l'acétonitrile, puis à l'éther, et séché sous vide.
Produit : poudre blanche
Rendement : 82%.

RMN ^{1}H δ (ppm) ($CDCl_3$, 298K)
1,74-1,78 (m, 4H, CH_2 β-N); 2,45-2,48 (m, 4H, CH_2 α-N); 2,77-2,81 (m, 8H, CH_2 α-N); 3,22-3,26 (m, 4H, CH_2 α-N), 3,87 (s, 4H, N-CH_2-aniline); 5,39 (s, 4H, C$H_{2\ aminal}$); 7,50-7,57 (t, 2H, C$H_{\ aromatique}$); 7,63-7,68 (m, 4H, C$H_{\ aromatique}$); 7,87-7,90(d, 2H, C$H_{\ aromatique}$).

RMN ^{13}C δ (ppm) ($CDCl_3$, 298K)
26,4 (2C, CH_2 β-N); 46,0 (2C, CH_2 α-N); 46,1(2C, CH_2 α-N) ; 51,0 (2C, CH_2 α-N); 53,8 (2C, CH_2 α-N); 58,3 (2C, N-CH_2-aniline); 84,5 (2C, $CH_{2\ aminal}$); 127,8 (2C, $CH_{aromatique}$); 132,3 (2C, $CH_{aromatique}$); 134,0 (2C, $CH_{aromatique}$); 136,0 (2C, $CH_{aromatique}$); 136,5 (2C, $CH_{aromatique}$); 152,3 (2C, $CH_{aromatique}$).

1,8-bis(2-nitrobenzyl)-1,4,8,11-tetraazacyclotetradecane (C)

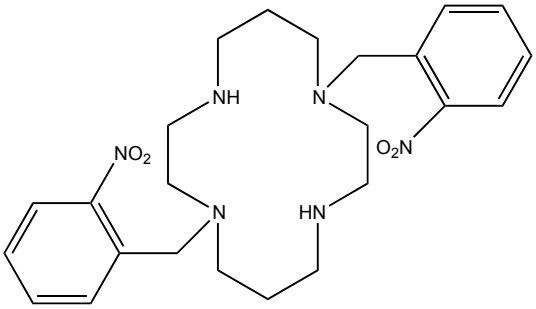

470,26 g/mol $C_{24}H_{34}N_6O_4$

Référence: G. Royal, V. Dahaoui-Gindrey, A. Dahaoui, R. Guilard, P. Pullumbi, C. Lecomte, *Eur. J. Org. Chem.* **1998**, 1971.

Réaction: 50 mL d'une solution aqueuse de NaOH (3M) est ajouté à 1 g (1,5 mmole) de **B**. Le mélange réactionnel est laissé sous agitation à température ambiante pendant vingt quatre heures. On extrait la phase aqueuse par trois fois 50 mL de chloroforme. Les phases organiques sont réunies, séchées sur sulfate de magnésium et concentrées à l'évaporateur rotatif. Après purification par chromatographie sur alumine neutre (CH_2Cl_2-MeOH, 0-1%), on obtient une poudre jaune.

Produit : solide jaune

Rendement : 42%.

RMN ^{1}H δ (ppm) ($CDCl_3$, 298K)

1,83-1,85(m, 4H, CH_2 β-N); 2,50-2,54 (m, 4H, CH_2 α-N); 2,67-2,69 (m, 12H, CH_2 α-N); 3,25 (s, 2H, NH); 3,8 (s, 4H, N-CH_2-aniline); 7,40-7,45 (t, 2H, C$H_{aromatique}$); 7,56-7,67 (m, 4H, C$H_{aromatique}$); 7,78-7,82 (d, 2H, C$H_{aromatique}$).

RMN ^{13}C δ (ppm) ($CDCl_3$, 298K)

24,6 (2C, CH$_2$ β-N); 48,0 (2C, CH$_2$ α-N); 48,9 (2C, CH$_2$ α-N); 51,4 (2C, CH$_2$ α-N); 52,9 (2C, CH$_2$ α-N); 57,4 (2C, N-CH$_2$-aniline); 124,3 (2C, CH$_{aromatique}$) ; 128,5 (2C, CH$_{aromatique}$); 132,2 (2C, CH$_{aromatique}$); 132,8 (2C, CH$_{aromatique}$); 133,0 (2C, CH$_{aromatique}$); 149,9 (2C, $CH_{aromatique}$).

2,2'-((1,4,8,11-tetraazacyclotetradecane-1,8-diyl)bis(methylene))dianiline (L'2) (D)

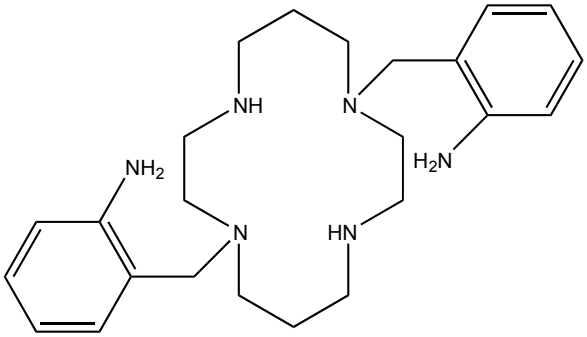

410,32 g/mol $C_{24}H_{38}N_6$

Réaction: On ajoute à 1 g de **C** mis en solution dans de l'éthanol absolu (50 mL), 4 mL d'hydrate d'hydrazine et une spatule de charbon actif. Le mélange réactionnel est mis au reflux sous diazote pendant 48 H. Après refroidissement et filtration, l'éthanol et l'hydrazine sont évaporés à l'évaporateur rotatif. Le solide formé est redissout dans le chloroforme. Cette phase organique est séchée par du sulfate de magnésium. Le mélange est filtré puis concentré à l'aide de l'évaporateur rotatif.

Produit : poudre blanche.

Rendement : 98%.

RMN ^{1}H δ (ppm) ($CDCl_3$, 298K) :

1,62-1,65(m, 4H, CH_2 β-N); 2,46-2,49 (m, 8H, CH_2 α-N); 2,58-2,62 (m, 2H, CH_2 α-N); 2,74-2,77 (m, 4H, CH_2 α-N); 3,4 (s, 4H, N-CH_2-aniline); 6,59-6,64 (m, 4H, C$H_{aromatique}$); 6,95-6,97 (d, 2H, C$H_{aromatique}$); 7,01-7,11 (d, 2H, C$H_{aromatique}$).

RMN ^{13}C δ (ppm) ($CDCl_3$, 298K) :

26,0 (2C, CH_2 β-N); 47,0 (2C, CH_2 α-N); 50,1 (2C, CH_2 α-N); 51,4 (2C, CH_2 α-N); 53,7 (2C, CH_2 α-N); 56,1 (2C, N-CH_2-aniline); 114,8 (2C, $CH_{aromatique}$); 116,1 (2C, $CH_{aromatique}$); 122,0 (2C, $CH_{aromatique}$); 128,1 (2C, $CH_{aromatique}$); 131,3 (2C, $CH_{aromatique}$); 146,74 (2C, $CH_{aromatique}$).

Chapitre III

Réseau monodimensionnel

Introduction

De par leur nature, les espèces polymériques favorisent la coopérativité dans les systèmes à transition de spin. Dans le but d'obtenir de la bistabilité, nous nous sommes orientés dans cette voie. Dans le chapitre précédent, la synthèse du complexe du fer(II) était basée sur un ligand hexadentate N_6, les contre-ions assurant l'électroneutralité. Une autre voie de synthèse repose sur l'utilisation d'un ligand neutre de denticité inférieure (penta-, tétra-dentate…) avec des atomes d'azote donneur associé à un co-ligand ayant pour rôle de compléter la sphère de coordination du cation fer(II). Pour obtenir des édifices polymériques, ce co-ligand doit être pontant. De plus, afin d'augmenter la coopérativité pour obtenir de la bistabilité, ce co-ligand doit être le plus contraignant possible.

Parmi les ligands neutres N-donneurs à notre disposition remplissant les critères définis ci-dessus, l'équipe avait étudié le ligand abpt (4-amino-3,5-bis(pyridin-2-yl)-1,2,4-triazole). Associé à l'anion $(tcpd)^{2-}$, un système polymérique (chaîne) avait été obtenu présentant une transition de spin graduelle en deux étapes et des propriétés photo-magnétiques. [2,3]

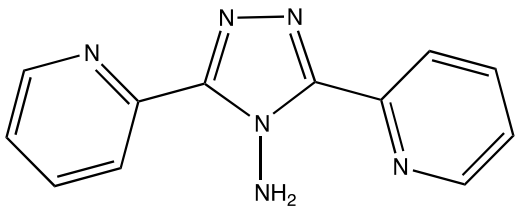

Figure III.1 Ligand abpt

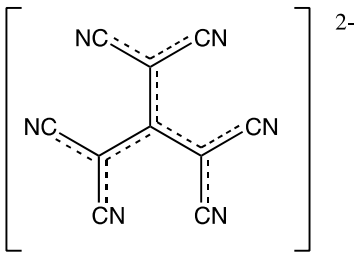

ligand $tcpd^{2-}$

Afin de modifier les caractéristiques de la transition de spin ($T_{1/2}$, T_{LIESST},… etc.), l'anion $(tcpd)^{2-}$ a été substitué par des anions tétracyanoplatinates $[Pt(CN)_4]^{2-}$, pontants et plus rigides, ce qui a conduit à l'obtention d'une chaîne monodimensionnelle $[Fe(abpt)_2(Pt(CN)_4)]$[4]. Ce complexe présente une $T_{1/2}$ au-dessus de 298 K. Afin de l'abaisser, une modulation du champ de ligand était nécessaire. Nous avons choisi de comparer le complexe précédent à celui formé avec le ligand 8-

[2] G. Dupouy, M. Marchivie, S. Triki, J. Sala-Pala, C. J. Gomez-Garcia, S. Pillet, C. Lecomte, J.-F. Létard, *Chem. Commun.*, **2009**, 3404–3406.
[3] G. Dupouy, S. Triki, M. Marchivie, N. Cosquer, C. J. Gómez-García, S. Pillet, E.-E. Bendeif, C. Lecomte, S. Asthana, J.-F. Létard, *Inorg. Chem.* **2010**, *49*, 9358-9368
[4] C. Charles, F. Setifi, F. Thétiot, S. Triki, C. J. Gómez-García, *Polyhedron*, **2013**, 61, 242–247.

aminoquinoline (aqin) qui présente des similitudes avec le ligand abpt en terme de noyaux aromatiques et atomes N-donneurs.

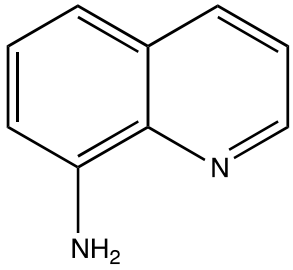

Figure III.2 Ligand 8-aminoquinoline (aqin)

Nous avons obtenu une série de complexes $[Fe(aqin)_2(\mu_2\text{-}Ni(CN)_4)]$ et $[Fe(aqin)_2(\mu_2\text{-}Pt(CN)_4)]$ en associant le complexe de l'ion fer(II) par l'aminoquinoline avec le co-ligand $[M(CN)_4]^{2-}$ (avec M= Pt, Ni). Dans une première partie, la synthèse, la caractérisation et les propriétés magnétiques de ces deux complexes, publiées en 2014 dans Inorganic Chemistry, seront présentées. Pour poursuivre l'étude, nous avons remplacé le métal central M (Ni, Pt) par le palladium (Pd). Les résultats obtenus avec le complexe $[Fe(aqin)_2(\mu^2\text{-}Pd(CN)_4)]$ feront l'objet de la seconde partie.

1. Synthèses, structures et caractérisations des complexes $[Fe(aqin)_2(\mu_2\text{-}M(CN)_4)]$ avec M=Ni,Pt

Spin Crossover (*SCO*) Iron (II) Coordination Polymer Chains: Syntheses, Structures and Magnetic Characterizations of $[Fe(aqin)_2(\mu_2\text{-}M(CN)_4)]$ (M = Ni(II), Pt(II), aqin = Quinolin-8-amine).

Fatima Setifi,[†,§] Eric Milin,[†] Catherine Charles,[†] Franck Thétiot,[†] Smail Triki,[*,†] Carlos J. Gómez-García.[‡], *Inorganic Chemistry*, **2013**, 53(1), 97-104

[†]UMR CNRS 6521, Chimie, Electrochimie Moléculaires, Chimie Analytique, Université de Bretagne Occidentale, BP 809, 29285 Brest Cedex, France.

E-mail: smail.triki@univ-brest.fr

[§]Laboratoire de Chimie, Ingénierie Moléculaire et Nanostructures (LCIMN), Université Ferhat Abbas de Sétif, 19000 Sétif, Algeria.

[‡]Instituto de Ciencia Molecular (ICMol), Parque Científico, Universidad de Valencia, C/ Catedrático José Beltrán, 2, 46980 Paterna, Valencia, Spain.

ABSTRACT: New Fe(II) coordination polymeric neutral chains of formula $[Fe(aqin)_2(\mu_2\text{-}M(CN)_4)]$ (M = Ni^{II} (**1**) and Pt^{II} (**2**)) (aqin = Quinolin-8-amine) have been synthesized and characterized by infrared spectroscopy, X-ray diffraction and magnetic measurements. The crystal structure determinations of **1-2** reveal in both cases a one-dimensional structure in which the planar $[M(CN)_4]^{2-}$ (M = Ni^{II} (**1**)

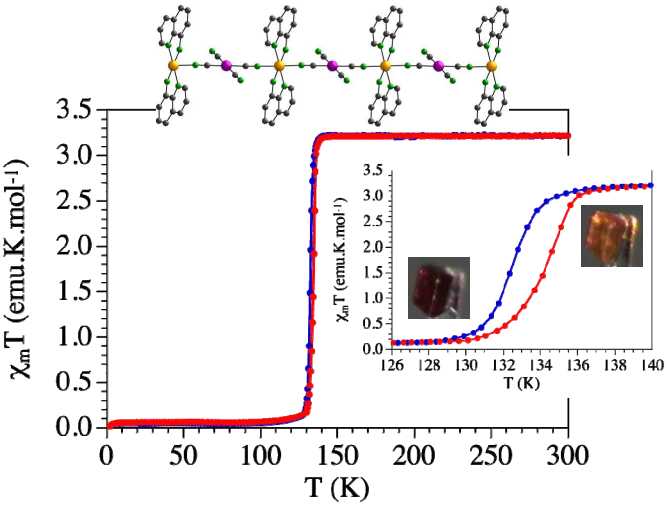

and Pt^{II} (**2**)) anion acts as a μ_2-bridging ligand, and the two aqin molecules as chelating co-ligands. Examination of the intermolecular contacts in the two compounds reveals that the main contacts are ascribed to hydrogen bonding interactions involving the amine groups of the aqin chelating ligands and the nitrogen atoms of the two non bridging CN groups of the

$[M(CN)_4]^{2-}$ (M = Ni^{II} (**1**) and Pt^{II} (**2**)) anion. The average values of the six Fe-N distances observed respectively at room temperature (293 K) and low temperature (120 K) – *i.e.* 2.142(3) and 2.035(2) Å for **1**, and 2.178(3) and 1.990(2) Å for **2** – and the thermal variation of the cell parameters (performed on **2**) are indicative of the presence of an abrupt *HS*-*LS* spin crossover (*SCO*) transition in both compounds. The thermal dependence of the product of the molar magnetic susceptibility times the temperature ($\chi_m T$), in cooling and warming modes, confirms the *SCO* behavior at *ca.* 145 and 133 K in **1** and **2**, respectively, and reveals the presence of a small thermal hysteresis of *ca.* 2 K for each compound.

INTRODUCTION

The design of new coordination complexes exhibiting the spin crossover phenomenon (*SCO*) is one of the most relevant challenges in the field of magnetic molecular materials.[1-9] The *SCO* systems relate to the pseudo-octahedral d^4-d^7 transition metal complexes for which the high spin (*HS*) and the low spin (*LS*) electron configurations can be reversibly switched by external stimuli such as temperature, pressure, magnetic field or light irradiation.[5-20] Nevertheless, the primary investigated systems to date remain those based on Fe(II) (d^6 configuration), for which a paramagnetic-diamagnetic transition from the *HS* (*S* =2) state to the *LS* (*S* = 0) state is observed. Up to now, most of the reported *SCO* Fe(II)-based examples refer to mononuclear compounds.[21-28] In such discrete systems, the intermolecular interactions (π-stacking, hydrogen bonding and van der Waals interactions), which generate the supramolecular architecture in the solid state, play a crucial role in the information transmission of the magneto-elastic cooperative effects at the origin of the magnetic bistability. However, the non covalent character of those contacts hardens the anticipated design of the supramolecular organization in the crystal, and consequently makes difficult the tailoring of the *SCO* characteristics.

To better explore the cooperative effect between the active metal ions, a new approach based on the use of neutral suitable bridging ligands, able to create covalent links between the metal centers, has been introduced. The first mono-dimensional polymeric SCO compound, $[Fe(Htrz)_2(trz)](BF_4)$ (trz^- = 1,2,4-triazolate anion) was reported by J. G. Haasnoot and co-workers in 1977, it exhibits successfully a large thermal hysteresis.[29] Similarly, the use of substituted 1,2,4-triazole ligands led to other 1D SCO polymers for which some of them undergo cooperative SCO close to room temperature.[30] In parallel, the extension of such polymeric approach to poly-N-donating heterocyclic ligands and to the bis(azolyl)alkanes resulted in the preparation of several iron (II) SCO coordination polymers exhibiting rich and

fascinating structural features ranging from 1D to 3D networks, and various magnetic behaviors.[31-35]

However, the limited number of potentially appropriate bridging ligands slows down the emergence of extended polymeric systems exhibiting covalent links between the metal active centers. In this context, we have noticeably extended, in recent years, this polymeric approach to the highly conjugated cyanocarbanion ligands involving several potentially donating nitrogen atoms.[36] This led us to the first *SCO* iron (II) molecular neutral chain $[Fe(abpt)_2(tcpd)]$ ($(tcpd)^{2-}$ = $(C[C(CN)_2]_3)^{2-}$ = 2-dicyanomethylene-1,1,3,3-tetracyanopropanediide anion; abpt = 4-amino-3,5-bis(pyridin-2-yl)-1,2,4-triazole) involving an anion as bridging ligand.[37] In our ongoing work on innovative potentially bridging ligands appropriate for the design of novel *SCO* polymeric systems, we have reported recently two new polymeric chains $[Fe(abpt)_2(M(CN)_4)]$ (M = Ni^{II}, Pt^{II}) involving more rigid anionic bridging ligands.[38] However, these 1-D compounds display *SCO* transitions above room temperature, making difficult to reach any structural and electronic informations on the *HS* state. Thus, with the purpose to better control the transition temperature in such systems involving inorganic planar anions, and more distinctly to shift the *SCO* transition below room temperature, we have substituted abpt co-ligand by other chelating co-ligands displaying lower crystal field energies, such as the quinolin-8-amine (aqin).[39] We report herein the syntheses and the full structural characterizations including thermal variation of the crystallographic structural data, and magnetic properties of two new *SCO* Fe(II) coordination polymer chains of formula $[Fe(aqin)_2(\mu_2\text{-}M(CN)_4)]$ (M = Ni^{II} (**1**) and Pt^{II} (**2**)) involving tetracyanonometallate anions as bridging ligands. Note that this study can be viewed as an extension of large series employing these planar anions or other parent cyano anions such as $[M(CN)_2]^-$ (M = Ag^I, Au^I) to design SCO materials exhibiting multidimensional networks such as the 3D Hofmann-like Networks.[12,40]

EXPERIMENTAL SECTION

General remarks. All reactions were carried out under aerobic conditions. The starting materials and solvents were purchased from commercial sources (analytical reagent grade) and used without further purification.

Syntheses of $[Fe(aqin)_2(\mu_2\text{-}M(CN)_4)]$ (M = Ni^{II} (1) and Pt^{II} (2)). An ethanolic solution (5 mL) of aqin (0.5 mmol, 72.08 mg) was added progressively, under continuous stirring, to an aqueous solution (10 mL) of $Fe(BF_4)_2 \cdot 6H_2O$ (0.25 mmol, 84.39 mg). The mixture was stirred at room temperature for 15 min and then an aqueous solution (10 mL) of $K_2[M(CN)_4]$

(for M = Ni^{II}: 0.25 mmol, 60.25 mg; for M = Pt^{II}: 0.25 mmol, 94.34 mg) was added dropwise. The resulting orange precipitate was filtered off, washed with cold water and ethanol and dried. Yield: 92.6 mg, 73.0 % for **1** and 122.8 mg, 76.3 % for **2**. For **1**: *Anal.* Calc. (%) for $C_{22}H_{16}FeN_8Ni$: C, 52.1; H, 3.2; N, 22.1. Found: C, 52.3; H, 3.3; N, 21.9. IR (cm^{-1}): 3278(m), 3183(m), 3131(m), 2140(s), 2120(s), 1626(m), 1579(s), 1503 (s), 1471(m), 1424(w), 1400(m), 1375(m), 1320(m), 1223(w), 1203(w), 1173(w), 1134(m), 1103(m) 1071(m), 1053(m), 1026(s), 826(s), 789(s), 772 (s), 717(m), 633(m), 581(m), 520(m), 602(w), 583(w), 555(w), 524(w), 436(s), 420(s). For **2**: *Anal.* Calc. (%) for $C_{22}H_{16}FeN_8Pt$: C, 41.1; H, 2.5; N, 17.4. Found: C, 41.5; H, 2.4; N, 17.6. IR (cm^{-1}): 3283(m), 3181(m), 3130(m), 2146(s), 2131(s), 1625(m), 1578(m), 1502 (s), 1470(m), 1397(w), 1372(w), 1319(m), 1133(w), 1099(w), 1069(m), 1050(s), 1024(s), 827(s), 789(s), 772(s), 714(m), 631(m), 581(m), 555(m), 525(m), 498(m), 470(m).

Single crystal preparation of $[Fe(aqin)_2(\mu_2\text{-}M(CN)_4)]$ (M = Ni^{II} (1) and Pt^{II} (2)). Single-crystals of compounds **1**-**2** were synthesized using a silica gel diffusion technique in straight tube. The gel phase was obtained by addition of tetramethoxysilane (1 mL) to an aqueous solution (9 mL) of $K_2[M(CN)_4]$ (0.45 mmol; 108.4 mg for **1** and 169.8 mg for **2**) with stirring; the gel was formed from the resulting solution left standing for six hours. Then, two aqueous solutions (6 mL) of $Fe(SO_4)\bullet 7H_2O$ (0.15 mmol, 41.7 mg) and aqin ligand (0.33 mmol, 47.6 mg), were prepared and carefully layered onto the respective gels. Single-crystals of compounds **1** (dark orange) and **2** (orange), suitable for X-ray analyses, were formed within two weeks. As expected, the IR data for single crystals of both compounds are similar to those observed for the corresponding powders described above.

X-ray Crystallography. Crystallographic studies of the two derivatives (**1**-**2**) were performed at 293 K and 120 K, using an Oxford Diffraction Xcalibur κ-CCD diffractometer equipped with a graphite monochromated Mo$K\alpha$ radiation (λ= 0.71073 Å). The full sphere data collections were performed using 1.0° ω-scans with an exposure time of 150 s and 200 s per frame for **1**, 60 s and 80 s per frame for **2** at 293 K and 120 K, respectively. Data collection and data reduction were done with the CRYSALIS-CCD and CRYSALIS-RED programs on the full set of data.[41] The crystal structures were solved by direct methods and successive Fourier difference syntheses, and were refined on F^2 by weighted anisotropic full-matrix least-square methods.[42] All non-hydrogen atoms were refined anisotropically, while the hydrogen atoms were calculated and therefore included as isotropic fixed contributors to

F_c. All other calculations were performed with standard procedures (WINGX).[43] Crystal data, structure refinement and collection parameters are listed in table 1.

Physical measurements. Infrared spectra were recorded in the range 4000-200 cm^{-1} on a FT-IR BRUKER ATR VERTEX70 Spectrometer. Diffraction analyses were performed using an Oxford Diffraction Xcalibur κ-CCD diffractometer. Variable temperature magnetic susceptibility measurements were carried out in the temperature range 2-300 K in cooling and warming scans with an applied magnetic field of 0.5 T on polycrystalline samples of compounds **1** and **2** (with masses of 6.805 and 3.600 mg, respectively) with a Quantum Design MPMS-XL-5 SQUID magnetometer. The susceptibility data were corrected for the sample holders previously measured under the same conditions, and for the diamagnetic contributions as deduced by using Pascal´s constant tables (χ_{dia} = -245.36x10^{-6} and -273.36x10^{-6} emu•mol^{-1} for **1** and **2**, respectively).[44] The magnetic measurements were performed with different cooling and warming rates in the range 0.5-5 K/min. The results obtained, within experimental error, were independent of the rate. Elemental analyses were performed at the "Service de microanalyse", CNRS, 91198 Gif-sur-Yvette.

Table 1. Crystal data and structural refinement parameters for compounds [Fe(aqin)$_2$(μ_2-M(CN)$_4$)]; M = Ni^{II} (**1**) and Pt^{II} (**2**).

	1		**2**	
Temperature / K	293(2)	120(2)	293(2)	120(2)
Empirical formula	$C_{22}H_{16}N_8FeNi$		$C_{22}H_{16}N_8FePt$	
Formula weight	506.99		643.37	
Wavelength / Å	0.71073		0.71073 Å	
Crystal system	Monoclinic		Monoclinic	
Space group	*P2$_1$/c*		*P2$_1$/c*	
a / Å	9.1819(6)	9.0033(5)	9.3073(3)	9.0290(2)
b / Å	12.0719(7)	12.0053(6)	12.1228(4)	12.0904(3)
c / Å	9.7282(5)	9.6117(5)	9.9073(3)	9.8107(3)
β /°	100.258(6)	100.043(6)	101.670(4)	101.124(3)
Volume / Å^3	1061.07(11)	1022.98(9)	1094.74(6)	1050.86(5)
Z	2	2	2	2
D_{calc} / g.cm^{-3}	1.587	1.646	1.952	2.033
Abs. coef. / mm^{-1}	1.598	1.658	7.072	7.367
F(000)	516	516	616	616
Crystal size / mm^3	0.16x0.08x 0.05	0.13x0.11x0.04	0.16x0.15x0.08	0.16x0.15x0.08
2θ range / °	6.56-63.30	6.66-60.00	6.42 – 60.00	6.56-60.00
Refl. collected	10548	7201	10604	10188
Unique refl. / Rint	3324 / 0.0785	2884 / 0.0340	3174 / 0.0330	3057 / 0.0230
Data / restr. / N_v	1273 / 0 / 148	1571 / 0 / 148	2017 / 0 / 148	2094 / 0 / 148
[b]R1/[c] wR2	0.0423 / 0.0732	0.0385 / 0.0984	0.0226 / 0.0494	0.0186 / 0.0480
[d]GooF	0.906	0.910	0.973	1.125
$\Delta\rho_{max/\ min}$ (eÅ^{-3})	+0.543 / -0.376	+1.319 / -0.337	+0.890 / -0.351	+1.371 / -0.442

[a]The asymmetric unit contains 0.5 of the chemical formula.
[b]$R1 = \sum|F_o-F_c|/F_o$.
[c]$wR2= \{\Sigma[w(F_o^2-F_c^2)^2]/ \Sigma[w(F_o^2)^2]\}^{1/2}$
[d]$GooF= \{\Sigma[w(F_o^2-F_c^2)^2]/ (N_{obs}-N_{var})\}^{1/2}$

■ RESULTS AND DISCUSSION

Single-crystals of compounds **1** and **2** were synthesized using a silica gel diffusion since the direct mixture of the precursors yielded microcrystalline powders in all cases. Single-crystals of compounds **1** (dark orange) and **2** (orange), suitable for X-ray analysis, were formed within two weeks. As expected, the IR data of the single crystals of both compounds are similar to those observed for the corresponding powders described above. The IR spectra of compounds **1** and **2** show two characteristic $\nu_{(CN)}$ bands (2140(s), 2120(s) for **1** and 2146(s), 2131(s) for **2**) which are distinct from the stretching vibration modes observed in $K_2[M(CN)_4]\bullet xH_2O$ ($M = Ni^{II}$ and Pt^{II}).[45] These values can be respectively assigned to the presence of bridging and terminal CN groups, in agreement with the bridging coordination mode of the $[M(CN)_4]^{2-}$ anions in both compounds.

The crystal structures of compounds **1-2** were performed at room temperature (293 K) and at 120 K. The unit cell parameters, crystal and refinement data are summarized in table 1. Selected bond lengths and angles for the iron (II) coordination sphere, including distortion parameters, are summarized in table 2.

Table 2. Selected bond lengths (Å), bond angles and distortion parameters (°) of the Fe(II) coordination spheres for compounds **1-2**.

Compound	**1** ($M = Ni^{II}$)		**2** ($M = Pt^{II}$)	
T / K	293	120	293	120
Fe-N1	2.131(3)	2.022(2)	2.170(3)	1.989(2)
Fe-N2	2.161(2)	2.071(2)	2.206(3)	2.031(2)
Fe-N3	2.133(3)	2.011(2)	2.157(3)	1.949(2)
<Fe-N>	2.142(3)	2.035(2)	2.178(3)	1.990(2)
N1-Fe-N3	87.41(10)	87.67(10)	87.68(11)	87.46(10)
N1-Fe-N3$^{(i)}$	92.59(10)	92.33(10)	92.32(11)	92.54(10)
N1-Fe-N2	78.88(10)	82.22(9)	77.48(10)	83.02(10)
N1-Fe-N2$^{(i)}$	101.12(10)	97.78(9)	102.52(10)	96.98(10)
N2-Fe-N3	93.14(9)	93.68(9)	92.85(10)	93.98(10)
N2-Fe-N3$^{(i)}$	86.86(9)	86.32(9)	87.15(10)	86.02(10)
[a] Σ	67	55	71	54
[b] Θ	207	154	233	144

Codes of equivalent positions: (i) -x,-y,1-z.

[a] Σ is the sum of the deviation from 90° of the 12 *cis*-angles of the FeN_6 octahedron.[46] [b] Θ is the sum of the deviation from 60°of the 24 trigonal angles of the projection of the FeN_6 octahedron onto its trigonal faces.[47]

The following general structural descriptions are specified at 293 K for both compounds. The pertinent structural modifications induced by cooling or warming will be discussed further in the paragraph dealing with structural and magnetic properties relationships. The two compounds are isostructural as the structure is built from one Fe(II) cation, one $[M(CN)_4]^{2-}$ anion (M = Ni^{II}(**1**) and Pt^{II} (**2**)), both located on inversion centers, and one chelating aqin ligand located on a general position. As shown in figure 1, the Fe(II) ion adopts a distorted FeN_4N_2 octahedral geometry, with four equatorial nitrogen atoms from two aqin chelating ligands (N1, N2, $N1^{(i)}$ and $N2^{(i)}$), and two axial nitrogen atoms (N3 and $N3^{(i)}$) from two equivalent $[M(CN)_4]^{2-}$ ligands. At room temperature, the average values of the six Fe-N distances are 2.142(3) and 2.178(3) Å for **1** and **2**, respectively. The bond lengths and angles of the two $[M(CN)_4]^{2-}$ (M = Ni^{II}, Pt^{II}) anions are similar to those observed in other coordination complexes involving this moiety.[48,49] The trigonal distortion of the octahedral Fe(II) environment is highlighted by the Σ and Θ parameters (see details in table 2).[46,47] Indeed, the relatively high values of the Σ and Θ parameters observed for both compounds at room temperature are indicative of the high degree of distortion of the FeN_6 octahedrons, typical of a *HS* coordination sphere. The resulting molecular structures for **1**-**2** can be described as a chain running along the crystallographic [001] direction, in which the planar $[M(CN)_4]^{2-}$ (M = Ni^{II}, Pt^{II}) anion acts as a μ_2-bridging ligand *via* two nitrogen atoms of two trans cyano groups (figure 1).

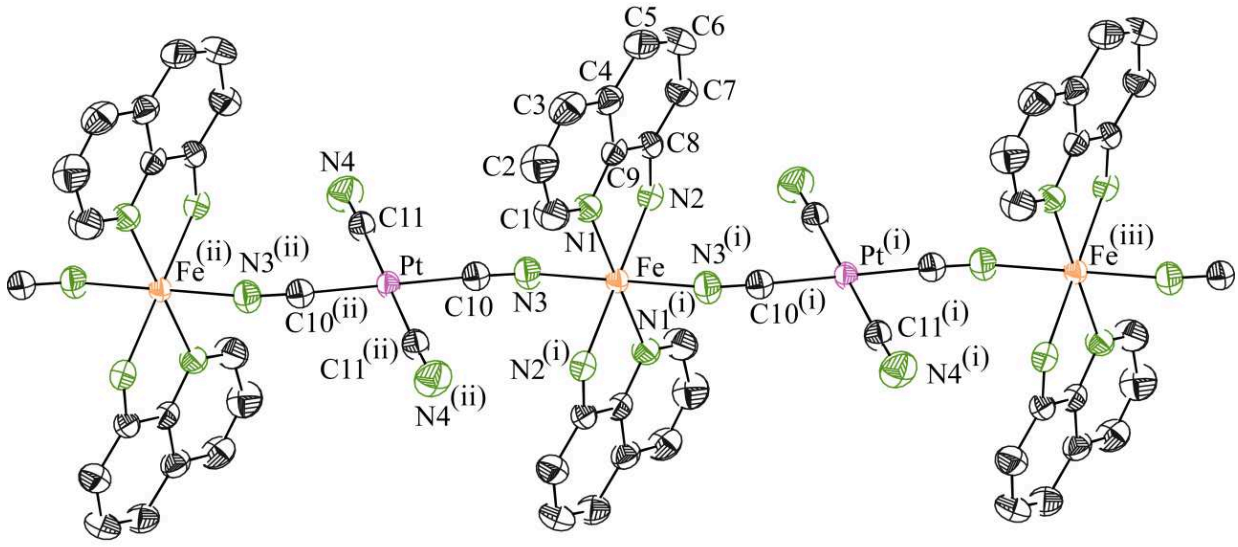

Figure 1. Ortep[50] plot (50 % probability ellipsoids) of the 1-D neutral structure of **2** at 293 K showing the asymmetric unit, the atom labeling scheme and the metal ion environment. Codes of equivalent positions: *(i)* -x,-y,1-z; *(ii)* -x,-y,-z; *(iii)* x,y,z+1 (similar figure for the Ni^{II} analogue (**1**)).

Along the neutral chains, the shortest Fe…Fe (Fe…Fe$^{(iii)}$ in figure 1) and M….M distances (see figure 1 for M = Pt^{II}) are simply defined by the length of the crystallographic *c* cell parameter (see table 1). Consequently and as clearly depicted in figure 1, these intrachain separations (Fe…Fe and M….M, with M = Ni^{II} (**1**) and Pt^{II} (**2**)) impose the shortest Fe…M distance to equal half of the crystallographic *c* cell parameter (4.8641(5) and 4.9536(3) Å at 293 K for **1** and **2**, respectively), in agreement with the linear arrangement of the metal ions along the [001] direction. The crystal packing of **1**-**2** is generated from the regular chains which are arranged in an eclipsed fashion along the [100] direction, leading to the structural arrangement depicted in figure 2.

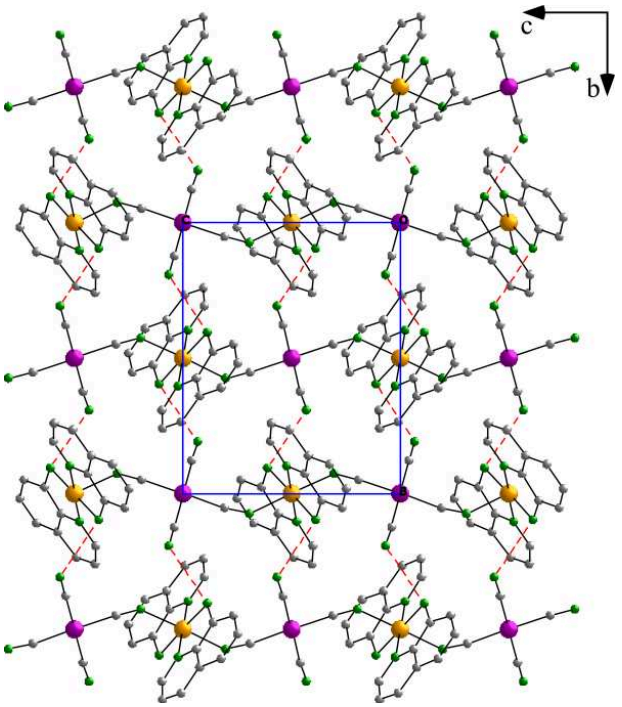

Figure 2. Projection view of the overall molecular structure of compound **2** (similar to **1**) showing the eclipsed packing of the 1-D bimetallic coordination polymer along the [100] direction, and the interchain hydrogen bonding (red dashed lines) along the [010] direction.

Careful examination of the intermolecular separations in the two compounds (figures 2-3 and table 3) reveals two main types of interchain contacts, both occurring in the [010] direction: *(i)* hydrogen bonding interactions involving one of the hydrogen atom of the amine group (N2 and N2$^{(i)}$) of the chelating aqin ligands and the nitrogen atom of the two non bridging CN groups (N4 and N4$^{(ii)}$) from the $[M(CN)_4]^{2-}$ anion of an adjacent chain (N2…N4$^{(b)}$ 3.123(4) and 3.132(4) Å for **1** and **2**, respectively), leading to the structural arrangement depicted in figure 2 and *(ii)* the π-stacking interactions between two aqin ligands

from two adjacent chains, as shown in figure 3. The shortest interchain contacts observed for both compounds, as well as their thermal evolution, are gathered in table 3.

Table 3. Main interchain π-stacking C…C contacts and shortest N…N hydrogen bonding (Å) in **1**-**2**.

Compound		**1** (M = Ni^{II})		**2** (M = Pt^{II})	
T / K		**293**	**120**	**293**	**120**
π-stacking C…C contacts	C3…C7$^{(iv)}$	3.497(1)	3.465(1)	3.505(1)	3.490(1)
	C5…C9$^{(iv)}$	3.567(1)	3.558(1)	3.564(1)	3.588(1)
	C4…C7$^{(iv)}$	3.548(1)	3.483(1)	3.621(1)	3.534(1)
	C5…C8$^{(iv)}$	3.540(1)	3.491(1)	3.628(1)	3.544(1)
	C4…C8$^{(iv)}$	3.643(1)	3.640(1)	3.674(1)	3.718(1)
	C6…C9$^{(iv)}$	3.604(1)	3.561(1)	3.676(1)	3.608(1)
	C4…C6$^{(iv)}$	3.708(1)	3.654(1)	3.762(1)	3.658(1)
N…N H-bonding	N2…N4$^{(v)}$	3.123(4)	3.069(3)	3.132(4)	3.059(4)

Codes of equivalent positions: *(iv)* 1-x,-y,1-z, *(v)* x,-1/2-y,1/2+z

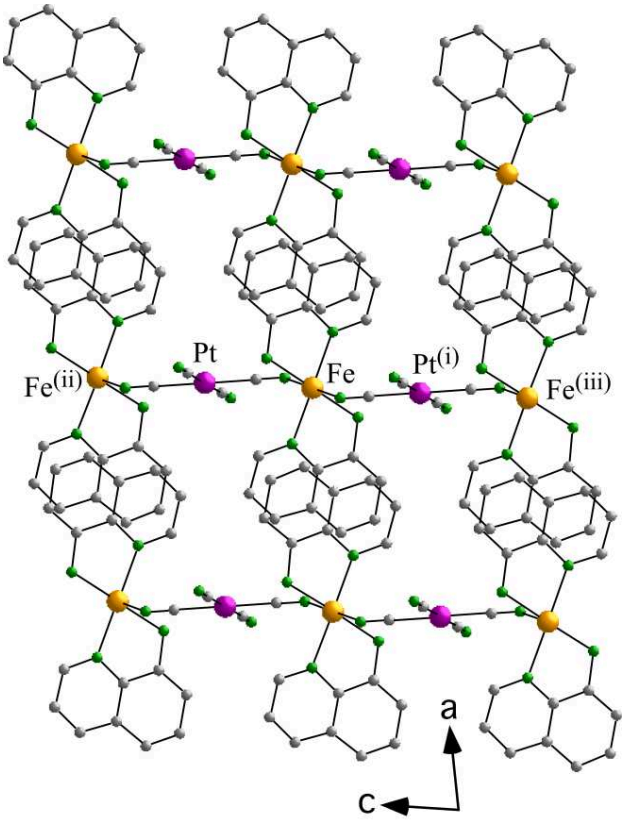

Figure 3. Projection view of **2** (similar to **1**) showing the interchain π-stacking contacts between aqin co-ligands from adjacent chains. Codes of equivalent positions: *(i)* -x,-y,1-z; *(ii)* -x,-y,-z; *(iii)* x,y,z+1.

The thermal dependence of the product of the molar magnetic susceptibility per Fe(II) ion times the temperature ($\chi_m T$) is depicted in figures 4-5. For compound **1**, the $\chi_m T$ value observed at room temperature (300 K) is *ca.* 2.65 emu•K•mol^{-1}. This value is significantly lower than the value expected for an hexacoordinated *HS* (S = 2, $^5T_{2g}$) Fe(II) ion. This relatively low $\chi_m T$ value indicates the existence, at room temperature, of a fraction of *ca.* 20 % of Fe(II) ions in the *LS* configuration. It is also noteworthy to indicate that even upon heating of the sample above 300 K, the $\chi_m T$ product remains almost constant and the transition is not fully achieved at 400 K. Upon cooling, the $\chi_m T$ product of **1** decreases gradually, down to a value of *ca.* 2.3 emu.K.mol^{-1} at a temperature of *ca.* 150 K. Below this temperature, a sharp decrease is observed, indicating the occurrence of an abrupt *HS-LS SCO* transition, with a transition temperature ($T_{1/2}$) of *ca.* 145 K. Below 120 K, the $\chi_m T$ value is close to *ca.* 0.50 cm^3•K•mol^{-1}, in agreement with the presence of a residual fraction (*ca.* 15 %) of Fe(II) ions in the *HS* configuration. The presence of a ca. 1/5 fraction of Fe(II) centers which remain in the HS configuration at low temperatures may be attributed to the presence of defects and vacancies in the chain that lead to the formation of more or less large 1D islands where the *HS* to *LS* transition of one Fe(II) center prevents its neighbors to transit, resulting in a fraction of *HS* Fe(II) centers. On the other hand, the presence of a similar fraction of Fe(II) centers that remain in the LS configuration even at high temperatures (400 K) may be attributed to the possible linkage isomerism of a small fraction of the CN bridges. Thus, the conversion of some Ni-CN-Fe bridges into Ni-NC-Fe ones, would significantly increase the ligand field at the Fe(II) centers, resulting in a *LS* configuration even at high temperatures, as observed in the Ni compound (**1**).[51] Interestingly, this CN linkage isomerism is not observed in the Pt derivative (**2**), in agreement with the much softer character of the Pt(II) ion as compared with the Ni(II) one.

Furthermore, the warming mode reveals a very small hysteresis of *ca.* 2 K (insets in figure 4). At very low temperatures, the residual fraction of *HS* Fe(II) ions shows the expected zero field splitting (*ZFS*), leading to a slight decrease of the $\chi_m T$ product, to reach a value of *ca.* 0.35 emu•K•mol^{-1} at 2 K.

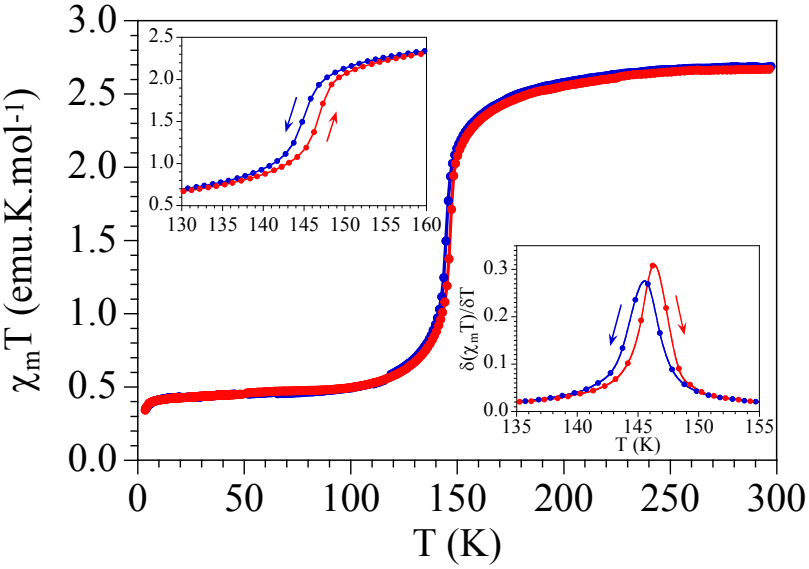

Figure 4. Thermal variation of the $\chi_m T$ product in **1** in the cooling (blue) and warming (red) scans. Left inset shows a zoom of the transition. Right inset shows the thermal variation of the derivative of $\chi_m T$.

For the Pt analogue (**2**), the $\chi_m T$ value observed in the high temperature region is *ca.* 3.30 emu.K.mol^{-1}. This value is consistent with a $S = 2$ *HS* state of the octahedral Fe(II) ions with $g \approx 2.1$. Upon cooling, the $\chi_m T$ product remains constant, down to a temperature of *ca.*134 K. Below this temperature, the sharp decrease on display is indicating the occurrence of an abrupt *HS-LS SCO* transition, as expected from the abrupt colour change observed for the single crystals (figure 5). Below 132 K, the $\chi_m T$ value is close to 0.0 cm^3•K•mol^{-1}, hence revealing the absence of any significant residual fraction of *HS* Fe(II) ions. The warming mode shows a slight thermal hysteresis; indeed, the spin transition temperatures ($T_{½}$) for the cooling ($T_{½}^{down}$) and warming ($T_{½}^{up}$) scans are 132.5 and 134.5 K, respectively, indicating the occurrence, as in **1**, of a *ca.* 2 K wide hysteresis loop (see insets Figure 5).The presence of these narrow thermal hysteresis in both compounds can be explained thanks to the existence of weak intermolecular interactions (H-bonds and π-π stacking in both compounds) described above.

Based on the conclusions derived from the magnetic data, the crystal structures have been determined at 293 K and 120 K for both compounds, and the temperature dependence of the lattice parameters of a single crystal of **2** was performed in the range 293-100 K. The corresponding structural parameters are depicted in figures 6-7 and in table 2. Some of these parameters, such as the average coordination distance <Fe-N> and trigonal distortion

parameters Σ and Θ (previously defined in table 2), are known to be highly sensitive to the Fe(II) spin configuration, and will thus be used hereafter to assign the spin state on each Fe crystallographic site (<Fe-N>$_{LS}$ ~ 2.0 Å; <Fe-N>$_{HS}$ ~ 2.2 Å).[37,46,47]

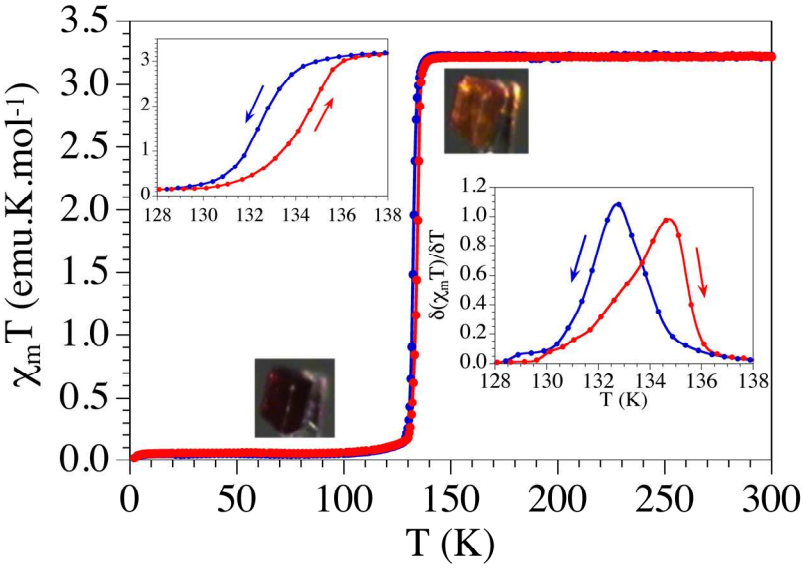

Figure 5. Thermal variation of the $\chi_m T$ product in **2** in the cooling (blue) and warming (red) scans. Left inset shows a zoom of the transition. Right inset shows the thermal variation of the derivative of $\chi_m T$.

The thermal variation of the average values of the six Fe-N distances observed for **1**-**2** at room and low temperatures (2.142(3) and 2.035(2) Å for **1**; and 2.178(3) and 1.990(2) Å for **2,** at 293 K and 120 K, respectively) reveals strong modifications of the iron coordination spheres in both compounds. For compound **2**, the averaged values observed at 293 K and 120 K are in the range of those expected for the *HS* (~ 2.2 Å) and the *LS* (~ 2.0 Å) states of the Fe(II) ion, in complete agreement with the corresponding magnetic data aforementioned for this compound. Conversely, the averaged Fe-N value observed at room temperature for **1** (2.142(3) Å) is lower than the value expected for 100 % *HS* state of the Fe(II) ions (~ 2.2 Å), and so in agreement with the presence, at room temperature, of a remaining *LS* fraction of Fe(II) ions of *ca.* 19 %, and very close to the corresponding value calculated with the magnetic data (*ca.* 20 %). At low temperature (120 K), the averaged Fe-N value for **1** (2.035(2) Å) is significantly higher than the one expected for a complete magnetic transition (~ 2.0 Å). The latter value suggests the presence of a *HS* fraction of *ca.* 17 %, again very close to the corresponding value resulting from the analysis of the magnetic data (15 %) of **1**.

For both compounds, the trigonal distortion parameters Σ and Θ are significantly reduced from room to low temperatures (for **1**, Σ decreases from 67° to 55° and Θ from 207°

to 154° at 293 and 120 K, respectively; while for **2**, Σ is reduced from 71° to 54° and Θ from 233° to 144° at 293 K and 120 K, respectively). Owing to the more regular FeN_6 octahedral geometry in the *LS* state, those observations are in line with the presence of a *SCO* transition from *HS* to *LS* in both compounds. Furthermore, the variations of the Σ and Θ parameters are significantly stronger in **2** (17º and 89º, respectively) than in **1** (12º and 53º, respectively), suggesting that the transition is more complete in **2** than in **1**which is in agreement with both magnetic measurements and Fe-N bond lengths arguments. It is also worth to indicate that the modifications of the iron coordination spheres in the two compounds affect more significantly the Fe-N3 bonds running along the chain direction (For **1**: 2.133(3) and 2.011(2) Å at 293 K and 120 K respectively, Δ(Fe-N) = 0.122 Å; for **2**: 2.157(3) and 1.949(2) Å at 293 K and 120 K respectively, Δ(Fe-N) = 0.208 Å). Interestingly, the significant decrease of the Fe-N3 bond lengths, from room to low temperature, does not affect strongly the shortest Fe…Fe distance along the polymeric chain (Fe-(NC-M-CN)-Fe: 9.7282(5) and 9.6117(5) Å for **1** and 9.9073(3) and 9.8107(3) Å for **2**, at 293 K and 120 K, respectively). This result is due to the increase of the Fe-N3-C10 bond angles from room to low temperature (from 145.6(3)º to 151.5(2)° in **1** and from 142.0(3)º to 156.2(2)° in **2**, at 293 K and 120 K, respectively), that partially compensate the strong decrease of the Fe-N3 bond lengths and mitigate its effect on the Fe…Fe distances along the molecular chain.

In order to clearly establish how the crystal and the lattice parameters were affected by the magnetic transition, we have performed the temperature dependence of the lattice parameters of a single crystal of **2** in the range 293-100 K. As can be seen in figures 5-6, the *a*, *b, c* and β unit cell parameters, as well as the unit cell volume (*V*) show abrupt decreases at the same temperature than the one obtained from the magnetic data, *i.e.* 132 K. This behaviour is typical of *SCO* transitions and, together with the abrupt colour change in the single crystal also observed at *ca.* 132 K (figures 5-7), confirms the presence of a SCO transition at *ca.* 132 K. The *a*, *c* and β unit cell parameters remain relatively constant and do not reveal any significant decrease in the temperature range 293-132 K *i.e.* before the SCO transition. However, the unit cell volume and the *b* parameter exhibit nearly similar gradual decreases, in the temperature range 293-132 K. According to the magnetic data (figure 5), those structural data clearly demonstrate that the single crystal of **2** contracts anisotropically on cooling, since the more significant changes occur essentially along the *b* axis. Additionally, this anisotropic contraction is confirmed by the thermal evolution, on cooling,

of the hydrogen bonds (N2…N4$^{(b)}$: 3.123(4) and 3.069(3) for **1**; 3.132(4) and 3.059(4) for **2**, at 293 K and 120 K, respectively) running along the *b* axis (table 3).

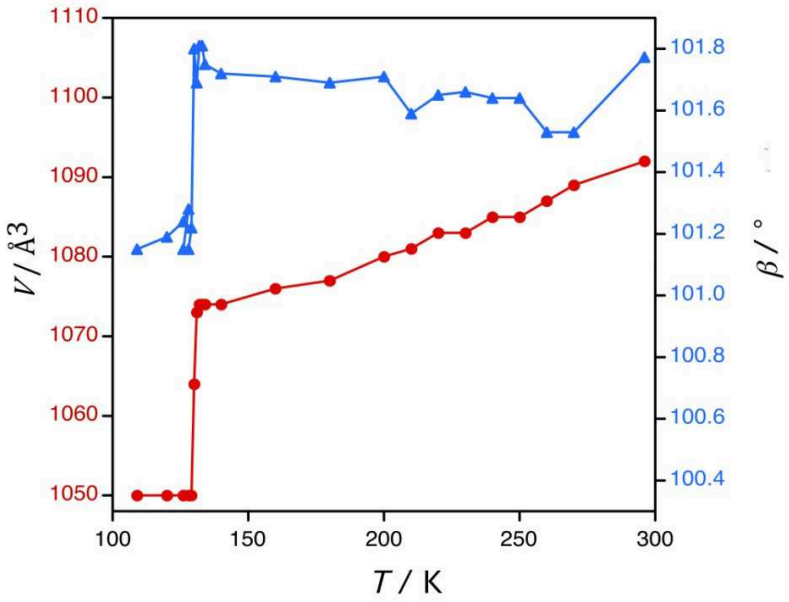

Figure 6. Thermal variation of the unit cell volume (•) and the angular β (▲) parameter in **2** (the blue and red lines are indicated simply to guide the eye).

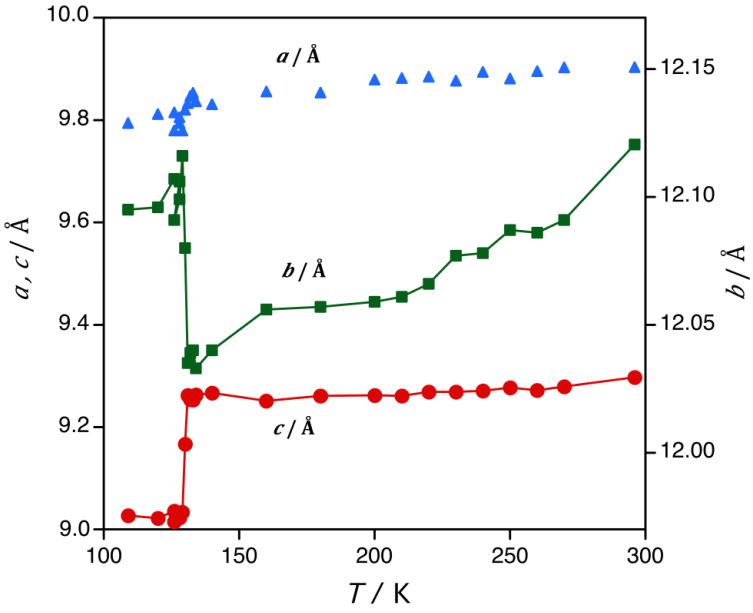

Figure 7. Thermal variations of the lattice parameters of compound **2**; *a* (▲), *b* (■) and *c* (•) parameters revealing the abrupt SCO transition, the transition temperature and the anisotropic contraction of the crystal (the green and red lines are indicated simply to guide the eye).

■ CONCLUSIONS

In summary, we have reported here the syntheses, the structural characterizations at high and low temperature, the temperature dependence of the lattice parameters and the magnetic properties of the two isostructural *SCO* Fe(II) molecular neutral chain $[Fe(aqin)_2(M(CN)_4)]$ (M = Ni^{II}(**1**) and Pt^{II} (**2**)). The molecular chain structure of both compounds is generated by the $[M(CN)_4)]^{2-}$ moiety acting as a μ_2-bridging ligand *via* two nitrogen atoms from two trans cyano groups. The X-ray diffraction studies, in the range 293-120 K, show strong modifications of the iron coordination spheres, in agreement with the presence of a *SCO* transition in compounds **1**-**2**; also clearly confirmed by the thermal variation of the $\chi_m T$ product. Additionally and in parallel with the thermal evolution of the interchain hydrogen bonding, the thermal dependence of the lattice parameters reveals that the single crystal of **2** contracts anisotropically on cooling, since the more significant changes occur essentially along the *b* axis. From a synthetic point of view, this study confirms the ability of the polycyanometallate anions to generate novel *SCO* complexes exhibiting original extended arrangements. An additional advantage of the use of such anions resides in their structural similarity with their parent analogues, such as the paramagnetic hexacyanometallate anions. Thus, besides their high ability to coordinate and bridge transition metal ions, these paramagnetic anions can transmit magnetic coupling between the metal active centers. Accordingly, attempts to prepare multidimensional bimetallic architectures combining *SCO* behavior and magnetic interactions using such magnetic polybridging anions are underway.

■ ASSOCIATED CONTENT

Supporting information

Crystallographic data have been deposited in the Cambridge Crystallographic Data Centre under the CCDC numbers **(**938438 and 931126 for **1** at 293 K and 120 K, respectively; 924207 and 924208 for **2** at 293 K and 120 K, respectively) that contains the supplementary crystallographic data for the two compounds. These data can be obtained free of charge *via* the web application at www.ccdc.cam.ac.uk/conts/retrieving.html [or from the Cambridge Crystallographic Data Center, 12 Union Road, Cambridge CB2 1EZ, UK: Fax: (internt.) + 44-1223-336-033; E-mail: deposit@ccdc.cam.ac.uk].

■ AUTHOR INFORMATION

Corresponding author

*E-mail: smail.triki@univ-brest.fr. Phone: +33 298 016 146, Fax: +33 298 017 001

Notes

The authors declare no competing financial interest.

■ ACKNOWLEDGMENTS

The authors acknowledge the CNRS ("Centre National de la Recherche Scientifique"), the Brest University, the french "Ministère de la Recherche" and "Ministère des Affaires Etrangères et Européennes" (PHC Maghreb project **N° 30255ZJ)**, the "Agence Nationale de la Recherche" (ANR project BISTA-MAT: ANR-12-BS07-0030-01), the "Spanish Ministerio de Economía y Competitividad" (Project CTQ2011-26507), and the "Generalitat Valenciana" (projects Prometeo 2009/095 and ISIC).

■ REFERENCES

(1) Eds. Gütlich, P.; Goodwin, H. A., Spin Crossover in Transition Metal Compounds I-III, *Top. Curr. Chem.*, Springer Verlag, Berlin-Heidelberg-New York, **2004**, vol. *233-235.*

(2) Gamez, P.; Costa, J. S.; Quesada,M.; Aromí, G., *Dalton Trans*. **2009**, 7845-7853, and references therein.

(3) Létard, J.-F.; Guionneau, P.; Goux-Capes, L., *Top. Curr. Chem.* **2004**, *235*, 221-249.

(4) Cobo, S.; Molnár, G.; Real, J. A.; Bousseksou, A., *Angew. Chem. Int. Ed.* **2006**, *45*, 5786-5789.

(5) Olguin, J.; Brooker, S., *Coord. Chem. Rev.* **2011**, *255*, 203-240.

(6) Halcrow, M. A., *Chem. Soc. Rev.* **2011**, *40*, 4119-4142.

(7) Prins, F.; Monrabal-Capilla, M.; Osorio, E. A.; Coronado, E.; J. van der Zant, H. S., *Adv. Mater.* **2011**, *23*, 1545-1549.

(8) Muñoz-Lara, F. J.; Arcís-Castillo, Z.; Muñoz, M.-C.; Rodríguez-Velamazán, J.-A.; Gaspar, A.-B.; Real, J.-A., *Inorg. Chem.* **2012**, *51*, 11126-11132.

(9) Gütlich, P; Gaspar, A.-B.; Garcia, Y., *Beilstein J. Org. Chem.* **2013**, *9*, 342–391

(10) Decurtins, S.; Gütlich, P.; Köhler, C. P.; Spiering, H.; Hauser, A., *Chem. Phys. Lett.* **1984**, *105*, 1-4.

(11) Létard, J.-F., *J. Mater. Chem.* **2006**, *16*, 2550–2559.

(12) Rodríguez-Velamazán, J.A.; Castro, M.; Palacios, E.; Burriel, R.; Kitazawa, T.; Kawasaki, T., *J. Phys. Chem. B* **2007**, *111*, 1256-1261; Niel, V.; Muñoz, M. C.; Gaspar,

A. B.; Galet, A.; Levchenko, G.; Real, J. A., *Chem. Eur. J.* **2002**, *8*, 2446-2453; Kosone, T.; Kanadani, C.; Saito, T.; Kitazawa, T., *Polyhedron* **2009**, *28*, 1991–1995

(13) Garcia, Y.; Gütlich, P., *Top. Curr. Chem.* **2004**, *234*,49-62.

(14) Morgan, G. G.; Murnaghan, K. D.; Müller-Bunz, H.; McKee, V.; Harding, C. J., *Angew. Chem. Int. Ed.* **2006**, *45*, 7192–7195.

(15) Sim, P. G.; Sinn, E., *J. Am. Chem. Soc.* **1981**, *103*, 241–243.

(16) Halepoto, D. M.; Holt, D. G. L.; Larkworthy, L. F.; Leigh, G. L.; Povey, D. C.; Smith, G .W., *J. Chem. Soc. Chem. Commun.* **1989**, 1322–1323.

(17) van Konigsbruggen, P. J.; Maeda, Y.; Oshio, H., *Top. Curr. Chem.* **2004**, *233*, 259–324.

(18) Costes, J.-P.; Dahan, F.; Laurent, J.-P., *Inorg. Chem.* **1990**, *29*, 2448–2452.

(19) Ishikawa, R.; Matsumoto, K.; Onishi, K.; Kubo, T.; Fuyuhiro, A.; Hayami, S.; Inoue, K.; Kaizaki, S.; Kawata, S., *Chem. Lett.* **2009**, *38*, 620-621.

(20) Hayami, S.; Moriyama, R.; Shigeyoshi, Y.; Kawajiri, R.; Mitani, T.; Akita, M.; Inoue, K.; Maeda, Y., *Inorg. Chem.,* **2005**, *44*, 7295-7297.

(21) Galet, A.; Gaspar, A. B.; Muñoz, M. C.; Levchenko, G.; Real, J. A., *Inorg. Chem.* **2006**, *45*, 9670-9679.

(22) Dupouy, G.; Marchivie, M.; Triki, S.; Sala-Pala, J.; Salaün, J.-Y.; Gómez-García, C. J.; Guionneau, P., *Inorg. Chem.* **2008**, *47*, 8921-8931.

(23) Sheu, C.-F.; Pillet, S.; Lin, Y.-C.; Chen, S.-M.; Hsu, I.-J.; Lecomte, C.; Wang, Y.; *Inorg. Chem.* **2008**, *47*, 10866–10874.

(24) El Hajj, F.; Sebki, G.; Patinec, V.; Marchivie, M.; Triki, S.; Handel, H.; Yefsah, S.; Tripier, R.; Gómez-García, C. J.; Coronado, E., *Inorg. Chem.* **2009**, *48*, 10416-10423.

(25) Weber, B.; Bauer, W.; Obel, J., *Angew. Chem. Int. Ed.* **2008**, *47*, 10098–10101.

(26) Weber, B.; Kaps, E.; Weigand, J.; Carbonera, C.; Létard , J.-F.; Achterhold, K.; Parak, F.-G.; *Inorg. Chem.* **2008**, *47*, 487–496.

(27) Reger, D. L.; Gardinier, J. R.; Elgin, J. D.; Smith, M. D.; Hautot, D.; Long, G. J.; Grandjean, F., *Inorg. Chem.* **2006**, *45*, 8862-8875.

(28) Weber, B.; Jäger, E.-G., *Eur. J. Inorg. Chem.* **2009**, 465-477.

(29) Haasnoot, J. G.; Vos, J. G.; Groeneveld, W. L., *Z. Naturforsch. B* **1977**, *32*, 1421-1430.

(30) Garcia, Y.; van Koningsbruggen, P. J.; Lapouyade, P.; Rabardel, L.; Khan, O.; Wierczorek, M.; Bronisz, R.; Ciunik, Z.; Rudolf, M. F., *C. R. Acad. Sci. Paris IIc* **1998**, *1*, 523; Kahn, O.; Martinez, C. J., *Science* **1998**, *279*, 44-48; Dîrtu, M. M.; Schmit, F.; Naik, A. D.; Rotaru, A.; Marchand-Brynaert, J.; Garcia, Y., *Int. J. Mol. Sci.* **2011**, *12*, 5339-5351.

(31) Garcia, Y.; Kahn, O.; Rabardel, L.; Chansou, B.; Salmon, L.; Tuchagues, J.-P., *Inorg. Chem.* **1999**, *38*, 4663-4670. R. Bronisz, *Inorg. Chem.* **2005**, *44,* 4463.

(32) Genre, C.; Jeanneau, E.; Bousseksou, A.; Luneau, D.; Borshch S. A.; Matouzenko, G. S., *Chem. Eur. J.* **2008**, *14*, 697-705; Matouzenko, G. S.; Jeanneau, E.; D. Luneau, *New J. Chem.* **2006**, *30*, 1669-1674.

(33) Moliner, N.; Muñoz, M. C.; Létard, S.; Salmon, L.; Tuchagues, J.-P.; Bousseksou, A.; Real, J. A., *Inorg. Chem.* **2002**, *41*, 6997-7005; G. S. Matouzenko, M. Perrin, B. Le Guennic, C. Genre, G. Molnár, A. Bousseksou, S. A. Borshch, *Dalton Trans.* **2007**, 934; Genre, C.; Matouzenko, G. S.; Molnár, G.; Bréfuel, N.; Perrin, M.; Bousseksou, A.; Borshch, S. A., *Chem. Mater.* **2003**, *15*, 550-556.

(34) Real, J. A.; Gaspar, A. B.; Niel, V.; Muñoz, M. C., *Coord. Chem. Rev.* **2003**, *236*, 121-141; Garcia, Y.; Niel, V.; Muñoz, M. C.; Real, J. A., *Top. Curr. Chem.* **2004**, ***233***, 229-257.

(35) Murray, K. S.; Kepert, C. J., *Top. Curr. Chem.* **2004**, ***233***, 195-228.

(36) Benmansour, S.; Atmani, C.; Setifi, F.; Triki, S.; Marchivie, M.; Gómez-García, C. J.; *Coord. Chem. Rev.* **2010**, *254*, 1468-1478.

(37) a) Dupouy, G.; Marchivie, M.; Triki, S.; Sala-Pala, J.; Gomez-Garcia, C. J.; Pillet, S.; Lecomte, C.; Létard, J.-F., *Chem. Commun.* **2009**, 3404-3406; b) Dupouy, G.; Triki, S.; Marchivie, M.; Cosquer, N.; Gómez-García, C. J.; Pillet, S.; Bendeif, E.-E.; Lecomte, C.; Asthana, S.; Létard, J.-F., *Inorg. Chem*. **2010**, *49*, 9358-9368.

(38) Setifi, F.; Charles, C.; Houille, S.; Thétiot, F.; Triki, S.; Gómez-García, C. J.; Pillet. P., *Polyhedron* **2013,** *61*, 242–247.

(39) Malassa, A.;Görls, H.; Buchholz, A.; Plass, W.; Westerhausen, M., *Z. Anorg. Allg. Chem.* **2006**, *632*, 2355-2362.

(40) Kitazawa, T.; Gomi, Y.; Takahashi, M.; Takeda, M.; Enomoto, M.; Miyazaki, A.; Enoki, T., *J. Mater. Chem.* **1996**, *6*, 119-121; Niel, V.; Martinez-Agudo, J. M.; Muñoz, M. C.; Gaspar, A. B.; Real, J. A., *Inorg. Chem.* **2001**, *40*, 3838-3839; Molnar, G.; Niel, V.; Gaspar, A. B.; Real, J. A.; Zwick, A.; Bousseksou, A.; McGarvey, J. J., *J. Phys. Chem. B* **2002**, *106*, 9701-9707.

(41) *CRYSALIS-CCD 170*, Oxford-Diffraction, **2002**; *CRYSALIS-RED 170*, Oxford-Diffraction, **2002**.

(42) Sheldrick, M., SHELX97, *Program for Crystal Structure Analysis*, University of Gottingen, Gottingen, Germany, **1997**.

(43) Farrugia, L.J., *J. Appl. Crystallogr.* **1999**, *32*, 837-838.

(44) Bain, G. A.; Berry J. F., *J. Chem. Educ.* **2008***, 85*, 532-536.

(45) Infrared data (cm^{-1}). $K_2[Ni(CN)_4].xH_2O$: 3640(br), 3565(br), 3546(w), 2120(s), 2084(s), 1621(m), 1599(s), 1381(w); $K_2[Pt(CN)_4].xH_2O$ (cm^{-1}): 3593(br), 3544(br), 3469(w), 2165(s), 2133(s), 2121(s), 1654(w), 1616(s), 502(m).

(46) Guionneau, P.; Brigouleix, C.; Barrans, Y.; Goeta, A. E.; Létard, J.-F.; Howard, J. A. K.; Gaultier, J.; Chasseau, D., *C.R. Acad. Sci., Ser. IIc: Chim.* **2001**, *4*, 161-171.

(47) Marchivie, M.; Guionneau, P.; Létard, J.-F.; Chasseau, D., *Acta Cryst. B* **2003**, *59*, 479-486.

(48) W. Wong-Ng, J. T. Culp, Y. S. Chen, P. Zavalij, L. Espinal, D. W. Siderius, A. J. Allen, S. Scheins, C. Matranga, *CrystEngComm***, 2013**, **15**, 4684-4693; b) Tao, B.; Xia, H.; Jiang, X.; Zhu, Y. F.*, Russ. J. Coord. Chem.* **2011**, *37*, 367-370.

(49) Loosli, A; Wermuth, M; Güdel, H.U.; Capelli, S.; Hauser, J.; Bürgi, H.B., *Inorg Chem.* **2000**, *39*, 2289-2293; Mühle, C.; Nuss, J.; Jansen, M., *Z. Kristallogr.* **2009**, *224*, 9-10.

(50) L. J. Farrugia, J. Appl. Cryst. 30 (1997) 565; L. J. Farrugia, *J. Appl. Cryst.* 45 **2012** 849-854.

(51) Zueva, E. M.; Ryabikh, E. R.; Kuznetsov, A. M.; Borshch, S. A., *Inorg Chem*. **2011**, *50*, 1905-1913.

2. Synthèse, structure et caractérisation magnétique du complexe $[Fe(aqin)_2(\mu_2\text{-}Pd(CN)_4)]$

2.1. Synthèse et caractérisation infrarouge

Les monocristaux ont été obtenus par la même méthode que pour les 2 autres complexes $[Fe(aqin)_2(\mu_2\text{-}M(CN)_4)]$ avec M=Ni,Pt. La synthèse détaillée des monocristaux et de la poudre est détaillée dans la partie expérimentale. Le spectre infra-rouge de ce complexe a été enregistré sur des cristaux broyés. Les bandes d'absorption en Infra-Rouge pour ce complexe sont regroupées dans le tableau III.1 dans lequel sont également rappelés les spectres des deux précédents complexes en cm^{-1}.

Tableau III.1 Spectres Infra-Rouge des composés 1, 2 et 3 et $K_2[Pd(CN)_4^{2-}]$

$[Fe(aqin)_2(\mu_2\text{-}Ni(CN)_4)]$ (1)		$[Fe(aqin)_2(\mu_2\text{-}Pt(CN)_4)]$ (2)		$[Fe(aqin)_2(\mu_2\text{-}Pd(CN)_4)]$ (3)		$K_2[Pd(CN)_4]$
3278(m)	3183(m)	3283(m)	3181(m)	3283(m)	3181(m)	3644(br)
3131(m)		3130(m)		3129(m)		3566 (br)
2140(s)	2120(s)	2146(s)	2131(s)	2150(s)	2133(s)	2133(s)
1626(m)	1579(s)	1625(m)	1578(m)	1624(m)	1577(s)	1618(m)
1503(s)	1471(m)	1502(s)	1470(m)	1502(s)	1470(m)	1599(s)
1424(w)	1400(m)	1397(w)	1372(w)	1397(w)	1373(w)	424(w)
1375(m)	1320(m)	1319(m)	1133(w)	1319(m)	1223(w)	
1223(w)	1203(w)	1099(w)	1069(m)	1172(w)	1133(m)	
1173(w)	1134(m)	1050(s)	1024(s)	1098(w)	1068(m)	
1103(m)	1071(m)	827(s)	789(s)	1049(s)	1023(s)	
1053(m)	1026(s)	772(s)	714(m)	827(s)	789(s)	
826(s)	789(s)	631(m)	581(m)	773(m)	714(m)	
772(s)	717(m)	555(m)	525(m)	631(m)	580(m)	
633(m)	602(w)	498(m)	470(m)	555(m)	525(m)	
583(w)	581(m)			487(m)	425(m)	
555(w)	524(w)					
436(s)	420(s)					

Le spectre infra-rouge du composé 3 montre les deux bandes $\nu_{(CN)}$ 2150(s), 2133(s) caractéristiques de deux types de groupement nitrile: l'un terminal non coordiné (2133 cm^{-1}) également présent dans le spectre IR de $K_2[Pd(CN)_4]$ et l'autre pontant (2150 cm^{-1}) coordiné au fer en accord avec la structure.

2.2. Caractérisation structurale et propriétés magnétiques

Ce complexe cristallise dans le même groupe d'espace $P_{2_1/c}$ du système monoclinique que les deux autres complexes. Ces trois complexes sont isostructuraux avec des paramètres de maille similaires (Tableau III.2). L'ion fer(II) est au centre d'un octaèdre déformé, les quatre atomes d'azote de l'aminoquinoline se trouvent en position équatoriale et deux atomes d'azote provenant de $[Pd(CN)_4]^{2-}$ sont situés en position axiale. La moyenne des six longueurs de liaison Fe-N à 120 K est de 1,985 Å (BS) et 2,174 Å (HS) à 293 K.

L'arrangement monodimensionnel se présente sous la forme d'une chaîne comme pour les systèmes $[Fe(aqin)_2(\mu_2\text{-}M(CN)_4)]$ (M=Ni, Pt). Le caractère pontant (μ_2) de l'anion est caractérisé par deux groupements nitrile situés en *trans* sur le palladium qui sont reliés à deux centres métalliques Fe^{II}. L'ion fer se trouve au centre d'un pseudo-octaèdre constitué des quatres atomes d'azote des deux ligands aqin en position équatoriale et deux atomes d'azote provenant des groupements $[Pd(CN)_4]^{2-}$ en positions axiales.

Tableau III.2 Paramètres structuraux et résultats des affinements pour [Fe(aqin)$_2$(μ_2-M(CN)$_4$)]; M = Ni^{II} (**1**), Pt^{II} (**2**) et Pd^{II}(**3**).

	1		**2**		**3**	
Temperature/K	293(2)	120(2)	293(2)	120(2)	293(2)	120(2)
Empirical formula	$C_{22}H_{16}N_8FeNi$		$C_{22}H_{16}N_8FePt$		$C_{22}H_{16}N_8FePd$	
Formula weight	506.99		643.37		554,68	
Wavelength / Å	0.71073		0.71073 Å		0.71073 Å	
Crystal system	Monoclinic		Monoclinic		Monoclinic	
Space group	$P2_1/c$		$P2_1/c$		$P2_1/c$	
a / Å	9.1819(6)	9.0033(5)	9.3073(3)	9.0290(2)	9,3058(5)	9.0454(3)
b / Å	12.0719(7)	12.0053(6)	12.1228(4)	12.0904(3)	12,0844(6)	12.0676(3)
c / Å	9.7282(5)	9.6117(5)	9.9073(3)	9.8107(3)	9,928(4)	9.8133)
β /°	100.258(6)	100.043(6)	101.670(4)	101.124(3)	101,321(5)	101.124(3)
Volume / Å^3	1061.07(11)	1022.98(9)	1094.74(6)	1050.86(5)	1094,16(9)	1051,84(5)
Z	2	2	2	2	2	2
D_{calc} / g.cm^{-3}	1.587	1.646	1.952	2.033	1,684	1,751
Abs. coef. / mm^{-1}	1.598	1.658	7.072	7.367	1,512	1,572
F(000)	516	516	616	616	552	552
Crystal size / mm^3	0.16x0.08x0.05	0.13x0.11x0.04	0.16x0.15x0.08	0.16x0.15x0.08	0.09x0.12x0.22	0.09x0.12x0.22
2θ range / °	6.56-63.30	6.66-60.00	6.42 – 60.00	6.56-60.00	6.42 – 60.00	6.56-60.00
Refl. collected	10548	7201	10604	10188	10522	10154
Unique refl. / Rint	3324 / 0.0785	2884 / 0.0340	3174 / 0.0330	3057 / 0.0230	3170/0,0505	3059 / 0.0320
Data / restr. / N_v	1273 / 0 / 148	1571 / 0 / 148	2017 / 0 / 148	2094 / 0 / 148	3170/0/148	3059 / 0 / 148
[b]R1/[c] wR2	0.0423 /0.0732	0.0385 /0.0984	0.0226 /0.0494	0.0186 /0.0480	000362/0,0650	0.0280 /0.0595
[d]GooF	0.906	0.910	0.973	1.125	0,936	0,977
$\Delta\rho_{max/\ min}$ (eÅ^{-3})	+0.543 / -0.376	+1.319 / -0.337	+0.890 / -0.351	+1.371 / -0.442	+0,503 / -0,390	+0,647 / -0.346

[a]The asymmetric unit contains 0.5 of the chemical formula.

[b]$R1 = \sum|F_o-F_c|/F_o$.

[c]$wR2 = \{\Sigma[w(F_o^2-F_c^2)^2]/\ \Sigma[w(F_o^2)^2]\}^{1/2}$

[d]$GooF = \{\Sigma[w(F_o^2-F_c^2)^2]/\ (N_{obs}-N_{var})\}^{1/2}$

Tableau III.3 Longueurs (Å) et angles de liaison(°) pour [Fe(aqin)$_2$(μ_2-M(CN)$_4$)]; M = Ni^{II} (**1**), Pt^{II} (**2**) et Pd^{II}(**3**).

Compound	**1** (M =Ni^{II})		**2** (M =Pt^{II})		**3** (M =Pd^{II})	
T / K	293	120	293	120	293	120
Fe-N1	2.131(3)	2.022(2)	2.170(3)	1.989(2)	2,168(2)	1.986(17)
Fe-N2	2.161(3)	2.071(2)	2.206(3)	2.031(2)	2,197(2)	2.027(17)
Fe-N3	2.133(3)	2.011(2)	2.157(3)	1.949(2)	2,158 (2)	1.943(17)
<Fe-N>	2.142(3)	2.035(2)	2.178(3)	1.990(2)	2,174(2)	1.985(2)
N1-Fe-N3	87.41(10)	87.67(10)	87.68(11)	87.46(10)	87,55(9)	87.57(7)
N1-Fe-N3$^{(i)}$	92.59(10)	92.33(10)	92.32(11)	92.54(10)	92,45(9)	92.43(7)
N1-Fe-N2	78.88(10)	82.22(9)	77.48(10)	83.02(10)	71,36(8)	83.12(7)
N1-Fe-N2$^{(i)}$	101.12(10)	97.78(9)	102.52(10)	96.98(10)	102,64(8)	96.88(7)
N2-Fe-N3	93.14(9)	93.68(9)	92.85(10)	93.98(10)	92,86(8)	93.97(7)
N2-Fe-N3$^{(i)}$	86.86(9)	86.32(9)	87.15(10)	86.02(10)	87,14(2)	86.03(7)

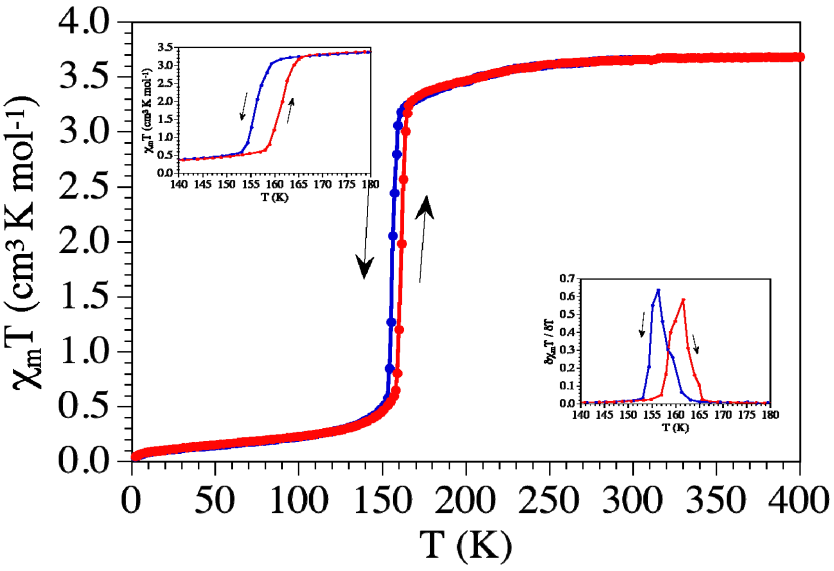

Figure III.8 Variation du produit $\chi_m T$ en fonction de la température pour le complexe [Fe(aqin)$_2$(μ_2-Pd(CN)$_4$)].

Le produit de la susceptibilité magnétique par la température $\chi_m T$ en fonction de la température a une valeur proche de 3,30 emu.K.mol^{-1}. Cette valeur correspond à la valeur attendue pour l'ion fe(II) dans un environnement octaédrique à l'état HS (S=2) avec g≈2,1. Quand on abaisse la température, le produit $\chi_m T$ reste constant jusqu'à la température de 156 K puis une baisse brutale de $\chi_m T$ est observée donnant lieu une transition de spin abrupte de l'état HS vers l'état BS. Ces mesures confirment le thermochromisme des cristaux qui passent de la couleur orange à rouge à la température de 158 K. En dessous de 120 K, la valeur de $\chi_m T$ est proche de 0 cm^3.K.mol^{-1} , ce qui montre que la transition est complète contrairement à ce qui avait été observé avec le composé **1** [Fe(aqin)$_2$(μ_2-Ni(CN)$_4$)]. En augmentant la température, on observe une hystérésis d'une largeur de 4 K centrée sur la $T_{1/2}$=160 K, caractérisée par $T_{1/2}\nearrow$=162 K et $T_{1/2}\searrow$=158 K. La coopérativité observée est en accord avec les contacts intermoléculaires (π stacking et liaisons hydrogène) présents dans ce système. La $T_{1/2}$ du système palladié est supérieure de 27 K à celle du composé 2 avec le Pt. Plus le métal central du ligand anionique est petit, plus l'état de plus faible volume est stabilisé ce qui explique la $T_{1/2}$ plus élevée. Ici, l'atome de Pd (Z=46) est plus petit que celui du Pt (Z=78), l'état BS est donc stabilisé pour le composé du Pd qui présente une $T_{1/2}$ plus élevée.

Conclusion

Dans ce chapitre, nous avons décrit une chaîne de type [Fe(aqin)$_2$(μ_2-M(CN)$_4$)] basée sur un complexe du fer (II), un ligand 8-aminoquinoline (aqin) et un co-ligand anionique pontant et rigide $[M(CN)_4]^{2-}$. Les trois dérivés avec M=Ni, Pd et Pt ont été caractérisés par diffraction de rayons X sur monocristal à la température ambiante et à 120 K. Ils sont iso-structuraux, et leur structure peut être décrite comme une chaîne générée par le mode de coordination pontant de l'anion tétracyanométallate. L'examen des sphères de coordination dans les trois dérivés révèle dans chaque cas la présence d'une transition de spin. Pour mieux étudier ces transitions, nous avons réalisé des études magnétiques. La caractérisation de ces chaînes pour M=Ni, Pd, Pt montrent une transition abrupte complète avec une légère hystérésis, contrairement au complexe similaire à base de $[Ni(CN)_4]^{2-}$. Ce dernier présentait une transition de spin incomplète attribuée à des lacunes au sein de la chaîne et/ou à une isomérie portant sur le mode de coordination des fonctions nitrile. La substitution de Ni par Pd ou Pt entraîne une disparition des lacunes et/ou de l'isomérie. Nous avons également mis en évidence dans les transitions complètes une diminution de la $T_{1/2}$ avec l'augmentation de la taille du métal (Pd,Pt), en accord avec les données de la littérature[5]. Enfin, l'étude des paramètres cristallographiques en fonction de la température nous a permis de montrer que, dans ce système, le π-stacking était l'interaction prépondérante devant les liaisons hydrogène pour expliquer la coopérativité observée. Les anions $[M(CN)_4]^{2-}$ en particulier l'anion $[Pt(CN)_4]^{2-}$, sont des co-ligands de choix pour concevoir de nouveaux systèmes polymériques commutables. Dans le dernier chapitre, nous verrons donc la conception d'un nouveau système bi-dimensionnel à base de $[Pt(CN)_4]^{2-}$.

[5] Garcia, Y., Niel, V., Munoz, M. C., Real, J. A. *Top. Curr. Chem*, Spin Crossover in Transition Metal Compounds I, Spinger-Verlag, Berlin, **2004**, 233, 229-257

Partie expérimentale

Synthèse des complexes $[Fe(aqin)_2(\mu_2\text{-}M(CN)_4)]$ (M = Ni^{II} (1), Pd^{II}(2) et Pt^{II} (3))

Poudre $[Fe(aqin)_2(\mu_2\text{-}M(CN)_4)]$ (M = Ni^{II} (1), Pd^{II}(2) et Pt^{II} (3))

Réaction : 72,08 mg (0,5 mmol) de 8-aminoquinoline est dissout dans 5 mL d'éthanol. Cette solution est ajoutée goutte à goutte, à température ambiante, sous agitation, à 10 mL d'une solution aqueuse de $Fe(BF_4)_2,6H_2O$ (0,25 mmol, 84,39 mg). On maintient l'agitation pendant 15 minutes. On y ajoute ensuite goutte à goutte 10 mL d'une solution aqueuse de tétracyanométallate de potassium $K_2[M(CN)_4]$. (M= Ni^{II} 0,25mmol, 60,25 mg; M=Pd^{II} 0,25 mmol, 72,17 mg; Pt^{II} 0,25mmol, 94,34 mg). Le précipité orange est filtré, lavé à l'eau froide et éthanol, puis séché.

Rendement: 92,6 mg, 73% pour (1), 102,6 mg, 74% pour (2) et 122,8 mg, 77% pour (3).
Composé (2) : Formule brute $C_{22}H_{16}FeN_8Pd$

Monocristaux $[Fe(aqin)_2(\mu_2\text{-}M(CN)_4)]$ (M = Ni^{II} (1), Pd^{II}(2) et Pt^{II} (3))

Les monoscristaux (1), (2) et (3) ont été obtenus par diffusion lente dans un xerogel dans un tube à essai. Le gel est préparé en ajoutant, sous agitation, à 9 mL d'une solution aqueuse de tétracyanométallate de potassium $K_2[M(CN)_4]$ (M= Ni^{II}: 0,45 mmol, 108,4 mg; M=Pd^{II}: 0,45 mmol, 129,9 mg; Pt^{II} 0,45 mmol, 94,34 mg), 1mL de tétraméthoxysilane (TMOS). Le gel se forme en laissant reposer la solution 6h. Puis, on prépare 6mL de solution aqueuse «Fer-ligand»: $Fe(SO_4).7H_2O$ (0,15 mmol, 41,7 mg) et amq (0,33 mmol, 47,6 mg). On dégaze la solution en faisant buller du diazote 15 minutes puis on ajoute les 6 mL délicatement à l'abri de la lumière au-dessus des gels respectifs. Des monocristaux sont isolés au bout de deux semaines.

Chapitre IV

Réseaux bi- et tri-dimensionnels

Introduction

Parmi tous les systèmes à transition de spin, les systèmes à base de triazole sont les plus étudiés. En effet, les complexes obtenus forment des chaînes présentant de larges hystérésis autour de la température ambiante. Le complexe $[Fe(Htrz)_2(trz)](BF_4)$ (trz^- = 1,2,4-triazolate anion)[6,7] est un exemple particulièrement connu. Bien que très étudié, le premier système à base de triazole montrant des propriétés photo-magnétiques n'a cependant été décrit que très récemment[8].

Afin de concevoir de nouveaux systèmes bistables, nous avons cherché à accroître la denticité du triazole pour obtenir des réseaux 2D ou 3D en utilisant le ligand trz-py dont la synthèse avait déjà été décrite[9]. L'idée est d'associer ce ligand neutre aux co-ligands anioniques pontants $(tcpd)^{2-}$ et $[Pt(CN)_4]^{2-}$ pour favoriser la formation de réseaux 3D.

Dans une première partie, nous étudierons le système $[Fe(trz\text{-}py)(tcpd)(H_2O)]$ obtenu avec le co-ligand $(tcpd)^{2-}$. La synthèse, la caractérisation et les propriétés magnétiques du réseau 3D obtenu seront développées.

Dans une seconde partie, nous étudierons le réseau 2D à base de l'anion $[Pt(CN)_4]^{2-}$. Ce dérivé, $[Fe(trz\text{-}py)_2(Pt(CN)_4)].3H_2O$, peut être considéré comme de type clathrate d'Hofmann. Le premier réseau d'Hofmann à partir de ligand dérivé du triazole est très récent et a été décrit en 2014[10] . Le dérivé, $[Fe(trz\text{-}py)_2(Pt(CN)_4)].3H_2O$ a montré des propriétés magnétiques et photo-magnétiques originales (effet LIESST, Reverse LIESST, LITH). Ces propriétés se distinguent par la présence d'une hystérésis cachée révélée par photo-irradiation. Les études structurales en fonction de la température et en fonction de la photoexcitation, et les études photomagnétiques approfondies seront détaillées dans la seconde partie de ce chapitre.

---

[6] J. G. Haasnoot and Col. *Z. Naturforsch. B* **1977**, *32*, 1421**.**
[7] O. Kahn, C. J. Martinez, *Science,* 1998, 279, 44-48
[8] Xin Cheng, Qian Yang, Chan Gao, Bing-Wu Wang, Takuya Shiga, Hiroki Oshio, Zhe-Ming Wang, Song Gao, *Dalton Trans.,* **2015**, 44, 11282-11285.
[9] R.H. Wiley, A. J. Hart, *J.Org.Chem.* **1953**, *18*,1368-1371
[10] Y.Maximilian Klein, Natasha F. Sciortino, Florence Ragon, Catherine E. Housecroft, Cameron J. Kepert, Suzanne M. Neville, *Chem. Comm*, **2014,** 50, 3838-3840.

1. Réseau tridimensionnel: [Fe(trz-py)(tcpd)(H_2O)] (1)

1.1. Synthèse

Le ligand trz-py a été préparé selon la méthode décrite par R.H Wiley en 1953[11]. On prépare 5 mL de solution aqueuse à 0,01 M en mélangeant 12,7 mg (0,05 mmole) de perchlorate de Fer(II) et 6,1 mg (0,05 mmole) de ligand 4-(2-pyridyl)-1,2,4,4*H*-triazole (trz-py). On place 2 mL de cette solution dans un tube fin sur laquelle on ajoute délicatement 2 mL d'une solution aqueuse à 0,01 M (14,1 mg, 0,05 mmole) de 2-dicyanométhylène-1,1,3,3-tétracyano-propènediure de potassium K_2(tcpd). On obtient au bout de quelques semaines des aiguilles jaunes.

1.2. Caractérisation structural et magnétique

La structure de ce complexe a été déterminée à 150 K. Ce composé cristallise dans le groupe d'espace $P_{2_1/n}$ du système monoclinique.

Tableau II.1 Paramètres structuraux et résultats des affinements pour [Fe(trz-py)(tcpd)(H_2O)] à 150 K

	[Fe(trz-py)(tcpd)(H_2O)]
Formule brute	$C_{34}H_{16}Fe_2N_{20}O_2$
Forme/couleur	Aiguille jaune
M/g.mol^{-1}	848,37
Système	monoclinique
Groupe d'espace	$P_{2_1/n}$
a/Å	12,334(4)
b/Å	19,922(7)
c/Å	14,687(5)
α/°	90
β/°	91,84(4)
γ/°	90
V/Å^3	3607(2)
R1	0,2250
R2	0,4977
GooF	1,184

L'unité asymétrique de ce composé comprend un anion $(tcpd)^{2-}$, un cation $[Fe(trz\text{-}py)]^{2+}$ et une molécule d'eau. L'environnement du cation métallique présente une

[11] R.H Wiley, A.J. Hart, *J.Org. Chem.* **1953**, 18, 1368-1371

géométrie pseudo-octaédrique de type FeN_5O dans laquelle le cation métallique est coordiné à un atome d'oxygène provenant d'une molécule d'eau et à cinq atomes d'azote provenant des ligands pontants trz-py(μ^2) et $(tcpd)^{2-}$(μ^4). La moyenne des longueurs de liaison Fe-N est de 2,167 Å.

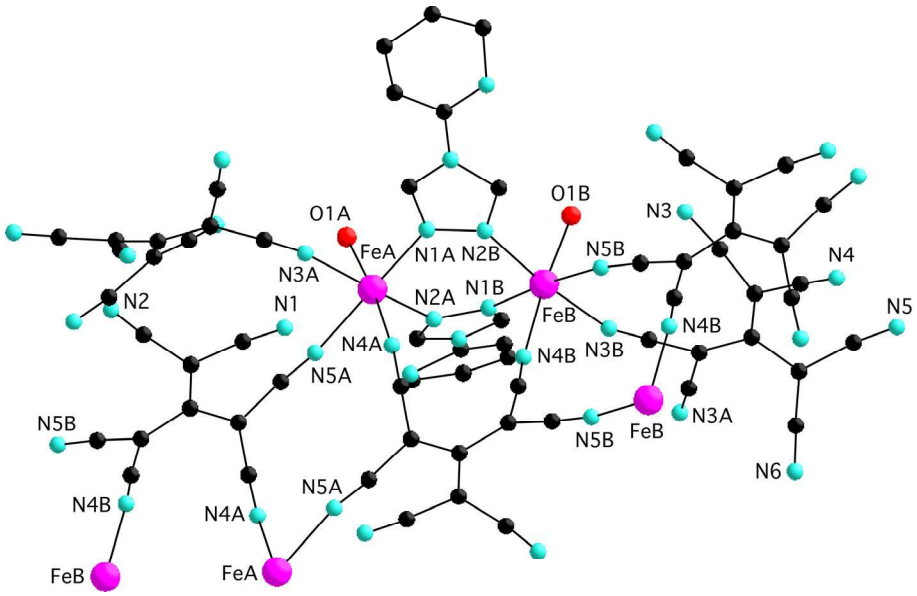

Figure IV.1 Structure moléculaire du système [Fe(trz-py)(tcpd)(H_2O) où les atomes d'hydrogène ont été volontairement omis.

Les atomes de fer (FeA et FeB) sont pontés par deux ligands trz-py. Ce caractère pontant du ligand triazole a déjà été décrit[12]. Ce mode de coordination génère une chaine 1D de type Fe-(trz-py)-Fe. La distance entre deux atomes de fer pontés par trz-py est de 4,167 Å. Le mode de coordination du ligand $(tcpd)^{2-}$ est quant à lui de type μ^4. Les atomes N4A, N4B, N5A et N5B d'un ligand $(tcpd)^{2-}$ sont reliés à quatres centres métalliques. Ce mode de coordination pour l'anion $(tcpd)^{2-}$ n'a été décrit qu'une seule fois[13]. Ce mode de coordination pontant engendre une structure tridimensionnelle (3D). Cette structure 3D complexe peut être décrite simplement de la manière suivante: les entités dinucléaires Fe(II)-(trz-py)-Fe(II) sont connectées de part et d'autre par deux ligands $(tcpd)^{2-}$ pour générer un réseau tridimensionnel (3D).

[12] Grosjean, A., Daro, N., Kauffmann, B., Kaiba, A., Létard, J.-F., Guionneau, P., *Chem. Comm*, 2011, 47, 12382-12384
[13] S.Triki, J. Sala Pala, M. Decoster, P. Molinié, L. Toupet, *Angew. Chem. Int. Ed.*, **1999**, 38, 113-115

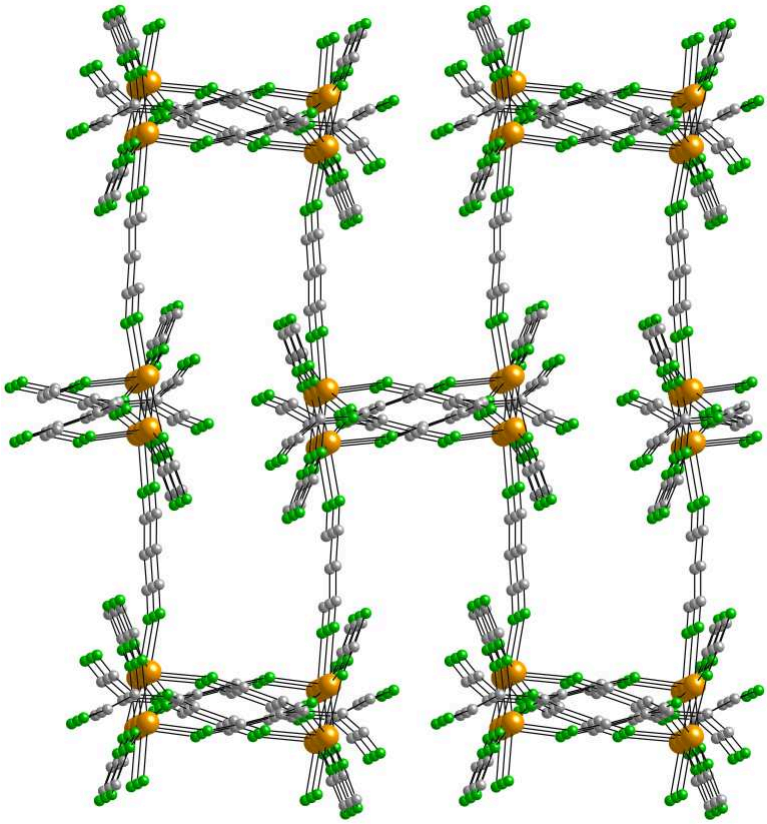

Figure IV.2 Structure cristalline 3D de [Fe(trz-py)(tcpd)(H_2O)
(les atomes d'hydrogène et les cycles aromatiques ont été volontairement omis)

Tableau IV.1 Longueurs (Å) de liaison autour des cations Fe(II) dans [Fe(trz-py)(tcpd)(H_2O)].

	[Fe(trz-py)(tcpd)(H_2O)]		[Fe(trz-py)(tcpd)(H_2O)]
FeA-N1A	2,159(17)	FeB-N1B	2,186(14)
FeA-N2A	2,222(15)	FeB-N2B	2,206(15)
FeA-N3A	2,151(19)	FeB-N3B	2,150(17)
FeA-N4A	2,118(15)	FeB-N4B	2,185(16)
FeA-N5A	2,188(16)	FeB-N5B	2,107(14)
FeA-O1A	2,098(14)	FeB-O1B	2,091(17)
<Fe-N>	2,167	<Fe-N>	2,167

Tableau IV.2 Angles (°) de liaison autour du Fe(II) dans [Fe(trz-py)(tcpd)(H_2O)].

	[Fe(trz-py)(tcpd)(H_2O)]		[Fe(trz-py)(tcpd)(H_2O)]
N4A-FeA-N3A	93,7(6)	N4B-FeB-N3B	90,8(6)
N4A-FeA-N1A	89,4(6)	N4B-FeB-N1B	92,9(6)
N3A-FeA-N1A	88,8(7)	N3B-FeB-N1B	88,3(6)
N4A-FeA-N5A	85,5(6)	N4B-FeB-N5B	85,2(6)
N3A-FeA-N5A	88,1(6)	N3B-FeB-N5B	87,4(6)
N1A-FeA-N5A	173,9(6)	N1B-FeA-N5B	175,2(5)
N4A-FeA-N2A	97,6(5)	N4B-FeB-N2B	94,2(6)
N3A-FeA-N2A	168,1(6)	N3B-FeB-N2B	172,9(6)
N1A-FeA-N2A	95,1(6)	N1B-FeB-N2B	96,5(5)
N5A-FeA-N2A	89,0(6)	N5B-FeB-N2B	88,0(6)
O1A-FeA-N4A	175,2(6)	O1B-FeB-N4B	174,7(6)
O1A-FeA-N3A	84,0(6)	O1B-FeB-N3B	85,7(7)
O1A-FeA-N1A	94,6(6)	O1B-FeB-N1B	91,0(6)
O1A-FeA-N5A	90,3(6)	O1B-FeB-N5B	90,7(6)
O1A-FeA-N2A	84,5(5)	O1B-FeB-N2B	88,9(6)

Les mesures magnétiques du composé **1** sont représentées sous la forme du produit $\chi_m T$ en fonction de la température T (figure 9).

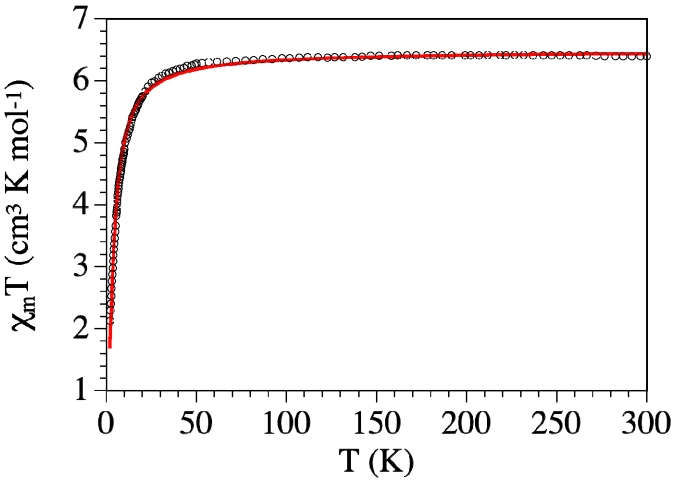

Figure IV.3 Variations thermiques du produit $\chi_m T$ du composé **1**; la ligne continue en rouge représente le résultat de la modélisation.

A température ambiante, la valeur du produit $\chi_m T$ de **1**, donnée par groupement formulaire $[Fe_2(trz\text{-}py)_2(tcpd)_2(H_2O)_2]$ contenant deux cations Fe^{II}, est de 6.4 emu.K.mol^{-1}. Cette valeur est du même ordre de grandeur que celle attendue pour deux ions Fe^{II} (S=2) magnétiquement isolés (état fondamental $^5T_{2g}$). La moyenne des longueurs de liaison <Fer-Azote> est de 2,167 Å en accord avec un état HS.

Lors de l'abaissement de la température, le produit $\chi_m T$ reste constant jusqu'à une température voisine de 80 K puis décroît rapidement et tend vers zéro à 2K (Figure IV.1). Ce comportement suggère un couplage de type antiferromagnétique entre les deux porteurs de spins. Les données expérimentales du composé **1** ont été modélisées avec un modèle de dimère ne tenant compte que de l'interaction d'échange via le ligand pontant trz-py à partir de l'équation de Van Vleck :

$H = -2JS_aS_b$ avec $S_a = S_b = 2$ et $\chi_m = \frac{2Ng^2\beta^2}{k_BT}\left(\frac{e^{2x}+5e^{6x}+14e^{12x}+30e^{20x}}{1+3e^{2x}+5e^{6x}+7e^{12x}+9e^{20x}}\right)$

avec N = nombre d'Avogadro, g = facteur de Landé, β = magnéton de Bohr, k_B = constante de Boltzmann, T température, $x = \frac{J}{k_BT}$, J = constante d'échange.

Les meilleurs résultats ont été obtenus avec : $g = 2.079$, $J = -0{,}8$ cm^{-1}.

Si la structure tridimensionnelle peut augmenter la coopérativité du système , la présence d'une molécule d'eau induisant une sphère de coordination de type $[N_5O]$ du cation Fe^{2+} laissait cependant prévoir l'absence de transition de spin.

2. Réseau bidimensionnel: $[Fe(trz\text{-}py)_2(Pt(CN)_4).3H_2O]$ (1)

Hidden Hysteresis Revealed by Photo-switching in a Multi-Stable Two-Dimensional Hoffman-Like Spin-Crossover Metal-Organic Framework

Eric Milin,[†] Véronique Patinec,[†] Smail Triki,[†,*] El-Eulmi Bendeif,[‡] Sébastien Pillet,[‡] Mathieu Marchivie,[§] Guillaume Chastanet,[§] Kamel Boukheddaden.[II]

[†]UMR CNRS 6521, Chimie, Electrochimie Moléculaires, Chimie Analytique, Université de Bretagne Occidentale, BP 809, 29285 Brest Cedex, France.

[‡]CRM2, UMR CNRS 7036, Institut Jean Barriol, Université de Lorraine, B.P. 70239, F-54506 Vandoeuvre-lès-Nancy, France.

[§]CNRS, Université Bordeaux, ICMCB, 87 Av. Doc. A. Schweitzer, F-33608 Pessac, France.

[II]GEMaC, Université Paris-Saclay, CNRS-Université de Versailles Saint-Quentin-en-Yvelines, 45 Avenue des Etats-Unis 78035 Versailles cedex, France.

■ **ABSTRACT:** We report a new 2D Hoffman-type framework spin crossover (SCO) system $[Fe(trz\text{-}py)_2\{Pt(CN)_4\}].3H_2O$, built from $[FePt(CN)_4]$ layers separated by interdigited 4-(2-pyridyl)-1,2,4,4*H*-triazole (trz-py) ligands with two inequivalent Fe^{II} sites. This compound exhibits an incomplete sharp SCO first-order phase transition centered at 153 K from a HS-HS to a HS-LS structurally ordered state. It undergoes a bidirectional photoswitching to HS-HS and LS-LS states by irradiation with green and near-infrared light, respectively, with markedly different T(LIESST) and T(reverse-LIESST) values of 52 and 85K. Photomagnetic results show that (i) the photo-induced HS-HS state is metastable and relaxes to the intermediate configuration through a self-accelerated dynamical process; (ii) the HS-LS state (plateau) remains stable or metastable with an extremely long lifetime; and (iii) the reverse-LIESST process enables access to a hidden stable LS-LS state, corresponding to a hidden low temperature hysteresis. Detailed crystallographic investigations indicate that the very strong metastability of the intermediate HS-LS state originates from antiferroelastic interactions (frustration) within the $[FePt(CN)_4]$ layers, accommodated by NC-Pt-CN bridges between inequivalent SCO active Fe^{II} sites. The existence of the stable LS-LS state paves the way for a multi-photoswitching between these three states.

■ INTRODUCTION

Spin crossover materials (SCO), in particular those exhibiting thermal and photo-induced magnetic bistability, are likely among the most studied switchable molecular solids in the last few years. In general, this property occurs for the first row transition metal complexes of the d^4-d^7 electronic configurations when the spin pairing energy is close to the ligand field strength, producing changes in their magnetic, optical and structural properties.[1] So far, the most studied examples are those based on Fe(II) (d^6 configuration), for which a paramagnetic-diamagnetic transition from the HS (S = 2, $^5T_{2g}$) to the LS (S = 0, $^1A_{1g}$) state is observed with temperature.[1] The photo-conversion between the LS and the HS state has been shown to be reversible in some complexes through metastable states.[2] This allows a bidirectional photo-switching between a reference state (0) and an excited state (1) with a long lifetime, as long as the experiment is performed at low-temperature. Going further, it is of huge interest to be able to reach different states from the same reference state, with a high contrast in at least one physical property. Such multi-addressable systems with at least three states (0, +1, -1) are quite rare[3,4,5]. Except the particular case of the $[Fe(ptz)_6](BF_4)_2$ compound for which the multistability comes from the single-molecule magnet behavior of the photo-induced metastable state, the observation of multi(meta)stability arises from the presence of multiple switchable sites. In the binuclear example $\{[Fe(bt)(NCS)_2]_2(bpm)\}$, irradiation in the visible range induced the population of the fully paramagnetic HS-HS state while an irradiation in the near infrared populates the intermediate HS-LS phase[5]. Regarding mononuclear compound, the presence of at least two inequivalent Fe(II) sites can lead to a stepped spin-crossover or an incomplete transition with one iron(II) that remains in the HS state.[6] Using the reverse-LIESST approach, this thermally-trapped HS state can be switched to LS. From this new state, a new spin-crossover temperature can be recorded that corresponds to the spin-crossover of the second iron(II) site.[3] One interesting but rarely observed property is that this trapped site may undergo a first-order phase transition giving rise to a hidden hysteresis[7,8].

To generate such multi(meta)stability, we followed an original approach, based on the design of SCO Hoffman-like metal-organic framework (MOF) with flexible ligands allowing reversible photoswitching[8] and organized on surfaces or dots for applications in molecular electronics.[9] Our approach is based on such processable Hoffman-like metal-organic framework (MOF) to introduce multi(meta)stability[10] which will help in the observation of the (0, +1, -1) configuration.

During the last years, the Brest's group and others have directed their investigation towards the so-called polymeric strategy to better control the supramolecular organization in the crystal packing and possibly to enhance cooperative effects and magnetic interactions.[11-14] With the aim of growing networks with cyanide donors, we have investigated the flexible cyanocarbanion ligands which can act as polybridging ligands through their nitrile groups.[12,15] With the aim of improving the elastic interactions between the active Fe(II) centers in these extended SCO complexes, we have extended this polymeric approach to the use of more rigid bridging ligands such as the inorganic tetracyanometallate anions ($[M(CN)_4]^{2-}$, M = Ni(II), Pt(II), Pd(II)). In this context, we have recently reported two series of molecular bimetallic coordination neutral chains formulated as $[FeL_2][\mu_2\text{-}M(CN)_4]$ (M = Ni(II), Pt(II); L = 4-amino-3,5-bis(pyridin-2-yl)-1,2,4-triazole (abpt), quinolin-8-amine (aqin)).[16,17] In these reports we have shown that the coordination mode of inorganic planar anions, and consequently the 1-D character of the bimetallic material, can be imposed by the choice of the iron (II) $[Fe(L)_2]^{2+}$ precursor (L = bidentate ligand) (Scheme 1a); and the ligand field of the Fe(II) centers can be tuned by the nature of the chelating co-ligand (L).

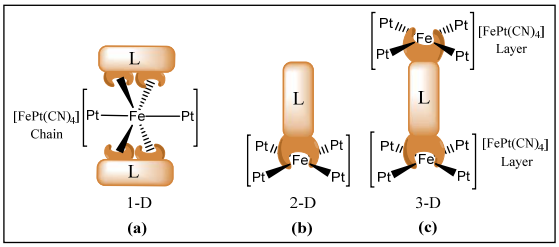

Scheme 1. Coordination modes of the ancillary L ligands for the design of bimetallic coordination polymers, including 2-D and 3-D Hoffman-type Metal-Organic Frameworks (MOFs).

In such bimetallic frameworks the structural features, and correlatively the magnetic properties, are significantly influenced by the nature of ancillary ligand (L) since the number and geometrical orientation of its N-donor atoms allow the prediction of the structural dimension (see Scheme 1). In addition, the tuning of its flexibility/rigidity allows the control of the interlayer interactions, which affects their equilibrium magnetic properties (transition temperature and/or thermal hysteresis loop) and their nonequilibrium behavior, such as light-induced excited spin-state trapping (LIESST) effects.[14]

Based on such 2-D and 3-D Hoffman-type systems and on our achievements derived from the study of bimetallic chains, we have extended our investigations to bimetallic systems involving the $[Fe^{II}M^{II}(CN)_4]$ 2-D layers and other mono-dentate or bridging aromatic N-donor co-ligands (Schemes b and c). Since the 2-D and 3-D Hoffman-type Frameworks are essentially limited to the pyridyl N-donor ligands, we have focused our investigations to other

aromatic N-donor ligands such as functionalized azole based ligands involving two or more N-donor atoms.

We report herein the synthesis of the SCO 2-D Hoffman-like system [Fe(trz-py)$_2${Pt(CN)$_4$}].3H$_2$O (**1**) (trz-py = 4-(2-pyridyl)-1,2,4,4*H*-triazole), based on the N-donor functionalized triazole ligand and its full characterizations, including thermal variation of the crystallographic structural data, magnetic and photomagnetic properties, and full photo-crystallographic studies including details on the photoswitching processes involved in the multi(meta)stable and bidirectional photoswitching process. Note that recently, the coordination polymer [Fe(thtrz)$_2$Pd(CN)$_4$].(EtOH)(H$_2$O) (thtrz = N-thiophenylidene-4*H*-1,2,4-triazol-4-amine) was communicated as the first 2-D Hoffman-type coordination polymer based on a functionalized triazole ligand.[18] The magnetic properties reveal an incomplete spin transition leading to an HS-LS configuration at low temperature. This state can be either switched by light irradiation to HS-HS or LS-LS configurations whose stability has been investigated. The present manuscript is organized as follows: section II presents the experimental investigations including the synthesis of the material, the crystallographic, magnetic, calorimetric and photomagnetic properties; section III is devoted to the discussion of the obtained results and we conclude in section IV.

■ RESULTS AND DISCUSSIONS.

Compound **1** has been prepared as polycrystalline powder by adding K$_2$[Pt(CN)$_4$].*x*H$_2$O to an aqueous solution containing 4-(2-pyridyl)-1,2,4,4*H*-triazole and iron (II) perchlorate in 1:2:1 ratio respectively. The corresponding single crystals suitable for X-ray diffraction have been synthesized using diffusion technique in fine glass tube (3.0 mm diameter) by carefully layering an aqueous solution containing 4-(2-pyridyl)-1,2,4,4*H*-triazole and iron (II) perchlorate onto an aqueous solution of K$_2$[Pt(CN)$_4$].*x*H$_2$O. The room-temperature X-ray powder diffraction spectrum (XRPD) of the polycrystalline powder has been performed to confirm the phase purity of the powder by comparison with the simulated XRPD pattern for the corresponding single crystal sample. As clearly indicated by Figure S1, the measured pattern of microcrystalline powder of **1** is indeed qualitatively similar to the pattern calculated from the single-crystal crystallographic data. The absence of any non crystalline impurities in this powder has been confirmed by IR spectroscopy that showed that the spectrum of the single crystals is identical to that observed for the white powder of **1** (see Figures S2 and S3). The IR spectrum of **1** shows sharp peaks attributed to the distinctive bond vibration modes of the trz-py molecule. Except the bands attributed to the [Pt(CN)$_4$]$^{2-}$ anion (Figure. S4), the IR

spectrum of **1** is similar to that measured for the free trz-py molecule (see 1600-400 cm^{-1} region in Figures S2 and S3). Thus, this observation does not allow any direct conclusion on the coordinating character of this organic ligand. However, the blue shift of the characteristic intense C-N stretching band $\nu_{(CN)}$ observed at 2167 cm^{-1}, which was located at 2133 and 2122 cm^{-1} in $K_2[Pt(CN)_4].xH_2O$ (See Figure S4), reveals the μ_4-bridging coordination mode of the $[Pt(CN)_4]^{2-}$ moiety in compound **1**. In the low frequency region, the strong asymmetric doublet, observed at 229 and 225 cm^{-1}, is assigned to the Fe-N stretching vibrations in agreement with the presence of HS Fe(II) centers; the presence of two distinct bands is indicative of the presence of two types of Fe-N bond lengths as revealed by the crystal structure determination (see below).[19]

The magnetic susceptibility (χ_m) for **1** was determined over the 2-300 K range on a polycrystalline sample. The $\chi_m T$ versus T plot (where T is the temperature) is displayed in Figure 1. In the high-temperature region, the $\chi_m T$ value (3.51 $cm^3 \cdot K \cdot mol^{-1}$) is consistent with a high spin (HS, S = 2) configuration of the hexacoordinated Fe(II) ions. Upon cooling, $\chi_m T$ remains almost constant down to a temperature value of *ca.* 155 K, at which it abruptly decreases to ca. 2.0 $cm^3 \cdot K \cdot mol^{-1}$, indicating the presence of an incomplete sharp HS-LS SCO first-order phase transition. Below 150 K, the $\chi_m T$ product remains constant with a residual fraction of *ca.* 55 % Fe(II) ions in the HS configuration. This $\chi_m T$ value is slightly higher than half of the high temperature value of 3.51 $cm^3 \cdot K \cdot mol^{-1}$ probably because of defects, anisotropy or different g value for the two iron (II) sites. At very low temperatures, the fraction of HS Fe(II) ions shows the expected zero field splitting (ZFS) leading to a decrease of $\chi_m T$ product.

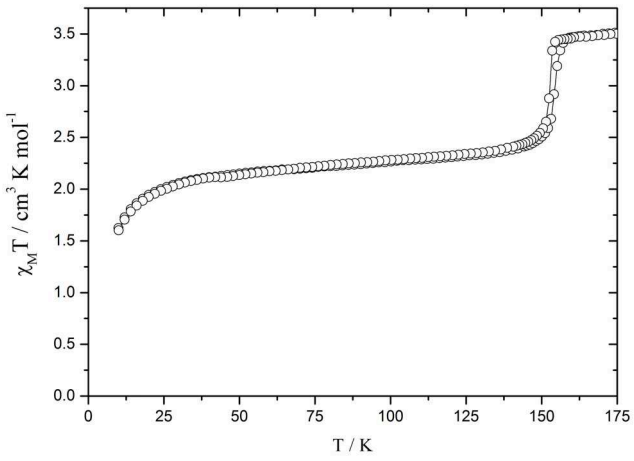

Figure 1. Thermal dependence of the $\chi_m T$ product for **1** showing the abrupt incomplete spin transition around 153 K. Inset shows the first-order character of the thermal dependence of the $\chi_m T$ product around the transition, which is accompanied with a ~2K wide hysteresis loop.

The warming mode shows a slight thermal hysteresis; the spin transition temperatures ($T_{½}$) for the cooling ($T_{½}^{down}$) and warming ($T_{½}^{up}$) scans are 152 and 154 K, respectively (see inset of Figure 1). This bistability was clearly confirmed by DSC studies in which the thermal variation of the heat flow shows exo- and endothermic transitions at 151.8 and 154.4 K, respectively (see Figure S5), in excellent agreement with magnetic data. Furthermore, we found that the phase transition occurs with an enthalpy and entropy changes of $\Delta H = 4.8$ $kJ.mol^{-1}$ and $\Delta S = 30$ $J.K^{-1}.mol^{-1}$, respectively. These values are in good agreement with those reported in literature for SC compounds.[20]

Based on the conclusions derived from the thermal variation of the magnetic data and from the calorimetric measurements, the crystal structure of **1** has been determined at 296 K and at 120 K. The relevant structural modifications induced by light irradiation will be detailed in the following sections. Compound **1** crystallizes in the monoclinic C2/c space group. Crystallographic data, selected bond lengths and angles are listed in Tables 1 and 2 respectively.

Table 1. Crystallographic data for compound **1**

	HS-1	IP-1	IP-2	LS	HS-2
Temperature / K	**296**	**120**	**10**	**10**	**10**
[a]Chemical formula	$C_{18}H_{18}FeN_{12}O_3Pt$	$C_{18}H_{18}FeN_{12}O_3Pt$	$C_{18}H_{18}FeN_{12}O_3Pt$	$C_{18}H_{18}FeN_{12}O_3Pt$	$C_{18}H_{18}FeN_{12}O_3Pt$
Formula weight	701.38	701.38	701.38	701.38	701.38
Crystal system	monoclinic	monoclinic	monoclinic	monoclinic	monoclinic
Space group	C2/c	C2/c	C2/c	C2/c	C2/c
a/Å	25.248(5)	24.795(6)	24.7216(15)	24.5780(12)	24.9520(19)
b/Å	7.4044(18)	7.247(2)	7.2484(3)	7.0841(2)	7.3964(5)
c/Å	27.293(6)	27.105(6)	27.060(2)	26.8551(15)	27.129(2)
α/°	90	90	90	90	90
β/°	111.451(11)	111.487(13)	111.429(8)	111.843(6)	111.264(9)
γ/°	90	90	90	90	90
Volume/$Å^3$	4749(2)	4532(2)	4513.8(5)	4340.2(4)	4665.9(7)
Z	8	8	8	8	8
ρ_{calc} g/cm^3	1.962	2.056	2.064	2.147	1.997
μ/mm^{-1}	6.543	6.857	6.884	7.159	6.659
F(000)	2704.0	2704.0	2704.0	2704.0	2704.0
Crystal size/mm^3	0.015 × 0.025 × 0.25	0.015 × 0.025 × 0.25	0.051*0.15*0.16	0.060*0.13*0.14	0.051*0.15*0.16
Radiation	MoKα (λ = 0.71073)	MoKα (λ = 0.71073)	MoKα (λ = 0.71073)	MoKα (λ = 0.71073)	MoKα (λ = 0.71073)
2Θ range /°	3.206 to 50.7	5.892 to 55.048	2.946 to 30.508	3.011 to 30.505	2.890 to 30.507
hkl range	-30/30, -8/8, -32/32	-32/32, -9/9, -35/35	-35/35, -10/9, -38/35	-34/34, -10/10, -35/38	-35/34, -10/9, -38/29
collected reflections	76227	78436	28489	25996	15577
Independent reflections	4335 [R_{int} = 0.033]	5210 [R_{int} = 0.029]	6909 [R_{int} = 0.080]	6617 [R_{int} = 0.050]	6978 [R_{int} = 0.057]
parameters /restraints	327/0	342/9	336/48	336/6	336/85
[b]Final R indexes	R_1 = 0.013, wR_2 = 0.030	R_1 = 0.019, wR_2 = 0.047	R_1 = 0.057, wR_2 = 0.098	R_1 = 0.027, wR_2 = 0.046	R_1 = 0.062, wR_2 = 0.106
[c]Goodness-of-fit on F^2	1.089	1.093	1.172	1.008	1.189
Largest diff. peak/hole / e^- $Å^{-3}$	0.21/-0.37	0.74/-0.70	2.68/-2.92	1.197/-1.522	3.33/-2.77

[a]There is 1 chemical formula in the asymmetric unit. [b]$R1 = \Sigma(|Fo-Fc|/Fo)$ [I>=2σ (I)] and $wR2 = [\Sigma((\omega(Fo^2-Fc^2))^2/(\omega(Fo^2))^2)]^{1/2}$ [all data]. [c]$G.O.F = [(\Sigma(\omega(Fo^2-Fc^2))^2/(Nobs-Nvar)]^{1/2}$

The crystal structure of **1** is built from the two crystallographically independent Fe(II) sites, Fe1 and Fe2, respectively located on an inversion center (¼ -¼ ½) and a two-fold axis (½ b ¾), one $[Pt(CN)_4]^{2-}$ anion, two monodentate trz-py ligands and three water solvent molecules located on general positions (Figure 2).

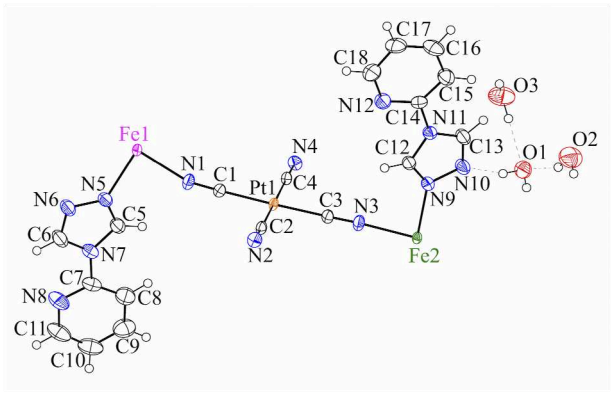

5.

Figure 2. Thermal ellipsoid drawing[21] (30% probability ellipsoids) of the asymmetric unit of **1** at 296 K showing the labeling scheme.

Table 2. Selected bond lengths and distortion parameters of the coordination sphere of compound **1**.

Atoms	**distance** / Å	
	296 K (HS1)	**120 K (IP1)**
Fe1-N1	2.143(2)	1.943(3)
Fe1-N2[1]	2.162(2)	1.944(2)
Fe1-N5	2.178(2)	1.974(2)
<Fe1-N>	**2.161(2)**	**1.954(2)**
Fe2-N3	2.141(2)	2.140(3)
Fe2-N4[2]	2.151(2)	2.151(2)
Fe2-N9	2.209(2)	2.188(2)
<Fe2-N>	**2.167(2)**	**2.160(2)**
	distortion	
[a]Σ(Fe1) (°)	7(1)	7(1)
[b]Θ(Fe1) (°)	18(2)	22(2)
Σ(Fe2) (°)	15(1)	19(1)
Θ(Fe2) (°)	46(2)	52(2)

[1]1/2-x,1/2-y,1-z; [3]x,-1+y,z; [2]1-x,1+y,3/2-z.

[a]Σ is the sum of the deviation from 90° of the 12 *cis*-angles of the FeN_6 octahedron;[22,23] [b]Θ is the sum of the deviation from 60° of the 24 trigonal angles of the projection of the FeN_6 octahedron onto its trigonal faces.[23,24]

The iron centers Fe1 and Fe2 are alternately linked by $[Pt(CN)_4]^{2-}$ anions to form a 2-D coordination polymer within corrugated layers corresponding to the **a**+**c** and **b** directions. The 2-D network can be described as a succession of Fe_4 pseudo-squares which diagonals are formed by Fe1-Pt1-Fe2 bridges leading to an alternation of Fe1 and Fe2 along the **a**+**c** direction (Figure 3a). As NC-Pt-CN bridges are a little longer than the pseudo squares

diagonals, the $[Pt(CN)_4]^{2-}$ moieties lie slightly out of the plane, leading to the corrugation of the 2D layers by a tilt of the FeN_4 planes around Fe1 (Figure 3b).

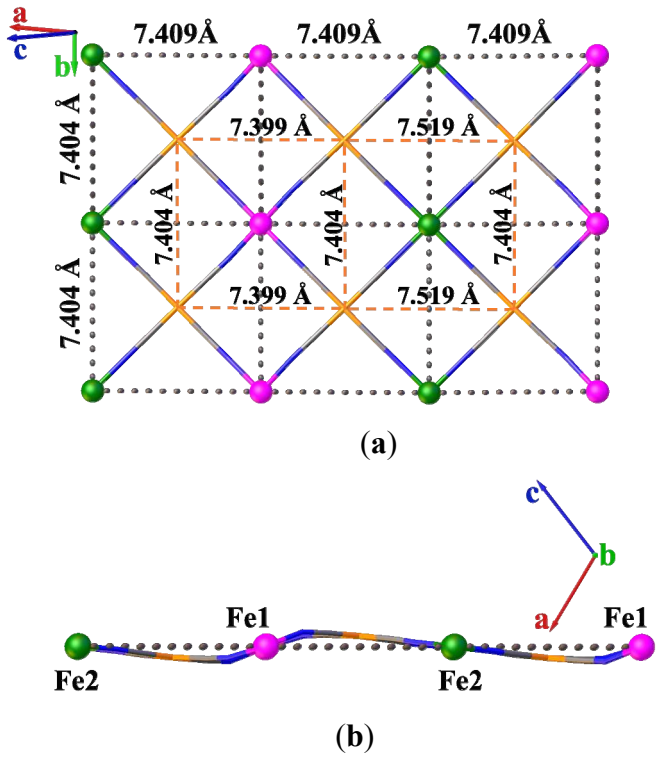

Figure 3. View of the 2D arrangement of **1** at ambient temperature (296 K): (**a**) Projection along the [-1 0 1] direction showing the Fe_4 pseudo-squares; (**b**) view along the [0 1 0] direction showing the tilted $Fe1N_4$ planes. Fe1 and Fe2 atoms are respectively drawn in purple and green, N in blue, C in grey and Pt in orange.

The 2D layers are furthermore stacked along the **a-c** direction; the cohesion of the crystal network is assisted in this direction by π-π interactions between the trz-py ligands and a strong hydrogen-bonding network that involves the three water molecules and the non coordinated nitrogen atom of the triazole part of the trz-py ligand (Tables S1, S2 and Figures 4 and S6). It is worth to note that the hydrogen bonding network links only the trz-py ligands which are coordinated to the Fe2 centers (Figure 4b).

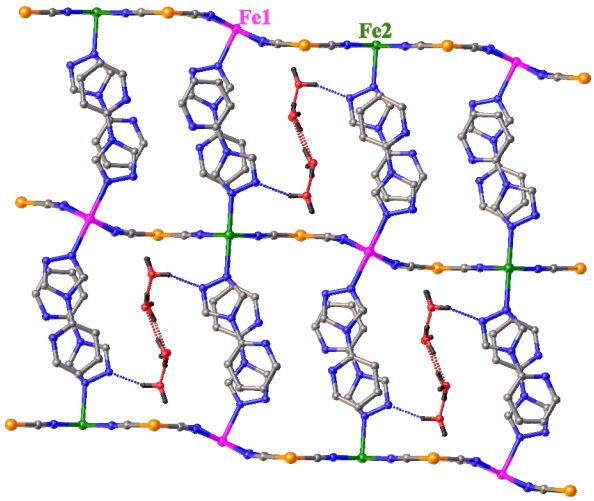

(**a**)

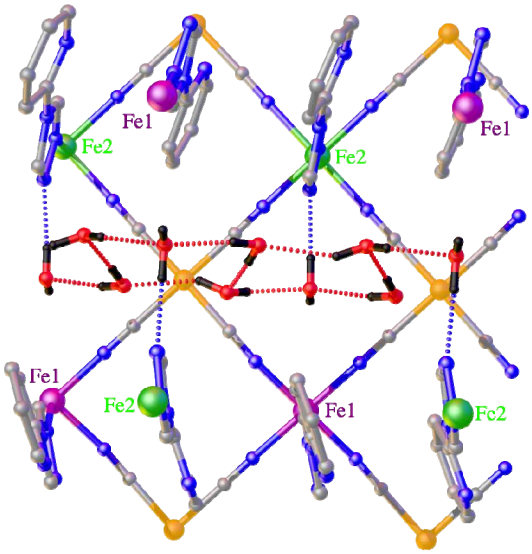

(**b**)

Figure 4. 3D crystal packing of **1** at ambient temperature (296 K): (**a**) View along the [0 1 0] direction; (**b**).view along the [2 0 -1] direction showing the hydrogen-bonding network between Fe2 sites. Dashed lines show the hydrogen-bonding network

At 296 K, the two iron sites present an octahedral geometry involving an FeN_4 equatorial plane arising from four nitrogen atoms of the $[Pt(CN)_4]^{2-}$ anion and two N atoms in axial positions from the trz-py ligands. As shown in Table 2**,** the mean Fe2-N distance ~2.167(2) Å, is slightly longer than the mean Fe1-N distance, 2.161(2). A difference mainly due to the Fe-N(trz-py) bonds (Fe1-N5 = 2.178(2) Å and Fe2-N9 = 2.209(2) Å). A meticulous inspection of the bond distances reveals a more distorted coordination sphere for the Fe2 ion (see Table 2), which then experiences a significant elastic strain. According to the mean Fe-N distances, both iron centers are in the HS state at 296K. Nevertheless, the distortion of the octahedral geometries are found very small in the HS state for both metal centers, as usually observed for "Hoffman like" spin crossover compounds.[13] The equatorial plane for Fe2 is found aligned

with that of the $[Pt(CN)_4]^{2-}$, while it deviates significantly by 24.8° for Fe1, to lead to a corrugation of the 2D network (Figure 5).

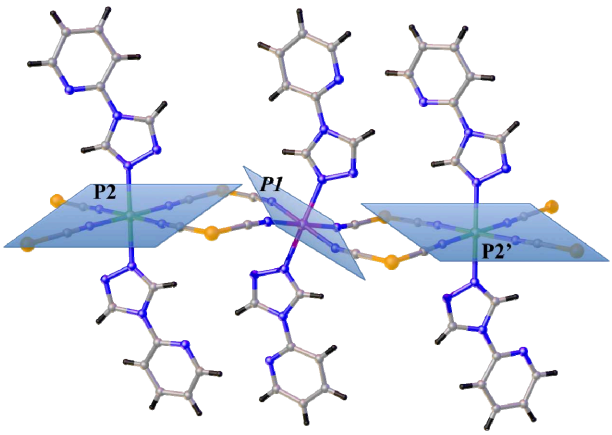

Figure 5. View along the **b** direction at ambient temperature (296 K) showing the FeN_4 equatorial plane aligned with the $PtCN_4$ plane for Fe2 (P2 and P2') while $Fe1N_4$ plane appears clearly tilted for Fe1 (P1).

At 120 K, the octahedral geometries of the two iron atoms are significantly different. While the Fe2 environment remains almost unchanged, the Fe1-N bond lengths drastically decrease to reach a mean value of 1.954(2) Å. This feature is the signature of the change of the spin state of Fe1 from HS to LS at low temperature while Fe2 remains trapped in the HS state, most probably due to the above mentioned distortion of its coordination sphere. The angular octahedral geometry of Fe1 is already very regular in the HS state, and therefore does not regularize further during the spin transition as shown by the distortion parameters (see Table 2) that remain almost unchanged between 296 and 120 K. Such a behavior is typical for "Hoffman like" systems.[13] The FeN_4 equatorial plane remains in the $[Pt(CN)_4]^{2-}$ plane for Fe2 while the deviation from this plane is still significant for Fe1 (deviation angle = 21.7°) but less pronounced than that observed at room temperature (24.8°) (Figure 5). These structural features result in an antiferroelastic interaction between the two types of metal centers that prevents the spin transition of Fe2 that remains trapped HS and explain therefore the magnetic behavior below 150K. Such elastic interactions are illustrated by Figure S7 that shows the deformation of the Fe_2Pt_2 pseudo-squares in the low-temperature region. While the Fe_4 squares appear very regular at room temperature (Figure 3a), they progressively distort at 120 K to reach a pseudo rectangular geometry. The inter-layer distances observed at 120 K are similar to those observed at room temperature but with systematically shorter distances, which is a characteristic of the natural thermal contraction (Tables S1 and S2).

Photo-magnetic properties were first studied on the polycrystalline sample at 10 K. From the intermediate HS-LS state, a photo-excitation with green light (510 nm)

induces an increase of the $\chi_m T$ product from 1.64 to 2.10 $cm^3 \cdot K \cdot mol^{-1}$ (Figure 6), after 30 min of irradiation (see also Figure 7). This reveals the occurrence of LIESST effect and the photo-transformation of LS species into HS, thus leading to a sizeable population of neighboring molecules in the HS-HS configuration. Applying the usual T(LIESST) procedure[25], that is a warming in the dark at 0.3 $K \cdot mn^{-1}$, the $\chi_m T$ curves increases up to 3.11 $cm^3 \cdot K \cdot mol^{-1}$ at 42 K. This $\chi_m T$ value indicates a photo-conversion efficiency of ~ 75%. This partial transformation is mainly due to incomplete light absorption inside the polycrystalline sample. Upon further warming in the dark, the $\chi_m T$ product decreases rapidly, due to thermal relaxation, to recover the value of the intermediate state. The derivative of the curve indicates a T(LIESST) value of 52 K. A set of relaxation kinetics were recorded in the dark at several temperatures to derive the physical parameters (activation energy, interaction strength and frequency factor) governing the relaxation of the photo-induced metastable HS fraction (Figure S12).

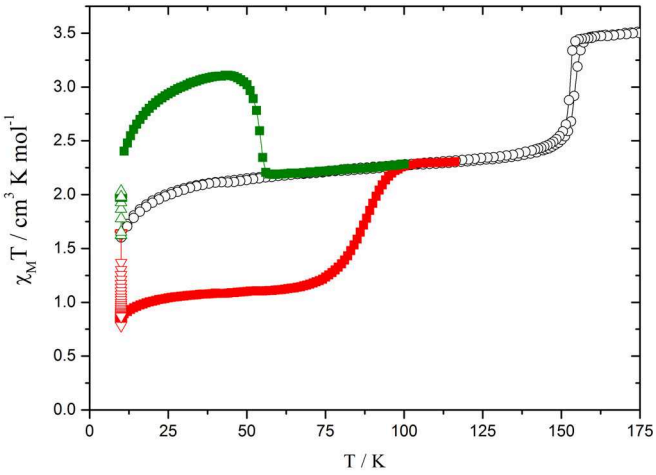

Figure 6. Thermal evolution of the $\chi_m T$ product from high temperature to low temperature in the dark (o), under (Δ) and in the dark after (■) green light irradiation or under (∇) and after in the dark (■) near-infrared irradiation.

We found that the relaxation curves follow a sigmoidal behaviour, in agreement with the cooperative character of the thermal spin transition. To extract the relaxation rate constant at each temperature, we have considered the self-accelerated Hauser's model,[26] whose physical origin and mean-field character were demonstrated in reference 27. In this model, the time dependence of the photo-converted HS fraction, γ_{HS}, follows the macroscopic master equation

$$d\gamma_{HS}/dt = - \gamma_{HS} k_{HL}(T,\gamma_{HS}), \text{ eq. 1}$$

where *t* stands for time, and $k_{HL}(T,\gamma_{HS})$ is the relaxation rate from HS to LS, which depends non-linearly (due to cooperative effects) on the HS fraction as follows

$$k_{HL}(T,\gamma_{HS}) = k^{0}_{HL}(T).\exp[(1-\gamma_{HS}).E_a^*/k_BT], \qquad \text{eq. 2}$$

where the pre-exponential factor, $k^{0}_{HL}(T) = k_\infty.\exp(-E^{0}_a/k_BT)$ is the relaxation rate in the HS state ($\gamma_{HS} = 1$), E_a the corresponding energy barrier and k_∞ is the "spin flip" frequency from HS to LS at infinite temperature and E_a^* is an effective parameter accounting for the interactions between the SCO units, assumed in this simple model as uniform and temperature-independent. We used this model and fitted all experimental relaxation curves of Figure S11, on which we have superimposed the theoretical findings (red lines). The obtained parameter values of the refinement are summarized in Table S3. An excellent agreement is found between the simulation and the experiments. The following values of the thermodynamic parameters E_a = 590(18) K, k_∞ = 8.2 s^{-1} and E_a^* ~ 180(18) K were extracted from the Arrhenius plot (ln k_{HL} vs 1/T, inset Figure S11). To judge the relevance of these data, we compared them to those of heat capacity measurements. The effective energy barrier $E_a(\gamma_{HS}) = E^{0}_a - E_a^*(1-\gamma_{HS})$ is exactly equal to the enthalpy of transformation for $\gamma_{HS} = 1/2$. According to current photomagnetic data, we derive $E_a(\gamma_{HS} = 1/2)$ = 500 K, that compares well to the value ΔH~560 K, obtained from heat capacity measurements.

A 10K, irradiation of the HS-LS state in the near-infrared region (830 nm) during 60 min (Figure 6) induces a decrease of $\chi_m T$ product from 1.64 to 0.82 cm^3•K•mol^{-1}. This fact indicates the occurrence of reverse-LIESST effect and the presence of a population of neighboring molecules in the LS-LS configuration. Here also, we could not reach the pure LS state due to absorption of light inside the sample. Applying the T(LIESST) procedure, the $\chi_m T$ curves, measured in the dark, slightly increase up to a plateau of around 1.1 cm^3•K•mol^{-1} between 30 and 60 K (Figure 6). This slight increase is attributed to the zero-field splitting of the non-transformed fraction of HS Fe(II) centers (Fe2). Upon further warming, the $\chi_m T$ product increases to recover the value of the intermediate state at ~100 K. The derivative of the curve indicates a T(reverse-LIESST) value of 85 K. The stability of this photo-excited state has been checked through relaxation kinetics at different temperatures. At 75 K, 85 K and 90 K, a small increase of $\chi_m T$ is observed, reaching after one hour a stationary state whose HS fraction value is lower than that of the HS-LS plateau (Figure S12). Interestingly, and contrary to the thermal relaxation of the HS fraction after green light irradiation, none of the relaxation curves starting for the thermal relaxation curve subsequent to near-infra-red

irradiation reached the plateau. Even those performed at high temperature (~90 K) saturated after one hour below the plateau region. Moreover, we observed that the T(reverse-LIESST) is weakly influenced by the temperature sweep rate change. Taken together, these results suggest that the LS state induced by the near-infrared irradiation most likely correspond to a stable state. On heating, this state undergoes a spin transition at $T_{1/2}$~85K, during which only Fe2 sites convert from LS to HS, while Fe1 remain trapped in the LS state. Thus, reverse-LIESST process enabled access to a hidden stable LS state, which was unreachable on cooling from the high-temperature phase.

Let us briefly summarize the key multi-stability features of the current system at low-temperature, according to the data of LIESST and reverse-LIESST experiments: the stability of the three macroscopic configurations is different. The photo-induced (green light) HS-HS state is metastable and then relaxes back to the intermediate configuration according to a dynamical process described by a self-accelerated model. The HS-LS state (plateau) remains stable or metastable with an extremely long lifetime, as confirmed by the relaxation kinetics from the photo-induced HS-HS state which stop at the HS-LS plateau and do not cross this limit. Furthermore, relaxations kinetics, recorded at 75 K, 85 K and 90 K in the intermediate state during 4 hours, did not show any change in the $\chi_m T$ product (Figure S13). This very strong metastability of the intermediate state should be correlated to the above mentioned distortion of the structure at low-temperature, which generates an elastic energy barrier around Fe2 sites, thus enhancing their metastable character. Finally, the existence of the stable LS-LS state paves the way for an interplay and photo-multi-switching between these three states. Thus, at 10 K, the HS-LS intermediate state can be either switched to the HS-HS or the LS-LS states, depending on the wavelength used. Moreover, the LS-LS configuration can be directly reached from the HS-HS state by irradiation at 830 nm and reversely the HS-HS configuration is obtained by irradiation at 510 nm of the LS-LS state (see Figure 7). This bidirectional photoswitching remains effective until 50 K. Above this temperature,the green light irradiation from the HS-LS state is no more efficient, due to the shortening of the lifetime of the photo-induced metastable states, while it is still efficient from the LS-LS state from 1.07 to 2.27 $cm^3 \bullet K \bullet mol^{-1}$. This limit of the $\chi_m T$ value under green light irradiation at this temperature of 50 K is due to the presence of light-induced hysteresis (LITH).

Under permanent light irradiation, upon warming and cooling, the competition between the non-linear relaxation and the light excitation leads to a photo-induced instability, that manifests itself through the presence of LITH (light-Induced Thermal Hysteresis) curves for both irradiation wavelengths (Figure 8).[27,28] The record of several isothermal relaxations

under green light irradiation on the direct-LITH curve of Figure 8a[29] led to photostationnary points that allow to draw the envelop of the quasi-static LITH hysteresis loop, whose width is estimated to be ~ 4 K. At 50 K, isothermal relaxations either from the HS-LS state or from the LS-LS one leads to photo-stationary states with $\chi_m T$ product equal to 2.27 $cm^3 \bullet K \bullet mol^{-1}$ after irradiation for 4 hours. This value is very close to the $\chi_m T$ value of the intermediate plateau. At 45 K and lower, the photoexcitation (resp. relaxation) process becomes fully efficient (resp. inefficient) and a complete LS-LS→HS-HS conversion could be achieved, as shown in Figure 7, at T = 10 K.

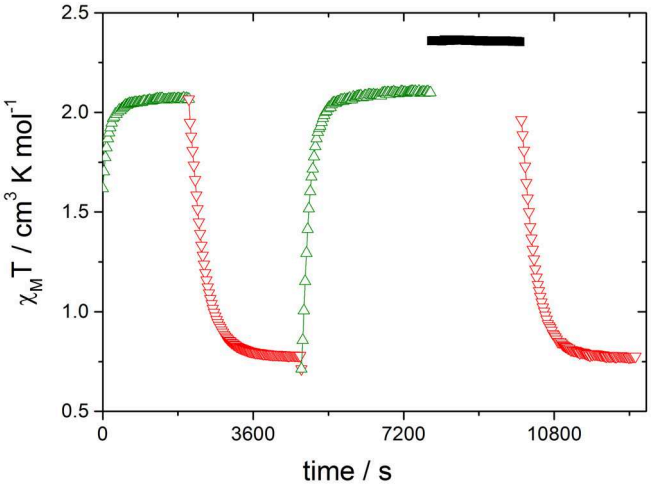

Figure 7. Temporal evolution of the $\chi_m T$ product under 510 nm (Δ) or 830 nm (∇) irradiation, at 10 K. The filled black squares stand for a kinetic recorded in the dark after switching off the light, demonstrating that the decrease observed under 830 nm irradiation is not due to thermal relaxation effects.

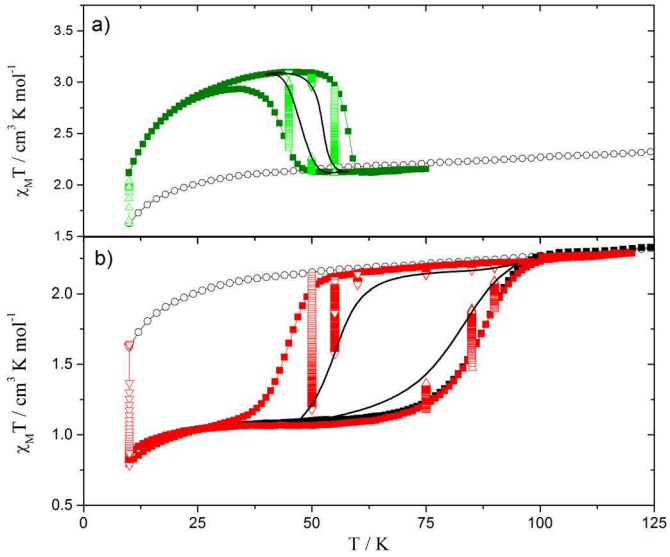

Figure 8. a) Thermal evolution of the $\chi_m T$ product from high temperature to low temperature in the dark (o) and under green light irradiation in warming and cooling mode (■). Photo-stationary points from the HS-LS state (Δ) and from the HS-HS state (∇) were recorded at 45, 50 and 55 K. The black curve stands for the quasi-static hysteresis loop. b) Thermal evolution

of the $\chi_m T$ product from high temperature to low temperature in the dark (o) and under red light irradiation in warming and cooling mode (■). Photo-stationary points from the HS-LS state (∇) and from the LS-LS state (Δ) were recorded at 45, 50 and 55 K. The black curve stands for the quasi-static hysteresis loop. The temperature scan rate was 0.4 K•min^{-1} for both experiments.

LITH curve associated with the reverse-LIESST process (under 830 nm irradiation) is sketched in Figure 8b. It consists in a wide thermal hysteresis with a 25 K wide quasi-static hysteresis loop. Interestingly, on heating, the $\chi_m T$ temporal evolution under this irradiation from the LS-LS state matches perfectly that of the evolution in the dark (Figure S14). Furthermore, the quasi-static curve (black curve in Figure 8b) resulting from the photo-stationary also matches very well that of the dark (Figure S13). The absence of influence of 830 irradiation on the thermal evolution and the relaxation kinetics of the LS-LS state strengthens the argument that the heating branch of the reverse-LITH curve describes the thermal behavior of a stable LS-LS state which undergoes a spin transition towards the LS-HS phase around 80 K. On cooling from the plateau region, near-infrared irradiation favored the occurrence of the reversible HS-LS→LS-LS transition around 50 K. This way, a closed thermal hysteresis loop related to the transition of Fe2 center is observed, while in the dark the system stays desperately trapped in the intermediate state. This behavior indicates the presence of a hidden hysteresis in the HS-LS plateau, which was not accessible due to the slowing down of the relaxation processes on cooling. To look for clear evidence of the existence of the equilibrium cooling branch of the hidden thermal hysteresis we carried out partial excitations using near infrared light at 10 K and measured the thermal dependence of the magnetic response in the dark. The obtained results are summarized in Figure 9. All partial reverse-LIESST photo-excitations (blue, red and olive curves) of Fe2 centers from HS to LS, show on heating, typical trends of thermal relaxation of a part of the residual Fe2 HS fraction towards the LS state, with a relaxation temperature (located at the inflection points of the curves, dashed line) which decreases as the photoexcitation progresses. Besides, the location of the relaxation temperatures, represented by the dashed black curve in Figure 9, matches exactly that of the photo-stationary states, reported in Figure 8b (full black line).

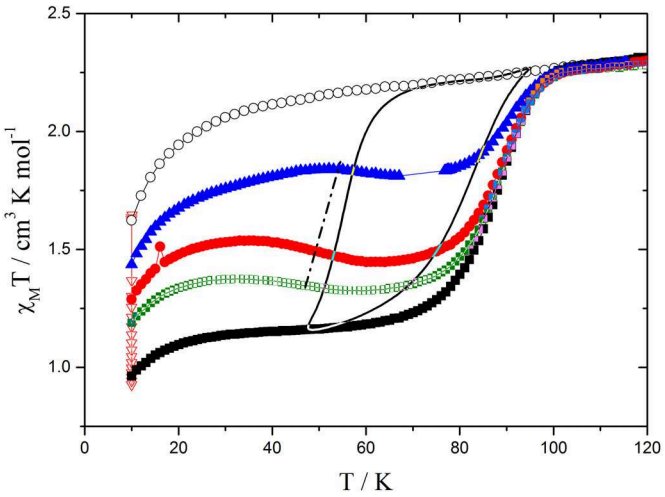

Figure 9. Thermal evolution of the magnetic response in the dark, subsequent to partial photoexcitations using 830 nm wavelength for 4 min (blue) 6 min (red) and 8 min (green). All curves show first an increase of the magnetic signal due to zero field splitting effects, followed by a thermal relaxation of the residual HS fraction towards the "LS" state, before to join the upper heating branch at which the system reaches the limit of the metastability. The temperature sweep rate was 0.4 K•.min^{-1}. The dashed black curve, representing the locus of the inflection points (relaxation temperatures), stand for the "equilibrium" cooling branch of the hidden thermal hysteresis revealed by near-infrared irradiation.

In the light of these photomagnetic studies, the crystal structure has been further derived at 10 K in the three relevant configurations, i.e. in the [HS-LS] state upon cooling from 120 K, after irradiation with 532 nm solid state laser, and after irradiation with 808 nm diode laser. These three states are called IP2, HS2, and LS hereafter. The structural topology described above is retained at 10 K in all the three states, no phase transition or space group change occurs. Upon temperature decrease from 120 K (IP1) to 10 K (IP2), only marginal modifications attributed to thermal contraction effects occurred; the mean Fe1-N and Fe2-N bond distances only slightly decreased within standard deviations. Upon irradiation with 808nm from IP2 phase, the Fe2-N bond distances drastically decreased to a mean value of 1.964(3) Å, which is characteristic of a complete HS to LS spin state change for this Fe2 site, while Fe1 remained in the LS state, in agreement with the photomagnetic data. In contrast, irradiation with 532nm from the IP2 phase led to a large increase in the Fe1-N bond distances, indicative of a LS to HS spin state change for Fe1. Altogether, the crystallographic results (see Table 3) confirm the multi-directional photo-switching features, observed in photomagnetic studies, between the three states [LS-LS], [LS-HS], and [HS-HS] at 10 K. Although, not shown here, reversible direct photo-switching between photo-excited HS-HS and LS-LS states were also possible in photo-crystallography. In all the three states, the

difference in angular distortion between Fe1 and Fe2, that is a higher distortion for Fe2, was preserved, especially in the HS2 state while Fe1 and Fe2 are both assigned a HS state.

Table 3. Selected bond lengths and distortion parameters of the coordination sphere of compound **1**.

Atoms	**distance / Å**		
	10 K (IP2)	**10 K (LS)**	**10K (HS2)**
Fe1-N1	1.944(8)	1.939(3)	2.128(7)
Fe1-N2[1]	1.933(7)	1.947(3)	2.148(7)
Fe1-N5	1.984(5)	1.976(3)	2.183(6)
<Fe1-N>	**1.954(7)**	**1.954(3)**	**2.153(7)**
Fe2-N3	2.146(7)	1.939(3)	2.127(7)
Fe2-N4[2]	2.132(8)	1.956(3)	2.143(7)
Fe2-N9	2.191(5)	1.996(3)	2.201(6)
<Fe2-N>	**2.156(7)**	**1.964(3)**	**2.157(7)**
	Distortion / °		
[a]Σ(Fe1)	5(3)	12(3)	6(3)
[b]Θ(Fe1)	13(2)	34(2)	19(2)
Σ(Fe2)	21(3)	12(3)	18(3)
Θ(Fe2)	53(2)	37(2)	57(2)

[1] 1/2-x,1/2-y,1-z; [2] 1-x,1+y,3/2-z.

[a] Σ is the sum of the deviation from 90° of the 12 *cis*-angles of the FeN_6 octahedron;[22,23] [b] Θ is the sum of the deviation from 60° of the 24 trigonal angles of the projection of the FeN_6 octahedron onto its trigonal faces.[23,24]

The corrugation of the 2D layer, as evidenced by the tilt of the $Fe1N_4$ plane with respect to the $Fe2N_4$ plane, increases continuously from the LS (19.3°) to IP2 (22.4°) to HS2 (28.6°) states (Figure 10). The deformation of the Pt-Fe-Pt-Fe squares within the 2D layers is much reduced in the LS and HS2 states compared to the IP2 state, which exhibits therefore the most important elastic distortion (Table 4). The latter is most likely at the origin of the stabilization of the ordered antiferro-elastic HS-LS structure of the plateau region. The corresponding Fe…Fe, and Pt…Pt distances (Table 4 and Figures S8-S10) range from 7.064 to 7.662 Å in the IP2 state. It is interesting to note that in each case, the difference within Fe…Fe distances is much smaller than those within Pt…Pt distances, which then absorb a part of the structure change resulting from the HS to LS conversion of Fe1.

This is obvious for the IP2 case, where Pt…Pt distances range from 7.064 to 7.662 Å, while the Fe…Fe distances range only from 7.248 to 7.308 Å. An additional inspection of the temperature changes of the Fe…Fe and Pt…Pt distances shows that, from the outset at ambient temperature, the three Pt-Fe-Pt-Fe pseudo-squares show that the largest Pt-Pt distance is systematically obtained for Fe2-Pt-Fe2-Pt pseudo-square. This introduces an elastic frustration maintaining the Fe2 site in the HS state. On decreasing temperature from

296 K, and contrary to the two others, this distance first increases at 120 K, before to collapse at lower temperatures.

Looking more closely to the Fe-N distances between the three states, this elastic distortion becomes obvious. The average Fe-N distances do not change significantly if the corresponding spin state does not change. That is to say <Fe1-N> is identical for LS and IP2, while <Fe2-N> is identical for HS and IP2. On the contrary, individual Fe-N distances exhibit significant changes of about two to three standard deviations. This results from the local distortion of the Fe1 (resp. Fe2) octahedron as a response to the spin state change of Fe2 (resp. Fe1) from IP2 to LS (resp. HS2). The indirect elastic distortion is then mediated by the bridging $[Pt(CN)_4]^{2-}$ entities within the 2D lattice.

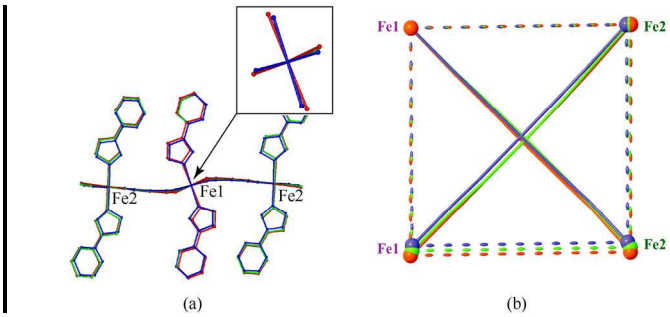

Figure 10. Overlay of the HS2 (red), IP2 (green) and LS (blue) structures at 10 K along the [0 1 0] direction, showing the difference in corrugation. On the left, note especially the rotation of the central Fe1 basal plane (corresponding to P1 in Figure 5).

Table 4. Fe…Fe, Fe…Pt and Pt…Pt distances in the pseudo-squares within the 2D layers (see Figure 3 and Figure S8-S10).

	distance / Å				
	10 K (IP2)	**10 K (LS)**	**10 K (HS2)**	**120 K (IP1)**	**296 K (HS1)**
Fe1…Fe1	7.248	7.084	7.396	7.247	7.404
Fe1…Fe2	7.308	7.220	7.364	7.319	7.409
Fe2…Fe2	7.248	7.084	7.396	7.247	7.404
Pt…Pt[a]	7.064	7.218	7.362	7.073	7.399
Pt…Pt[b]	7.662	7.296	7.506	7.669	7.519
Pt…Pt[c]	7.248	7.084	7.396	7.247	7.404

[a] within Fe1-Pt-Fe1-Pt pseudo square, [b] within Fe2-Pt-Fe2-Pt pseudo square, [c] within Fe1-Pt-Fe2-Pt pseudo square.

■ CONCLUSIONS

A new Hoffman-type framework spin crossover (SCO) system $[Fe(trz\text{-}py)_2\{Pt(CN)_4\}].3H_2O$ has been prepared. Its structure consists of $[FePt(CN)_4]$ layers separated by interdigited 4-(2-pyridyl)-1,2,4,4*H*-triazole (trz-py) ligands with two inequivalent Fe^{II} sites. The 2D network can be described as a succession of Fe_4 pseudo-squares which diagonals are formed by Fe1-Pt1-Fe2 bridges. Interlayer contacts are assisted by π-π interactions between the trz-py ligands

and a strong hydrogen-bonding network that involves three non-coordinated water molecules. $[Fe(trz\text{-}py)_2\{Pt(CN)_4\}].3H_2O$ exhibits an incomplete sharp SCO first-order phase transition centered at 153 K from a HS-HS to a HS-LS structurally ordered state.

Irradiation at 10K with green light induces a photoswitching to HS-HS state, characterized by a T(LIESST) value of 52 K. Photomagnetic measurements show that the HS-HS state is metastable, and relaxes back to the intermediate HS-LS plateau with self-accelerated relaxations, typical for a highly cooperative SCO system. On the contrary, the irradiation of the HS-LS state with near infrared light is efficient only below the T(LIESST) value of the direct LIESST process, and leads to a hidden stable LS-LS state with a markedly different T(reverse-LIESST) value of 85 K. Contrary to the relaxation behavior of the HS-HS state, relaxations from the LS-LS state do not reach the HS-LS plateau, which shows that the LS-LS state is a stable one, and correlatively, the HS-LS state is metastable. The LITH curve associated with the reverse-LIESST process consists in a wide thermal hysteresis whose quasi-static hysteresis loop ranges between 55 and 85 K. All together, these results indicate the presence of a hidden hysteresis in the HS-LS plateau, which was not accessible due to the slowing down of the relaxation processes on cooling; the Fe2 site being trapped in the HS state. Irradiation with near infrared light induces its switching to the LS state.

The photocrystallographic investigations for the three 10 K states at 10K indicate that no structural phase transition and no space group change occur along the bidirectional switching. The very strong metastability of the intermediate HS-LS state originates from antiferroelastic interactions (frustration) within the $[FePt(CN)_4]$ layers, accommodated by NC-Pt-CN bridges between inequivalent SCO active Fe^{II} sites. This elastic distortion manifests itself in the corrugation of the 2D layers and deformation of the square Fe-Pt-Fe-Pt structural topology. The HS-LS state exhibits the most important elastic distortion, which explains its stability.

Most interestingly, these results, and especially the existence of the stable LS-LS state pave the way for an interplay and photo-multi-switching between the three states.

■ EXPERIMENTAL SECTION

2-aminopyridine, diformylhydrazine, potassium tetracyanoplatinate and iron (II) perchlorate were purchased from Sigma-Aldrich and used without further purification. Solvents were used and purified by standard procedures. The 4-(2-pyridyl)-1,2,4, *4H*-triazole (trz-py) was prepared following the procedure described in reference 30. Elemental analyses were performed by the "Service Central d'Analyses du CNRS", Gif-sur-Yvette, France. Infrared

spectra were recorded in the range 4000-50 cm^{-1} on a FT-IR Brucker ATR Vertex 70 Spectrometer.

Synthesis of $[Fe(trz\text{-}py)_2\{Pt(CN)_4\}].3H_2O$ (1). An aqueous solution (10 mL) containing the 4-(2-pyridyl)-1,2,4,4*H*-triazole (146 mg, 1.0 mmol), iron (II) perchlorate (127.5 mg, 0.5 mmol) was left standing overnight. To the resulting light yellow solution, was added $K_2[Pt(CN)_4].xH_2O$ (188.5 mg, 0.5 mmol) and the mixture was stirred at room temperature. The resulting white precipitate was filtered off and dried (yield 41%, 139 mg). Anal. Calcd for $C_{18}H_{18}FeN_{12}O_3Pt$: C, 30.8; H, 2.6; N, 24.0 %. Found: C, 31.1; H, 2.7; N, 24.4 %. IR data (ν/cm^{-1}): 3609(w), 3141(m), 2167(s), 1620(s), 1594(s), 1525(s), 1491(m), 1469(m), 1441(m), 1348(w), 1337(w), 1258(m), 1240(m), 1212(w), 1162(w), 1094(w), 1054(s), 1030(w), 996(w), 863(m), 778(s), 714(w), 671(m), 630(s), 511(m), 460(s), 406(s), 383(s), 332(w), 277(m), 229(s), 225(s), 165(s), 146(m), 100(m), 86(m), 77(m), 68(m), 59(m).Single-crystals of **1** were prepared by slow diffusion, in a fine glass tube (3.0 mm diameter) of two aqueous solutions: the first solution was obtained by dissolving $K_2[Pt(CN)_4].xH_2O$ (37.7mg, 0,1mmol) in 10 mL. The second solution was prepared by dissolving $Fe(ClO_4)_2.xH_2O$ (25.5 mg, 0.1 mmol) in a solution (10 mL) of 4-(2-pyridyl)-1,2,4,4H-triazole (29.2 mg, 0.2 mmol). After standing overnight, a light yellow coloration was appeared. 2 mL of the $K_2[Pt(CN)_4].xH_2O$ solution was placed in the fine glass tube and similar volume of the yellow solution was added carefully in order to limit mixture of the two solutions. The resulting system was allowed to stand undisturbed at room temperature. After two days, colorless small fine square crystals of **1** were formed by slow diffusion. The IR spectrum of such single crystals is identical to that observed for the white powder of **1**. IR data (ν/cm^{-1}): 3609(w), 3141(m), 2167(s), 1619(s), 1594(s), 1525(s), 1490(m), 1468(m), 1441(m), 1337(w), 1258(m), 1239(m), 1212(w), 1161(w), 1094(w), 1054(s), 1029(w), 996(w), 863(m), 778(s), 713(w), 671(m), 630(s), 511(m), 460(s), 406(s), 383(s), 332(m), 277(m), 229(s), 225(s), 199(m), 164(s), 146(m), 100(m), 86(m), 77(m), 68(m), 58(s), 52(m).

Physical characterizations. Single crystal X-ray studies were performed at 296 K and 120 K using a Bruker APEX2 κ-CCD diffractometer using Mo Kα radiation (λ = 0.71073 Å). 10K single crystal diffraction data were collected on a Microfocus Supernova diffractometer equipped with a two dimensional ATLAS detector, using Mo Kα radiation, and a Helijet He open flow cryosystem. Numerical absorption correction was performed. In situ photo-excitations were carried out using a 808 nm diode laser (duration 15 min), and a 532 nm solid state laser (duration 20 min) until the photostationnary state was reached in each case to

populate the LS and HS-2 states respectively. The single crystal sample was rotated continuously during excitation to ensure a homogeneous and complete excitation. The corresponding structures were solved by direct methods with the SHELXS program and refined on F^2 by weighted full matrix least-squares methods using the SHELXL program.[31] All non-hydrogen atoms were refined anisotropically, hydrogen atoms were located in difference Fourier maps and treated using a riding model. Crystallographic data and refinement details are provided in Table 1. Room-temperature X-ray powder diffraction spectrum (XRPD) was recorded on a PANalytical Empyrean X-ray powder diffractometer at 45 kV, 40 mA with a Cu-target tube (see Figure SI-1). NMR spectra were recorded on a Brucker DRX 300MHz. DSC measurements were performed on a DSC-1/LN2 Mettler Toledo calorimeter setting the heat flow scan rate at s = 0.3 K•min^{-1}. Magnetic and photomagnetic measurements were performed with a Quantum Design MPMS-XL-5 SQUID magnetometer in the 2-300 K temperature range with an applied magnetic field of 2 Tesla on assembly of single crystals of compound **1** (with mass of 0.68 mg). The photomagnetic characterizations of compound **1** were carried out using a set of photodiodes. Irradiation was carried out at 10 K several times using different wavelengths (i.e. 405 nm, 510 nm, 650 nm, 830 nm and 980 nm) and power intensities up to 5 mW.cm^{-2} to determine the most efficient conditions to reach a strong photoconversion yield at photo-saturation. LIESST experiments were performed using a 510 nm wavelength. After switching off the irradiation, the temperature was increased at a rate of 0.4 K•min^{-1} up to 100 K, to determine the T(LIESST) value,[28,32-33] and over the range 100–300–10 K, to follow the thermal spin transition. The T(LIESST) value was determined as the minimum of the $\partial\chi_m T/\partial T$ versus T plot (maximum slope in the $\chi_m T$ vs. T plot), corresponding to the temperature at which the light induced HS information is erased.[28] For the kinetic study, the sample was irradiated at 10 K until the saturation of the HS fraction and then the temperature was set to 10, 20, 25, 30, 35 and 40 K and the light was switched off in order to study the relaxation kinetics at these temperatures. Reverse-LIESST experiments were performed by irradiating the sample at 10 K in the plateau region with a 830 nm Diode-Laser (5 mW.cm^{-2}), until reaching the saturation of the LS state.

■ ASSOCIATED CONTENT

Supporting Information

The Supporting Information is available free of charge on the ACS Publications website at DOI: xx.xxxx/jacs.xxxxx

Synthesis and characterization, XRPD, DSC calorimetry; additional structural characterization and photocristallography; supplementary thermal and photo-induced magnetic characterizations (Tables S1-S3 and Figures S1-S14) of **1** (PDF).

Crystallographic data (CIFs)

■ AUTHOR INFORMATION

Corresponding Author

*smail.triki@univ-brest.fr

Notes

The authors declare no competing financial interest.

■ ACKNOWLEDGMENTS

This work was supported by the CNRS ("Centre National de la Recherche Scientifique"), the Brest University, the "Agence Nationale de la Recherche" (ANR project BISTA-MAT: ANR-12-BS07-0030-01), the French ″Ministère de la Recherche et Ministère des Affaires Etrangères et Européennes (PHC MAGHREB Project N° 30255ZJ)″, the Région Aquitaine, the University of Lorraine and University of Paris-Saclay. Authors especially thank the "Service Commun" of NMR facilities of the University of Brest.

■ REFERENCES

(1) see for example: a) Gütlich, P; Goodwin, H. A. (Eds.), *Top. Curr. Chem.* **2004**, *233-235*; b) Real, J.-A.; Gaspar, A.-B.; Niel, V.; Muñoz, M.-C. *Coord. Chem. Rev.* **2003**, *236*, 121; c) Halcrow, M. A. *Coord. Chem. Rev.* **2009**, *253*, 2493; d) Olguin, J.; Brooker, S. *Coord. Chem. Rev.* **2011**, *255*, 203; e) Halcrow, M. A. *Chem. Soc. Rev.* **2011**, *40*, 4119; f) Muñoz-Lara, F. J.; Arcís-Castillo, Z.; Muñoz, M.-C.; Rodríguez-Velamazán, J.-A.; Gaspar, A.-B.; Real, J.-A. *Inorg. Chem.* **2012**, *51*, 11126; g) Gütlich, P; Gaspar, A.-B.; Garcia, Y. *Beilstein J. Org. Chem.* **2013**, *9*, 342.

(2) a) Decurtins, S.; Gütlich, P.; Köhler, C.P.; Spiering, H.; Hauser, A., *Chem. Phys. Lett.* **1984**, *105*, 1-4; b) Hauser, A., *Chem. Phys. Lett.,* **1986**, *124*, 543.

(3) a) Hinek, R.; Spiering, H.; Schollmeyer, D.; Gütlich, P.; Hauser, A. *Chem. Eur. J.* **1996**, *2*, 1427, b) Hinek, R.; Spiering, H.; Gütlich, P.; Hauser, A. *Chem. Eur. J.* **1996**, *2*, 1435.

(4) Feng, X.; Mathonière, C.; Jeon, I.R.; Rouzières, M.; Ozarowski, A.; Aubrey, M.L.; Gonzalez, M.I.; Clérac, R.; Long, J.R. *J. Am. Chem. Soc*. **2013**, 135, 15880.

(5) a) Létard, J.-F.; Real, J.A.; Moliner, N.; Gaspar, A.B., Capes, L.; Cador, O.; Kahn, O. *J. Am. Chem. Soc.* **1999**, *121*, 10630-; b) Chastanet, G.; Carbonera, C.; Mingotaud, C.; Létard, J.-F. *J. Mat. Chem.* **2004**, *14*, 3516; c) Ould Moussa, N.; Molnar, G.; Bonhommeau, S.; Zwick, A.; Mouri, S.; Tanaka, K.; Real, J.A.; Bousseksou, A. *Phys. Rev. Lett.* **2005**, *94*, 107205(4); d) Ould Moussa, N.; Trzop, E.; Mouri, S.; Zein, S.; Molnar, G.; Gaspar, A.B.; Collet, E.; Buron-Le Cointe, M.; Real, J.A.; Borshch, S.; Tanaka, K.; Cailleau, H.; Bousseksou, A. *Phys. Rev. B*. **2007**, *75*, 054101(8).

(6) Wei, R.-J.; Li, B.; Tao, J.; Huang, R.-B.; Zheng L.-S.; Zheng, Z. *Inorg. Chem.* **2011**, *50*, 1170.

(7) a) Chakraborty, P.; Enachescu, C.; Humair, A.; Egger, L.; Delgado, T.; Tissot, A.; Guénée, L.; Besnard, C.; Bronisz, R.; Hauser, A. *Dalton Trans.* **2014**, *43*, 17786; b) Chakraborty, P.; Pillet, S.; Bendeif, E.-E.; Enachescu, C.; Bronisz, R.; Hauser, A. *Chem. Eur. J.* **2013**, *19*, 11418; c) Chakraborty, P.; Enachescu, C.; Walder, C.; Bronisz, R.; Hauser, A. *Inorg. Chem.* **2012**, *51*, 9714; d) Chakraborty, P.; Bronisz, R.; Besnard, C.; Guénée, L.; Hauser, A. *J. Am. Chem. Soc.* **2012**, *134*, 4049.

(8) Létard, J.-F.; Chastanet, G.; Tokoro, H.; Ohkoshi, S. *Curr. Inorg. Chem*. Accepted for publication.

(9) Cobo, S.; Molnar, G.; Real, J. A.; Bousseksou, A. *Angew. Chem. Int. Ed. Engl.* **2006**, *45*, 5786.

(10) Sciortino, N. F.; Scherl-Gruenwald, K. R.; Chastanet, G.; Halder, G. J.; Chapman, K. W.; Létard, J.-F.; Kepert, C. J. *Angew. Chem. Int. Ed. Engl.* **2012**, *51*, 10154.

(11) a) Genre, C.; Jeanneau, E.; Bousseksou, A.; Luneau, D.; Borshch, S. A.; Matouzenko, G. S. *Chem. Eur. J.* **2008**, *14*, 697; b) Matouzenko, G. S.; Molnár, G.; Bréfuel, N.; Perrin, M.; Bousseksou, A.; Borshch, S. A. *Chem. Mater.* **2003**, *15*, 550; c) Moliner, N.; Muñoz, M. C.; Létard, S.; Salmon, L.; Tuchagues, J.-P.; Bousseksou, A.; Real, J. A. *Inorg. Chem.* **2002**, *41*, 6997; d) Garcia, Y.; Kahn, O.; Rabardel, L.; Chansou, B.; Salmon, L.; Tuchagues, J.-P. *Inorg. Chem.* **1999**, *38*, 4663; e) Kahn, O.; Martinez, C. J. *Science* **1998**, *279*, 44; f) Vreugdenhil, W.; van Diemen, J. H.; de Graaff, R. A. G.; Haasnoot, J. G.; Reedjik J.; van Der Kraan, A. M.; Kahn, O.; Zarembowitch, J. *Polyhedron* **1990**, *9*, 2971; g) Haasnoot, J. G.; Vos, J. G.; Groeneveld, W. L. *Z. Naturforsch. B* **1977**, *32*, 14211430.

(12) a) Dupouy, G.; Triki, S.; Marchivie, M.; Cosquer, N.; Gómez-García, C. J.; Pillet, S.; Bendeif, E.-E.; Lecomte, C.; Asthana, S.; Létard, J.-F. *Inorg. Chem*. **2010**, *49*, 9358; b) Dupouy, G.; Marchivie, M.; Triki, S.; Sala-Pala, J.; Gomez-Garcia, C. J.; Pillet, S.; Lecomte, C.; Létard, J.-F. *Chem. Commun.* **2009**, 3404.

(13) a) Bao, X.; Shepherd, H. J.; Salmon, L.; Molnar, G.; Tong, M.-L.; Bousseksou, A. *Angew. Chem., Int. Ed.* **2013**, *52*, 1198; b) Martinez, V.; Arcis Castillo, Z.; Muñoz, M. C.; Gaspar, A. B.; Etrillard, C.; Létard, J.-F.; Terekhov, S. A.; Bukin, G. V.; Levchenko, G; Real, J. A. *Eur. J. Inorg. Chem.* **2013**, 813; c) Ohtani, R.; Yoneda, K.; Furukawa, S.; Horike, N.; Kitagawa, S.; Gaspar, A. B.; Muñoz, M. C.; Real J. A.; Ohba, M. *J. Am. Chem. Soc.* **2011**, *133*, 8600; d) Seredyuk, M.; Gaspar, A. B.; Ksenofontov, V.; Verdaguer, M.; Villain, F.; Gütlich, P. *Inorg. Chem.* **2009**, *48*, 6130; e) Martinez, V.; Gaspar, A. B.; Muñoz, M. C.; Bukin, G. V.; Levchenko, G.; Real, J. A. *Chem. Eur. J.* **2009**, *15*, 10960; f) Southon, P. D.; Liu, L.; Fellows, E. A.; Price, D. J.; Halder, G. J.; Chapman, K. W.; Moubaraki, B.; Murray, K. S.; Létard, J.-F.; Kepert, C. J. *J. Am. Chem. Soc.* **2009**, *131*, 10998; g) Niel, V.; Martinez-Agudo, J. M.; Muñoz, M. C.; Gaspar, A. B.; Real, J. A. *Inorg. Chem.* **2001**, *40*, 3838; h) Kitazawa, T.; Gomi, Y.; Takahashi, M.; Takeda, M.; Enomoto, M.; Miyazaki, A.; Enoki, T. *J. Mater. Chem.* **1996**, *6*, 119; i) Lemus-Santana, A. A.; Rodríguez-Hernández, J.; González, M.; Demeshko, S.; Ávila, M.; Knobel, M.; Reguera, E. *J. Solid State Chem.,* **2011,** *184*, 2124.

(14) a) Sciortino, N. F.; Neville, S. M.; Létard, J.-F.; Moubaraki, B.; Murray, K. S.; Kepert, C. J. *Inorg. Chem.* **2014**, *53*, 7886;; b) Otahani, R.; Arai, M.; Ohba, H.; Hori, A.; Takata, M.; Kitagawa, S.; Ohba, M. *Eur. J. Inorg. Chem.* **2013**, 738.

(15) Dupouy, G.; Marchivie, M.; Triki, S.; Sala-Pala, J.; Salaün, J.-Y.; Gómez-García, C. J.; Guionneau, P. *Inorg. Chem.* **2008**, *47*, 8921.

(16) Setifi, F.; Charles, C.; Houille, S.; Thétiot, F.; Triki, S.; Gómez-García, C. J.; Pillet, S. *Polyhedron* **2013**, *61*, 242.

(17) Setifi, F.; Milin, E.; Charles, C.; Thétiot, F.; Triki, S.; Gómez-García, C. J. *Inorg. Chem.* **2014**, *53*, 97.

(18) Klein, Y. M.; Sciortino, N. F.; Ragon, F.; Housecroft, C. E.; Kepert, C. J.; Neville, S. M. *Chem. Commun.* **2014**, *50*, 3838.

(19) a) Ronayne, K. L.; Paulsen, H.; Höfer, A.; Dennis, A. C.; Wolny, J. A.; Chumakov, A. I.; Schünemann, V.; Winkler, H.; Spiering, H.; Bousseksou, A.; Gütlich, P.; Trautwein, A.X.; McGarvey, J. J. *Phys. Chem. Chem. Phys.* **2006**, *8*, 4685; b) Tuchagues, J. P.; Bousseksou, A.; Molnar, G.; McGarvey, J. J.; Varret, F. *Top. Curr. Chem.* **2004**, *235*, 85.

(20) Sorai, M.; Seki, S. *J. Phys. Chem. Solids* **1974**, *35*, 555.

(21) Dolomanov, O. V.; Bourhis, L. J.; Gildea, R. J.; Howard J. A. K.; Puschmann, H. *J. Appl. Cryst.* **2009**, *42*, 339.

(22) Deeney, F. A;. Harding, C. J.; Morgan, G. G.; McKee, V.; Nelson, J.; Teat, S. J.; Clegg, W. *Dalton trans.* **1998,** 11, 1837.

(23) Guionneau, P.; Marchivie, M.; Bravic, G.; Létard J.-F.; Chasseau, D. *Top. Curr. Chem.* **2004,** 234, 97.

(24) Marchivie, M.; Guionneau, P.; Létard, J.-F.; Chasseau, D. *Acta Cryst.* **2005**, *B61*, 25.

(25) Létard, J.-F. *J. Mater. Chem.*, **2006**, *16*, 2550.

(26) Hauser, A.; Jeftic, J.; Romstedt, H.; Hinek, R.; Spiering, H. *Coord. Chem. Rev.* **1999**, *190-192*, 471.

(27) a) Boukheddaden, K.; Shteto, I.; Hôo, B.; Varret, F. *Phys. Rev. B* **2000**, 6, 14796.

b) Desaix, A.; Roubeau, O.; Jeftic, J.; Haasnoot, J.G.; Boukheddaden, K.; Codjovi, E.; Linarès, J.; Noguès, M.; Varret, F. *Eur. Phys. J. B* **1998**, *6*, 183.

(28) Létard, J-F.; Guionneau, P.; Rabardel, L.; Howard, J. A.-K.; Goeta, A.; Chasseau, D.; Kahn, O. *Inorg. Chem*, **1998**, *37*, 4432.

(29) a) Jeftic, J.; Matsarski, M.; Hauser, A.; Goujon, A.; Codjovi, E.; Linarès, J.; Varret, F. *Polyhedron* **2001**, *20*, 1599; b) Létard, J.-F.; Chastanet, G.; Nguyen, O.; Marcèn, S.; Marchivie, M.; Guionneau, P.; Chasseau, D.; Gütlich, P. *"Molecular Magnets Recent Highlights",* Eds W. Linert & M. Verdaguer**,** Springer Wien N.-Y. **2003**, 49; c) Enachescu, C.; Tanasa, R.; Stancu, A.; Chastanet, G.; Létard, J.-F.; Linares, J.; Varret, F. *J. Appl. Phys*. **2006**, *99*, 08J504.

(30) Wiley, R.H;. Hart, A. J. *J. Org. Chem.* **1953**, *18*, 1368.

(31) Sheldrick, G. M. *Acta Cryst*. **2008**, *A64*, 112.

(32) a) Létard, J.-F.; Capes, L.; Chastanet, G.; Moliner, N.; Létard, S.; Real, J.A.; Kahn, O. *Chem. Phys. Lett*. **1999**, *313*, 115; b) Marcen, S.; Lecren, L.; Capes, L.; Goodwin, H-A.; Létard, J-F. *Chem. Phys. Lett*, **2002**, *358*, 87; c) Létard, J-F.; Guionneau, P.; Nguyen, O.; Costa, J-S.; Marcen, S.; Chastanet, G.; Marchivie, M.; Capes, L. *Chem. Eur. J.* **2005**, *11*, 4582; d) Létard, J-F. *J. Mater. Chem*. **2006**, *16*, 2550.

(33) Létard, J.-F.; Chastanet, G.; Guionneau, P.; Desplanches, C. *In Spin-crossover materials: properties and applications, Ed. M. A. Halcrow,John Wiley & sons, Ltd* **2013**, 475.

Supplementary Information

Hidden Hysteresis Revealed by Photo-switching in a Multi-Stable Two-Dimensional Hoffman-Like Spin-Crossover Metal-Organic Framework

Eric Milin,[a] Véronique Patinec,[a] Smail Triki,[a] El-Eulmi Bendeif,[b] Sébastien Pillet,[b] Mathieu Marchivie,[c] Guillaume Chastanet,[c] Kamel Boukheddaden.[d]

[a]UMR CNRS 6521, Chimie, Electrochimie Moléculaires, Chimie Analytique, Université de Bretagne Occidentale, BP 809, 29285 Brest Cedex, France.

[b]CRM2, UMR CNRS 7036, Institut Jean Barriol, Université de Lorraine, B.P. 70239, F-54506 Vandoeuvre-lès-Nancy, France.

[c]CNRS, Université Bordeaux, ICMCB, 87 Av. Doc. A. Schweitzer, F-33608 Pessac, France.

[d]GEMaC, Université Paris-Saclay, CNRS-Université de Versailles Saint-Quentin-en-Yvelines, 45 Avenue des Etats-Unis 78035 Versailles cedex, France.

---

1 - Synthesis of 4-(2-pyridyl)-1,2,4, 4H-triazole (trz-py) and characterizations.

The 4-(2-pyridyl)-1,2,4, 4H-triazole (trz-py) was prepared the procedure described in reference S1 (Yield: 1.21 g, 36 %). m.p. 169 °C. IR data (ν/cm^{-1}): 3220(w), 3124(w), 2907(w), 2134(m), 2123(m), 1615(m), 1593(m), 1518(m), 1502(w), 1481(s), 1463(w), 1463 (m), 1441(m), 1367(m), 1338(m), 1264(m), 1238(m), 1160(m), 1112(m), 1095(m), 1053(m), 1012(m), 991(m), 945(w), 896(w), 877(w), 838(w), 787(s), 737(m), 712(m), 632 (m), 621(m), 520(m), 464(m). NMR ^{1}H (300 MHz, D_2O): 7.35-7.39 (t, 1H); 7.68-7.71 (d, 1H); 7.92-7.96 (t,1H); 8.45-8.47 (d,1H); 9.17 (s, 2H (trz)). NMR ^{13}C (75 MHz, D_2O): 118.1(C-H(pyr)); 127.3(C-H(pyr)); 143.6(C-H(pyr)); 144.2(C(α-Npyr)); 151.8(C-H(α-Npyr); 165.2(C-H (trz)).

References.

(S1) Wiley, R.H.; Hart, A. J. *J. Org. Chem.* **1953**, *18*, 1368-1371

2 - X-ray powder diffraction.

Room-temperature X-ray powder diffraction spectrum (XRPD) was recorded on a PANalytical Empyrean X-ray powder diffractometer at 45 kV, 40 mA with a Cu-target tube. As clearly indicated by Figure S1, the measured pattern of microcrystalline powder of **1** is qualitatively similar to the pattern derived from the single-crystal crystallographic data.

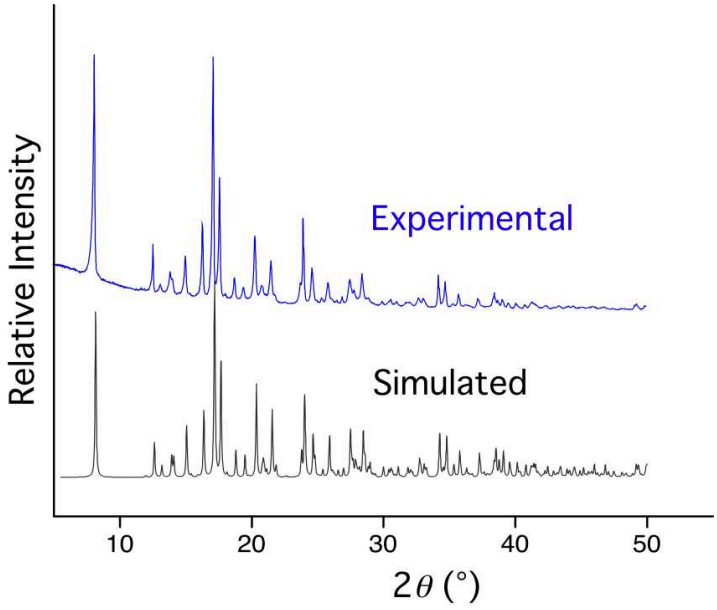

Figure S1. Observed and calculated X-ray powder diffraction patterns for [Fe(trz-py)$_2${Pt(CN)$_4$}].3H_2O (**1**)

3 - Infrared spectra

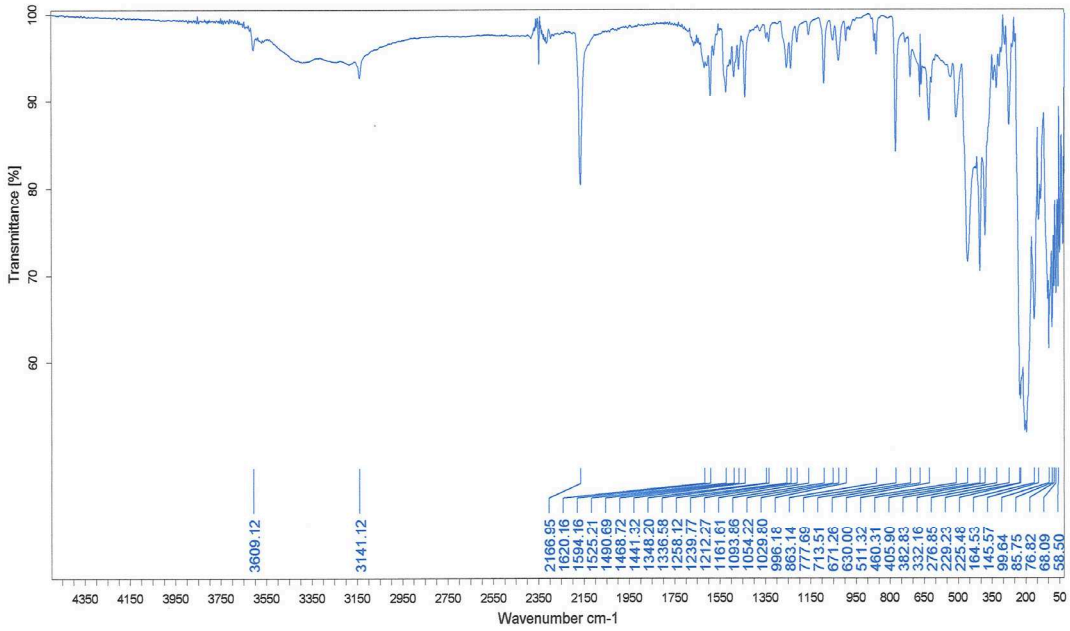

Figure S2. IR spectrum of the microcrystalline powder of $[Fe(trz\text{-}py)_2\{Pt(CN)_4\}].3H_2O$ (**1**)

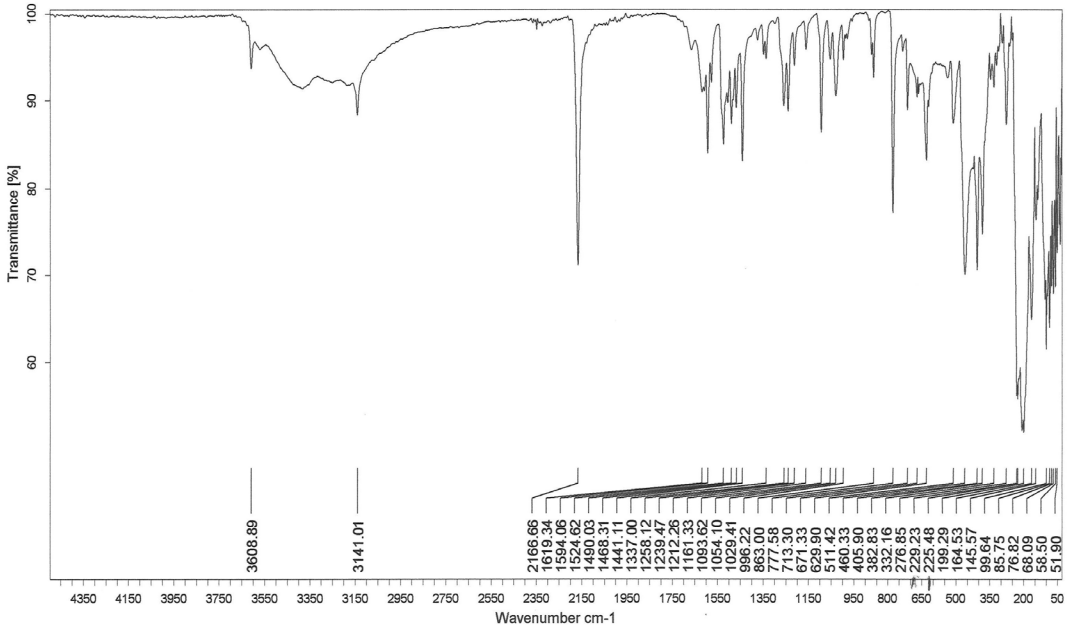

Figure S3. IR spectrum of the single crystals of $[Fe(trz\text{-}py)_2\{Pt(CN)_4\}].3H_2O$ (**1**)

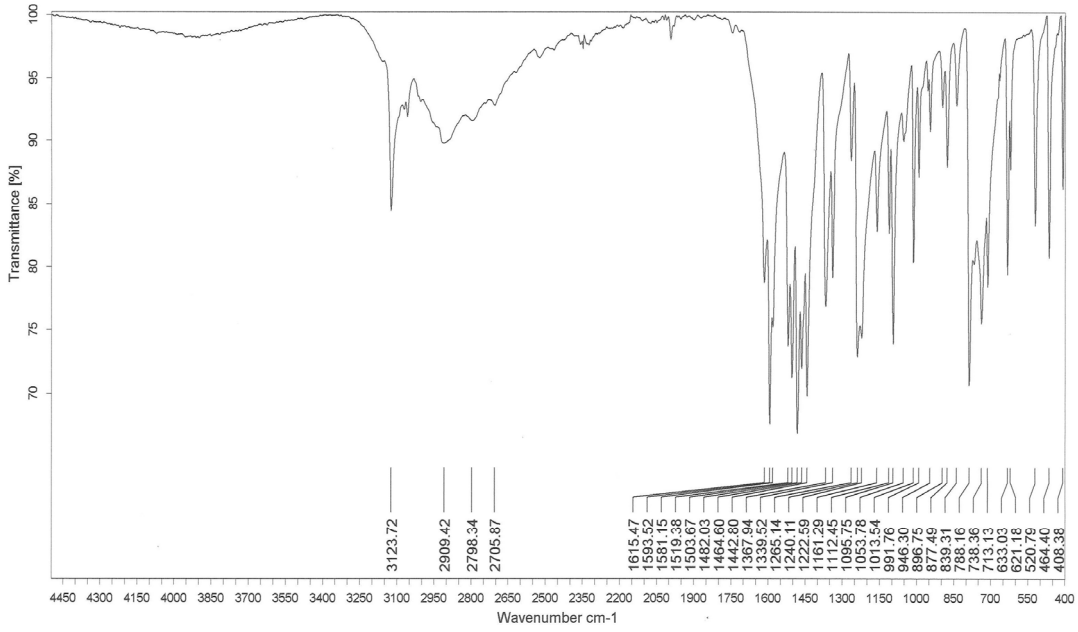

(**a**)

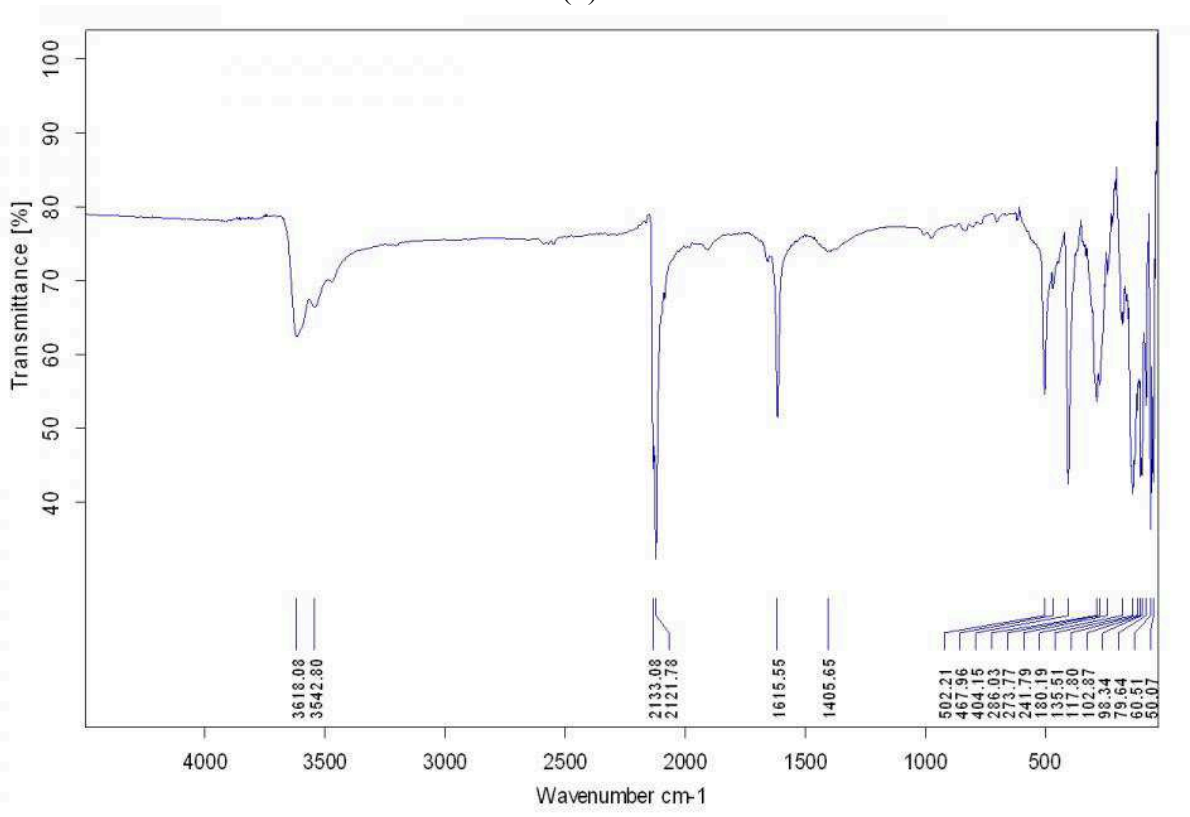

(**b**)

Figure S4. IR spectra of 4-(2-pyridyl)-1,2,4,4*H*-triazole (trz-py) (a) and $K_2[Pt(CN)_4]$ (**b**)

4 – DSC measurements

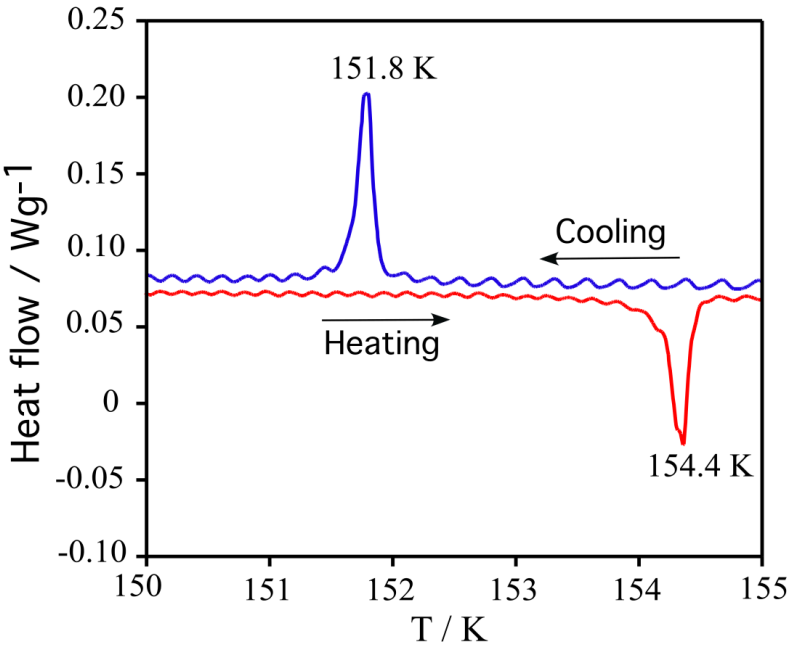

Figure S5. DSC study for sample **1** showing the exo- (cooling mode) and endothermic (heating mode) transitions. The upper and lower transition temperatures, 151.8 and 154.4K, are in excellent agreement with those of magnetic data.

5 – Structural characterization and photocristallography

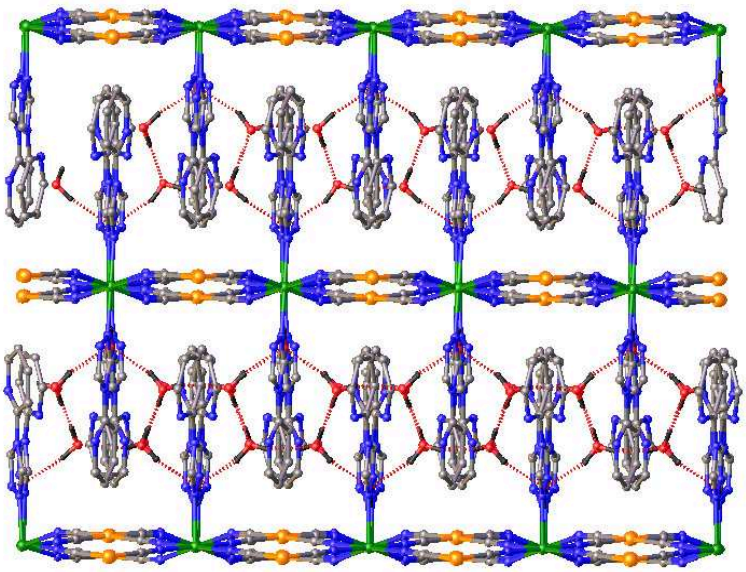

Figure S6. 3D View of the crystal packing of **1** at ambient temperature (296 K) along the [1 0 1] direction. Dashed lines show the hydrogen-bonding network.

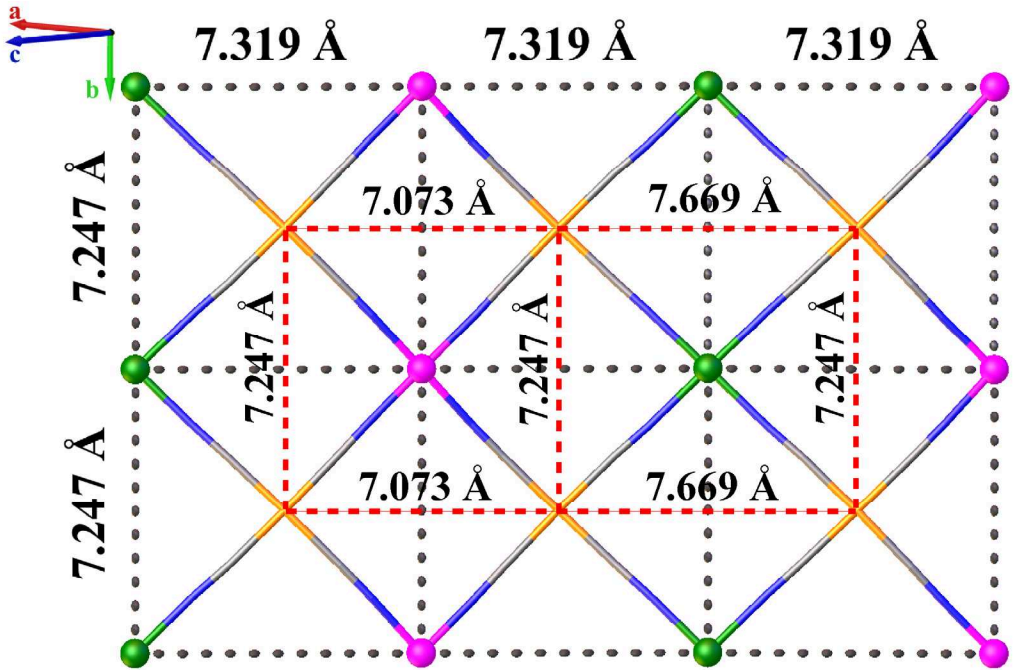

Figure S7. View of the 2D arrangement of **1** at 120 K projected along the [-1 0 1] direction showing the Fe_4 pseudo-squares, Fe…Fe (black dotted lines) and Pt…Pt (red dotted lines) distances.

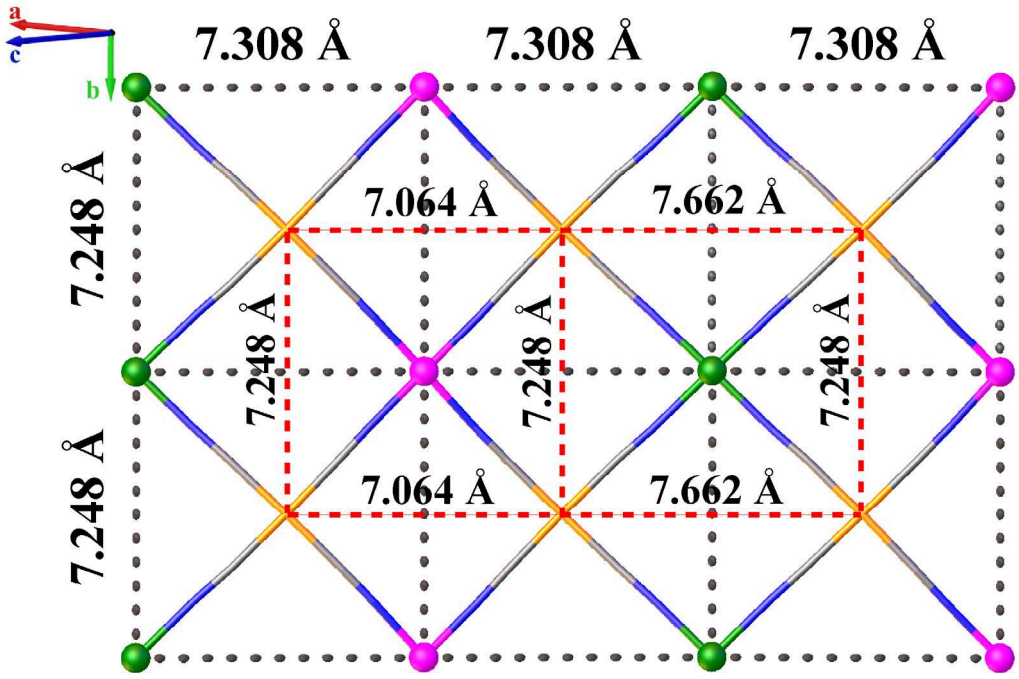

Figure S8. View of the 2D arrangement of **1** at 10 K in the IP2 phase projected along the [-1 0 1] direction showing the Fe_4 pseudo-squares, Fe…Fe (black dotted lines) and Pt…Pt (red dotted lines) distances.

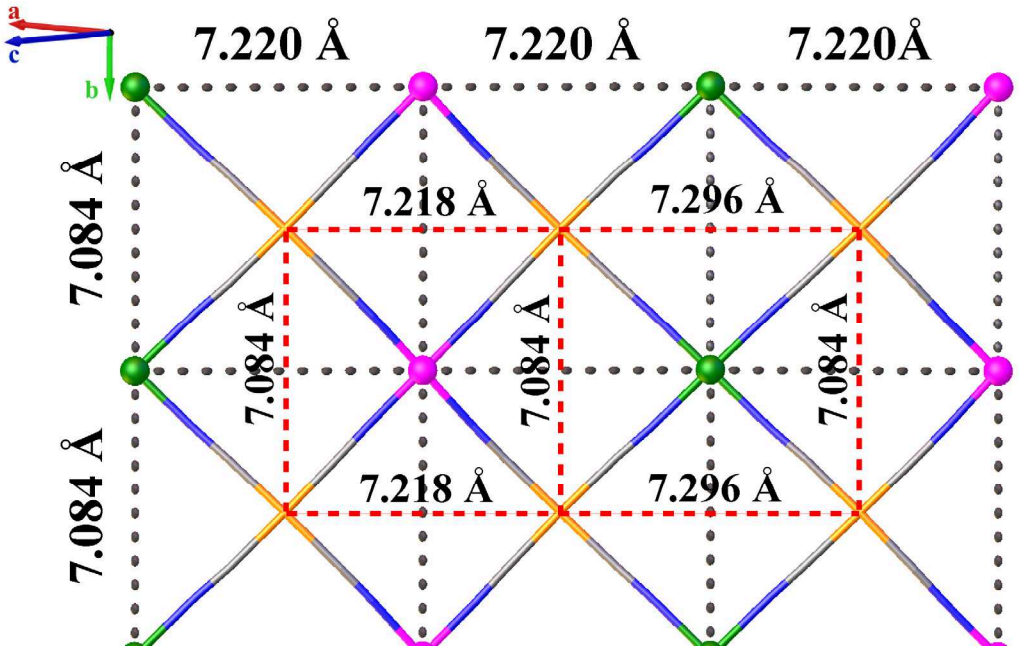

Figure S9. View of the 2D arrangement of **1** at 10 K in the LS phase projected along the [-1 0 1] direction showing the Fe_4 pseudo-squares, Fe…Fe (black dotted lines) and Pt…Pt (red dotted lines) distances.

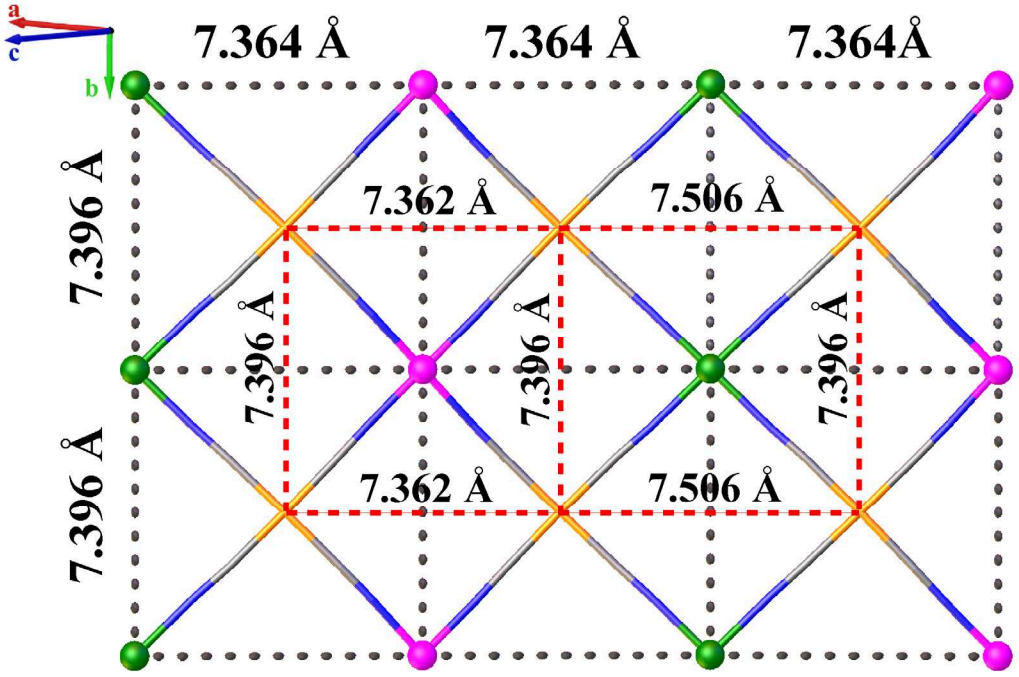

Figure S10. View of the 2D arrangement of **1** at 10 K in the HS2 phase projected along the [-1 0 1] direction showing the Fe_4 pseudo-squares, Fe…Fe (black dotted lines) and Pt…Pt (red dotted lines) distances.

Table S1. Intermolecular hydrogen bonds in **1**.

296 K

D-H···A	d(D-H)/Å	d(H-A)/Å	d(D-A)/Å	D-H-A/°
O1-H1B···N10	0.85	1.98	2.792(3)	160
O3-H3A···O2[1]	0.85	1.98	2.824(4)	175
O3-H3B···O1	0.85	2.04	2.879(3)	169
O2-H2A···O1	0.85	2.05	2.855(3)	158
O2-H2B···O3[2]	0.85	2.06	2.825(3)	148

120 K

D-H···A	d(D-H)/Å	d(H-A)/Å	d(D-A)/Å	D-H-A/°
O1-H1B···N10	0.86(2)	1.94(2)	2.765(3)	160(4)
O3-H3A···O2[1]	0.86(2)	1.95(2)	2.801(4)	175(4)
O3-H3B···O1	0.86(2)	1.97(2)	2.831(3)	172(4)
O2-H2A···O1	0.86(2)	2.03(2)	2.841(3)	158(4)
O2-H2B···O3[2]	0.85(2)	1.99(2)	2.782(4)	155(4)

[1]3/2-x,-1/2+y,3/2-z; [2]+x,1+y,+z

Table S2. π-π contacts in compound **1**.

296 K

Plane 1	Plane 2	c-c (Å)[1]	shift (Å)[2]	Angle (°)[3]
(N9-C12-N11-C13-N10)	(N8-C11-C10-C9-C8-C7)[(a)]	4.008	1.474	11.74
	(N8-C11-C10-C9-C8-C7)[(b)]	3.670	0.777	11.74
(N5-C5-N7-C6-N6)	(N12-C18-C17-C16-C15-C14)[(c)]	3.928	1.526	8.10
	(N12-C18-C17-C16-C15-C14)[(d)]	3.753	1.126	8.10

120 K

(N9-C12-N11-C13-N10)	(N8-C11-C10-C9-C8-C7)[(a)]	3.929	1.513	11.37
	(N8-C11-C10-C9-C8-C7)[(b)]	3.588	0.853	11.37
(N5-C5-N7-C6-N6)	(N12-C18-C17-C16-C15-C14)[(c)]	3.893	1.505	10.87
	(N12-C18-C17-C16-C15-C14)[(d)]	3.677	1.082	10.87

Codes of equivalent positions: (a) = 1/2+x,1/2+y,+z; (b) =1/2+x,3/2+y,+z; (c) = -1/2+x,-3/2+y,+z; (d) = -1/2+x,-1/2+y,+z. [1]centroid-centroid distance; [2]shift distance; [3]angle between planes.

6 – Thermal and photo-induced magnetic studies

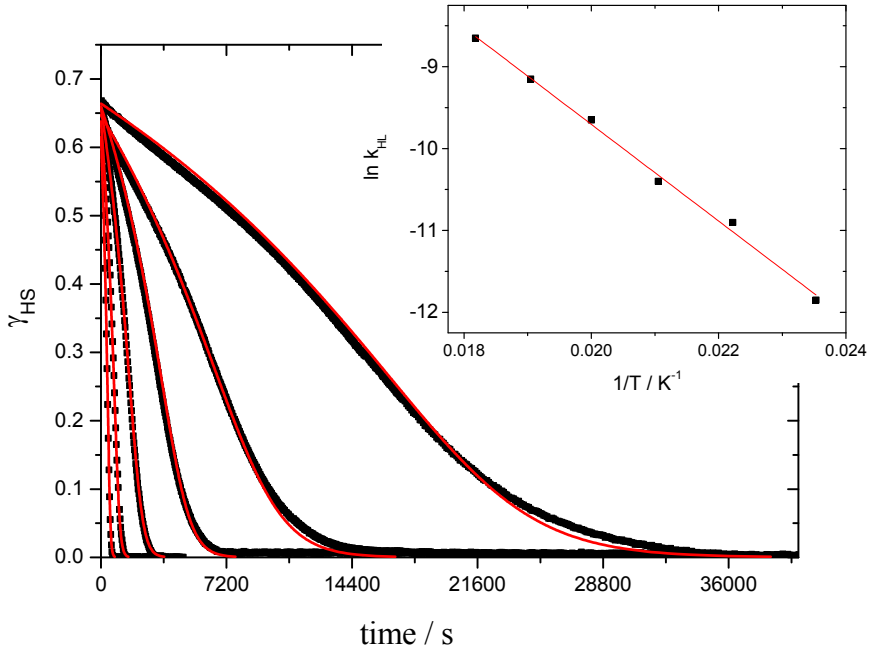

8.

Figure S11. Time dependence, in the dark, of the photo-transformed metastable HS fraction in Figure 6, at temperatures: 42.5, 45, 47.5, 50, 52.5 and 55 K. The inset reports the Arrhenius plot with the relaxation rate value extracted from the simulation discussed in the text (red lines).

Table S3. Relaxation rate and alpha parameters extracted from the relaxation kinetic simulations.

T (K)	**k_{HL} (s^{-1})**	**α**
42.5	$7.14\ 10^{-6}$	3.8
45	$1.84\ 10^{-5}$	3.6
47.5	$3.04\ 10^{-5}$	4
50	$6.44\ 10^{-5}$	4
52.5	$1.06\ 10^{-4}$	4.4
55	$1.75\ 10^{-4}$	4.6

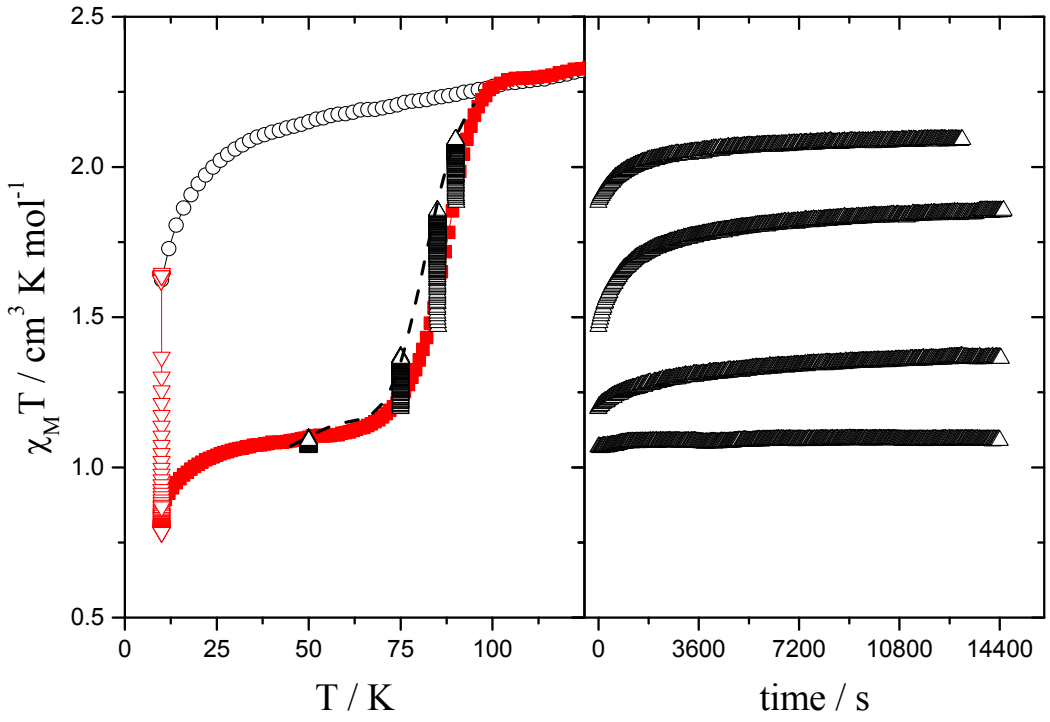

Figure S12. Left) Thermal evolution of the $\chi_m T$ product from high temperature to low temperature in the dark (o), under 830 nm light irradiation at 10 K (▽), and in the dark after irradiation (□). Isothermal relaxations from the LS-LS state, recorded at 50, 75, 85 and 90 K (Δ). Right) temporal evolution of the $\chi_m T$ product of the corresponding kinetics at 50, 75, 85 and 90 K (Δ).

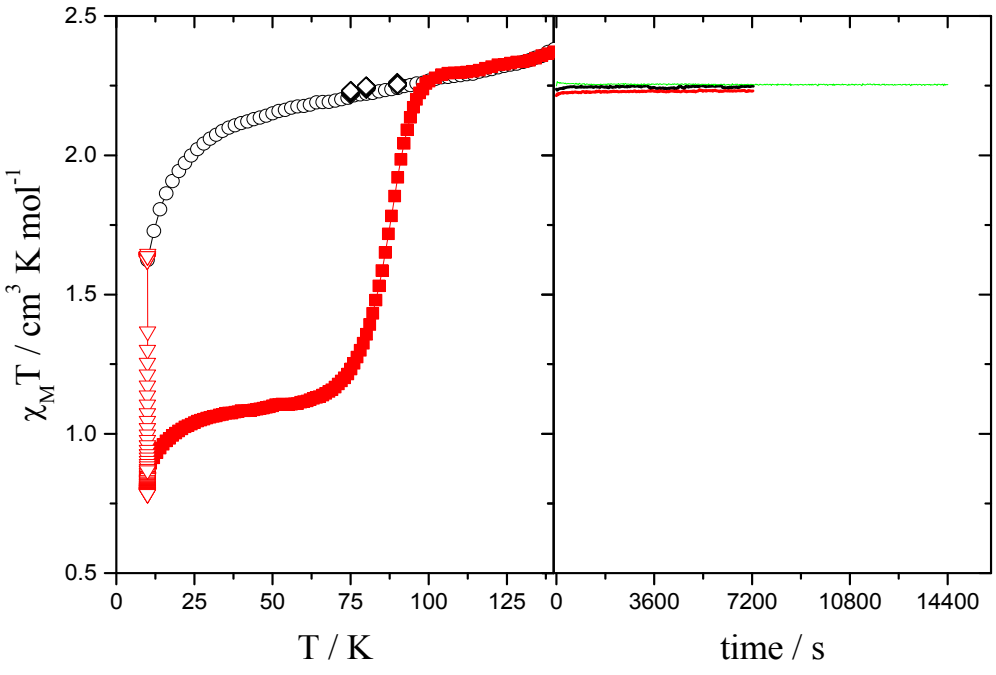

Figure S13. Left) Thermal evolution of the $\chi_m T$ product from high temperature to low temperature in the dark (o), under 830 nm light irradiation at 10 K (▽), and in the dark after irradiation (■). Relaxation kinetics from the HS-LS state were recorded at 75, 85 and 90 K (▽). Right) temporal evolution of the $\chi_m T$ product of the corresponding kinetics at 75, 85 and 90 K (Δ).

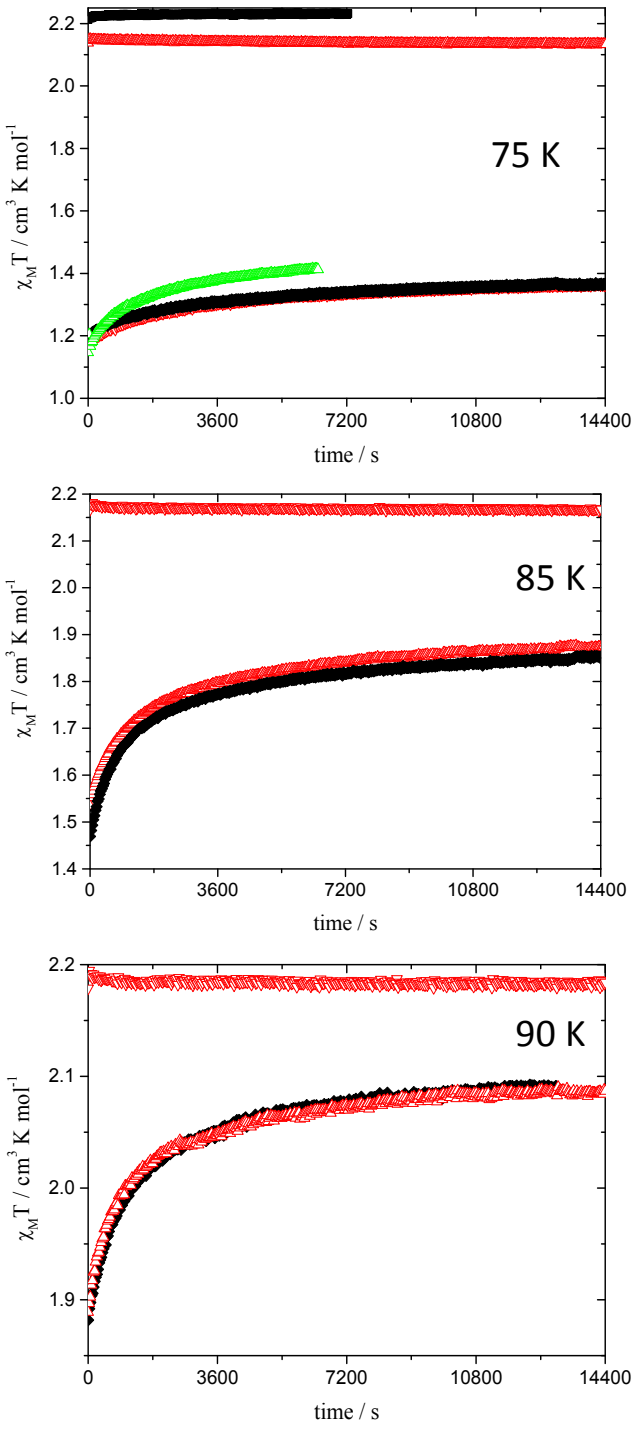

Figure S14. Temporal evolution of the $\chi_m T$ product at 75, 85 and 90 K from both the HS-LS and LS-LS states. Black curves stand for the evolution in the dark. Red curve stand for evolution under 830 nm irradiation. Green curve stand for the evolution under green light irradiation.

Conclusion

Nous avons vu dans ce chapitre la synthèse de deux systèmes polymériques à base du ligand trz-py. Le premier système a généré un réseau 3D. La présence d'une molécule d'eau dans la sphère de coordination du fer a empêché la présence d'une transition de spin et a mis en évidence un mode de coordination du co-ligand anionique $tcpd^{2-}$ pontant μ^4 rencontré une seule fois auparavant.

La substitution du co-ligand anionique $tcpd^{2-}$ par $[Pt(CN)_4]^{2-}$ a permis la synthèse d'un réseau de type Hofmann $[Fe(trz\text{-}py)_2(Pt(CN)_4)].3H_2O$. Ce nouveau réseau à transition de spin est le deuxième de ce type. La transition de spin incomplète montrant une faible hystérésis s'explique par les interactions π-π entre les noyaux aromatiques des ligands trz-py et par les liaisons hydrogène générées par les trois molécules d'eau. L'irradiation dans le vert de ce complexe a montré un effet LIESST (T_{LIESST}=52 K) et l'irradiation dans le rouge un effet reverse LIESST ($T_{REVERSE\text{-}LIESST}$=85 K). Cet écart entre T_{LIESST} et $T_{REVERSE\text{-}LIESST}$ montre que l'état LS-LS photo-induit par irradiation dans le rouge est un état stable et qu'en conséquence le palier observé correspondant à l'état HS-LS est métastable. Cette métastabilité relativement importante s'explique par la présence de deux types de fer et la création d'interactions antiferromagnétiques entre ces deux sites. Cet état LS-LS stable et la présence d'un effet LITH montrent la présence d'une hystérésis cachée qui est mise en évidence en irradiant dans le rouge. Il est donc possible à basse température sous irradiation de photo-commuter le système entre trois états. Ce résultat intéressant ouvre la voie à la synthèse de nouveaux systèmes à transition de spin photo-induite entre trois états.

Conclusion générale

Les objectifs principaux de ce travail étaient l'optimisation des caractéristiques de la transition de spin et l'allongement de la durée de vie des états HS métastables photo-induits. Pour atteindre ces objectifs, notre méthodologie passe nécessairement par la conception de nouveaux systèmes à transition de spin.

Dans le but d'accroître la coopérativité, nous avons adopté deux stratégies. La première consiste à associer un contre-ion à un complexe du fer (II) coordiné par un ligand hexadentate. La nature du contre-ion et les interactions qu'il génère permettent d'augmenter la coopérativité et d'obtenir de la bistabilité thermique. La seconde stratégie consiste à associer à un complexe du fer(II), coordiné par un ligand polydentate contraignant de moindre denticité, un co-ligand ; pour mieux contrôler les interactions intermoléculaires et/ou d'augmenter la dimension du système, plusieurs co-ligands polydentates se différenciant essentiellement par leurs modes de coordination et par leurs rigidités ont été utilisés.

En suivant la première approche, nous avons obtenu le premier système basé sur un macrocycle fonctionnalisé se caractérisant par de la bistabilité moléculaire. Dans cet exemple, de formule $[Fe(L2)](tcm)_2,2H_2O$, la bistabilité thermique est créée par des liaisons hydrogène entre les anions $(tcm)^-$ et les molécules d'eau. Cet exemple pourrait être considéré comme un cas d'école dans lequel nous avons clairement montré qu'une simple modification de l'environnement du complexe, comme la nature du contre-ion, pourrait générer des nouvelles propriétés telles que la bistabilité magnétique. En plus de l'effet du contre-ion, nous avons également étudié dans cette première partie, l'influence d'une modification du ligand sur les caractéristiques de la transition de spin. La substitution des bras pyridine du ligand L2 par des groupements aniline a conduit à un nouveau ligand que nous avons étudié. Nous n'avons pas pu isoler de systèmes avec les ions fer(II) mais obtenu un complexe de Cu(II) de formule $[Cu(L'2)](BF_4)_2$. L'étude structurale de ce dernier a montré que le cation métallique s'est parfaitement inséré dans la cavité macrocyclique. Une fois de plus, nous avons montré, dans cette première partie, qu'une simple modification chimique du ligand (substitution de bras pyridines par des groupements anilines) entraine un mode de coordination différent. Cette modification a été transposée à un autre ligand le tmpa (tris(2-pyridylmethyl) amine) où

nous avons remplacé un groupement pyridine par une aniline. Après avoir préparé le complexe dinucléaire $[Fe_2(tmpa)_2(\mu_2\text{-}tcpd)_2]\bullet 2CH_3OH$ à base du ligand tris(2-pyridylmethyl) amine (tmpa), nous avons examiné l'effet de la substitution de groupement pyridine par des groupements aniline en préparant la complexe de formule $[Fe_2(andmpa)_2(\mu_2\text{-}tcpd)_2].2CH_3OH$. Les études magnétiques ont montré que les deux types de complexes à transition de spin se distinguent par des températures de transition très différentes ($T_{1/2}$ = 350 K pour $[Fe_2(tmpa)_2(\mu_2\text{-}tcpd)_2]\bullet 2CH_3OH$; $T_{1/2}$ = 200 K pour $[Fe_2(andmpa)_2(\mu_2\text{-}tcpd)_2].2CH_3OH$.

Dans les chapitres suivants (Chapitres 3 et 4), nous avons envisagé d'étudier des systèmes à structures étendues pour mieux comprendre l'effet de la dimension du réseau et des contacts covalents entre les centres actifs sur les caractéristiques de la transition de spin. Pour aboutir à des systèmes polymériques, nous avons associé des co-ligands anioniques potentiellement pontants tels que le cyanocarbanion $(tcpd)^{2-}$ et les anions inorganiques tétracyanométallates $[M^{II}(CN)_4]^{2-}$, (M = Ni, Pd, Pt) à des ligands organiques se différenciant par leurs modes de coordination (Cf. Schéma V.1).

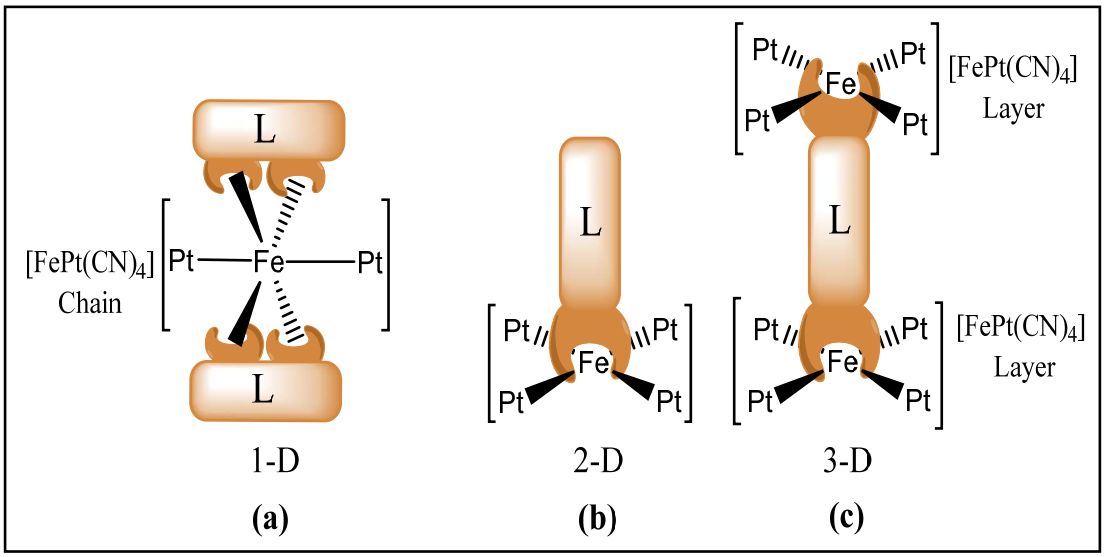

Schéma V.1. Exemple de stratégie utilisée pour la conception des systèmes à dimensions variées.

Dans le chapitre 3, l'association du précurseur $[Fe(aqin)_2]^{2+}$ (aqin = 8-aminoquinoline) aux anions $[M^{II}(CN)_4]^{2-}$ (M = Ni, Pd, Pt) a conduit à une série de trois matériaux bimétalliques à structure monodimensionnelle. Les études magnétiques ont montré que les trois dérivés présentent des transitions de spin abruptes et la coopérativité, dans ces trois exemples, dépend de la nature de l'anion inorganique.

Pour obtenir des systèmes bi- et tridimensionnels (2D et 3D), nous avons envisagé, dans la dernière partie (chapitre 4), l'utilisation de ligands pour lesquels le mode de coordination chélate est exclu. Ainsi, notre choix s'est porté sur le ligand trz-py (4-(2-pyridyl)-1,2,4,4*H*-triazole), susceptible de conduire aux modes de coordinations pontant ou terminal selon la nature du ligand anionique utilisé (Schéma V.2).

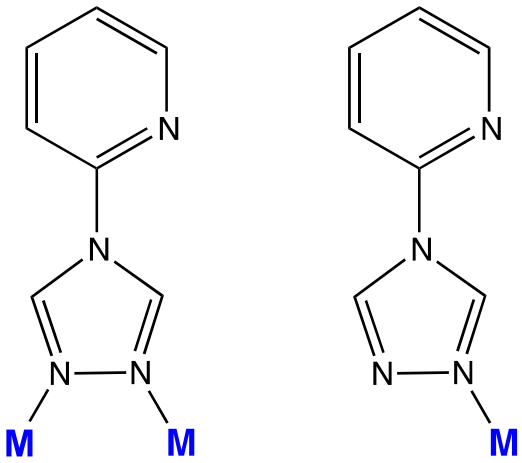

Schéma V.2. Modes de coordinations observés pour le ligand trz-py

Dans un premier temps, l'association du ligand trz-py à l'anion organique $(tcpd)^{2-}$ a conduit à un système tridimensionnel $[Fe(trz\text{-}py)(tcpd)(H_2O)]$. La caractérisation structurale de ce dérivé a montré que les deux types de ligands sont en mode de coordinations pontants. Cependant, la présence d'une molécule d'eau dans la sphère de coordination du fer empêche la présence de toute transition de spin. Ceci a été clairement confirmé par les études magnétiques.

Dans un second temps, nous avons synthétisé un autre système en substituant le ligand anionique $(tcpd)^{2-}$ par l'anion inorganique $[Pt(CN)_4]^{2-}$, potentiellement pontant. Ainsi, nous avons préparé et caractérisé le dérivé bimétallique de formule $[Fe(trz\text{-}py)_2(Pt(CN)_4)].3H_2O$. Les études structurales ont montré que ce dérivé est un réseau bi-dimensionnel se caractérisant par deux sites de Fe(II) différents. Les études détaillées de magnétisme, de photomagnétisme et de photocristallographie ont montré que ce dérivé présente de la multistabilité magnétique et une hystérèsis cachée révélée par de la photo-excitation : une transition partielle ($T_{1/2}$= 85 K) avec une légère hystérésis (3 K) confirmée par calorimétrie (DSC) ; l'étude des propriétés magnétiques sous irradiation a montré un effet LIESST (T_{LIESST}= 52 K) et reverse-LIESST ($T_{REVERSE\ LIESST}$= 85 K) ; nous avons montré que l'état photo-induit BS-BS était un état stable accessible uniquement par photoexcitation dans le rouge ; le palier observé HS-BS est un état métastable avec

une cinétique de relaxation très importante ; l'ensemble de ces observations a révélé la présence d'une hystérésis cachée. Ces résultats ouvrent de belles perspectives pour de la photo-commutation entre 3 états de spin (BS-BS, BS-HS, HS-HS).

Bien que la synthèse de nouveaux complexes à transition de spin soit difficile pour les raisons évoquées en introduction, les principaux objectifs de ce travail sont atteints. L'obtention de ces différents systèmes a permis d'enrichir notre connaissance sur les modes de coordination des ligands neutres et des co-ligands anioniques utilisés. S'il est difficile de prévoir les caractéristiques de la transition de spin, la connaissance de la dimension du système est prévisible. Les nouveaux systèmes décrits dans ce manuscrit, et d'autres systèmes étudiés au laboratoire à partir de triazole fonctionnalisé et des anions tétracyanométallates (thèses en cours de Mame Ndiaye Nguenar et Narsimha Pittala) nous ont permis de mettre en évidence le lien entre la denticité du ligand neutre associé à $[Pt(CN)_4]^{2-}$ et la dimension du réseau.

Dans le but d'obtenir les systèmes les plus coopératifs possibles, nous envisageons d'utiliser des ligands susceptibles de conduire à des modes de coordination de type pontant (Schéma V.3).

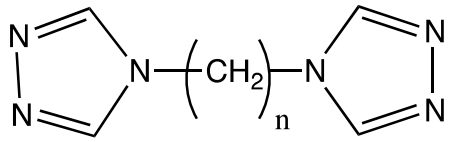

Schéma V.3. Exemple de ligand pontant envisagé

De tels ligands permettraient de moduler l'interaction entre les plans métalliques pour mieux comprendre la coopérativité dans ce type de système.

D'autre part, la substitution des anions tétracyanométallates par des ligands anioniques organiques, plus flexibles pourra également nous permettre de mieux comprendre l'effet de la flexibilité de ces ligands anioniques sur la coopérativité des systèmes polymériques.

Annexe 1

Publications acceptées

Inorganic Chemistry

Article

pubs.acs.org/IC

Spin Crossover Iron(II) Coordination Polymer Chains: Syntheses, Structures, and Magnetic Characterizations of $[Fe(aqin)_2(\mu_2\text{-}M(CN)_4)]$ (M = Ni(II), Pt(II), aqin = Quinolin-8-amine)

Fatima Setifi,[†,‡] Eric Milin,[†] Catherine Charles,[†] Franck Thétiot,[†] Smail Triki,*[,†] and Carlos J. Gómez-García[§]

[†]UMR CNRS 6521, Chimie, Electrochimie Moléculaires, Chimie Analytique, Université de Bretagne Occidentale, BP 809, 29285 Brest Cedex, France

[‡]Laboratoire de Chimie, Ingénierie Moléculaire et Nanostructures (LCIMN), Université Ferhat Abbas de Sétif, 19000 Sétif, Algeria

[§]Instituto de Ciencia Molecular (ICMol), Parque Científico, Universidad de Valencia, C/Catedrático José Beltrán, 2, 46980 Paterna, Valencia, Spain

Supporting Information

ABSTRACT: New Fe(II) coordination polymeric neutral chains of formula $[Fe(aqin)_2(\mu_2\text{-}M(CN)_4)]$ (M = Ni^{II} (**1**) and Pt^{II} (**2**)) (aqin = Quinolin-8-amine) have been synthesized and characterized by infrared spectroscopy, X-ray diffraction, and magnetic measurements. The crystal structure determinations of **1**–**2** reveal in both cases a one-dimensional structure in which the planar $[M(CN)_4]^{2-}$ (M = Ni^{II} (**1**) and Pt^{II} (**2**)) anion acts as a μ_2-bridging ligand, and the two aqin molecules as chelating coligands. Examination of the intermolecular contacts in the two compounds reveals that the main contacts are ascribed to hydrogen bonding interactions involving the amine groups of the aqin chelating ligands and the nitrogen atoms of the two non bridging CN groups of the $[M(CN)_4]^{2-}$ (M = Ni^{II} (**1**) and Pt^{II} (**2**)) anion. The average values of the six Fe–N distances observed respectively at room temperature (293 K) and low temperature (120 K), that is, 2.142(3) and 2.035(2) Å for **1**, and 2.178(3) and 1.990(2) Å for **2**, and the thermal variation of the cell parameters (performed on **2**) are indicative of the presence of an abrupt *HS*-*LS* spin crossover (*SCO*) transition in both compounds. The thermal dependence of the product of the molar magnetic susceptibility times the temperature ($\chi_m T$), in cooling and warming modes, confirms the *SCO* behavior at about 145 and 133 K in **1** and **2**, respectively, and reveals the presence of a small thermal hysteresis of about 2 K for each compound.

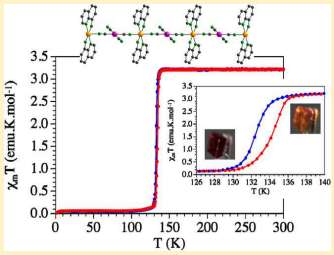

INTRODUCTION

The design of new coordination complexes exhibiting the spin crossover phenomenon (*SCO*) is one of the most relevant challenges in the field of magnetic molecular materials.[1−9] The *SCO* systems relate to the pseudo-octahedral d^4-d^7 transition metal complexes for which the high spin (*HS*) and the low spin (*LS*) electron configurations can be reversibly switched by external stimuli such as temperature, pressure, magnetic field, or light irradiation.[5−20] Nevertheless, the primary investigated systems to date remain those based on Fe(II) (d^6 configuration), for which a paramagnetic-diamagnetic transition from the *HS* ($S = 2$) state to the *LS* ($S = 0$) state is observed. Up to now, most of the reported *SCO* Fe(II)-based examples refer to mononuclear compounds.[21−28] In such discrete systems, the intermolecular interactions (π-stacking, hydrogen bonding, and van der Waals interactions), which generate the supramolecular architecture in the solid state, play a crucial role in the information transmission of the magneto-elastic cooperative effects at the origin of the magnetic bistability. However, the non covalent character of those contacts hardens the anticipated design of the supramolecular organization in the crystal, and consequently makes difficult the tailoring of the *SCO* characteristics.

To better explore the cooperative effect between the active metal ions, a new approach based on the use of neutral suitable bridging ligands, able to create covalent links between the metal centers, has been introduced. The first monodimensional polymeric *SCO* compound, $[Fe(Htrz)_2(trz)](BF_4)$ (trz^- = 1,2,4-triazolate anion) was reported by Haasnoot and co-workers in 1977; it exhibits successfully a large thermal hysteresis.[29] Similarly, the use of substituted 1,2,4-triazole ligands led to other one-dimensional (1D) *SCO* polymers for which some of them exhibit cooperativity at high temperature.[30] In parallel, the extension of such polymeric approach to poly-N-donating heterocyclic ligands and to the bis(azolyl)-alkanes resulted in the preparation of several iron(II) *SCO* coordination polymers exhibiting rich and fascinating structural features ranging from 1D to three-dimensional (3D) networks, and various magnetic behaviors.[31−35]

Received: July 4, 2013

dx.doi.org/10.1021/ic401721x | Inorg. Chem. XXXX, XXX, XXX–XXX

Table 1. Crystal Data and Structural Refinement Parameters for Compounds $[Fe(aqin)_2(\mu_2\text{-}M(CN)_4)]$; M = Ni^{II} (1) and Pt^{II} (2)

	1		2	
temperature/K	293(2)	120(2)	293(2)	120(2)
[a]empirical formula	$C_{22}H_{16}N_8FeNi$		$C_{22}H_{16}N_8FePt$	
formula weight	506.99		643.37	
wavelength/Å	0.71073		0.71073 Å	
crystal system	monoclinic		monoclinic	
space group	$P2_1/c$		$P2_1/c$	
a/Å	9.1819(6)	9.0033(5)	9.3073(3)	9.0290(2)
b/Å	12.0719(7)	12.0053(6)	12.1228(4)	12.0904(3)
c/Å	9.7282(5)	9.6117(5)	9.9073(3)	9.8107(3)
β/deg	100.258(6)	100.043(6)	101.670(4)	101.124(3)
volume/Å^3	1061.07(11)	1022.98(9)	1094.74(6)	1050.86(5)
Z	2	2	2	2
D_{calc}/g.cm^{-3}	1.587	1.646	1.952	2.033
abs. coef./mm^{-1}	1.598	1.658	7.072	7.367
F(000)	516	516	616	616
crystal size/mm^3	0.16 × 0.08 × 0.05	0.13 × 0.11 × 0.04	0.16 × 0.15 × 0.08	0.16 × 0.15 × 0.08
2θ range/deg	6.56−63.30	6.66−60.00	6.42−60.00	6.56−60.00
refl. collected	10548	7201	10604	10188
unique refl./R_{int}	3324/0.0785	2884/0.0340	3174/0.0330	3057/0.0230
data/restr./N_v	1273/0/148	1571/0/148	2017/0/148	2094/0/148
[b]R1/[c] wR2	0.0423/0.0732	0.0385/0.0984	0.0226/0.0494	0.0186/0.0480
[d]GoF	0.906	0.910	0.973	1.125
$\Delta\rho_{max/min}$ (e Å^{-3})	+0.543/−0.376	+1.319/−0.337	+0.890/−0.351	+1.371/−0.442

[a]The asymmetric unit contains 0.5 of the chemical formula. [b]$R1 = \sum||F_o| - |F_c||/\sum|F_o|$. [c]$wR2 = \{\sum[w(F_o^2 - F_c^2)^2]/\sum[w(F_o^2)^2]\}^{1/2}$. [d]$GoF = \{\sum[w(F_o^2 - F_c^2)^2]/(N_{obs} - N_{var})\}^{1/2}$.

However, the limited number of potentially appropriate bridging ligands slows down the emergence of extended polymeric systems exhibiting covalent links between the metal active centers. In this context, we have noticeably extended, in recent years, this polymeric approach to the highly conjugated cyanocarbanion ligands involving several potentially donating nitrogen atoms.[36] This led us to the first *SCO* iron(II) molecular neutral chain $[Fe(abpt)_2(tcpd)]$ ($(tcpd)^{2-}$ = $(C[C(CN)_2]_3)^{2-}$ = 2-dicyanomethylene-1,1,3,3-tetracyanopropanediide anion; abpt = 4-amino-3,5-bis(pyridin-2-yl)-1,2,4-triazole) involving an anion as bridging ligand.[37] In our ongoing work on innovative potentially bridging ligands appropriate for the design of novel *SCO* polymeric systems, we have reported recently two new polymeric chains $[Fe(abpt)_2(M(CN)_4)]$ (M = Ni^{II}, Pt^{II}) involving more rigid anionic bridging ligands.[38] However, these 1D compounds display *SCO* transitions above room temperature, making it difficult to reach any structural and electronic informations on the *HS* state. Thus, with the purpose to better control the transition temperature in such systems involving inorganic planar anions and more distinctly to shift the *SCO* transition below room temperature, we have substituted abpt ligand by other chelating ligands such as the quinolin-8-amine (aqin). This chelating ligand is expected to display lower crystal field energy than the abpt ligand since the discrete $[Fe(abpt)_2(dca)_2]$ complex shows a *SCO* transition at $T_{1/2}$ of 86 K,[39a] while the corresponding aqin discrete complex ($[Fe(aqin)_2(dca)_2]$) is paramagnetic and does not exhibit any *SCO* transition.[39b] We report herein the syntheses and the full structural characterizations including thermal variation of the crystallographic structural data, and magnetic properties of two new *SCO* Fe(II) coordination polymer chains of formula $[Fe(aqin)_2(\mu_2\text{-}M(CN)_4)]$ (M = Ni^{II} (**1**) and Pt^{II} (**2**)) involving tetracyanonometallate anions as bridging ligands. Note that this study can be viewed as an extension of large series employing these planar anions or other parent cyano anions such as $[M(CN)_2]^-$ (M = Ag^I, Au^I) to design *SCO* materials exhibiting multidimensional networks including the 3D Hofmann-like Networks.[12,40]

EXPERIMENTAL SECTION

General Remarks. All reactions were carried out under aerobic conditions. The starting materials and solvents were purchased from commercial sources (analytical reagent grade) and used without further purification.

Syntheses of $[Fe(aqin)_2(\mu_2\text{-}M(CN)_4)]$ (M = Ni^{II} (1) and Pt^{II} (2)). An ethanolic solution (5 mL) of aqin (0.5 mmol, 72.08 mg) was added progressively, under continuous stirring, to an aqueous solution (10 mL) of $Fe(BF_4)_2{\cdot}6H_2O$ (0.25 mmol, 84.39 mg). The mixture was stirred at room temperature for 15 min and then an aqueous solution (10 mL) of $K_2[M(CN)_4]$ (for M = Ni^{II}: 0.25 mmol, 60.25 mg; for M = Pt^{II}: 0.25 mmol, 94.34 mg) was added dropwise. The resulting orange precipitate was filtered off, washed with cold water and ethanol, and dried. Yield: 92.6 mg, 73.0% for **1** and 122.8 mg, 76.3% for **2**. For **1**: *Anal.* Calc. (%) for $C_{22}H_{16}FeN_8Ni$: C, 52.1; H, 3.2; N, 22.1. Found: C, 52.3; H, 3.3; N, 21.9. IR (cm^{-1}): 3278(m), 3183(m), 3131(m), 2140(s), 2120(s), 1626(m), 1579(s), 1503 (s), 1471(m), 1424(w), 1400(m), 1375(m), 1320(m), 1223(w), 1203(w), 1173(w), 1134(m), 1103(m) 1071(m), 1053(m), 1026(s), 826(s), 789(s), 772 (s), 717(m), 633(m), 581(m), 520(m), 602(w), 583(w), 555(w), 524(w), 436(s), 420(s). For **2**: *Anal.* Calc. (%) for $C_{22}H_{16}FeN_8Pt$: C, 41.1; H, 2.5; N, 17.4. Found: C, 41.5; H, 2.4; N, 17.6. IR (cm^{-1}): 3283(m), 3181(m), 3130(m), 2146(s), 2131(s), 1625(m), 1578(m), 1502 (s), 1470(m), 1397(w), 1372(w), 1319(m), 1133(w), 1099(w), 1069(m), 1050(s), 1024(s), 827(s), 789(s), 772(s), 714(m), 631(m), 581(m), 555(m), 525(m), 498(m), 470(m).

Single Crystal Preparation of $[Fe(aqin)_2(\mu_2\text{-}M(CN)_4)]$ (M = Ni^{II} (1) and Pt^{II} (2)). Single-crystals of compounds **1**−**2** were synthesized using a silica gel diffusion technique in a straight tube. The gel phase was obtained by addition of tetramethoxysilane (1 mL) to an aqueous solution (9 mL) of $K_2[M(CN)_4]$ (0.45 mmol; 108.4 mg for **1** and 169.8 mg for **2**) with stirring; the gel was formed from the resulting

dx.doi.org/10.1021/ic401721x | *Inorg. Chem.* XXXX, XXX, XXX−XXX

solution left standing for 6 h. Then, two aqueous solutions (6 mL) of $Fe(SO_4)\cdot 7H_2O$ (0.15 mmol, 41.7 mg) and aqin ligand (0.33 mmol, 47.6 mg) were prepared and carefully layered onto the respective gels. Single-crystals of compounds **1** (dark orange) and **2** (orange), suitable for X-ray analyses, were formed within two weeks. As expected, the IR data for single crystals of both compounds are similar to those observed for the corresponding powders described above.

X-ray Crystallography. Crystallographic studies of the two derivatives (**1**–**2**) were performed at 293 and 120 K, using an Oxford Diffraction Xcalibur κ-CCD diffractometer equipped with a graphite monochromated Mo Kα radiation (λ = 0.71073 Å). The full sphere data collections were performed using 1.0° ω-scans with an exposure time of 150 and 200 s per frame for **1**, 60 and 80 s per frame for **2** at 293 and 120 K, respectively. Data collection and data reduction were done with the CRYSALIS-CCD and CRYSALIS-RED programs on the full set of data.[41] The crystal structures were solved by direct methods and successive Fourier difference syntheses, and were refined on F^2 by weighted anisotropic full-matrix least-squares methods.[42] All non-hydrogen atoms were refined anisotropically, while the hydrogen atoms were calculated and therefore included as isotropic fixed contributors to F_c. All other calculations were performed with standard procedures (WINGX).[43] Crystal data, structure refinement and collection parameters are listed in Table 1. The room-temperature X-ray powder diffraction spectra (XRPD) were recorded on a PANalytical Empyrean X-ray powder diffractometer at 45 kV, 40 mA with a Cu-target tube.

Physical Measurements. Infrared spectra were recorded in the range 4000–200 cm^{-1} on a FT-IR BRUKER ATR VERTEX70 Spectrometer. Diffraction analyses were performed using an Oxford Diffraction Xcalibur κ-CCD diffractometer. Variable temperature magnetic susceptibility measurements were carried out in the temperature range 2–300 K in cooling and warming scans with an applied magnetic field of 0.5 T on polycrystalline samples obtained grinding single crystals of compounds **1** and **2** (with masses of 6.805 and 3.600 mg, respectively) with a Quantum Design MPMS-XL-5 SQUID magnetometer. The susceptibility data were corrected for the sample holders previously measured under the same conditions, and for the diamagnetic contributions as deduced by using Pascal's constant tables (χ_{dia} = -245.36×10^{-6} and -273.36×10^{-6} emu.mol^{-1} for **1** and **2**, respectively).[44] The magnetic measurements were performed with different cooling and warming rates in the range 0.5–5 K/min. The results obtained, within experimental error, were independent of the rate. Elemental analyses were performed at the "Service de microanalyse", CNRS, 91198 Gif-sur-Yvette, France.

RESULTS AND DISCUSSION

Single-crystals of compounds **1** and **2** were synthesized using a silica gel diffusion since the direct mixture of the precursors yielded microcrystalline powders in all cases. Single-crystals of compounds **1** (dark orange) and **2** (orange), suitable for X-ray analysis, were formed within two weeks. The room-temperature XRPD of compound **1** has been performed to confirm that the sample used for magnetic and infrared measurements is effectively identical to the corresponding single crystals used for X-ray structure study (see Supporting Information, Figure S1). The IR spectra of compounds **1** and **2** show two characteristic $\nu_{(CN)}$ bands (2140(s), 2120(s) for **1** and 2146(s), 2131(s) for **2**) which are distinct from the stretching vibration modes observed in $K_2[M(CN)_4]\cdot xH_2O$ (M = Ni^{II} and Pt^{II}).[45] These values can be respectively assigned to the presence of bridging and terminal CN groups, in agreement with the bridging coordination mode of the $[M(CN)_4]^{2-}$ anions in both compounds.

The crystal structures of compounds **1**–**2** were performed at room temperature (293 K) and at 120 K. The unit cell parameters, crystal and refinement data are summarized in Table 1. Selected bond lengths and angles for the iron(II) coordination sphere, including distortion parameters, are summarized in Table 2. The following general structural descriptions are specified at 293 K for both compounds. The pertinent structural modifications induced by cooling or warming will be discussed further in the paragraph dealing with structural and magnetic properties relationships. The two compounds are isostructural as the structure is built from one Fe(II) cation, one $[M(CN)_4]^{2-}$ anion (M = Ni^{II}(**1**) and Pt^{II} (**2**)), both located on inversion centers, and one chelating aqin ligand located on a general position. As shown in Figure 1, the Fe(II) ion adopts a distorted FeN_4N_2 octahedral geometry, with four equatorial nitrogen atoms from two aqin chelating ligands (N1, N2, $N1^{(i)}$, and $N2^{(i)}$), and two axial nitrogen atoms (N3 and $N3^{(i)}$) from two equivalent $[M(CN)_4]^{2-}$ ligands. At room temperature, the average values of the six Fe–N distances are 2.142(3) and 2.178(3) Å for **1** and **2**, respectively. The bond lengths and angles of the two $[M(CN)_4]^{2-}$ (M = Ni^{II}, Pt^{II}) anions are similar to those observed in other coordination complexes involving this moiety.[46,47] The trigonal distortion of the octahedral Fe(II) environment is highlighted by the Σ and Θ parameters (see details in Table 2).[48,49]

Table 2. Selected Bond Lengths (Å), Bond Angles, and Distortion Parameters (deg) of the Fe(II) Coordination Spheres for Compounds 1–2[a]

	1 (M = Ni^{II})		**2** (M = Pt^{II})	
T/K	293	120	293	120
Fe–N1	2.131(3)	2.022(2)	2.170(3)	1.989(2)
Fe–N2	2.161(2)	2.071(2)	2.206(3)	2.031(2)
Fe–N3	2.133(3)	2.011(2)	2.157(3)	1.949(2)
⟨Fe–*N*⟩	2.142(3)	2.035(2)	2.178(3)	1.990(2)
N1–Fe–N3	87.41(10)	87.67(10)	87.68(11)	87.46(10)
N1–Fe–$N3^{(i)}$	92.59(10)	92.33(10)	92.32(11)	92.54(10)
N1–Fe–N2	78.88(10)	82.22(9)	77.48(10)	83.02(10)
N1–Fe–$N2^{(i)}$	101.12(10)	97.78(9)	102.52(10)	96.98(10)
N2–Fe–N3	93.14(9)	93.68(9)	92.85(10)	93.98(10)
N2–Fe–$N3^{(i)}$	86.86(9)	86.32(9)	87.15(10)	86.02(10)
[b]Σ	67	55	71	54
[c]Θ	207	154	233	144

[a]Codes of equivalent positions: (i) $-x,-y,1-z$. [b]Σ is the sum of the deviation from 90° of the 12 *cis*-angles of the FeN_6 octahedron.[48] [c]Θ is the sum of the deviation from 60° of the 24 trigonal angles of the projection of the FeN_6 octahedron onto its trigonal faces.[49]

Indeed, the relatively high values of the Σ and Θ parameters observed for both compounds at room temperature are indicative of the high degree of distortion of the FeN_6 octahedrons, typical of a *HS* coordination sphere. The resulting molecular structures for **1**–**2** can be described as a chain running along the crystallographic [001] direction, in which the planar $[M(CN)_4]^{2-}$ (M = Ni^{II}, Pt^{II}) anion acts as a μ_2-bridging ligand via two nitrogen atoms of two trans cyano groups (Figure 1). Along the neutral chains, the shortest Fe···Fe (Fe···$Fe^{(iii)}$ in Figure 1) and M···M distances (see Figure 1 for M = Pt^{II}) are simply defined by the length of the crystallographic *c* cell parameter (see Table 1). Consequently and as clearly depicted in Figure 1, these intrachain separations (Fe···Fe and M···M, with M = Ni^{II} (**1**) and Pt^{II} (**2**)) impose the shortest Fe···M distance to equal half of the crystallographic *c* cell parameter (4.8641(5) and 4.9536(3) Å at 293 K for **1** and **2**, respectively), in agreement with the linear arrangement of the metal ions along the [001] direction. The crystal packing of **1**–

dx.doi.org/10.1021/ic401721x | *Inorg. Chem.* XXXX, XXX, XXX–XXX

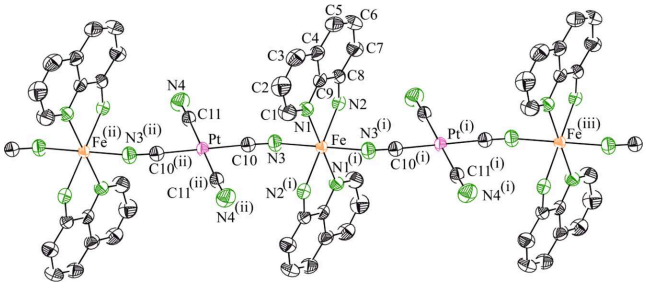

Figure 1. Ortep[50] plot (50% probability ellipsoids) of the 1D neutral structure of **2** at 293 K showing the asymmetric unit, the atom labeling scheme, and the metal ion environment. Codes of equivalent positions: (i) $-x,-y,1-z$; (ii) $-x,-y,-z$; (iii) $x,y,z+1$ (similar figure for the Ni^{II} analogue (**1**)).

2 is generated from the regular chains which are arranged in an eclipsed fashion along the [100] direction, leading to the structural arrangement depicted in Figure 2.

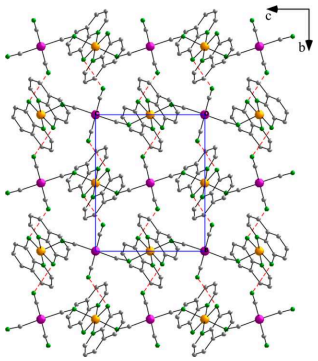

Figure 2. Projection view of the overall molecular structure of compound **2** (similar to **1**) showing the eclipsed packing of the 1D bimetallic coordination polymer along the [100] direction, and the interchain hydrogen bonding (red dashed lines) along the [010] direction.

Careful examination of the intermolecular separations in the two compounds (Figures 2–3 and Table 3) reveals two main types of interchain contacts, both occurring in the [010] direction: (i) hydrogen bonding interactions involving one of the hydrogen atoms of the amine group (N2 and $N2^{(i)}$) of the chelating aqin ligands and the nitrogen atom of the two non bridging CN groups (N4 and $N4^{(ii)}$) from the $[M(CN)_4]^{2-}$ anion of an adjacent chain ($N2\cdots N4^{(b)}$ 3.123(4) and 3.132(4) Å for **1** and **2**, respectively), leading to the structural arrangement depicted in Figure 2 and (ii) the π-stacking interactions between two aqin ligands from two adjacent chains, as shown in Figure 3. The shortest interchain contacts observed for both compounds, as well as their thermal evolution, are gathered in Table 3.

The thermal dependence of the product of the molar magnetic susceptibility per Fe(II) ion times the temperature ($\chi_m T$) is depicted in Figures 4–5. For compound **1**, the $\chi_m T$ value observed at room temperature (300 K) is about 2.65 emu·K·mol^{-1}. This value is significantly lower than the value expected for a hexacoordinated *HS* ($S = 2$, $^5T_{2g}$) Fe(II) ion.

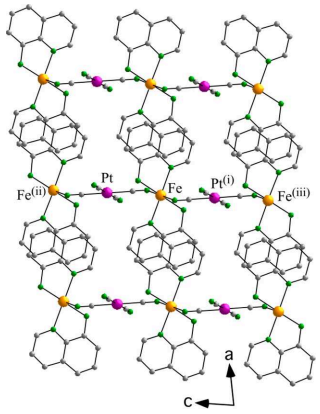

Figure 3. Projection view of **2** (similar to **1**) showing the interchain π-stacking contacts between aqin coligands from adjacent chains. Codes of equivalent positions: (i) $-x,-y,1-z$; (ii) $-x,-y,-z$; (iii) $x,y,z+1$.

This relatively low $\chi_m T$ value indicates the existence, at room temperature, of a fraction of about 20% of Fe(II) ions in the *LS* configuration. It is also noteworthy to indicate that even upon heating the sample above 300 K, the $\chi_m T$ product remains almost constant, and the transition is not fully achieved at 400 K. Upon cooling, the $\chi_m T$ product of **1** decreases gradually, down to a value of about 2.3 emu·K·mol^{-1} at a temperature of about 150 K. Below this temperature, a sharp decrease is observed, indicating the occurrence of an abrupt *HS-LS SCO* transition, with a transition temperature ($T_{1/2}$) of about 145 K. Below 120 K, the $\chi_m T$ value is close to about 0.50 cm^3·K·mol^{-1}, in agreement with the presence of a residual fraction (ca. 15%) of Fe(II) ions in the *HS* configuration. The presence of about 1/5 fraction of Fe(II) centers which remain in the *HS* configuration at low temperatures may be attributed to the presence of defects and vacancies in the chain that lead to the formation of more or less large 1D islands where the *HS* to *LS* transition of one Fe(II) center prevents its neighbors to transit, resulting in a fraction of *HS* Fe(II) centers. The presence of a similar fraction of Fe(II) centers in **1** that remain in the *LS* configuration even at high temperatures (400 K) may be attributed to vacancies or defects in the lattice, or to the possible linkage isomerism of a small fraction of the CN

dx.doi.org/10.1021/ic401721x | *Inorg. Chem.* XXXX, XXX, XXX–XXX

Table 3. Main Interchain π-Stacking C···C contacts and shortest N···N hydrogen bonding (Å) in 1–2[a]

		1 (M = Ni^{II})		2 (M = Pt^{II})	
		T = 293 K	T = 120 K	T = 293 K	T = 120 K
π-stacking C···C contacts	C3···C7$^{(iv)}$	3.497(1)	3.465(1)	3.505(1)	3.490(1)
	C5···C9$^{(iv)}$	3.567(1)	3.558(1)	3.564(1)	3.588(1)
	C4···C7$^{(iv)}$	3.548(1)	3.483(1)	3.621(1)	3.534(1)
	C5···C8$^{(iv)}$	3.540(1)	3.491(1)	3.628(1)	3.544(1)
	C4···C8$^{(iv)}$	3.643(1)	3.640(1)	3.674(1)	3.718(1)
	C6···C9$^{(iv)}$	3.604(1)	3.561(1)	3.676(1)	3.608(1)
	C4···C6$^{(iv)}$	3.708(1)	3.654(1)	3.762(1)	3.658(1)
N···N H-bonding	N2···N4$^{(v)}$	3.123(4)	3.069(3)	3.132(4)	3.059(4)

[a]Codes of equivalent positions: (iv) 1−x,−y,1−z, (v) x,−1/2−y,1/2+z.

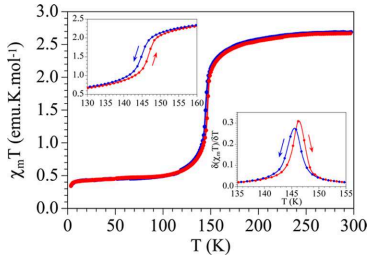

Figure 4. Thermal variation of the $\chi_m T$ product in **1** in the cooling (blue) and warming (red) scans. Left inset shows a zoom of the transition. Right inset shows the thermal variation of the derivative of $\chi_m T$.

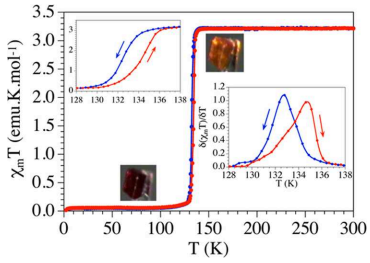

Figure 5. Thermal variation of the $\chi_m T$ product in **2** in the cooling (blue) and warming (red) scans. Left inset shows a zoom of the transition. Right inset shows the thermal variation of the derivative of $\chi_m T$.

bridges. However, this last hypothesis could not be *clear-cut* verified with the IR spectra study since the new bands expected for the small fraction of putative Fe-CN-Ni isomer were not unambiguously detectable, possibly as a consequence of their supposed weak intensity with also the potential masking effect from the more intense bands assigned to the two non bridging and the two bridging CN groups. In addition, there are no structurally characterized examples of Fe^{II}-CN-Ni^{II} linkage isomerism, even if they are known in other CN-bridged systems with Cr^{III} and different M^{II} ions as Fe, Co, and Cu.[51] Interestingly, this CN linkage isomerism would not be expected in the Pt derivative (**2**), in agreement with the much softer character of the Pt(II) ion as compared with the Ni(II) one. Furthermore, the warming mode reveals a very small hysteresis of about 2 K (insets in Figure 4). At very low temperatures, the residual fraction of *HS* Fe(II) ions shows the expected zero field splitting (*ZFS*), leading to a slight decrease of the $\chi_m T$ product, to reach a value of about 0.35 emu·K·mol^{-1} at 2 K.

For the Pt analogue (**2**), the $\chi_m T$ value observed in the high temperature region is about 3.30 emu K mol^{-1}. This value is consistent with a S = 2 *HS* state of the octahedral Fe(II) ions with $g \approx 2.1$. Upon cooling, the $\chi_m T$ product remains constant, down to a temperature of about 134 K. Below this temperature, the sharp decrease on display is indicating the occurrence of an abrupt *HS-LS SCO* transition, as expected from the abrupt color change observed for the single crystals (Figure 5). Below 132 K, the $\chi_m T$ value is close to 0.0 cm^3·K·mol^{-1}, hence revealing the absence of any significant residual fraction of *HS* Fe(II) ions. The warming mode shows a slight thermal hysteresis; indeed, the spin transition temperatures ($T_{1/2}$) for the cooling ($T_{1/2}^{down}$) and warming ($T_{1/2}^{up}$) scans are 132.5 and 134.5 K, respectively, indicating the occurrence, as in **1**, of an about 2 K wide hysteresis loop (see insets Figure 5). The presence of these narrow thermal hysteresis in both compounds can be explained thanks to the existence of weak intermolecular interactions (H-bonds and π–π stacking in both compounds) described above.

On the basis of the conclusions derived from the magnetic data, the crystal structures have been determined at 293 and 120 K for both compounds, and the temperature dependence measurement of the lattice parameters of a single crystal of **2** was performed in the range 293–100 K. The corresponding structural parameters are depicted in Figures 6–7 and in Table 2. Some of these parameters, such as the average coordination distance ⟨Fe-*N*⟩ and trigonal distortion parameters Σ and

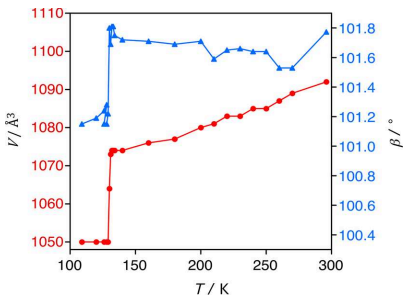

Figure 6. Thermal variation of the unit cell volume (●) and the angular β (▲) parameter in **2** (the blue and red lines are indicated simply to guide the eye).

dx.doi.org/10.1021/ic401721x | *Inorg. Chem.* XXXX, XXX, XXX–XXX

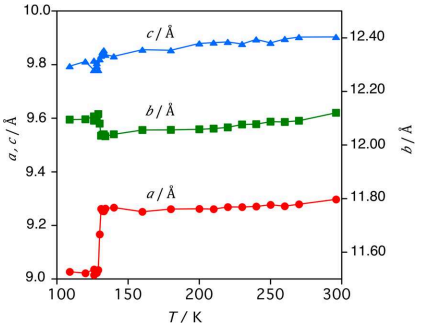

Figure 7. Thermal variations of the lattice parameters of compound **2**; *a* (●), *b* (■), and *c* (▲) parameters revealing the abrupt *SCO* transition, the transition temperature, and the anisotropic contraction of the crystal. The two vertical axis are drawn using the same scale (the blue, green, and red lines are indicated simply to guide the eye).

(previously defined in Table 2), are known to be highly sensitive to the Fe(II) spin configuration, and will thus be used hereafter to assign the spin state on each Fe crystallographic site ($\langle$Fe-*N*$\rangle_{LS}$ ∼ 2.0 Å; $\langle$Fe-*N*$\rangle_{HS}$ ∼ 2.2 Å).[37,46,47]

The thermal variation of the average values of the six Fe—N distances observed for **1**—**2** at room and low temperatures (2.142(3) and 2.035(2) Å for **1**; and 2.178(3) and 1.990(2) Å for **2**, at 293 and 120 K, respectively) reveals strong modifications of the iron coordination spheres in both compounds. For compound **2**, the averaged values observed at 293 and 120 K are in the range of those expected for the *HS* (∼ 2.2 Å) and the *LS* (∼ 2.0 Å) states of the Fe(II) ion, in complete agreement with the corresponding magnetic data aforementioned for this compound. Conversely, the averaged Fe—N value observed at room temperature for **1** (2.142(3) Å) is lower than the value expected for 100% *HS* state of the Fe(II) ions (∼ 2.2 Å), and so in agreement with the presence, at room temperature, of a remaining *LS* fraction of Fe(II) ions of about 19%, and very close to the corresponding value calculated with the magnetic data (ca. 20%). At low temperature (120 K), the averaged Fe—N value for **1** (2.035(2) Å) is significantly higher than the one expected for a complete magnetic transition (∼ 2.0 Å). The latter value suggests the presence of a *HS* fraction of about 17%, again very close to the corresponding value resulting from the analysis of the magnetic data (15%) of **1**.

For both compounds, the trigonal distortion parameters Σ and Θ are significantly reduced from room to low temperatures (for **1**, Σ decreases from 67° to 55° and Θ from 207° to 154° at 293 and 120 K, respectively; while for **2**, Σ is reduced from 71° to 54° and Θ from 233° to 144° at 293 and 120 K, respectively). Owing to the more regular FeN_6 octahedral geometry in the *LS* state, those observations are in line with the presence of a *SCO* transition from *HS* to *LS* in both compounds. Furthermore, the variations of the Σ and Θ parameters are significantly stronger in **2** (17° and 89°, respectively) than in **1** (12° and 53°, respectively), suggesting that the transition is more complete in **2** than in **1** which is in agreement with both magnetic measurements and Fe—N bond lengths arguments. It is also worth to indicate that the modifications of the iron coordination spheres in the two compounds affect more significantly the Fe—N3 bonds running along the chain direction (For **1**: 2.133(3) and 2.011(2) Å at 293 and 120 K respectively, Δ(Fe—N) = 0.122 Å; for **2**: 2.157(3) and 1.949(2) Å at 293 and 120 K respectively, Δ(Fe—N) = 0.208 Å). Interestingly, the significant decrease of the Fe—N3 bond lengths, from room to low temperature, does not affect strongly the shortest Fe···Fe distance along the polymeric chain (Fe-(NC-M-CN)-Fe: 9.7282(5) and 9.6117(5) Å for **1** and 9.9073(3) and 9.8107(3) Å for **2**, at 293 and 120 K, respectively). This result is due to the increase of the Fe—N3—C10 bond angles from room to low temperature (from 145.6(3)° to 151.5(2)° in **1** and from 142.0(3)° to 156.2(2)° in **2**, at 293 and 120 K, respectively), that partially compensate the strong decrease of the Fe—N3 bond lengths and mitigate its effect on the Fe···Fe distances along the molecular chain.

To clearly establish how the crystal and the lattice parameters were affected by the magnetic transition, we have measured the temperature dependence of the lattice parameters of a single crystal of **2** in the range 293—100 K. As can be seen in Figures 6—7, the *a*, *b*, *c* and *β* unit cell parameters, as well as the unit cell volume (*V*), show abrupt decreases at the same temperature than the one obtained from the magnetic data, that is, 132 K. This behavior is typical of *SCO* transitions and, together with the abrupt color change in the single crystal also observed at about 132 K (Figures 5-7), confirms the presence of a *SCO* transition at about 132 K. The unit cell parameters remain relatively constant and do not reveal any significant decrease in the temperature range 293—132 K, that is, before the *SCO* transition. According to the magnetic data (Figure 5), those structural data clearly demonstrate that the single crystal of **2** contracts anisotropically on cooling, since the more significant changes occur essentially along the *a* axis (Figure 7).

■ CONCLUSIONS

In summary, we have reported here the syntheses, the structural characterizations at high and low temperature, the temperature dependence of the lattice parameters, and the magnetic properties of the two isostructural *SCO* Fe(II) molecular neutral chain $[Fe(aqin)_2(M(CN)_4)]$ (M = Ni^{II}(**1**) and Pt^{II} (**2**)). The molecular chain structure of both compounds is generated by the $[M(CN)_4)]^{2-}$ moiety acting as a μ_2-bridging ligand via two nitrogen atoms from two trans cyano groups. The X-ray diffraction studies, in the range 293—120 K, show strong modifications of the iron coordination spheres, in agreement with the presence of a *SCO* transition in compounds **1**—**2**; also clearly confirmed by the thermal variation of the $\chi_m T$ product. Additionally, the thermal dependence of the lattice parameters *a*, *b*, *c* and *β*, as well as the unit cell volume (*V*), shows abrupt decreases at the same temperature than the one obtained from the magnetic data, and reveals that the single crystal of **2** contracts anisotropically on cooling, since the more significant changes occur essentially along the *a* axis. From a synthetic point of view, this study confirms the ability of the polycyanometallate anions to generate novel *SCO* complexes exhibiting original extended arrangements. An additional advantage of the use of such anions resides in their structural similarity with their parent analogues, such as the paramagnetic hexacyanometallate anions. Thus, besides their high ability to coordinate and bridge transition metal ions, these paramagnetic anions can transmit magnetic coupling between the metal active centers. Accordingly, attempts to prepare multidimensional bimetallic architectures combining *SCO* behavior and magnetic interactions using such magnetic polybridging anions are underway.

dx.doi.org/10.1021/ic401721x | *Inorg. Chem.* XXXX, XXX, XXX—XXX

■ ASSOCIATED CONTENT

Supporting Information

X-ray crystallographic data in CIF format (CCDC numbers: 938438 and 931126 for **1** at 293 and 120 K, respectively; 924207 and 924208 for **2** at 293 and 120 K, respectively) and observed and calculated X-ray powder diffraction patterns for (**1**). This material is available free of charge via the Internet at http://pubs.acs.org.

■ AUTHOR INFORMATION

Corresponding Author

*E-mail: smail.triki@univ-brest.fr. Phone: +33 298 016 146. Fax: +33 298 017 001.

Notes

The authors declare no competing financial interest.

■ ACKNOWLEDGMENTS

The authors acknowledge the CNRS ("Centre National de la Recherche Scientifique"), the Brest University, the French "Ministère de la Recherche" and "Ministère des Affaires Etrangères et Européennes" (PHC Maghreb project No. 13MAG08), the "Agence Nationale de la Recherche" (ANR project BISTA-MAT: ANR-12-BS07-0030-01), the "Spanish Ministerio de Economía y Competitividad" (Project CTQ2011-26507), and the "Generalitat Valenciana" (projects Prometeo and ISIC).

■ REFERENCES

(1) Gütlich, P., Goodwin, H. A., Eds.; Spin Crossover in Transition Metal Compounds I-III. In *Topics in Current Chemistry*; Springer Verlag: Berlin, Germany, 2004; Vols. *233*−*235*.

(2) Gamez, P.; Costa, J. S.; Quesada, M.; Aromí, G. *Dalton Trans.* **2009**, 7845−7853 and references therein.

(3) Létard, J.-F.; Guionneau, P.; Goux-Capes, L. *Top. Curr. Chem.* **2004**, *235*, 221−249.

(4) Cobo, S.; Molnár, G.; Real, J. A.; Bousseksou, A. *Angew. Chem., Int. Ed.* **2006**, *45*, 5786−5789.

(5) Olguin, J.; Brooker, S. *Coord. Chem. Rev.* **2011**, *255*, 203−240.

(6) Halcrow, M. A. *Chem. Soc. Rev.* **2011**, *40*, 4119−4142.

(7) Prins, F.; Monrabal-Capilla, M.; Osorio, E. A.; Coronado, E.; J. van der Zant, H. S. *Adv. Mater.* **2011**, *23*, 1545−1549.

(8) Muñoz-Lara, F. J.; Arcís-Castillo, Z.; Muñoz, M.-C.; Rodríguez-Velamazán, J.-A.; Gaspar, A.-B.; Real, J.-A. *Inorg. Chem.* **2012**, *51*, 11126−11132.

(9) Gütlich, P.; Gaspar, A.-B.; Garcia, Y. *Beilstein J. Org. Chem.* **2013**, *9*, 342−391.

(10) Decurtins, S.; Gütlich, P.; Köhler, C. P.; Spiering, H.; Hauser, A. *Chem. Phys. Lett.* **1984**, *105*, 1−4.

(11) Létard, J.-F. *J. Mater. Chem.* **2006**, *16*, 2550−2559.

(12) (a) Rodríguez-Velamazán, J. A.; Castro, M.; Palacios, E.; Burriel, R.; Kitazawa, T.; Kawasaki, T. *J. Phys. Chem. B* **2007**, *111*, 1256−1261. (b) Niel, V.; Muñoz, M. C.; Gaspar, A. B.; Galet, A.; Levchenko, G.; Real, J. A. *Chem.—Eur. J.* **2002**, *8*, 2446−2453. (c) Kosone, T.; Kanadani, C.; Saito, T.; Kitazawa, T. *Polyhedron* **2009**, *28*, 1991−1995.

(13) Garcia, Y.; Gütlich, P. *Top. Curr. Chem.* **2004**, *234*, 49−62.

(14) Morgan, G. G.; Murnaghan, K. D.; Müller-Bunz, H.; McKee, V.; Harding, C. J. *Angew. Chem., Int. Ed.* **2006**, *45*, 7192−7195.

(15) Sim, P. G.; Sinn, E. *J. Am. Chem. Soc.* **1981**, *103*, 241−243.

(16) Halepoto, D. M.; Holt, D. G. L.; Larkworthy, L. F.; Leigh, G. L.; Povey, D. C.; Smith, G .W. *J. Chem. Soc., Chem. Commun.* **1989**, 1322−1323.

(17) van Konigsbruggen, P. J.; Maeda, Y.; Oshio, H. *Top. Curr. Chem.* **2004**, *233*, 259−324.

(18) Costes, J.-P.; Dahan, F.; Laurent, J.-P. *Inorg. Chem.* **1990**, *29*, 2448−2452.

(19) Ishikawa, R.; Matsumoto, K.; Onishi, K.; Kubo, T.; Fuyuhiro, A.; Hayami, S.; Inoue, K.; Kaizaki, S.; Kawata, S. *Chem. Lett.* **2009**, *38*, 620−621.

(20) Hayami, S.; Moriyama, R.; Shigeyoshi, Y.; Kawajiri, R.; Mitani, T.; Akita, M.; Inoue, K.; Maeda, Y. *Inorg. Chem.* **2005**, *44*, 7295−7297.

(21) Galet, A.; Gaspar, A. B.; Muñoz, M. C.; Levchenko, G.; Real, J. A. *Inorg. Chem.* **2006**, *45*, 9670−9679.

(22) Dupouy, G.; Marchivie, M.; Triki, S.; Sala-Pala, J.; Salaün, J.-Y.; Gómez-García, C. J.; Guionneau, P. *Inorg. Chem.* **2008**, *47*, 8921−8931.

(23) Sheu, C.-F.; Pillet, S.; Lin, Y.-C.; Chen, S.-M.; Hsu, I.-J.; Lecomte, C.; Wang, Y. *Inorg. Chem.* **2008**, *47*, 10866−10874.

(24) El Hajj, F.; Sebki, G.; Patinec, V.; Marchivie, M.; Triki, S.; Handel, H.; Yefsah, S.; Tripier, R.; Gómez-García, C. J.; Coronado, E. *Inorg. Chem.* **2009**, *48*, 10416−10423.

(25) Weber, B.; Bauer, W.; Obel, J. *Angew. Chem., Int. Ed.* **2008**, *47*, 10098−10101.

(26) Weber, B.; Kaps, E.; Weigand, J.; Carbonera, C.; Létard, J.-F.; Achterhold, K.; Parak, F.-G. *Inorg. Chem.* **2008**, *47*, 487−496.

(27) Reger, D. L.; Gardinier, J. R.; Elgin, J. D.; Smith, M. D.; Hautot, D.; Long, G. J.; Grandjean, F. *Inorg. Chem.* **2006**, *45*, 8862−8875.

(28) Weber, B.; Jäger, E.-G. *Eur. J. Inorg. Chem.* **2009**, 465−477.

(29) Haasnoot, J. G.; Vos, J. G.; Groeneveld, W. L. *Z. Naturforsch. B* **1977**, *32*, 1421−1430.

(30) (a) Garcia, Y.; van Koningsbruggen, P. J.; Lapouyade, P.; Rabardel, L.; Khan, O.; Wierczorek, M.; Bronisz, R.; Ciunik, Z.; Rudolf, M. F. *C. R. Acad. Sci. Paris IIc* **1998**, *1*, 523. (b) Kahn, O.; Martinez, C. J. *Science* **1998**, *279*, 44−48. (c) Dîrtu, M. M.; Schmit, F.; Naik, A. D.; Rotaru, A.; Marchand-Brynaert, J.; Garcia, Y. *Int. J. Mol. Sci* **2011**, *12*, 5339−5351.

(31) Garcia, Y.; Kahn, O.; Rabardel, L.; Chansou, B.; Salmon, L.; Tuchagues, J.-P. *Inorg. Chem.* **1999**, *38*, 4663−4670. Bronisz, R. *Inorg. Chem.* **2005**, *44*, 4463.

(32) (a) Genre, C.; Jeanneau, E.; Bousseksou, A.; Luneau, D.; Borshch, S. A.; Matouzenko, G. S. *Chem.—Eur. J.* **2008**, *14*, 697−705. (b) Matouzenko, G. S.; Jeanneau, E.; Luneau, D. *New J. Chem.* **2006**, *30*, 1669−1674.

(33) (a) Moliner, N.; Muñoz, M. C.; Létard, S.; Salmon, L.; Tuchagues, J.-P.; Bousseksou, A.; Real, J. A. *Inorg. Chem.* **2002**, *41*, 6997−7005. (b) Matouzenko, G. S.; Perrin, M.; Le Guennic, B.; Genre, C.; Molnár, G.; Bousseksou, A.; Borshch, S. A. *Dalton Trans.* **2007**, 934. (c) Genre, C.; Matouzenko, G. S.; Molnár, G.; Bréfuel, N.; Perrin, M.; Bousseksou, A.; Borshch, S. A. *Chem. Mater.* **2003**, *15*, 550−556.

(34) (a) Real, J. A.; Gaspar, A. B.; Niel, V.; Muñoz, M. C. *Coord. Chem. Rev.* **2003**, *236*, 121−141. (b) Garcia, Y.; Niel, V.; Muñoz, M. C.; Real, J. A. *Top. Curr. Chem.* **2004**, *233*, 229−257.

(35) Murray, K. S.; Kepert, C. J. *Top. Curr. Chem.* **2004**, *233*, 195−228.

(36) Benmansour, S.; Atmani, C.; Setifi, F.; Triki, S.; Marchivie, M.; Gómez-García, C. J. *Coord. Chem. Rev.* **2010**, *254*, 1468−1478.

(37) (a) Dupouy, G.; Marchivie, M.; Triki, S.; Sala-Pala, J.; Gomez-Garcia, C. J.; Pillet, S.; Lecomte, C.; Létard, J.-F. *Chem. Commun.* **2009**, 3404−3406. (b) Dupouy, G.; Triki, S.; Marchivie, M.; Cosquer, N.; Gómez-García, C. J.; Pillet, S.; Bendeif, E.-E.; Lecomte, C.; Asthana, S.; Létard, J.-F. *Inorg. Chem.* **2010**, *49*, 9358−9368.

(38) Setifi, F.; Charles, C.; Houille, S.; Thétiot, F.; Triki, S.; Gómez-García, C. J.; Pillet, S. *Polyhedron* **2013**, *61*, 242−247.

(39) (a) Moliner, N.; Gaspar, A. B.; Muñoz, M. C.; Niel, V.; Cano, J.; Real, J.-A. *Inorg. Chem.* **2001**, *40*, 3986−3991. (b) Setifi, F.; Thétiot, F.; Triki, S.; Gómez-García, C. J. (manuscript in preparation).

(40) (a) Kitazawa, T.; Gomi, Y.; Takahashi, M.; Takeda, M.; Enomoto, M.; Miyazaki, A.; Enoki, T. *J. Mater. Chem.* **1996**, *6*, 119−121. (b) Niel, V.; Martinez-Agudo, J. M.; Muñoz, M. C.; Gaspar, A. B.; Real, J. A. *Inorg. Chem.* **2001**, *40*, 3838−3839. (c) Molnar, G.; Niel, V.; Gaspar, A. B.; Real, J. A.; Zwick, A.; Bousseksou, A.; McGarvey, J. J. *J. Phys. Chem. B* **2002**, *106*, 9701−9707.

(41) *CRYSALIS-CCD 170, CRYSALIS-RED 170*; Oxford-Diffraction: Abingdon, U.K., 2002.

(42) Sheldrick, M. *SHELX97, Program for Crystal Structure Analysis*; University of Göttingen: Göttingen, Germany, 1997.
(43) Farrugia, L. J. *J. Appl. Crystallogr.* **1999**, *32*, 837−838.
(44) Bain, G. A.; Berry, J. F. *J. Chem. Educ.* **2008**, *85*, 532−536.
(45) Infrared data (cm^{-1}). $K_2[Ni(CN)_4]\cdot xH_2O$: 3640(br), 3565(br), 3546(w), 2120(s), 2084(s), 1621(m), 1599(s), 1381(w); $K_2[Pt(CN)_4]\cdot xH_2O$ (cm^{-1}): 3593(br), 3544(br), 3469(w), 2165(s), 2133(s), 2121(s), 1654(w), 1616(s), 502(m).
(46) (a) Wong-Ng, W.; Culp, J. T.; Chen, Y. S.; Zavalij, P.; Espinal, L.; Siderius, D. W.; Allen, A. J.; Scheins, S.; Matranga, C. *CrystEngComm* **2013**, *15*, 4684−4693. (b) Tao, B.; Xia, H.; Jiang, X.; Zhu, Y. F. *Russ. J. Coord. Chem.* **2011**, *37*, 367−370.
(47) (a) Loosli, A.; Wermuth, M.; Güdel, H. U.; Capelli, S.; Hauser, J.; Bürgi, H. B. *Inorg Chem.* **2000**, *39*, 2289−2293. (b) Mühle, C.; Nuss, J.; Jansen, M. *Z. Kristallogr.* **2009**, *224*, 9−10.
(48) Guionneau, P.; Brigouleix, C.; Barrans, Y.; Goeta, A. E.; Létard, J.-F.; Howard, J. A. K.; Gaultier, J.; Chasseau, D. *C.R. Acad. Sci., Ser. IIc: Chim.* **2001**, *4*, 161−171.
(49) Marchivie, M.; Guionneau, P.; Létard, J.-F.; Chasseau, D. *Acta Crystallogr., Sect. B* **2003**, *59*, 479−486.
(50) (a) Farrugia, L. J. *J. Appl. Crystallogr.* **1997**, *30*, 565. (b) Farrugia, L. J. *J. Appl. Crystallogr.* **2012**, *45*, 849−854.
(51) (a) Shatruk, M.; Dragulescu-Andrasi, A.; Chambers, K. E.; Stoian, S. A.; Bominaar, E. L.; Achim, C.; Dunbar, K. R. *J. Am. Chem. Soc.* **2007**, *129*, 6104−6116. (b) Harris, T. D.; Long, J. R. *Chem. Commun.* **2007**, 1360−1362. (c) Coronado, E.; Gimenez-Lopez, M. C.; Korzeniak, T.; Levchenko, G.; Romero, F. M.; Segura, A.; Garcia-Baonza, V.; Cezar, J. C.; de Groot, F. M. F.; Milner, A.; Paz-Pasternak, M. *J. Am. Chem. Soc.* **2008**, *130*, 15519−15532. (d) Avendano, C.; Karadas, F.; Hilfiger, M.; Shatruk, M.; Dunbar, K. R. *Inorg. Chem.* **2010**, *49*, 583−594. (e) Zueva, E. M.; Ryabikh, E. R.; Kuznetsov, A. M.; Borshch, S. A. *Inorg Chem.* **2011**, *50*, 1905−1913.

Polyhedron 98 (2015) 18–25

Contents lists available at ScienceDirect

Polyhedron

journal homepage: www.elsevier.com/locate/poly

Hepta- and tetra-nuclear copper(II) clusters self-assembled by cyano- and azacyano-carbanions

Smail Triki [a,*], Eric Milin [a], Carlos J. Gómez-García [b], Samia Benmansour [b], Mathieu Marchivie [c]

[a] UMR CNRS 6521, Chimie, Electrochimie Moléculaires, Chimie Analytique, Université de Bretagne Occidentale, BP 809, 29285 Brest Cedex, France
[b] Instituto de Ciencia Molecular (ICMol), Universidad de Valencia, C/ Catedrático José Beltrán, 2, 46980 Paterna, Valencia, Spain
[c] CNRS, Univ. Bordeaux, ICMCB, UPR 9048, 87 Av. Doc. A. Schweitzer, F – 33600 Pessac, France

ARTICLE INFO

Article history:
Received 18 April 2015
Accepted 28 May 2015
Available online 5 June 2015

Keywords:
Cyanocarbanion ligands
Copper complexes
Polynuclear clusters
Hydrogen bonding
Magnetic properties

ABSTRACT

Two polynuclear copper(II) complexes with hydroxido-bridging ligands and polycyanide units, $[Cu\{Cu(tn)\}_6(\mu_2\text{-}OH)_2(\mu_3\text{-}OH)_4Cl_2](tcm)_4Cl_2\cdot 2H_2O$ (**1**) and $[\{Cu(bpy)\}_4(OH)_4(dca)_2](dca)_2\cdot bpy\cdot 2H_2O$ (**2**) (tn = $NH_2(CH_2)_3NH_2$; tcm^- = $[C(CN)_3]^-$, bpy = 2,2′-bipyridyl, dca^- = $[N(CN)_2]^-$) have been prepared by one-pot reactions. The structure of **1** consists of a centrosymmetric heptanuclear ion $[Cu\{Cu(tn)\}_6(\mu_2\text{-}OH)_2(\mu_3\text{-}OH)_4Cl_2]^{6+}$. The tcm^- and the halide anions which appear as counter-ions in the formula unit, play an important role in the stabilization of the complex since the hydrogen bonding between nitrogen atoms of the tcm^- anion and halide anions, and hydrogen atoms of the terminal water molecule and of the bridging hydroxido ligands generate an overall three-dimensional structure. The crystal structure of **2** is essentially built on discrete centrosymmetric tetranuclear $[\{Cu(bpy)\}_4(\mu_2\text{-}OH)_2(\mu_3\text{-}OH)_2(dca)_2]^{2+}$ units including two μ_2- and two μ_3-OH ligands. As observed for **1**, the dca^- anions form a network of hydrogen bonding between their nitrogen atoms and hydrogen atoms of water molecules generating a two-dimensional structure. The magnetic susceptibility data indicate antiferromagnetic interactions in **1** and ferromagnetic ones in **2**.

1. Introduction

Crystal engineering of polynuclear metal complexes, either with simple or sophisticated ligands, has been a very active area in the last decades. Thus, thousands of discrete polynuclear complexes with many different nuclearities and with many different bridging and terminal ligands have been prepared [1–10]. This activity has been fuelled by the fascinating physical and chemical properties of these complexes, with potential applications in magnetism [11–13], catalysts [14], gas storage [15], biological activity [16],... In the case of the Cu(II), polynuclear complexes with nuclearities of two [17–23], three [24–28] and four [29–32] have been widely investigated, in contrast with complexes of higher nuclearities as five [33], six [34], seven [35] or nine [36], which are more scarce. Nevertheless, the interesting properties of these high nuclearity Cu(II) complexes has provoked an increasing interest in these polynuclear complexes in the last decade. An aspect which has been less investigated concerns the role played by the counter-ions and/or solvent molecules in the crystal lattice cohesion in these polynuclear systems. In this context, we described in 2001 a rare example of heptanuclear complex presenting μ_2 and μ_3 hydroxido bridges: $[Cu\{Cu(tn)\}_6(\mu_2\text{-}OH)_2(\mu_3\text{-}OH)_4Cl_2](tcm)_4Cl_2\cdot 2H_2O$ (**1**) (tn = $NH_2(CH_2)_3NH_2$; tcm^- = $[C(CN)_3]^-$, see Scheme 1) [35]. In this complex the Cl^- and tcm^- anions were supposed to simply play the role of counter-ions in order to stabilize the dicubane heptanuclear cationic complex $[Cu\{Cu(tn)\}_6(\mu_2\text{-}OH)_2(\mu_3\text{-}OH)_4Cl_2]^{6+}$.

Albeit, recent studies of the role played by the polycyanide (dca^- or tcm^-) and halide anions on this system has allowed us to prepare a novel tetranuclear Cu(II) complex. When tcm^- is changed by dca^- and tn by bpy, a tetranuclear complex, formulated as $[\{Cu(bpy)\}_4(\mu_2\text{-}OH)_2(\mu_3\text{-}OH)_2(dca)_2](dca)_2\cdot bpy\cdot 2H_2O$ (**2**) (bpy = 2,2′-bipyridyl; dca^- = $(N(CN)_2)^-$ = dicyanamide, see Scheme 1) is obtained. The crucial role of the polycyanide anions (tcm^- and dca^-) as well as the N-donor chelating co-ligand will be discussed in both systems.

2. Experimental

2.1. Reagents and techniques

Infrared spectra were recorded on KBr pellets in the 4000–400 cm^{-1} range on a FT-IR BRUKER ATR VERTEX70 and on a Nexus-Nicolet 5700 spectrometers. Magnetic measurements were

* Corresponding author.
E-mail address: smail.triki@univ-brest.fr (S. Triki).

http://dx.doi.org/10.1016/j.poly.2015.05.037
0277-5387/

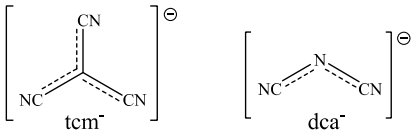

Scheme 1. Simple polycyanide anions.

performed with a Quantum Design MPMS-XL-5 SQUID magnetometer in the 2–300 K temperature range with an applied magnetic field of 0.1 T on ground single crystals of compound **2**. Isothermal magnetization measurements were performed at 2 K with magnetic fields of up to 5 T. The susceptibility data were corrected for the sample holders previously measured under the same conditions, and for the diamagnetic contributions as deduced by using Pascal's constant tables ($\chi_{dia} = -697 \times 10^{-6}$ emu mol^{-1}) [37]. Elemental analyses were performed at the "Service de microanalyse", CNRS, 91198 Gif-sur-Yvette.

All the reactions were carried out under aerobic conditions. The starting reagents and solvents were purchased from commercial sources (analytical reagent grade) and used without further purification.

2.2. Preparations

2.2.1. Synthesis of the cyanocarbanion salts

Potassium tricyanomethanide, K(tcm) was prepared following the previously described procedure [38]. *Anal.* Calc. for KC_4N_3: C, 37.2; N, 32.5. Found: C, 36.8; N, 32.0%. IR data (ν/cm^{-1}): 2169s, 1239w, 1127w, 1079w, 854w, 566s. The tetraethylammonium dicyanamide salt, (Et_4N)(dca), was prepared by metathesis using Na(dca) and (Et_4N)Cl in acetonitrile. IR data (ν/cm^{-1}): 3472w, 2989w, 2224m, 2191m, 2126s, 1670w, 1485m, 1395m, 1301m, 1173m, 1001w, 903m, 7860m, 524m.

2.2.2. Synthesis of the Cu complexes (**1** and **2**)

[Cu{Cu(tn)}$_6$(μ_2-OH)$_2$(μ_3-OH)$_4$Cl$_2$](tcm)$_4$Cl$_2$·2H$_2$O (**1**). This compound was prepared as described in reference [35]: to a warm aqueous solution (20 mL) of $CuCl_2·2H_2O$ (2.042 g, 12 mmol) was slowly added 1 mL (0.89 g, 12 mmol) of 1,3-diaminopropane (tn) and then an aqueous solution (20 mL) of sodium hydroxide (0.480 g, 12 mmol) with heating and continuous stirring. To the resulting clear solution were immediately and consecutively added concentrated aqueous solutions (5 mL) of $CuCl_2·2H_2O$ (0.340 g, 2 mmol) and potassium tricyano-methanide (1.031 g, 8 mmol). Slow evaporation of the solvent gave prismatic dark blue crystals of **1** suitable for X-ray structure determination. Yield 1.285 g, 42%; *Anal.* Calc. for $C_{34}H_{70}Cl_4Cu_7N_{24}O_8$ (**1**): C, 26.7; H, 4.6; Cl, 9.3; Cu, 29.1; N, 22.0. Found: C, 26.9; H, 4.6; Cl, 9.2; Cu, 29.2; N, 21.9%. IR data(ν/cm^{-1}): 3292m, 3136m, 2937w, 2886w, 2166s, 1586m, 1461w, 1397w, 1323w, 1283w, 1250w, 1190m, 1151w, 1112w, 1036w, 1021w, 951w, 897m, 707w, 688w, 649w, 559m, 489m.

[{Cu(bpy)}$_4$(μ_2-OH)$_2$(μ_3-OH)$_2$(dca)$_2$](dca)$_2$·bpy·2H$_2$O (**2**). To a methanolic solution (20 mL) of 2,2′-bipyridyl (312 mg, 2.0 mmol) was added with stirring a methanolic solution (10 mL) of $CuCl_2·2H_2O$ (341 mg, 2.0 mmol); the colour changes from blue to green. Aqueous solutions (13 mL) of sodium hydroxide (640 mg, 16 mmol) and sodium dicyanamide (178 mg, 2.0 mmol) were then successively added with stirring. The resulting suspension was filtered in order to eliminate a blue green precipitate and the filtrate was slowly concentrated by evaporation at room temperature. Compound **2** precipitated as pale blue crystals which were filtered and air dried. Yield 0.386 g, 55%. *Anal.* Calc. for $C_{58}H_{48}Cu_4N_{22}O_6$: C, 49.6; H, 3.5; Cu, 18.1; N, 22.0. Found: C, 49.4; H, 3.6; Cu, 17.9; N, 21.8%. IR data (ν/cm^{-1}): 3358br, 2272w, 2251m, 2205w, 2165s, 2142s, 1608w, 1600m, 1560w, 1473w, 1446m, 1350w, 1319m, 1250w, 1158w, 1031w, 1014w, 770s, 732m, 667w, 637w, 512m, 415w.

2.3. X-ray crystallography

Single crystal X-ray data were collected at $T = 296$ K on an Oxford Diffraction Xcalibur κ-CCD diffractometer, using a graphite monochromated Mo Kα radiation ($\lambda = 0.71073$ Å). The structures were solved by direct methods and successive Fourier difference syntheses, and were refined by weighted anisotropic full-matrix least-squares methods [39]. For compound **2**, except for the water molecules and hydroxyl moieties, whose H atoms position were deduced from the Fourier difference maps and refined with restraints, the positions of all other H atoms were calculated from coordinates of the non-H atoms [d(C–H) = 0.95 Å]; confirmed by Fourier synthesis and treated according to the riding model during refinement; the thermal parameters were taken as $U_{iso} = 1.3\ U_{equ}$(C) and therefore included as isotropic fixed contributors to F_c. Scattering factors and corrections for anomalous dispersion were taken from the *International tables for X-ray crystallography* [40]. The thermal ellipsoid drawings and all other illustrations were performed using the OLEX2 software [41]. Pertinent crystal data and selected bond distances and bond angles are listed in Tables 1–6.

3. Results and discussion

One-pot reactions with $CuCl_2·2H_2O$, sodium hydroxide, a polycyanide anion (Ktcm for **1**; Na(dca) for **2**) and a N-donor chelating ligand (tn for **1**, bpy for **2**) have been studied. When using Ktcm

Table 1
Crystallographic data for compounds **1** and **2**.

Compound	**1**	**2**
[a]Chemical formula	$C_{34}H_{70}N_{24}O_8Cl_4Cu_7$	$C_{58}H_{48}N_{22}O_6Cu_4$
[a]Formula weight	1529.68	1403.33
Space group	C2/c	$P\bar{1}$
a (Å)	24.8994(3)	9.4234(4)
b (Å)	11.9801(2)	12.7576(4)
c (Å)	21.4298(3)	13.2527(4)
α (°)	90	96.624(3)
β (°)	112.14(6)	104.021(3)
γ (°)	90	102.113(3)
V (Å^3)	5920(2)	1488.0(1)
Z	4	1
Crystal dim (mm)	0.32 × 0.22 × 0.22	0.14 × 0.09 × 0.06
D_{calc} (g cm^{-3})	1.72	1.57
F(000)	3108	714
μ (cm^{-1})	27.21	14.81
T (K)	288	296
λ (Å)	0.71073	0.71073
hkl range	0.32/0.15/−27.25	−10.11/−15.15/−15.15
2θ limits (°)	5.00–55.00	6.64–50.50
Refl. measured	11930	15681
Refl. unique/R_{int}	6593 / 0.021	5367 / 0.054
Refl. with $I > 2\sigma(I)$	3924	4469
N_v	351	422
[b]R	0.044	0.0398
[c]$R\omega$ or [d]wR_2	0.065 ($R\omega$)	0.112 (wR_2)
[e]Goodness-of-fit (GOF) on F^2	1.729	1.080 (on F^2)
$\Delta\sigma_{max}/\Delta\sigma_{min}$ (e Å^{-3})	+0.278/−0.091	+0.52/−0.34
Δ/σ	0.20	0.000

[a] There is 0.5 chemical formula in the asymmetric unit.
[b] $R = \Sigma||F_o| - |F_c||/|F_o|$.
[c] $R\omega = [(\Sigma\omega(F_o - F_c)^2/\omega\ (F_o)^2]^{1/2}$.
[d] $wR_2 = [\Sigma\omega(F_o^2 - F_c^2))^2/(\omega\ (F_o^2))^2)]^{1/2}$.
[e] G.O.F = $[(\Sigma\omega|F_o| - |F_c|)^2/$(Nobs-Nvar)$]^{1/2}$ on F or $[(\Sigma\omega F_o^2 - F_c^2))^2/$(Nobs-Nvar)$]^{1/2}$ on F^2.

Table 2
Bond distances (Å) and angles (°) in compound **1**.

Cu1–O1	1.960(3)	Cu3–O3	1.980(3)
Cu1–O2	1.979(3)	Cu3–Cl1	2.679(2)
Cu1–Cl1	3.029(2)	Cu4–O1	2.417(3)
Cu2–O1	1.991(3)	Cu4–O2	2.029(3)
Cu2–O3	1.977(3)	Cu4–O3	1.994(3)
Cu2–Cl1	2.654(2)	Cu4–O4	2.524(4)
Cu3–O2	2.016(3)		
O1–Cu1–O2	83.9(1)	O3–Cu4–O4	81.5(1)
O1–Cu1–Cl1	79.7(1)	Cu1–O1–Cu2	117.6(2)
O2–Cu1–Cl1	81.9(1)	Cu1–O1–Cu4	92.9(1)
O1–Cu2–O3	84.5(1)	Cu2–O1–Cu4	91.10(9)
O1–Cu2–Cl1	89.4(1)	Cu1–O2–Cu3	115.1(2)
O3–Cu2–Cl1	86.1(1)	Cu1–O2–Cu4	105.3(1)
O2–Cu3–O3	80.1(1)	Cu3–O2–Cu4	94.11(9)
O2–Cu3–Cl1	90.9(1)	Cu2–O3–Cu3	112.1(1)
O3–Cu3–Cl1	85.3(1)	Cu2–O3–Cu4	105.5(1)
O1–Cu4–O2	72.0(1)	Cu3–O3–Cu4	96.3(1)
O1–Cu4–O3	73.7(1)	Cu1–Cl1–Cu2	72.65(3)
O1–Cu4–O4	150.7(1)	Cu1–Cl1–Cu3	72.12(3)
O2–Cu4–O3	79.5(1)	Cu2–Cl1–Cu3	76.00(4)
O2–Cu4–O4	88.5(1)		

Table 3
Intermolecular hydrogen bonds in **1**.

O–H···A	*d*(O–H)/Å	*d*(H–A)/Å	*d*(O–A)/Å	O–H–A/°
O1–H01···N8$^{(b)}$	0.917(3)	2.080(5)	2.962(3)	160.6(2)
O2–H02···N7	0.846(3)	1.995(5)	2.826(3)	167.3(2)
O3–H03···Cl2	0.921(2)	2.078(5)	2.991(2)	170.5(2)
O4–H04H···Cl2	0.990(2)	2.581(5)	3.407(2)	140.9(3)
O4–H04G···Cl3	0.882(2)	2.407(5)	3.206(2)	150.7(3)

Codes of equivalent position: (b) = *x*, 1 + *y*, *z*.

Table 4
Selected bond distances (Å) and angles (°) in compound **2**.

Cu1–O1	1.960(2)	Cu2–O1	1.979(2)
Cu1–O1$^{(a)}$	2.292(2)	Cu2–O2	1.910(2)
Cu1–O2	1.915(2)	Cu2–N3	2.011(2)
Cu1–N1	2.036(2)	Cu2–N4	2.020(2)
Cu1–N2	1.996(2)	Cu2–N5	2.216(3)
N5–C21	1.100(4)	N6–C21	1.276(5)
N6–C22	1.270(6)	N7–C22	1.093(5)
O1–Cu1–O1$^{(a)}$	83.82(7)	O1–Cu1–O2	81.60(8)
O1$^{(a)}$–Cu1–O2	99.90(9)	O1–Cu2–O2	81.23(8)
Cu1–O1–Cu1$^{(a)}$	96.18(7)	Cu1–O1–Cu2	95.67(8)
Cu1$^{(a)}$–O1–Cu2	110.57(9)	Cu1–O2–Cu2	99.51(9)

Codes of equivalent positions: (a) = *1* − *x*, −*y*, 1 − *z*.

Table 5
Intermolecular hydrogen bonds in **2**.

O–H···A	d(O–H)/Å	d(H–A)/Å	d(O–A)/Å	O–H–A/°
O1–H1A···O3	0.81(2)	1.98(2)	2.789(3)	172(3)
O2–H2A···N8	0.83(2)	2.04(2)	2.858(4)	167(4)
O3–H3B···N10$^{(b)}$	0.85(2)	2.00(2)	2.831(5)	169(4)
O3–H3A···N7$^{(c)}$	0.82(2)	1.99(2)	2.794(5)	171(4)

Codes of equivalent positions: (b) = +*x*, −1 + *y*, +*z*; (c) = −*x*, −*y*, −*z*.

and 1,3-diaminopropane (tn), the heptanuclear complex $[Cu\{Cu(tn)\}_6(\mu_2\text{-}OH)_2(\mu_3\text{-}OH)_4Cl_2](tcm)_4Cl_2{\cdot}2H_2O$ (**1**) was obtained as dark blue prismatic crystals. The use of sodium dicyanamide (Na(dca)) and 2,2′-bipyridyl (bpy) resulted in the formation of the tetranuclear complex $[\{Cu(bpy)\}_4(\mu_2\text{-}OH)_2(\mu_3\text{-}OH)_2(dca)_2](dca)_2{\cdot}bpy{\cdot}2H_2O$ (**2**) as pale blue single crystals. As expected, the IR spectrum of **2** shows several absorption bands in the 2280–2140 cm^{-1} region (2272w, 2251m, 2205w, 2165s, 2142s), assignable to the *ν* (CN) vibrations of the dca^- units. In order to assign more clearly these *ν* (CN) vibration bands, we have performed the IR spectrum of the corresponding tetraethylammonium salt, $(Et_4N)(dca)$ containing the uncoordinated dca^- moiety (*ν* (CN): 2224m, 2191m and 2126s cm^{-1}). The absorption bands observed for **2** at 2205w, 2165s and 2142s are indicative of the presence of uncoordinated CN groups, while the two absorption bands (2272w, 2251m), shifted to higher wavenumbers of *ca.* 25–50 cm^{-1}, may be attributed to the coordination of CN groups in **2**. These observations are in agreement with the presence of a terminal coordination mode of the dca^- anion in **2**. It is well-known that IR spectroscopy can be used as a diagnostic tool for identifying the co-ordination mode of the bpy ligand [42,43]. Chelate coordination mode usually splits the strong γ(CH) absorption observed as an intense and sharp band at 757 cm^{-1} in the free bpy in an asymmetric doublet. The presence of such doublet on the spectrum of **2** (770(s) and 732(m) cm^{-1}) clearly indicates that the bpy ligands present their usual chelating coordination mode.

The structure of $[Cu\{Cu(tn)\}_6(\mu_2\text{-}OH)_2(\mu_3\text{-}OH)_4Cl_2](tcm)_4Cl_2{\cdot}2H_2O$ (**1**) was briefly described by us [35]. However, in this report the structural description was focused on the heptanuclear cluster $[Cu\{Cu(tn)\}_6(\mu_2\text{-}OH)_2(\mu_3\text{-}OH)_4Cl_2]^{6+}$, and no structural information on the intermolecular contacts and the crystal packing was detailed. Thus, in the following discussion, the crucial role of the tcm^- anions in **1** will be clarified. Compound **1** crystallizes in the monoclinic *C*2/*c* space group. Crystallographic data and selected bond lengths and angles and intermolecular distances are listed in Tables 1–3 respectively. The structure of **1** consists of a centrosymmetric hydroxido-bridged heptanuclear copper(II) cation which can be described as two Cu_4O_3Cl distorted cubanes sharing one copper cation (Cu1) (Fig. 1) [35].

The tcm units are non coordinated; however, this anion is involved in significant hydrogen bonds which contribute to the stabilization of the cluster conformation. The discrete copper clusters are connected together by intermolecular charge assisted hydrogen bonds to form a tridimensional network. The packing results firstly in a 2D network ensured by relatively strong hydrogen bonding between hydroxyl groups and Cl2 anion on one hand and tcm^- anion on the other hand (Fig. 2 and Table 3). The 3D network is obtained by weaker hydrogen bonding in the third direction between the water molecule and Cl2 and Cl3 anions (Fig. 3 and Table 3).

$[\{Cu(bpy)\}_4(\mu_2\text{-}OH)_2(\mu_3\text{-}OH)_2(dca)_2](dca)_2{\cdot}bpy{\cdot}2H_2O$ (**2**). This compound crystallizes in the triclinic $P\bar{1}$ space group. The asymmetric unit contains a dinuclear $[Cu_2(OH)_2(bpy)_2(dca)]^+$ unit located on an inversion centre, a dca^- anion and a water molecule both located on general positions, and a non-coordinated bpy molecule located on an inversion centre (Fig. 4).

In the tetranuclear unit, the two crystallographically independent Cu(II) centres differ markedly in their co-ordination geometry. The Cu1 ion presents a CuN_2O_3 environment arising from two N atoms of a bidentate bpy ligand and three oxygen atoms (O1, O1$^{(a)}$, O2) of bridging hydroxido ligands. The Cu2 ion presents a CuN_3O_2 environment arising from two nitrogen atoms (N3, N4) from a bidentate bpy ligand, an additional nitrogen atom (N5) of a monodentate dca ligand and two oxygen atoms (O1, O2) from two bridging hydroxido ligands. For the two metal centers, the X-ray structure reveals almost perfect square pyramidal coordination environments (τ = 0.12 for Cu1 and τ = 0.07 for Cu2) [44], and in both cases, the coordination polyhedra can be described as elongated square pyramids in which the basal CuN_2O_2 plane involves an almost symmetric bidentate bpy ligand (Cu–N bond lengths in the range 1.996(2)–2.036(2) Å) and two similar Cu–O bonds (1.960(2) and 1.979(2) Å for Cu–O1; 1.915(2) and 1.910(2) for Cu–O2 Å) (Table 4).

The apical positions are occupied by a nitrogen atom (N5) of a monodentate dca ligand for Cu2 and by an oxygen (O1$^{(a)}$) atom

Table 6
π–π interactions in compound **2**.

Plane 1	Plane 2	c–c (Å)[a]	Shift (Å)[b]	Angle (°)[c]
Inter-molecular contacts				
(N1C5C4C3C2C1)	(N1C5C4C3C2C1)$^{(d)}$	3.803	1.577	0
(N3C15C14C13C12C11)	(N3C15C14C13C12C11)$^{(e)}$	3.739	1.631	0
Intra-molecular contacts				
(N1C5C4C3C2C1)	(N4C20C19C18C17C16)$^{(f)}$	3.845	1.709	8.6
(N2C10C9C8C7C6)	(N3C15C14C13C12C11)$^{(f)}$	3.9	1.785	6.7

Codes of equivalent positions: (d) = −*x*, −*y*, 1 − *z*; (e) = 1 − *x*, −*y*, −*z*; (f) = 1 − *x*, −*y*, 1 − *z*.
[a] Centroid–centroid distance.
[b] Shift distance.
[c] Angle between planes.

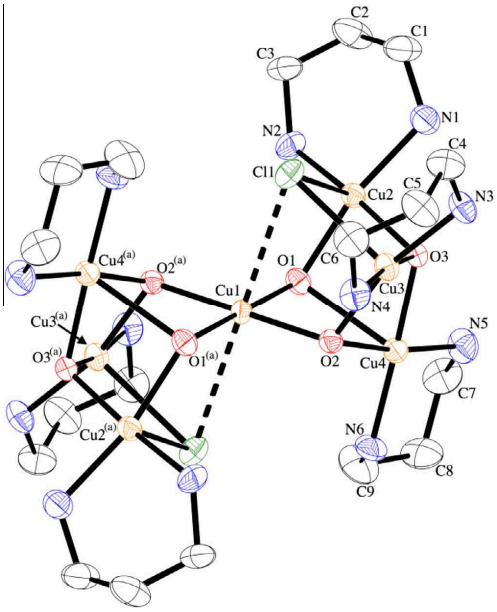

Fig. 1. Thermal ellipsoid drawing [41] (30% probability ellipsoids) of the cluster in compound **1** showing the labelling scheme of the asymmetric unit and some symmetrically equivalent atoms (a) = ½ − *x*, ½ − *y*, 1 − *z*.

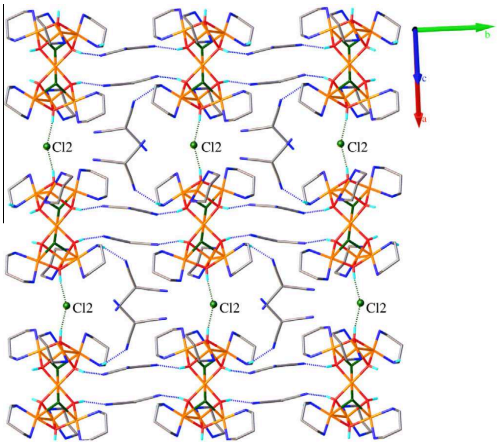

Fig. 2. Crystal packing of compound **1** along the [−102] lattice vector.

of a bridging hydroxido ligand for Cu1; this apical bond is more elongated for Cu1 (Cu1–O1$^{(a)}$ = 2.292(2) Å) than for Cu2 (Cu2–N5 = 2.216(3) Å). This double O1 bridge generates a tetranuclear unit with a central Cu_4O_4 core built on a perfectly planar Cu1O1Cu1$^{(a)}$O1$^{(a)}$ fragment (Cu1···Cu1$^{(a)}$ = 3.172(1) Å) articulated with two Cu1O1Cu2O2 lateral units (Cu1···Cu2 = 2.919(1) Å) (Fig. 4). Concerning the hydroxido bridges, it is worth to note that O2 is an almost perfect symmetric μ_2-bridge with two short Cu–O bonds (1.915(2) and 1.910(2) Å) while the μ_3-bridge built on O1 presents a very asymmetric coordination (1.960(2), 1.979(2) and 2.292(2) Å). The discrete tetranuclear copper clusters are connected together by relatively strong intermolecular hydrogen bonds between a water crystallization molecule and either hydroxido groups or dca^- anions (coordinated and uncoordinated ones). These four hydrogen bonding intermolecular interactions lead to a bidimensional network within almost the *bc* plane (Fig. 5 and Table 5). The packing cohesion is ensured in the third direction by strong intermolecular π–π interactions between the bpy aromatic ligands (Fig. 6 and Table 6).

The $\chi_m T$ product of compound **2** shows at room temperature a value of ca. 2.0 $cm^3\,K\,mol^{-1}$ (Fig. 7). On cooling the sample, $\chi_m T$ shows a smooth increase down to ca. 100 K and below this temperature it shows a progressive increase to reach a value of ca. 3.5 $cm^3\,K\,mol^{-1}$ at 2 K. This behaviour clearly indicates the presence of predominant ferromagnetic interactions inside the cluster.

Given the exchange scheme in this compound (Fig. 8) and the fact that the J_1 interaction takes place trough a basal–basal double hydroxido bridge whereas the J_2 interactions corresponds to a basal–axial double hydroxido bridge, we can consider, in a first approach, that by far, the larger coupling constant must be J_1 and, therefore, that compound **2** can be considered as two Cu(II) dimers connected through a much weaker inter-dimer interaction, J_2. In fact, this is the most common model used to fit the magnetic properties in these type of Cu(II) clusters (Table 7). This simple model of interacting $S = ½$ dimers reproduces very satisfactorily the magnetic properties of compound **2** in the whole temperature range with the following parameters: $g = 2.288(5)$, $J_1 = 18.1(9)\,cm^{-1}$ and $J_2 = 0.61(1)\,cm^{-1}$ (solid line in Fig. 7, the hamiltonian is written as $H = -JS_iS_{i+1}$).

Although a CCDC search shows that there are up to 28 different Cu(II) clusters with the same connectivity that compound **2** (Fig. 8), only nine have been magnetically characterized (Table 7). Among

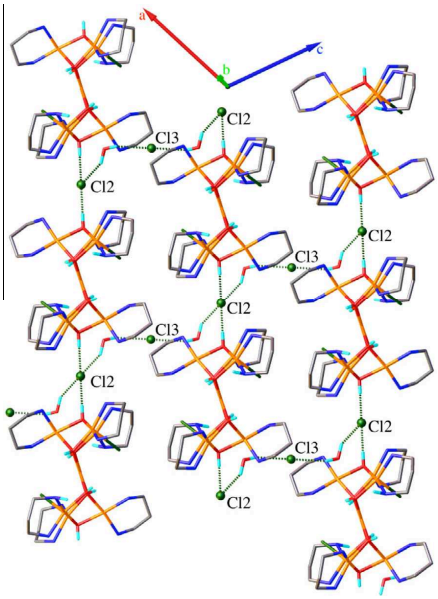

Fig. 3. Crystal packing of compound **1** along the [−170] lattice vector.

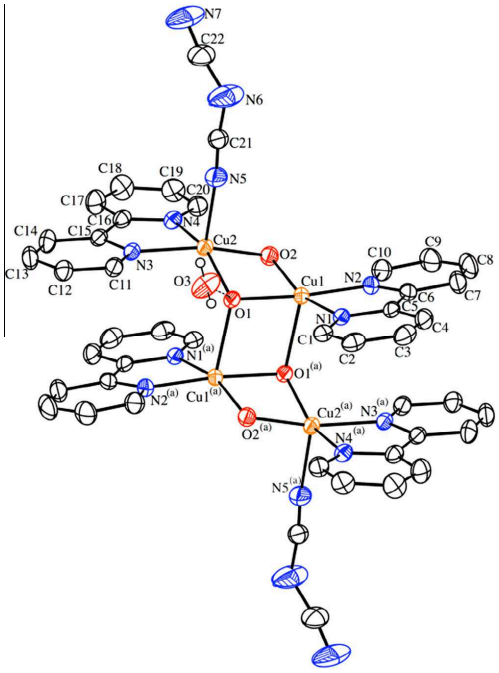

Fig. 4. Thermal ellipsoid drawing [41] (30% probability ellipsoids) of compound **2** showing the labelling scheme of the asymmetric unit and some symmetrically equivalent atoms (a) = 1 − *x*, −*y*, 1 − *z*. Uncoordinated dca anion and bipyridine are omitted for clarity.

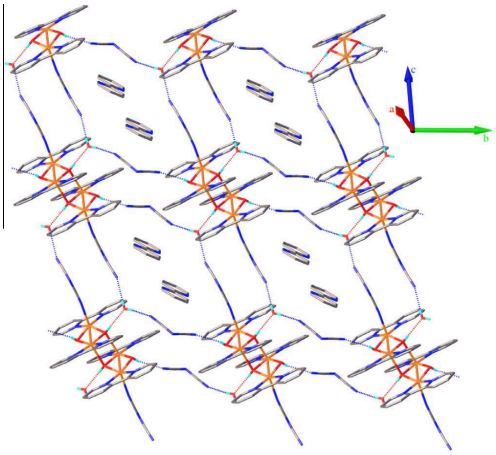

Fig. 5. Crystal packing of compound **2** along the [30 −1] lattice vector.

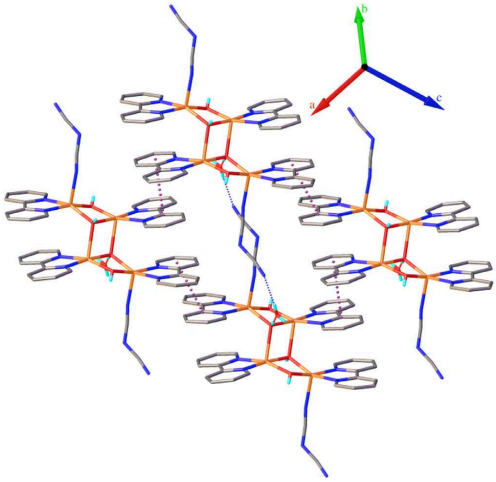

Fig. 6. Crystal packing of compound **2** along the [−2 −2 −1] lattice vector.

these nine, there are two cases where the connections between the terminal and central Cu(II) atoms are basal-axial (**type 2**, Fig. 8) [45]. The remaining seven examples (**type 1**, Fig. 8) have been fitted with different magnetic models, from a simple double isolated dimer model ($J_2 = 0$) [46] to a more complicated model including the connections between the terminal Cu(II) ions and the two central ones (J_1 and J'_1) [47]. The remaining five examples have been fitted using the interacting $S = ½$ dimers model, as we have done for compound **2**. These five examples show weak to moderate ferromagnetic J_1 (ca. 31–128 cm^{-1}) and J_2 (ca. 6–18 cm^{-1}) values in all cases (Table 7) [48,49]. In agreement with these five examples, the J_1 and J_2 parameters found in compound **2** are also weak and ferromagnetic although the values are slightly lower ($J_1 = +18.1(9)$ and $J_2 = 0.61(1)$ cm^{-1}). Despite there are several parameters that have

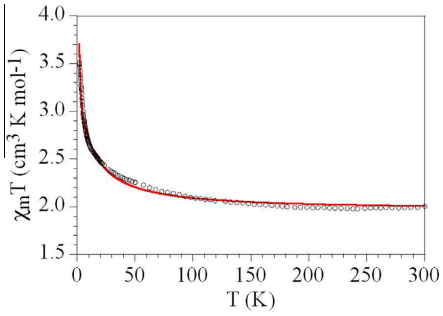

Fig. 7. Thermal dependence of $\chi_m T$ for compound **2**. Solid line is the best to the model (see text).

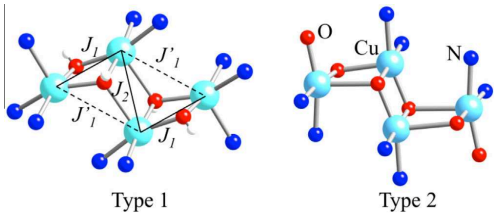

Fig. 8. Two different connectivity types observed in tetranuclear Cu(II) clusters similar to compound **2**.

to be considered in order to establish a magneto-structural correlation in these doubly bridged hydroxido Cu(II) dimers [50–54], and the number of reported examples is very limited, we have tried to establish a magneto-structural correlation between the J_1 values and the Cu–O–Cu bond angles in those **type 1** compounds that were fit with the same interacting dimer model (Table 7). As expected from orbital overlap considerations, this correlation shows an almost linear relationship between the J_1 values and the average Cu–O–Cu bond angles in the Cu_2O_2 dimer corresponding to this J_1 coupling (see Fig. 9). The only point that clearly deviates from this correlation is compound YOFXUN, that shows a magnetic coupling much higher than expected. If we look at the average Cu–O bond distances in the Cu_2O_2 dimers (Table 7) we can see that in compound YOFXUN this distance (1.918 Å) is much shorter than in the other five compounds (in the range 1.939–1.953 Å). Although less significant, compound UMICUP also deviates from the linear general trend. Interestingly, this compound presents the second shorter Cu–O average bond distance (1.939 Å).

The ferromagnetic nature of the interaction in compound **2** is also confirmed by the isothermal magnetization at 2 K that can be very well reproduced with a Brillouin function for a $S = 2$ spin ground state but not with the sum of four Brillouin functions for a $S = ½$ spin ground state (Fig. 10).

4. Conclusions

We have described two polynuclear Cu(II) complexes with μ_2- and μ_3-hydroxido-bridging ligands and polycyanide units, $[Cu\{Cu(tn)\}_6(\mu_2\text{-}OH)_2(\mu_3\text{-}OH)_4Cl_2](tcm)_4Cl_2{\cdot}2H_2O$ (**1**) and $[\{Cu(bpy)\}_4(OH)_4(dca)_2](dca)_2{\cdot}bpy{\cdot}2H_2O$ (**2**). The two types of structures consist of centrosymmetric heptanuclear and tetranuclear units respectively. A careful examination of the

Table 7
Magnetic and structural parameters of all the characterized Cu tetramers with the same connectivity than **2**.

CCDC	Formula	Type[a]	Cu–O–Cu (°)	Cu-O (Å)[h]	g	J_1 (cm^{-1})	J_2 (cm^{-1})	Ref.
ECUHIT[b]	$[Cu_4L^1Cl_2(OH)_2](ClO_4)_2$	1	99.94/103.80[f] 95.25/105.75[g]	1.971	2.086	$J_1 = -80.6$ $J'_1 = -75.0$	−541.6	[47]
MOGQAA[d]	$[Cu_4(dmbipy)_4(OH)_4(H_2O)_2](BF_4)_4(H_2O)_4$	1	97.07/98.22[f] 93.34/110.84[g]	1.953	2.14	31.1	8.76	[48]
RUYPOR[c]	$[Cu_4(OH)_2(bip)_2(NCS)_4(DMF)_2]$	1	100.65/104.38[f] 95.08/103.96[g]	1.951	2.2	−563	0	[46]
SIJBIX[e]	$Cu_4(OH)_2(ssal)_2(phen)_4{\cdot}7H_2O$	2	91.80/91.90/99.79[f] 97.99/108.75[g]	2.167	2.14	$\theta = 7.5$ K	0	[45]
SIJBOD[e]	$Cu_4(OH)_2(ssal)_2(bipy)_4{\cdot}2H_2O$	2	93.17/97.34[f] 99.30/108.73[g]	2.099	2.045	$\theta = -0.4$ K	0	[45]
UMICUP[d]	$[Cu_4(bpy)_4(OH)_4(H_2O)_2](NO_3)_2(C_5H_6O_4){\cdot}8H_2O$	1	95.93/99.23[f] 94.63/96.10[g] 107.68/109.85[g] 97.00/100.07[f]	1.939	2.32	40.6	17.8	[49]
UMIDAW[d]	$[Cu_4(bpy)_4(OH)_4(H_2O)_2](C_5H_6O_4)_2{\cdot}16H_2O$	1	95.73/99.00[f] 95.31/107.01[g] 95.65/98.74[f] 94.59/110.39[g]	1.942 1.941	2.02	70.8	6.8	[49]
UMIDEA[d]	$[Cu_4(bpy)_4(OH)_4(H_2O)_2](NO_3)_2(C_7H_5O_2)_2{\cdot}6H_2O$	1	94.86/98.00[f] 97.38/112.14[g]	1.944	2.06	128.2	11.4	[49]
YOFXUN[d]	$[Cu_4(bpy)_4(OH)_4(H_2O)_2](C_8H_4O_4)_2{\cdot}6H_2O$	1	98.00/99.36/100.25[f] 88.44/90.96[g] 101.94/104.25[g]	1.918	2.2	86.2	6.4	[49]
2[d]	$[Cu_4(bpy)_4(OH)_4(dca)_2](dca)_2{\cdot}bpy{\cdot}2H_2O$	1	95.99/99.66[f] 96.25/110.76[g]	1.940	2.288	18.1	0.61	this work

[a] See Fig. 8.
[b] Model with J_1 and J'_1 (see Fig. 8).
[c] Isolated dimers model ($J_2 = 0$).
[d] Interacting dimers model ($J_1 >> J_2$).
[e] Curie–Weiss model.
[f] Cu–O–Cu bond angles corresponding to J_1.
[g] Cu–O–Cu bond angles corresponding to J_2.
[h] Average Cu–O bond distances corresponding to J_1.

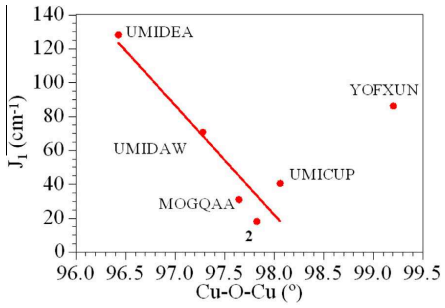

Fig. 9. Correlation between the average Cu–O–Cu bond angle corresponding to J_1 and the J_1 value found in **type 1** compounds of Table 7 with the interacting dimer model. Solid line is the linear fit to the data of all compounds except YOFXUN.

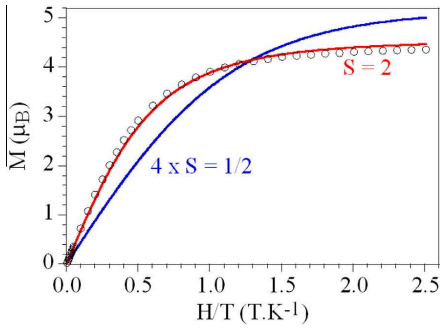

Fig. 10. Isothermal magnetization at 2 K for compound **2**. Solid lines are the Brillouin functions used to fit the data.

intermolecular contacts revealed strong hydrogen bonding interactions in both complexes, leading to 3D and 2D arrangements in **1** and **2** respectively. In addition, several attempts to prepare the hepta- and the tetranuclear clusters using other cyanocarbanions or other halogen anions failed. These results suggest that the role of such anions is not limited to ensure the packing cohesion but also to stabilize the cluster conformation.

Acknowledgments

We acknowledge the CNRS ("Centre National de la Recherche Scientifique"), the Brest University, the "Agence Nationale de la Recherche" (ANR project BISTA-MAT: ANR-12-BS07-0030-01), the French Ministère de la Recherche et Ministère des Affaires Etrangères et Européennes (PHC MAGHREB Project No 30255ZJ)", the Spanish MINECO (Project CTQ2011-26507), and the Generalitat Valenciana (projects Prometeo II/2014/076 and ISIC). Authors especially thank the "Service Commun" of NMR facilities of the University of Brest.

Appendix A.

Electronic Supplementary Information (ESI) available: This material is available free of charge via the Internet. CCDC 165568 and 1060081 (**1** and **2**, respectively) contains the supplementary crystallographic data for this paper. These data can be obtained free of charge from The Cambridge Crystallographic Data Centre via www.ccdc.cam.ac.uk/data_request/cif. See DOI: http://dx.doi.org/10.1039/b000000x/.

References

[1] G.F.S. Whitehead, J. Ferrando-Soria, L.G. Christie, N.F. Chilton, G.A. Timco, F. Moro, R.E.P. Winpenny, Chem. Sci. 5 (2014) 235.
[2] D.I. Alexandropoulos, A. Fournet, L. Cunha-Silva, A.M. Mowson, V. Bekiari, G. Christou, T.C. Stamatatos, Inorg. Chem. 53 (2014) 5420.
[3] T.R. Cook, Y. Zheng, P.J. Stang, Chem. Rev. 113 (2013) 734.
[4] G.F.S. Whitehead, F. Moro, G.A. Timco, W. Wernsdorfer, S.J. Teat, R.E.P. Winpenny, Angew. Chem., Int. Ed. 52 (2013) 9932.
[5] E.S. Koumousi, A. Routzomani, T.N. Nguyen, D.P. Giannopoulos, C.P. Raptopoulou, V. Psycharis, G. Christou, T.C. Stamatatos, Inorg. Chem. 52 (2013) 1176.
[6] C. Lampropoulos, M. Murugesu, A.G. Harter, W. Wernsdofer, S. Hill, N.S. Dalal, A.P. Reyes, P.L. Kuhns, K.A. Abboud, G. Christou, Inorg. Chem. 52 (2013) 258.
[7] V. Chandrasekhar, T. Senapati, A. Dey, E. Carolina Sañudo, Inorg. Chem. 50 (2011) 1420.
[8] Y. Zheng, M. Evangelisti, R.E.P. Winpenny, Angew. Chem., Int. Ed. 50 (2011) 3692.
[9] M. Murugesu, R. Clerac, C. Anson, A. Powell, Inorg. Chem. 43 (2004) 7269.
[10] M. Morse, Chem. Rev. 86 (1986) 1049.
[11] D.N. Woodruff, R.E.P. Winpenny, R.A. Layfield, Chem. Rev. 113 (2013) 5110.
[12] R. Sessoli, D. Gatteschi, A. Caneschi, M.A. Novak, Nature 365 (1993) 141.
[13] Y. Zheng, G. Zhou, Z. Zheng, R.E.P. Winpenny, Chem. Soc. Rev. 43 (2014) 1462.
[14] A.M. Kirillov, M.V. Kirillova, A.J.L. Pombeiro, Coord. Chem. Rev. 256 (2012) 2741.
[15] T. Shima, Y. Luo, T. Stewart, R. Bau, G.J. McIntyre, S.A. Mason, Z. Hou, Nat. Chem. 3 (2011) 814.
[16] M. Kuczer, M. Blaszak, E. Czarniewska, G. Rosinski, T. Kowalik-Jankowska, Inorg. Chem. 52 (2013) 5951.
[17] C.J. Gómez-García, E. Coronado, P. Gomez-Romero, N. Casañ-Pastor, Inorg. Chem. 32 (1993) 89.
[18] S. Thakurta, P. Roy, G. Rosair, C.J. Gómez-García, E. Garribba, S. Mitra, Polyhedron 28 (2009) 695.
[19] S. Naiya, C. Biswas, M.G.B. Drew, C.J. Gómez-García, J.M. Clemente-Juan, A. Ghosh, Inorg. Chem. 49 (2010) 6616.
[20] S. Basak, S. Sen, P. Roy, C.J. Gómez-García, D.L. Hughes, R.J. Butcher, E. Garribba, S. Mitra, Aust. J. Chem. 63 (2010) 479.
[21] S. Naiya, S. Biswas, M.G.B. Drew, C.J. Gómez-García, A. Ghosh, Inorg. Chim. Acta 377 (2011) 26.
[22] S. Shit, S.K. Dey, C. Rizzoli, E. Zangrando, G. Pilet, C.J. Gómez-García, S. Mitra, Inorg. Chim. Acta 370 (2011) 18.
[23] Z.G. Han, Y.L. Zhao, J. Peng, C.J. Gómez-García, Inorg. Chem. 46 (2007) 5453.
[24] M.Y. Wei, R.D. Willett, C.J. Gómez-García, Inorg. Chem. 43 (2004) 4534.
[25] A. Ray, D. Sadhukhan, G.M. Rosair, C.J. Gómez-García, S. Mitra, Polyhedron 28 (2009) 3542.
[26] S. Thakurta, C. Rizzoli, R.J. Butcher, C.J. Gómez-García, E. Garribba, S. Mitra, Inorg. Chim. Acta 363 (2010) 1395.
[27] A. Biswas, M.G.B. Drew, C.J. Gómez-García, A. Ghosh, Inorg. Chem. 49 (2010) 8155.
[28] S. Saha, A. Sasmal, C. Roy Choudhury, C.J. Gómez-García, E. Garribba, S. Mitra, Polyhedron 69 (2014) 262–269.
[29] C.J. Gómez-García, E. Coronado, J.J. Borrás-Almenar, Inorg. Chem. 31 (1992) 1667.
[30] H.S. Liu, C.J. Gómez-García, J. Peng, Y.H. Feng, Z.M. Su, J.Q. Sha, L.X. Wang, Inorg. Chem. 46 (2007) 10041.
[31] S. Banerjee, S. Sen, J. Chakraborty, R.J. Butcher, C.J. Gómez-García, R. Puchta, S. Mitra, Aust. J. Chem. 62 (2009) 1614.
[32] A. Ray, S. Mitra, A.D. Khalaji, C. Atmani, N. Cosquer, S. Triki, J.M. Clemente-Juan, S. Cardona-Serra, C.J. Gómez-García, R.J. Butcher, E. Garribba, D. Xu, Inorg. Chim. Acta 363 (2010) 3580.
[33] A. Ray, G.M. Rosair, G. Pilet, B. Dede, C.J. Gómez-García, S. Signorella, S. Bellú, S. Mitra, Inorg. Chim. Acta 375 (2011) 20.
[34] W. Cañón-Mancisidor, C.J. Gómez-García, G. Minguez Espallargas, A. Vega, E. Spodine, D. Venegas-Yazigi, E. Coronado, Chem. Sci. 5 (2014) 324–332.
[35] S. Triki, F. Thetiot, J.S. Pala, S. Golhen, J.M. Clemente-Juan, C.J. Gómez-García, E. Coronado, Chem. Commun. (2001) 2172.
[36] S. Delgado, P.J.S. Miguel, J.L. Priego, R. Jimenez-Aparicio, C.J. Gómez-García, F. Zamora, Inorg. Chem. 47 (2008) 9128.
[37] G.A. Bain, J.F. Berry, J. Chem. Educ. 85 (2008) 532.
[38] R.A. Carboni, Org. Synth. 39 (1959) 64.
[39] M. Sheldrick, SHELX97. Programs for Crystal Structure Analysis, University of Göttingen, Göttingen, Germany, 1997.
[40] International Tables for X-ray Crystallography, Vol. 4, Kynoch Press, Birmingham, 1975.
[41] O.V. Dolomanov, L.J. Bourhis, R.J. Gildea, J.A.K. Howard, H. Puschmann, J. Appl. Crystallogr. 42 (2009) 339.
[42] F. Setifi, A. Bouchama, J. Sala-Pala, J. Salaun, S. Triki, Inorg. Chim. Acta 359 (2006) 3269.
[43] F. Setifi, S. Benmansour, S. Triki, C.J. Gómez-García, M. Marchivie, J.Y. Salaun, M. Mustapha, Inorg. Chim. Acta 360 (2007) 3879.

[44] A.W. Addison, T.N. Rao, J. Chem. Soc., Dalton Trans. (1984) 1349.
[45] J. Song, Y. Chen, Z. Li, R. Zhou, X. Xu, J. Xu, T. Wang, Polyhedron 26 (2007) 4397.
[46] M. Sarkar, R. Clérac, C. Mathonière, N.G.R. Hearns, V. Bertolasi, D. Ray, Inorg. Chem. 49 (2010) 6575.
[47] S. Gou, M. Qian, Z. Yu, C. Duan, X. Sun, W. Huang, J. Chem. Soc., Dalton Trans. (2001) 3232.
[48] G.A. van Albada, I. Mutikainen, O. Roubeau, U. Turpeinen, J. Reedijk, Inorg. Chim. Acta 331 (2002) 208.
[49] Y. Zheng, D. Cheng, B. Liu, W. Huang, Dalton Trans. 40 (2011) 277.
[50] E. Ruiz, P. Alemany, S. Alvarez, J. Cano, Inorg. Chem. 36 (1997) 3683.
[51] E. Ruiz, P. Alemany, S. Alvarez, J. Cano, J. Am. Chem. Soc. 119 (1997) 1297.
[52] A. Rodriguez-Fortea, E. Ruiz, S. Alvarez, P. Alemany, Dalton Trans. (2005) 2624.
[53] V.H. Crawford, H.W. Richardson, J.R. Wasson, D.J. Hodgson, W.E. Hatfield, Inorg. Chem. 15 (1976) 2107.
[54] P.J. Hay, J.C. Thibeault, R. Hoffmann, J. Am. Chem. Soc. 97 (1975) 4884.

Annexe 2

Données cristallographiques

$[Cu(L'2)]^{2+}$

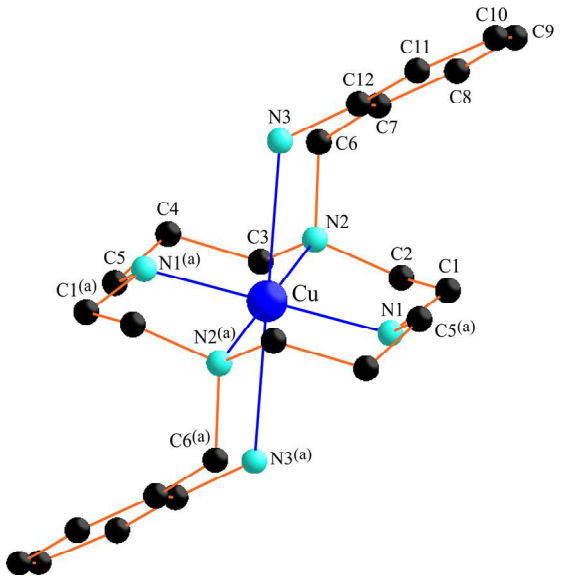

Tableau 1 Longueurs de liaisons en Å à 293K

	$[Cu(L'2)](BF_4)_2$		$[Cu(L'2)](BF_4)_2$
Cu1-N1	2.021(4)	C7-C8	1.387(8)
Cu1-N1^a	2.021(4)	C7-C12	1.393(8)
Cu1-N2^a	2.059(5)	C7-C6	1.493(8)
Cu1-N2	2.059(5)	C12-C11	1.377(8)
N2-C2	1.483(7)	C8-C9	1.360(10)
N2-C6	1.510(7)	C4-C3	1.503(9)
N2-C3	1.519(7)	C4-C5	1.506(9)
N1-C1	1.470(7)	C1-C2	1.519(8)
N1-C5^a	1.493(7)	C11-C10	1.393(10)
N3-C12	1.417(8)	C9-C10	1.374(11)
		C5-N1^a	1.493(7)

Position équivalente $^{(a)}$ –x+2;-y ;-z+2

Tableau 2 Angles (°) de liaison

	$[Cu(L'2)](BF_4)_2$		$[Cu(L'2)](BF_4)_2$
N1-Cu1-N1[(a)]	180.0	C8-C7-C6	119.8(6)
N1-Cu1-N2[(a)]	93.4(2)	C12-C7-C6	122.8(5)
N1[(a)]-Cu1-N2[(a)]	86.6(2)	C11-C12-C7	120.0(6)
N1-Cu1-N2	86.6(2)	C11-C12-N3	121.6(7)
N1[(a)]-Cu1-N2	93.4(2)	C7-C12-N3	118.3(6)
N2[(a)]-Cu1-N2	180.000(1)	C9-C8-C7	123.5(8)
C2-N2-C6	111.7(5)	C3-C4-C5	113.9(5)
C2-N2-C3	108.0(5)	N1-C1-C2	109.4(5)
C6-N2-C3	106.3(4)	C7-C6-N2	115.6(5)
C2-N2-Cu1	104.2(4)	C4-C3-N2	116.2(5)
C6-N2-Cu1	116.6(3)	C12-C11-C10	120.5(8)
C3-N2-Cu1	109.8(3)	C8-C9-C10	118.4(7)
C1-N1-C5[(a)]	111.2(5)	N2-C2-C1	111.8(5)
C1-N1-Cu1	109.4(4)	N1[(a)]-C5-C4	112.8(5)
C5[(a)]-N1-Cu1	116.7(4)	C9-C10-C11	120.1(8)
C8-C7-C12	117.4(6)		

Position équivalente [(a)] –x+2;-y ;-z+2

$[Fe(aqin)_2(\mu^2\text{-}M(CN)_4)]$

Tableau 3 Longueurs de liaisons en Å à 293K et 120K

	$[Fe(amq)_2(\mu^2\text{-}M(CN)_4)]$				
Liaisons	293K	120K	Liaisons	293K	120K
Pd-C(10)	1.977(3)	1.990(2)	C(4)-C(3)	1.415(4)	1.419(3)
PdC(10)#1	1.977(3)	1.990(2)	C(3)-C(2)	1.338(5)	1.362(3)
PdC(11)#1	1.988(3)	1.995(2)	C(3)-H(3)	0.9300	0.9300
Pd-C(11)	1.988(3)	1.995(2)	C(1)-C(2)	1.400(4)	1.408(3)
Fe-N(3)	2.158(2)	1.9432(17)	C(1)-H(1)	0.9300	0.9300
Fe-N(3)#2	2.158(2)	1.9432(17)	C(2)-H(2)	0.9300	0.9300
Fe-N(1)#2	2.168(2)	1.9864(17)	C(8)-C(7)	1.357(4)	1.360(3)
Fe-N(1)	2.168(2)	1.9864(17)	C(8)-N(2)	1.447(3)	1.452(3)
Fe-N(2)#2	2.197(2)	2.0274(17)	C(6)-C(5)	1.352(4)	1.363(3)
Fe-N(2)	2.197(2)	2.0274(17)	C(6)-C(7)	1.402(5)	1.417(3)
C(11)-N(4)	1.137(3)	1.144(3)	C(6)-H(6)	0.9300	0.9300
N(1)-C(1)	1.320(3)	1.327(3)	C(7)-H(7)	0.9300	0.9300
N(1)-C(9)	1.363(3)	1.373(3)	C(5)-H(5)	0.9300	0.9300
C(9)-C(4)	1.411(4)	1.409(3)	N(2)-H(2A)	0.9000	0.9000
C(9)-C(8)	1.413(3)	1.414(3)	N(2)-H(2B)	0.9000	0.9000
C(4)-C(5)	1.406(4)	1.417(3)	N(3)-C(10)	1.147(3)	1.149(3)

Position équivalente #1–x;-y ;-z #2 –x,-y,-z+1

Tableau 4 Angles (°) de liaison Position équivalente #1–x;-y ;-z #2 –x,-y,-z+1

[Fe(amq)$_2$(μ^2-M(CN)$_4$)]

Liaisons	293K	120K	Liaisons	293K	120K
C(10)-Pd-C(10)#1	180.0(2)	180.00(17)	C(5)-C(4)-C(3)	124.1(3)	124.4(2)
C(10)-Pd-C(11)#1	87.69(11)	86.12(8)	C(2)-C(3)-C(4)	119.8(3)	119.2(2)
C(10)#1-Pd-C(11)#1	92.31(11)	93.88(8)	C(2)-C(3)-H(3)	120.1	120.4
C(10)-Pd-C(11)	92.31(11)	93.88(8)	C(4)-C(3)-H(3)	120.1	120.4
C(10)#1-Pd-C(11)	87.69(11)	86.12(8)	N(1)-C(1)-C(2)	122.9(3)	123.0(2)
C(11)#1-Pd-C(11)	180.0(2)	180.00(16)	N(1)-C(1)-H(1)	118.5	118.5
N(3)-Fe-N(3)#2	180.0	180.0	C(2)-C(1)-H(1)	118.5	118.5
N(3)-Fe-N(1)#2	92.45(9)	92.43(7)	C(3)-C(2)-C(1)	119.8(3)	119.9(2)
N(3)#2-Fe-N(1)#2	87.55(9)	87.57(7)	C(3)-C(2)-H(2)	120.1	120.0
N(3)-Fe-N(1)	87.55(9)	87.57(7)	C(1)-C(2)-H(2)	120.1	120.0
N(3)#2-Fe-N(1)	92.45(9)	92.43(7)	C(7)-C(8)-C(9)	119.5(3)	120.06(19)
N(1)#2-Fe-N(1)	180.0	180.00(7)	C(7)-C(8)-N(2)	123.1(2)	124.35(19)
N(3)-Fe-N(2)#2	87.14(8)	86.03(7)	C(9)-C(8)-N(2)	117.4(2)	115.56(18)
N(3)#2-Fe-N(2)#2	92.86(8)	93.97(7)	C(5)-C(6)-C(7)	121.0(3)	120.5(2)
N(1)#2-Fe-N(2)#2	77.36(8)	83.12(7)	C(5)-C(6)-H(6)	119.5	119.7
N(1)-Fe-N(2)#2	102.64(8)	96.88(7)	C(7)-C(6)-H(6)	119.5	119.7
N(3)-Fe-N(2)	92.86(8)	93.97(7)	C(8)-C(7)-C(6)	120.6(3)	120.2(2)
N(3)#2-Fe-N(2)	87.14(8)	86.03(7)	C(8)-C(7)-H(7)	119.7	119.9
N(1)#2-Fe-N(2)	102.64(8)	96.88(7)	C(6)-C(7)-H(7)	119.7	119.9
N(1)-Fe-N(2)	77.36(8)	83.12(7)	C(6)-C(5)-C(4)	120.2(3)	120.5(2)
N(2)#2-Fe-N(2)	180.0	180.00(9)	C(6)-C(5)-H(5)	119.9	119.7
N(4)-C(11)-Pd	178.0(3)	176.30(19)	C(4)-C(5)-H(5)	119.9	119.7
C(1)-N(1)-C(9)	118.2(3)	117.41(18)	C(8)-N(2)-Fe	109.82(15)	109.43(12)
C(1)-N(1)-Fe	127.6(2)	129.07(15)	C(8)-N(2)-H(2A)	109.7	109.8
C(9)-N(1)-Fe	113.93(17)	113.52(13)	Fe-N(2)-H(2A)	109.7	109.8
N(1)-C(9)-C(4)	122.1(2)	123.17(19)	C(8)-N(2)-H(2B)	109.7	109.8
N(1)-C(9)-C(8)	118.3(2)	116.76(18)	Fe-N(2)-H(2B)	109.7	109.8
C(4)-C(9)-C(8)	119.6(2)	120.06(19)	H(2A)-N(2)-H(2B)	108.2	108.2
C(9)-C(4)-C(5)	118.8(3)	118.5(2)	C(10)-N(3)-Fe	143.0(2)	157.80(16)
C(9)-C(4)-C(3)	124.1(3)	117.1(2)	N(3)-C(10)-Pd	174.2(2)	168.06(18)

[Fe(trz-py)(tcpd)(H$_2$O)]

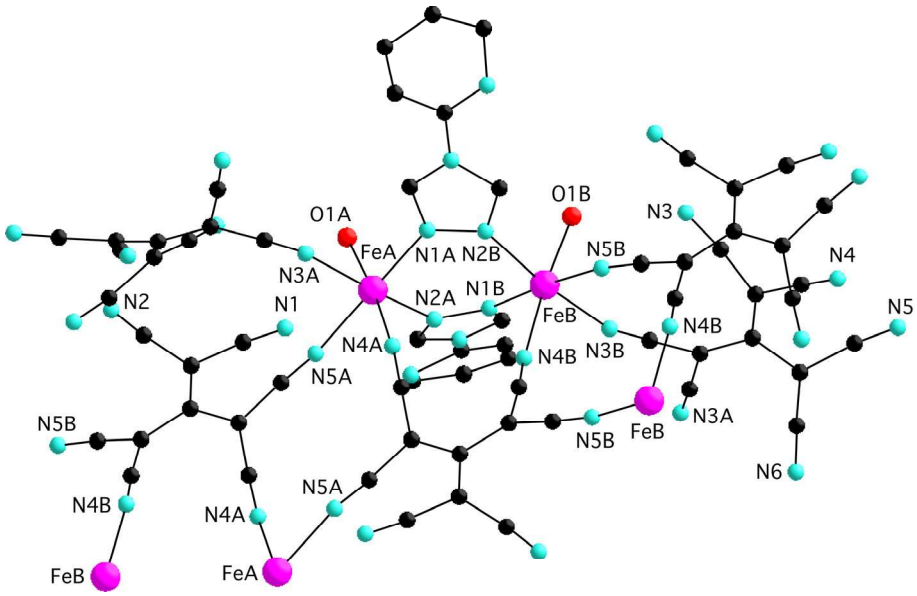

Tableau 5 Longueurs de liaisons en Å à 150K

Liaisons	150K	Liaisons	150K	Liaisons	150K
FeA-O(1A)	2.098(14)	C(18)-C(19)	1.43(2)	N(8)-C(9)	1.35(2)
FeA-N(4A)	2.118(15)	C(20)-C(21)	1.31(2)	N(8)-C(11)	1.41(2)
FeA-N(3A)	2.151(19)	C(20)-C(19)	1.41(2)	C(24)-C(25)	1.50(3)
FeA-N(1A)	2.159(17)	C(20)-C(24)	1.47(3)	C(35)-N(1)	1.21(3)
FeA-N(5A)#1	2.188(16)	N(2A)-C(9)	1.29(2)	C(6)-C(7)	1.28(3)
FeA-N(2A)	2.222(15)	N(1A)-C(2)	1.36(3)	C(4)-C(3)	1.29(3)
FeB-O(1B)	2.091(17)	N(1A)-N(2B)	1.42(2)	C(7)-N(1C)	1.52(4)
FeB-N(5B)#2	2.107(14)	N(2B)-C(1)	1.34(2)	C(1)-N(7)	1.41(2)
FeB-N(3B)#3	2.150(17)	N(5)-C(25)	1.12(2)	N(1C)-C(3)	1.31(4)
FeB-N(4B)	2.185(16)	C(36)-C(34)	1.45(3)	N(7)-C(2)	1.32(2)
FeB-N(1B)	2.186(14)	C(31)-C(33)	1.41(2)	N(7)-C(3)	1.38(3)
FeB-N(2B)	2.206(15)	C(31)-C(32)	1.42(2)	C(14)-C(13)	1.41(3)
N(2)-C(36)	1.10(2)	C(31)-C(30)	1.43(3)	N(2C)-C(13)	1.29(3)
C(10)-N(1B)	1.29(2)	C(15)-C(14)	1.32(3)	N(2C)-C(11)	1.51(3)
C(10)-N(8)	1.31(2)	C(15)-C(16)	1.42(3)	C(30)-C(28)	1.46(2)
C(27)-N(4A)	1.13(2)	C(19)-C(17)	1.48(2)	C(28)-C(29)	1.43(3)

C(27)-C(28)	1.40(3)	C(34)-C(30)	1.31(2)	C(29)-N(5A)	1.11(2)
N(1B)N(2A)	1.378(19)	C(34)-C(35)	1.48(3)	N(5A)-FeA1	2.188(16)
C(26)-N(6)	1.15(2)	C(5)-C(4)	1.35(3)	N(3B)-FeB4	2.150(17)
C(26)-C(24)	1.35(3)	C(5)-C(6)	1.47(3)	C(33)-N(5B)	1.20(2)
C(22)-N(3)	1.24(2)	C(21)-C(23)	1.46(2)	N(5B)-FeB2	2.107(14)
C(22)-C(21)	1.38(2)	N(4B)-C(32)	1.097(19)		
N(3A)-C(17)	1.11(2)	C(23)-N(4)	1.17(2)		
C(18)-N(3B)	1.16(2)	C(16)-C(11)	1.21(3)		

Positions équivalentes : #1 -x+1,-y,-z+2 #2 -x+1,-y,-z+1 #3 -x+1/2,y-1/2,-z+3/2 #4 -x+1/2,y+1/2,-z+3/2

Tableau 6 Angles de liaisons en (°) à 150K

Angle	150K	Angle	150K
O(1A)-FeA-N(4A)	175.2(6)	N(4A)-C(27)-C(28)	175(2)
O(1A)-FeA-N(3A)	84.0(6)	C(10)-N(1B)-N(2A)	105.9(15)
N(4A)-FeA-N(3A)	93.7(6)	C(10)-N(1B)-FeB	128.6(13)
O(1A)-FeA-N(1A)	94.6(6)	N(2A)-N(1B)-FeB	125.1(11)
N(4A)-FeA-N(1A)	89.4(6)	N(6)-C(26)-C(24)	176(2)
N(3A)-FeA-N(1A)	88.8(7)	C(27)-N(4A)-FeA	158.4(15)
O(1A)-FeA-N(5A)	90.3(6)	N(3)-C(22)-C(21)	175(2)
N(4A)-FeA-N(5A)	85.5(6)	C(17)-N(3A)-FeA	166.5(18)
N(3A)-FeA-N(5A)	88.1(6)	N(3B)-C(18)-C(19)	178(2)
N(1A)-FeA-N(5A)	173.9(6)	C(21)-C(20)-C(19)	118.4(17)
O(1A)-FeA-N(2A)	84.5(5)	C(21)-C(20)-C(24)	124.2(18)
N(4A)-FeA-N(2A)	97.6(5)	C(19)-C(20)-C(24)	117.4(18)
N(3A)-FeA-N(2A)	168.1(6)	C(9)-N(2A)-N(1B)	106.7(16)
N(1A)-FeA-N(2A)	95.1(6)	C(9)-N(2A)-FeA	120.0(13)
N(5A)1-FeA-N(2A)	89.0(6)	N(1B)-N(2A)-FeA	130.7(11)
O(1B)-FeB-N(5B)#2	90.7(6)	C(2)-N(1A)-N(2B)	104.8(15)
O(1B)-FeB-N(3B)#3	85.7(7)	C(2)-N(1A)-FeA	124.2(14)
N(5B)#2-FeB-N(3B)#3	87.4(6)	N(2B)-N(1A)-FeA	130.0(12)
O(1B)-FeB-N(4B)	174.7(6)	C(1)-N(2B)-N(1A)	108.0(15)

N(5B)#2-FeB-N(4B)	85.2(6)	C(1)-N(2B)-FeB	124.4(13)
N(3B)#3-FeB-N(4B)	90.8(6)	N(1A)-N(2B)-FeB	127.0(11)
O(1B)-FeB-N(1B)	91.0(6)	N(2)-C(36)-C(34)	172(2)
N(5B)#2-FeB-N(1B)	175.2(5)	C(33)-C(31)-C(32)	110.6(17)
N(3B)#3-FeB-N(1B)	88.3(6)	C(33)-C(31)-C(30)	121.8(17)
N(4B)-FeB-N(1B)	92.9(6)	C(32)-C(31)-C(30)	127.3(16)
O(1B)-FeB-N(2B)	88.9(6)	C(14)-C(15)-C(16)	120(2)
N(5B)#2-FeB-N(2B)	88.0(6)	C(20)-C(19)-C(18)	122.6(17)
N(3B)#3-FeB-N(2B)	172.9(6)	C(20)-C(19)-C(17)	1.29(2)
N(4B)-FeB-N(2B)	94.2(6)	C(18)-C(19)-C(17)	1.36(3)
N(1B)-FeB-N(2B)	96.5(5)	C(30)-C(34)-C(36)	1.42(2)
N(1B)-C(10)-N(8)	112.5(18)	C(30)-C(34)-C(35)	1.34(2)

Angle	293K	Angle	293K
C(36)-C(34)-C(35)	111.3(1)	N(1C)-C(3)-N(7)	122(3)
C(4)-C(5)-C(6)	117(3)	C(15)-C(14)-C(13)	121(2)
C(20)-C(21)-C(22)	123.9(1)	C(13)-N(2C)-C(11)	116(2)
C(20)-C(21)-C(23)	123.2(1)	N(7)-C(2)-N(1A)	112.6(19)
C(22)-C(21)-C(23)	112.3(1)	N(2A)-C(9)-N(8)	110.6(19)
C(32)-N(4B)-FeB	161.8(1)	C(16)-C(11)-N(8)	118(2)
N(4)-C(23)-C(21)	177(2)	C(16)-C(11)-N(2C)	123(2)
C(11)-C(16)-C(15)	119(2)	N(8)-C(11)-N(2C)	118.1(18)
C(10)-N(8)-C(9)	104.3(17)	N(3A)-C(17)-C(19)	175(2)
C(10)-N(8)-C(11)	122.7(1)	N(2C)-C(13)-C(14)	120(3)
C(9)-N(8)-C(11)	132.5(18)	C(34)-C(30)-C(31)	122.2(16)
C(26)-C(24)-C(20)	125(2)	C(34)-C(30)-C(28)	120.5(17)
C(26)-C(24)-C(25)	119.1(1)	C(31)-C(30)-C(28)	116.9(16)
C(20)-C(24)-C(25)	116.3(1)	C(27)-C(28)-C(29)	116.5(16)
N(1)-C(35)-C(34)	171(2)	C(27)-C(28)-C(30)	123.7(18)
C(7)-C(6)-C(5)	128(3)	C(29)-C(28)-C(30)	119.7(17)
C(3)-C(4)-C(5)	120(3)	N(5A)-C(29)-C(28)	175.0(19)
N(5)-C(25)-C(24)	170(2)	C(29)-N(5A)-FeA#1	169.4(15)
N(4B)-C(32)-C(31)	176.7(1)	C(18)-N(3B)-FeB#4	164.3(16)

C(6)-C(7)-N(1C)	108(3)	N(5B)-C(33)-C(31)	175(2)
N(2B)-C(1)-N(7)	108.3(18)	C(33)-N(5B)-FeB#2	167.4(14)
C(3)-N(1C)-C(7)	124(3)		
C(2)-N(7)-C(3)	123(2)		
C(2)-N(7)-C(1)	106.2(18)		
C(3)-N(7)-C(1)	130(2)		
C(4)-C(3)-N(1C)	122(3)		
C(4)-C(3)-N(7)	116(2)		

Positions équivalentes : #1 -x+1,-y,-z+2 #2 -x+1,-y,-z+1 #3 -x+1/2,y-1/2,-z+3/2 #4 -x+1/2,y+1/2,-z+3/2

Résumé

Depuis quelques années, les matériaux à transition de spin présentant une bistabilité thermique ou photoinduite sont très étudiés en raison des applications futures potentielles pour le stockage de l'information. Dans ce contexte, ce travail a pour objectif la synthèse de nouveaux systèmes bistables du fer (II). Pour ce faire, deux stratégies ont été utilisées : l'une consiste à augmenter les interactions intramoléculaires en substituant le contre-ion d'un système à transition de spin, l'autre consiste à associer un ligand neutre polydentate à un co-ligand anionique pontant.

Dans une première partie, la modification du contre-ion a permis l'obtention d'un système discret mononucléaire à base d'un ligand macrocyclique présentant de la bistabilité thermique. Le second système discret est un complexe dinucléaire à base du ligand tmpa (triméthylpyridyl amine) qui a permis de mettre en avant les effets de la substitution du ligand sur les caractéristiques de la transition de spin.

Dans un deuxième temps, nous nous sommes orientés vers la synthèse de systèmes à structures étendues en utilisant des ligands anioniques rigides pontants de type tétracyanométallate $[M(CN)_4]^{2-}$ associés au ligand organique 8-aminoquinoléine (aqin). Cette association a conduit à l'obtention de chaînes monodimensionnelles présentant une transition abrupte avec hystérésis.

Enfin, pour obtenir des systèmes bi- et tri-dimensionnels, nous avons associé le ligand 4-(2-pyridyl)-1,2,4, 4H-triazole (trz-py), potentiellement pontant, aux ligands anioniques $(tcpd)^{2-}$ et $[Pt(CN)_4]^{2-}$. Le système $[Fe(trz\text{-}py)_2(Pt(CN)_4)].3H_2O$ obtenu est un réseau 2D de type Hofmann avec des propriétés magnétiques et photo-magnétiques originales se distinguant par la présence d'une hystérésis cachée révélée par photo-irradiation.

Mots-clés: transition de spin, bistabilité thermique et photo-induite, hystérésis, réseau d'Hofmann

Abstract

In recent years, Spin Crossover materials (SCO) with thermal or light induced bistability are extensively studied because of their futur potential applications in memory display devices. In this context, the aim of this work is the synthesis of bistable new spin crossover systems based on Fe(II). Two strategies were used: the first one is to increase the intramolecular interactions by substituting the counter-ion nature in a spin crossover system, the second one is to associate a neutral ligand to a bridging polydentate co-ligand.

In the first part, the modification of the counter-ion enabled us to obtain a discrete mononuclear system based on macrocycle ligand with thermal bistability. The second discrete system is a dinuclear complex based on tmpa (trimethylpyridyl amine) which led us to study ligand substitution effects of the Spin Cross-Over behaviour.

In the second part, the aim is the synthesis of extended structures systems by using rigid anionic bridging ligands like tetracyanometallate anions $[M(CN)_4]^{2-}$ and the organic ligand quinolin-8-amine. This association allowed to obtain 1D chains with abrupt spin crossover presenting hysteresis.

Finally, to synthesise SCO 2D and 3D systems, we have associated the potentially bridging 4-(2-pyridyl)-1,2,4,4H-triazole (trz-py) ligand to inorganic bridging anions $tcpd^{2-}$ and $[Pt(CN)_4]^{2-}$. The $[Fe(trz\text{-}py)_2(Pt(CN)_4)].3H_2O$ system obtained is as Hofmann-like 2D network with novel magnetic and photomagnetic properties with hidden hysteresis revealed by photo-switching.

Key words: Spin Cross-over, thermical and photo-induced bistability, hysteresis, Hofmann network.